Searching for Dark Matter with the Antares Neutrino Telescope

Academisch Proefschrift

ter verkrijging van de graad van doctor
aan de Universiteit van Amsterdam
op gezag van de Rector Magnificus
prof. dr. D.C. van den Boom,
ten overstaan van een door het college voor promoties
ingestelde commissie, in het openbaar te verdedigen
in de Agnietenkapel
op donderdag 26 mei 2011, te 10:00 uur

door

Gordon Max Alphonsius Lim

geboren te Mission Viejo, Verenigde Staten van Amerika

Promotores :	Prof. Dr. P. M. Kooijman
	Prof. Dr. M. de Jong
Overige leden :	Prof. Dr. S. C. M. Bentvelsen
	Prof. Dr. B. van Eijk
	Prof. Dr. K. J. F. Gaemers
	Prof. Dr. U. F. Katz
	Prof. Dr. Ir. E. N. Koffeman
	Dr. D. F. E. Samtleben
	Dr. E. de Wolf

Faculteit der Natuurwetenschappen, Wiskunde en Informatica

Cover: Gordon Lim.

Top image courtesy of the Solar and Heliospheric Observatory, which orbits and monitors the Sun at the L1 Earth-Sun Lagrange point. The image was made with the Extreme Ultraviolet Imaging Telescope and shows the solar atmosphere and inner corona at a wavelength of 17.1 nm.

Bottom photograph courtesy of David Monniaux. The photograph shows the view from Mont Faron, France, over the city of Toulon and its harbor. The ANTARES detector is located 40 km offshore at the bottom of the Mediterranean Sea. The ANTARES control station is located at La Seyne-sur-Mer, close to where the peninsula in the middle of the photograph (Mandrier) is connected to the mainland.

Printed by Ipskamp Drukkers B.V.

ISBN 978-90-9026162-1

Aan mijn ouders

Contents

Introduction

In the 19th century, some astrophysicists noted that there was something unusual in the behaviour of the planet Uranus : Its observed motion differed from what Newtonian gravity predicted. In order to explain the disagreement, British and French astronomers John Couch and Urbain Le Verrier both independently hypothesized in 1846 the existence of a new planet that gravitationally influenced Uranus' orbit. The same year, Neptune was discovered at the position predicted by Couch and Le Verrier. Strange behaviour was also noted in the case of the planet Mercury : The precession of its perihelion was larger than what is predicted by Newtonian gravity. In 1859, Le Verrier tried the same approach as for Uranus and postulated that the excess was due to the presence of a new planet : Vulcan. However, subsequent attempts to observe this new planet failed and the discrepancy was not resolved until German physicist Albert Einstein introduced his theory of general relativity in 1916.

Today, a similar disagreement between the theory of gravity and experimental observations exists. During the past decades, a large amount of evidence has been accumulated which indicates that only a small fraction of the total matter content of the Universe resides in ordinary matter. As with the planetary problems in the 19th century, there are two solutions to explain the apparent absence of luminous matter in the Universe : A change in the theory of gravity versus the introduction of an invisible type of mass. The former implies that the Newtonian theory of gravity is not valid for small accelerations. Although the theory can be modified to correct for the observations [1], it results in an effective theory that is not based on fundamental principles. The second approach, in which the Universe is believed to contain a substantial amount of invisible matter, is more widely accepted. This invisible matter is called *dark matter* [2]. The existence of dark matter can be explained by new kinds of elementary particles produced in the early Universe. The most favoured class of dark matter candidates are *weakly interacting massive particles* (WIMPs), which are postulated to exist in many new theories that extend the Standard Model of elementary particles. A particularly well-motivated example of such a theory is *supersymmetry*.

The hypothesis that WIMP dark matter pervades our Galaxy can be experimentally verified in a number of ways. One particular way to study WIMP dark matter in our Galaxy is to use neutrinos. WIMP dark matter is expected to self-interact at the centre of massive astrophysical objects such as the Earth, the Sun and the Galaxy. Due to their unique nature, high energy neutrinos produced in the annihilation of WIMPs are able to escape from the centre of these objects and point straight back to their source. Hence, these high-energy neutrino fluxes could be detectable with sufficiently massive neutrino detectors on Earth such as the ANTARES deep-sea neutrino telescope, currently the largest operating neutrino detector in the Northern Hemisphere.

Outline

This thesis is organised as follows. The existence of dark matter in our Universe is discussed in chapter 1, followed by an overview of the WIMP dark matter scenario and the various WIMP detection possibilities. Chapter 2 gives a brief overview of supersymmetry and its prime dark matter candidate, the neutralino. Chapter 3 addresses WIMP capture and annihilation in massive astrophysical objects. In particular, the neutrino energy spectra from WIMP annihilation in the centre of the Earth and the Sun are calculated using Monte Carlo simulations. Chapter 4 concentrates on various aspects of neutralino dark matter. In particular, the neutrino fluxes from neutralino annihilation in the Sun and the Earth are calculated using Monte Carlo simulations. The neutrino detection principle is discussed in chapter 5, followed by an overview of the ANTARES neutrino telescope. Chapter 6 focuses on the ANTARES trigger algorithms and their performance. In particular, the source tracking trigger is described. In chapter 7, data from the ANTARES neutrino telescope are used to search for an excess of neutrinos from the Sun and the Galactic Centre, as an indication for the presence of WIMP dark matter at the centre of these sources. Finally, a summary and conclusion are given in chapter 8.

Chapter 1

Dark matter

This chapter gives a brief overview of dark matter in our Universe. One possible explanation of dark matter is the existence of weakly interacting massive particles (WIMPs). The WIMP dark matter scenario, the reason for its popularity and the main WIMP detection possibilities are discussed in the following.

1.1 Evidence

During the past decades, the presence of invisible matter has been confirmed by numerous independent astronomical observations at various length scales. In the following, a brief overview of the observational evidence is presented.

Galactic scales

The first indications for the absence of luminous matter in the Universe at galactic length scales were found in 1939 by American astronomer Horace Babcock. After analysing spectrographic data of the Andromeda galaxy [3], he concluded that the outer regions of Andromeda orbited much faster than what could be expected from its luminous mass. This was confirmed in the late 1960s and early 1970s by American astronomer Vera Rubin and coworkers, in a systematic study of edge-on spiral galaxies [4]. An example of an observed galactic rotation curve (i.e. the distribution of the rotational velocities of stars and gas in a galaxy) is shown in figure 1.1. Measurements of the velocity dispersion of stars in elliptical galaxies give further evidence for the absence of luminous matter at this length scale [6].

Galaxy cluster scales

The first signs of the absence of luminous matter in the Universe were noted by Bulgarian astrophysicist Fritz Zwicky in 1933 [7]. Zwicky made an estimate of the total mass of the Coma cluster of galaxies by applying the virial theorem to the galaxies near its edge. His mass estimate of the cluster was about four hundred times larger than what could be expected from the number of galaxies and total brightness of the cluster. Zwicky inferred that there must be some invisible form of matter, in his own

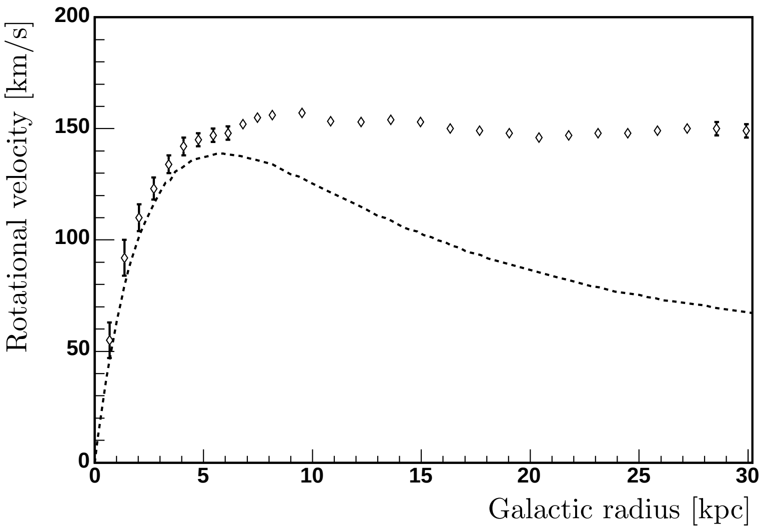

Figure 1.1:

Observed rotation curve of galaxy NGC 3198 (data points) and the prediction from its light distribution (dashed line). Figure adapted from [5].

words "*dunkle kalte Materie*", that provides the mass needed to prevent the cluster from disintegrating. More recently, measurements of the x-ray emission of intergalactic gas in galaxy clusters [8] and gravitational lensing of galaxy clusters [9] confirm his conclusions.

Cosmological scales

In the last part of the previous century, evidence for the absence of luminous matter in the Universe was also found at cosmological distances. Assuming that the structure forms in the Universe are due to the gravitational amplification of primordial fluctuations, comparison of galaxy surveys and measurements of the temperature anisotropies in the cosmic microwave background radiation (CMBR) show that there must be significantly more matter in the Universe than can be attributed to luminous matter [10].

1.2 Dark matter in the Universe

In order to quantify the amount of dark matter in the Universe, a brief overview of the standard cosmological model is presented [11]. The status of the measurements of the present energy budget in the Universe is summarised.

1.2.1 Cosmology

On cosmological scales, the only relevant force in the Universe is gravity. Therefore, the Einstein equations [1] can be used to describe the dynamics of the Universe in terms of its energy contents

$$R_{\mu\nu} - \frac{R}{2}\, g_{\mu\nu} - \Lambda\, g_{\mu\nu} = 8\pi\, T_{\mu\nu} \tag{1.1}$$

[1] In the following, the speed of light c and the gravitational constant G_N are set to one.

where $R_{\mu\nu}$ is the Ricci tensor, R is the Ricci scalar, $g_{\mu\nu}$ is the metric tensor, Λ is the cosmological constant and $T_{\mu\nu}$ is the energy-momentum tensor.

Assuming the Universe is homogeneous and isotropic at cosmological scales (as supported by observations), the metric tensor can be written in the Friedmann-Lemaître-Robertson-Walker form

$$g_{\mu\nu} \;=\; \mathrm{diag}\left(1\,,\; \frac{-a^2}{1-kr^2}\,,\; -a^2r^2\,,\; -a^2r^2\sin^2\theta\right) \tag{1.2}$$

using co-moving coordinates $x^\mu = (t, r, \theta, \phi)$. In this, k is the spatial curvature parameter and $a(t)$ is a scale factor describing the expansion of the universe as a function of time. Possible values for k are +1, 0 and -1 which correspond to a closed, flat and open universe respectively.

Assuming homogeneity and isotropy in the Universe, its energy content can be described by that of a perfect fluid. Hence the energy-momentum tensor can be expressed as

$$T_{\mu\nu} \;=\; \mathrm{diag}\,(\,\rho_{\mathrm{tot}}\,,\; p_{\mathrm{tot}}g_{11}\,,\; p_{\mathrm{tot}}g_{22}\,,\; p_{\mathrm{tot}}g_{33}\,) \tag{1.3}$$

where $\rho_{\mathrm{tot}}(t)$ and $p_{\mathrm{tot}}(t)$ are the total energy and momentum densities of the Universe.

Applying equations (1.2) and (1.3) to the Einstein equations, the Friedmann equation and the equation of continuity can be derived

$$H^2 \;=\; \frac{8\pi}{3}\,\rho_{\mathrm{tot}} \;-\; \frac{k}{a^2} \;+\; \frac{\Lambda}{3} \tag{1.4}$$

$$\dot{\rho}_{\mathrm{tot}} \;=\; -3H(\rho_{\mathrm{tot}} + p_{\mathrm{tot}}) \tag{1.5}$$

where the Hubble parameter H is defined as the ratio of the time derivative of the scale factor and the scale factor itself, $H(t) \equiv \dot{a}(t)/a(t)$, and $\dot{\rho}_{\mathrm{tot}}(t)$ is the time derivative of the total energy density of the Universe.

Assuming the equation of state (i.e. the relation between the energy and momentum density) of each substance that contributes to the total energy density of the Universe is known, equations (1.4) and (1.5) can be used to determine the time-evolution of the Universe. In particular, the Friedmann equation can be rewritten as a time-dependent expression of the energy budget in the Universe

$$\Omega_{\mathrm{R}} + \Omega_{\mathrm{M}} + \Omega_k + \Omega_\Lambda \;=\; 1 \tag{1.6}$$

by using normalised density parameters $\Omega_X(t) \equiv \rho_X(t)/\rho_{\mathrm{c}}(t)$ for every substance X in the Universe, where $\rho_{\mathrm{c}}(t) \equiv 3H(t)^2/8\pi$ is the so-called critical energy density

Substance	Density parameter	Equation of state
Radiation	$\Omega_{\mathrm{R}} \equiv \dfrac{8\pi}{3H^2}\rho_{\mathrm{R}}$	$p_{\mathrm{R}} = \dfrac{\rho_{\mathrm{R}}}{3}$
Matter	$\Omega_{\mathrm{M}} \equiv \dfrac{8\pi}{3H^2}\rho_{\mathrm{M}}$	$p_{\mathrm{M}} = 0$
Cosmological constant	$\Omega_{\Lambda} \equiv \dfrac{\Lambda}{3H^2}$	$p_{\Lambda} = -\rho_{\Lambda}$
Spatial curvature	$\Omega_k \equiv \dfrac{-k}{a^2H^2}$	n.a.

Table 1.1: Density parameters and equations of state of the main substances and curvature in the Universe.

of the Universe. The various contributions are summarised in table 1.1. In this, radiation refers to relativistic particles including photons while matter refers to non-relativistic particles.

1.2.2 Experimental observations

The present experimental values for the normalised density parameters in equation (1.6) are summarised in table 1.2. The quoted values are determined from the observed angular power spectrum of the temperature anisotropies in the CMBR, and the spatial distributions of supernovae and galaxies. As can be seen from this table, the Universe is spatially flat and is presently dominated by the energy contribution due to the cosmological constant (so-called dark energy). The total matter density Ω_{M} is defined as the sum of the ordinary (baryonic) matter density Ω_{B} and the (non-baryonic) dark matter density Ω_{DM}. The positions and relative heights of the peaks in the CMBR spectrum indicate that most of the total matter density in the Universe resides in non-baryonic form. This is in agreement with predictions from primordial nucleosynthesis. Consistency with the observed abundances of light elements in the Universe can only be achieved if $\Omega_{\mathrm{B}} = 0.041 \pm 0.009$ at 95 % C.L. [12]. In the case of our Galaxy, gravitational micro-lensing experiments that search for non-luminous objects such as brown dwarfs and dim stellar remnants (so-called massive astrophysical compact halo objects or MACHOs), seem to rule out the possibility that the local dark matter halo has a substantial baryonic component [13].

1.3 Non-baryonic dark matter candidates

Candidates for non-baryonic dark matter include new kinds of elementary particles produced in the early Universe which do not participate in the electromagnetic or the strong interaction. Non-baryonic dark matter can be categorised into hot and cold dark

Density parameter	Symbol		Present value (68 % C.L.)
Radiation	Ω_R		$4.97 \cdot 10^{-5}$
Baryonic matter	Ω_B	Ω_M	0.046 ± 0.002
Non-baryonic matter	Ω_{DM}		0.228 ± 0.013
Cosmological constant	Ω_Λ		0.726 ± 0.015
Spatial curvature	Ω_k		-0.005 ± 0.006

Table 1.2: Present energy budget of the observable Universe, assuming the central value of the present Hubble parameter $H = 70.5 \pm 1.3$ km/s/Mpc [10].

matter, referring to the velocity of its constituents at the time of decoupling from the thermal plasma in the Universe.

Hot dark matter

The prime candidate for hot dark matter is the neutrino. However, CMBR measurements in combination with supernova and galaxy surveys show that the neutrino relic density is not sufficiently large to account for all the non-baryonic dark matter density in the Universe: $\Omega_\nu < 0.014$ at 95 % C.L. [10]. From this, an upper limit on the neutrino mass can be derived, $m_\nu < 0.68$ eV at 95 % C.L.. This limit is in agreement with the upper limit obtained from laboratory experiments: $m_\nu < 2$ eV at 95 % C.L. [14]. Finally, N-body simulations of structure formation in a Universe dominated by hot dark matter do not agree with the observed structures in the Universe [15].

Cold dark matter

The most favoured class of cold dark matter candidates are weakly interacting massive particles (WIMPs). These will be discussed in the next section. Another notable cold dark matter candidate is the axion, a hypothetical elementary particle that has been postulated to explain the absence of CP-violation in Quantum Chromo Dynamics. Experiments to detect relic axions are ongoing but have not yet resulted in a conclusive answer whether they could make up a substantial fraction of the invisible matter in the Universe [16].

1.4 WIMP dark matter

In the WIMP scenario, the main constituent of cold dark matter is an electrically neutral and colorless elementary particle. This particle, denoted in this thesis by χ, should be sufficiently stable and massive to account for the present value of Ω_{DM}. Although the Standard Model does not contain an elementary particle that fits this description, many new theories that extend the Standard Model do. Examples of such theories are models of Universal Extra Dimensions [17] and little Higgs models [18]. The most prominent example is Supersymmetry, which will be discussed in chapter 2. The motivation for the WIMP scenario and the WIMP detection possibilities are discussed in the remainder of this chapter.

1.4.1 Motivation

In the generic WIMP scenario, WIMPs are in thermal equilibrium with other particles, after their creation in the early Universe, due to the weak interaction. As the Universe expands and cools down, the temperature eventually drops below the WIMP mass resulting in an exponential decrease of the WIMP equilibrium abundance. When the expansion rate of the Universe becomes larger than the WIMP annihilation rate, thermal equilibrium of the WIMP population is no longer maintained. The WIMPs are said to decouple, resulting in a relic WIMP abundance that could account for the present value of $\Omega_{\rm DM}$.

The time evolution of the WIMP number density $n_\chi(t)$ during this scenario can be described quantitatively by the Boltzmann equation [19]

$$\frac{dn_\chi}{dt} + 3Hn_\chi = \langle \sigma\, v\rangle \left((n_\chi^{\rm eq})^2 - n_\chi^2\right) \tag{1.7}$$

where the second term on the left is due the expansion of the Universe, and the first and second terms on the right are the WIMP creation and annihilation rates. Here, $\langle \sigma\, v\rangle$ is the thermally averaged product of the total WIMP annihilation cross section and the relative WIMP velocity v, H is the Hubble parameter, and $n_\chi^{\rm eq}(t)$ is the WIMP number density at thermal equilibrium. It is assumed that the only process affecting the WIMP number density is the CP-invariant creation/annihilation reaction $\chi\chi \leftrightarrow X\bar{X}$, where X stands for any particle into which WIMPs can annihilate. Using Maxwell-Boltzmann statistics, the WIMP number density at thermal equilibrium $n_\chi^{\rm eq}(t)$ can be written as [19]

$$n_\chi^{\rm eq} \propto \int \frac{d^3p_\chi}{(2\pi)^3}\, e^{-E_\chi/T} \propto \begin{cases} (m_\chi T)^{\frac{3}{2}}\, e^{-m_\chi/T} & \text{for } \; T \ll m_\chi \\ T^3 & \text{for } \; T \gg m_\chi \end{cases} \tag{1.8}$$

where E_χ, p_χ and m_χ are the WIMP energy, momentum and mass respectively, and T is the temperature.

It is convenient to rewrite equation (1.7) in terms of the number of WIMPs per unit volume co-moving with the expansion of the Universe, $\hat{n}_\chi \equiv n_\chi a^3$. Equation (1.7) can be solved for the co-moving WIMP number density $\hat{n}_\chi$ by using $x \equiv m_\chi/T$, since in the radiation-dominated Universe $T \propto t^{-1/2}$ (i.e. x is a measure for time). Solutions for three different annihilation cross sections are shown in figure 1.2. The co-moving equilibrium WIMP number density $\hat{n}_\chi^{\rm eq}$ is shown by the solid line. It is constant for small values of x and decreases exponentially as the temperature drops below the WIMP mass. This is expected from equation (1.8) and the fact that in the radiation-dominated Universe, $T \propto a^{-1}$. The three dashed lines show the co-moving WIMP number density $\hat{n}_\chi$ for three different annihilation cross sections, where $\sigma_1 < \sigma_2 < \sigma_3$. As can be seen, the

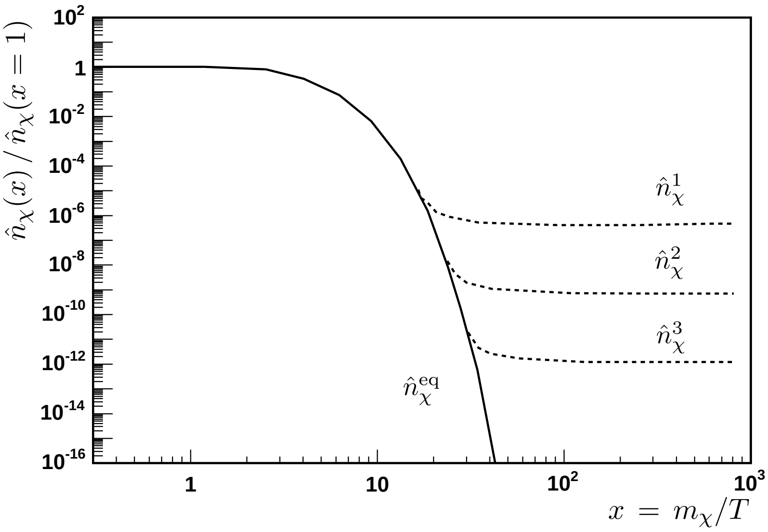

Figure 1.2:

Time evolution of the co-moving WIMP number density according to equation (1.7). Figure adapted from [19].

co-moving WIMP number densities follow the co-moving equilibrium WIMP number density until the expansion rate becomes larger than the annihilation rate. Therefore, the larger the WIMP annihilation cross section, the longer the WIMP number density follows the equilibrium value, the lower the final relic density.

The present WIMP energy density parameter $\Omega_\chi(t_0)$ can be expressed in first approximation as [19]

$$\Omega_\chi(t_0) \;\equiv\; \frac{m_\chi\, n_\chi(t_0)}{\rho_{\rm c}(t_0)} \;\simeq\; \frac{10^{-10}\ \mathrm{GeV}^{-2}}{\langle\sigma\, v\rangle} \tag{1.9}$$

A remarkable feature of this result is the size of the annihilation cross section needed to obtain the observed present dark matter density $\Omega_{\rm DM} \simeq \mathcal{O}(0.1)$ (see table 1.2). This size corresponds surprisingly well with cross sections involving the weak interaction. Typically, for processes involving non-relativistic particles and the weak interaction, $\sigma v \simeq (g/m_W)^4 \simeq 10^{-9}\ \mathrm{GeV}^{-2}$, where g is the coupling constant of the weak interaction and m_W is the mass of the W-boson. Therefore, theories that predict interaction probabilities and particle masses similar to those of the weak interaction provide suitable dark matter candidates.

1.4.2 The dark matter halo of our Galaxy

In the WIMP scenario, the decoupling of the WIMP population from the thermal plasma occurs at $T \simeq m_\chi/30$ GeV (see figure 1.2). For a Boltzmann distribution of particles with mass m and three-dimensional velocity v, the average kinetic energy per particle K and the temperature T are related by

$$K \;\equiv\; \frac{1}{2}\, m\, \langle v^2\rangle \;=\; \frac{3}{2}\, T \tag{1.10}$$

This implies that the WIMPs decoupled with an average velocity well below the speed of light ($v_\chi \simeq 0.3\,c$). Hence the name cold dark matter applies. After decoupling the WIMP population started to cluster into halos due to gravity. When the Universe expanded and became matter dominated, these WIMP halos act as the seeds for structure formation. Thus, in the WIMP scenario, galaxies are surrounded by dark matter halos that consist of non-relativistic relic WIMPs.

The simplest model to describe the structure of a dark matter halo is the so-called isothermal sphere. In this model, the probability density function of the three-dimensional WIMP velocity v is given by the Maxwell-Boltzman velocity distribution [20]

$$f(v) \;=\; 4\pi v^2 \left(\frac{1}{\pi v_0^2}\right)^{3/2} e^{-v^2/v_0^2} \tag{1.11}$$

with a characteristic one-dimensional WIMP velocity dispersion v_0.

The rotational velocity $v_{\mathrm{rot}}(r)$ of an object in an orbit with radius r and with a mass $M(r)$ inside its orbit can be expressed as

$$v_{\mathrm{rot}}(r) \;=\; \sqrt{\frac{G_N M(r)}{r}} \tag{1.12}$$

where G_N is the gravitational constant. Experimental evidence shows that galactic rotation curves typically exhibit a flat dependence beyond the visible stellar disk (e.g. see figure 1.1). Consequently, for a spherical matter distribution (i.e. $dM(r) = 4\pi r^2 \rho(r) dr$), the density ρ can be expressed in terms of the rotational velocity at large radius $v_{\mathrm{rot}}(\infty)$ as

$$\rho(r) \;=\; \frac{v_{\mathrm{rot}}^2(\infty)}{4\pi\, G_N\, r^2} \tag{1.13}$$

It can be shown that the velocity dispersion v_0 in equation (1.11) is equal to the asymptotic rotational velocity $v_{\mathrm{rot}}(\infty)$ [20]. The standard values for the radius of the solar orbit and the rotational velocity at the position of the Sun in our Galaxy are 8.5 kpc and 220 km/s, respectively [21]. It is usually assumed that the rotational velocity of the Sun corresponds to $v_{\mathrm{rot}}(\infty)$. Hence for our Galaxy, the root-mean-squared WIMP velocity $v_{\mathrm{rms}} = \sqrt{3/2}\, v_0 = 270$ km/s. The local dark matter halo density at the position of the Sun, ρ_0, can be calculated from equation (1.13) by taking into account the measured mass contributions from the stellar disk, interstellar gas, etcetera. The standard value for ρ_0 is 0.3 GeV/cm^3 [22]. However, there is considerable uncertainty in the dark matter density near the Galactic Centre. As can be seen from equation (1.13), the prediction of the isothermal sphere is singular at $r = 0$. This is avoided in parameterisations of the radial dark matter density distribution such as the Navarro-Frenk-White (NFW) profile [23].

1.5 WIMP dark matter detection

The hypothesis that relic WIMPs are the constituents of dark matter halos can be experimentally verified for the local dark matter halo of our Galaxy by using direct and indirect detection methods.

1.5.1 Direct detection

The direct detection principle is based on the detection of an interaction between a WIMP from the local dark matter halo and a nucleus inside a detector. After a WIMP interacts with a nucleus inside a detector, the recoil energy of the nucleus can produce various signals such as phonons (vibration), light (scintillation) and charge (ionisation).

Simultaneous measurement of two signals is often exploited to discriminate nuclear recoil events from electron recoil events caused by cosmic-ray spallation and radioactivity. Typically, the recoil energy of the nucleus is transformed into phonons and light. Electrons travel much larger distances and lose most of their energy through ionisation. However, cosmic-ray spallation and radioactivity can produce neutrons that also induce nuclear recoils inside the detector. These are indistinguishable from WIMP induced events. This background has to be minimised by appropriate shielding of the detector. The experiments are usually placed underground at depths of at least 1 km and surrounded by passive shielding made from high density and high purity materials, as well as active shielding based on particle detectors.

A further improvement in the discrimination of WIMP signals from background can be obtained by considering the movement of the Earth around the Sun. Since the orbital speed of the Earth around the Sun is about 30 km/s, and the inclination between the orbital plane of the Earth and the galactic plane is about 60°, the expected event rate has a seasonal variation of about 10 % [24]. In addition, the background can be reduced by taking into account the direction of the recoiling nucleus. Assuming an isotropic dark matter halo, the event rate will have a directional dependence due to the velocity of the Earth with respect to the dark matter halo. It has been shown that the forward-backward asymmetry in the expected event rate can reach 100 % [24].

Spin-dependent and spin-independent interactions

The differential interaction rate dR per unit detector mass can be written as [22]

$$dR \propto \frac{\rho_0}{m_\chi m_N} v f(v) \frac{d\sigma_{\chi N}}{dq^2} dq^2 \, dv \tag{1.14}$$

where ρ_0 is the WIMP density at the position of the detector, m_N is the mass of the nucleus, v and $f(v)$ are the WIMP velocity and WIMP velocity distribution function with respect to the nucleus, and $d\sigma_{\chi N}/dq^2$ is the differential WIMP-nucleon cross section which describes the interaction probability, and q is the momentum transfer.

The interaction is dependent on the nature of the WIMP. In general, by using an effective Lagrangian approach, the interaction term can be written as an interaction between two particle currents. Assuming Lorentz invariance, these currents can be classified as scalar, pseudoscalar, vector, axial-vector or tensor currents. For non-relativistic particles, only the interactions between two scalar currents, two vector currents or two axial-vector currents have to be considered. In addition, the axial-vector current is proportional to the spin of the particle, and the vector current vanishes for Majorana particles. For non-relativistic WIMPs, the interaction between the WIMP and nucleus axial-vector currents can thus be written as a coupling between the spin of the WIMP and the total spin of the nucleus.

The interaction probability between the WIMP and nucleus scalar currents is described by the spin-independent (SI) WIMP-nucleus cross section, while the interaction probability between the WIMP and nucleus axial-vector currents is described by the spin-dependent (SD) WIMP-nucleus cross section. The differential form of these cross sections can be written in terms of the total cross section for $q = 0$ as [22]

$$\begin{aligned}
\frac{d\sigma^{\mathrm{SI}}_{\chi N}}{dq^2} &= \frac{F^2(q)}{4\mu^2_{\chi N}v^2}\int_0^{4\mu^2_{\chi N}v^2} \left.\frac{d\sigma^{\mathrm{SI}}_{\chi N}}{dq^2}\right|_{q=0} dq^2 \equiv \frac{F^2(q)}{4\mu^2_{\chi N}v^2}\,\sigma^{\mathrm{SI}}_{\chi N}(0) \\
\frac{d\sigma^{\mathrm{SD}}_{\chi N}}{dq^2} &= \frac{F^2_{\mathrm{spin}}(q)}{4\mu^2_{\chi N}v^2}\int_0^{4\mu^2_{\chi N}v^2} \left.\frac{d\sigma^{\mathrm{SD}}_{\chi N}}{dq^2}\right|_{q=0} dq^2 \equiv \frac{F^2_{\mathrm{spin}}(q)}{4\mu^2_{\chi N}v^2}\,\sigma^{\mathrm{SD}}_{\chi N}(0)
\end{aligned} \tag{1.15}$$

in which

$$\begin{aligned}
\sigma^{\mathrm{SI}}_{\chi N}(0) &\propto \Big(f_p\,Z + f_n\,(A-Z)\Big)^2 \\
\sigma^{\mathrm{SD}}_{\chi N}(0) &\propto \frac{J+1}{J}\Big(\,|a_p\,\langle S_p\rangle| \pm |a_n\,\langle S_n\rangle|\,\Big)^2 \qquad (\text{if } J \neq 0)
\end{aligned} \tag{1.16}$$

In equations (1.15), $\mu_{\chi N} \equiv m_\chi\, m_N/(m_\chi + m_N)$ is the WIMP-nucleus reduced mass, and $F(q)$ and $F_{\mathrm{spin}}(q)$ are nuclear form factors that suppress the cross section when q increases. These form factors correspond to the Fourier transforms of the nucleon density of the nucleus and the spin distribution in the nucleus, respectively. In equations (1.16), Z and A are the atomic number and mass number of the nucleus (i.e. Z and $(A - Z)$ are the number of protons and neutrons in the nucleus), $\langle S_p\rangle$ and $\langle S_n\rangle$ are the expectation values of the spin content of the proton and neutron group in the nucleus, and J is the total angular momentum of the nucleus. The SD cross section is zero if $J = 0$. The dependency on the nature of the WIMP is contained in the WIMP-proton and WIMP-neutron scalar couplings f_p and f_n, and in the WIMP-proton and WIMP-neutron axial-vector couplings a_p and a_n. For the SD cross section, the relative sign between the parentheses is given by the sign of $(a_p\,\langle S_p\rangle)/(a_n\,\langle S_n\rangle)$.

In order to compare results from experiments using different detector materials independent of the nature of the WIMP, the detection sensitivity of a direct detection experiment is commonly expressed in terms of an upper limit on the WIMP scattering cross section with a single nucleon for $q = 0$. The SI and SD WIMP-nucleon cross

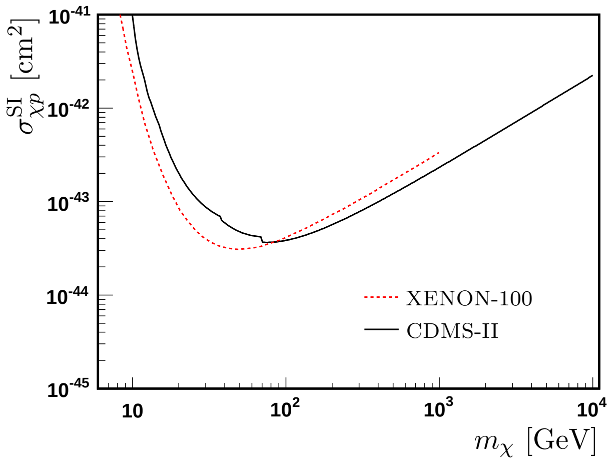

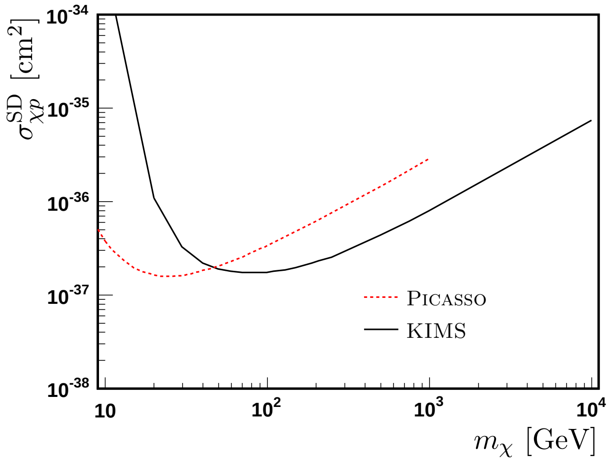

Figure 1.3: Experimental upper limits at 90 % C.L. on the SI (left) and SD (right) WIMP-proton cross section in the $q = 0$ limit, as a function of the WIMP mass m_χ. The most recent results from the CDMS [28], XENON [29], KIMS [30] and PICASSO [31] experiments are shown.

sections for $q = 0$ are defined as [25]

$$\begin{aligned}
\sigma^{\rm SI}_{\chi n/p} &\equiv \frac{1}{A^2}\,\frac{\mu^2_{\chi n/p}}{\mu^2_{\chi N}}\,\sigma^{\rm SI}_{\chi N}(0) \\
\sigma^{\rm SD}_{\chi p} &\equiv \frac{3\,J}{4\,\langle S_p\rangle^2\,(J+1)}\,\frac{\mu^2_{\chi p}}{\mu^2_{\chi N}}\,\sigma^{\rm SD}_{\chi N}(0) \qquad (1.17)\\
\sigma^{\rm SD}_{\chi n} &\equiv \frac{3\,J}{4\,\langle S_n\rangle^2\,(J+1)}\,\frac{\mu^2_{\chi n}}{\mu^2_{\chi N}}\,\sigma^{\rm SD}_{\chi N}(0)
\end{aligned}$$

where $\mu_{\chi n/p}$ is the WIMP-neutron/proton reduced mass. For the SI cross section, it is assumed that $f_p = f_n$, and the mass difference between the proton and the neutron mass has been neglected. As can be seen from equation (1.17), the conversion from WIMP-nucleus to WIMP-nucleon cross section is independent of the nature of the WIMP. Experimental limits on the SI cross section are set with the assumption that the total WIMP-nucleus cross section is dominated by the SI cross section (i.e. $\sigma^{\rm SD}_{\chi n/p} = 0$), and vice versa for the spin-dependent case.

Experimental status

Except for some notable exceptions [26, 27], no WIMP signal has yet been observed by direct detection experiments. Currently, the best upper limits have been obtained by the CDMS [28] and XENON [29] experiments for the SI WIMP-proton cross section, and by the KIMS [30] and PICASSO [31] experiments for the SD WIMP-proton cross section. These upper limits at 90 % C.L. are shown in figure 1.3. As can be seen, experiments are more sensitive to the SI cross section than the SD cross section. By using detector

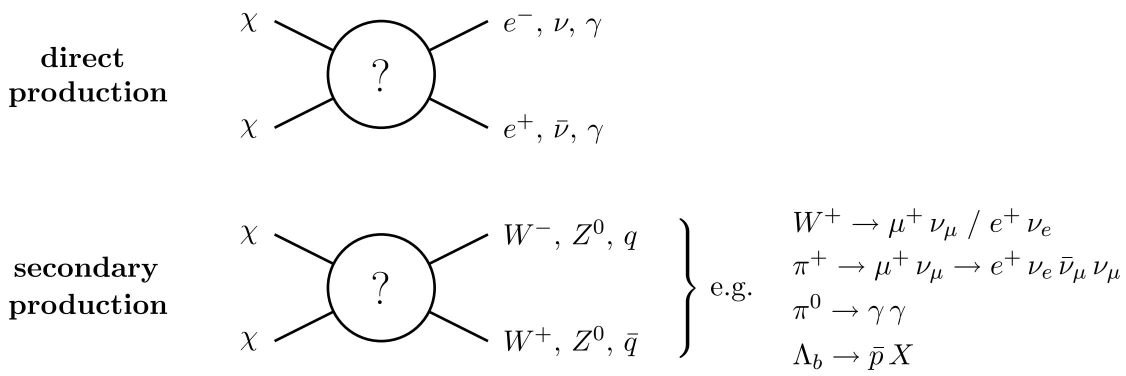

Figure 1.4: Possible WIMP-WIMP annihilation products. Positrons, gamma-rays and neutrinos can be produced directly or indirectly through the decay of other particles produced by WIMP-WIMP annihilation. The probability of each channel depends on the nature of the WIMP. For instance, for the neutralino in supersymmetry, the process can be replaced by the Feynman diagrams in figure 4.3.

materials with high mass number A, experiments can take advantage of the fact that $\sigma^{\rm SI}_{\chi N}(0) \propto A^2$ (e.g. germanium ($A = 73$) in the CDMS experiment and xenon ($A = 131$) in the XENON experiment).

1.5.2 Indirect detection

The indirect detection principle is based on the detection of particles that are produced by self-annihilation of WIMPs. Examples are shown in figure 1.4. The probability of each channel, i.e. the WIMP self-annihilation cross section of each channel, depends on the nature of the WIMP. However, independent of the nature of the WIMP, the WIMP self-annihilation cross section $\sigma_{\chi\chi}$ times the relative WIMP velocity v can be expanded in terms of v as [22]

$$\sigma_{\chi\chi} v \,=\, a \,+\, b\,(v/c)^2 \,+\, \mathcal{O}((v/c)^4) \tag{1.18}$$

where the first term on the right is due to s-wave annihilation (i.e. the orbital angular momentum of the initial state is zero), and the second term proportional to the relative velocity squared arises from both s- and p-wave initial states (i.e. the orbital angular momentum of the initial state is zero and one respectively). As explained in section 1.4, the average WIMP velocity in the halo is presently $v_{\rm rms} \simeq 270$ km/s $\simeq 10^{-3}\,c$. Consequently for indirect detection of WIMPs, only the first term in the expansion of the WIMP self-annihilation cross section is important and higher order terms can be safely neglected. Furthermore, if the WIMP is a Majorana fermion, the initial state must be anti-symmetric under interchange of particles due to Fermi statistics. In that case the WIMP annihilation cross section is determined only by the s-wave initial state with total spin angular momentum equal to zero. This means that the helicities of the WIMPs in the initial state are equal. Since helicity is conserved, the two final state particles must have equal helicity as well. The same holds for WIMPs that are scalar particles. Therefore, for self-annihilation of non-relativistic WIMPs that are Majorana fermions or scalar particles into a fermion anti-fermion pair (i.e. $\chi\chi \rightarrow f\bar{f}$), the annihilation cross section is proportional to the fermion mass squared [2]. The reason why the annihilation cross section of the $\chi\chi \rightarrow f\bar{f}$ process is proportional to the fermion mass squared will be discussed in more detail for the neutralino predicted by supersymmetry in section 4.2.1. The suppression of light fermion final states due to helicity conservation has consequences for indirect detection experiments, as will be discussed in the following.

The challenge for indirect detection experiments is the discrimination between WIMP annihilation induced signals and astrophysical signals. Nevertheless, some of the signals can be distinguished from the background.

Anti-matter

The dominance of normal matter in our Galaxy makes the search for anti-matter a viable option to find WIMP signals. This requires in most cases balloon or satellite detectors to overcome the absorption of anti-matter in the Earth's atmosphere. Two particularly interesting WIMP annihilation products are anti-protons and anti-electrons (positrons). These particles can be produced by various annihilation processes. For positrons, the ideal detection channel would be the direct $\chi\chi \rightarrow e^+e^-$ process. Since WIMPs are non-relativistic, this would result in mono-energetic positrons with energies equal to the WIMP mass. This feature could be used to distinguish these positrons from the background. The background is mainly due to cosmic-ray interactions with interstellar material, resulting in a continuous energy spectrum without a cut-off in the TeV range. However, for non-relativistic WIMPs that are scalar particles or Majorana fermions, this channel is suppressed as discussed in the beginning of this section. In that case, positrons are mainly produced after hadronisation and decay of other particles. The same holds for the anti-protons that are composite particles which cannot be produced directly. Examples can be found in the secondary production channel shown in figure 1.4. The result is a continuous anti-proton and positron energy spectrum which features a cut-off at the WIMP mass. Positrons and anti-protons are deflected by magnetic fields in our Galaxy due to their electric charge. They can only be observed as an increase in the total flux below the WIMP mass, independent of direction.

The anti-proton flux and the positron flux have recently been measured by the PAMELA experiment in the 1-100 GeV energy range [32, 33]. Although there is reasonable agreement between the measured anti-proton flux and the expected background, the measured positron flux is incompatible with the expected background. This could be an indication of dark matter annihilating preferably into leptons [34]. However, other alternative theories to explain this excess have been proposed (e.g. particle acceleration in magnetospheres of nearby pulsars producing electromagnetic cascades [35]) and a final conclusion has yet to be made.

[2] This is analogous to the decay of the charged pion, which decays mostly into $\mu\,\nu_\mu$ ($\sim 99.99\,\%$) instead of $e\,\nu_e$ ($\sim 0.01\,\%$), contrary to final state phase space considerations.

Gamma-rays

In contrast to anti-protons and positrons, gamma-rays point straight back to their source. This enables a search for WIMP annihilation in regions with a relatively high WIMP density, e.g. the Galactic Centre. The ideal detection channels would be $\chi\chi \rightarrow \gamma\gamma$ and $\chi\chi \rightarrow Z^0\gamma$. Since the WIMPs are non-relativistic, the resulting gamma-rays will be (nearly) mono-energetic with energies equal to the WIMP mass. However, these processes cannot occur at lowest order since WIMPs by definition do not couple directly to photons. Gamma-rays can also be produced through the $\chi\chi \rightarrow q\,\bar{q}$ process. Subsequent hadronisation of the quarks (and decay of the hadrons) can produce neutral pions, which decay into gamma-rays (see the secondary production channel in figure 1.4). This results in a continuous energy spectrum with a cut-off at the WIMP mass. The background, including neutral pion production in cosmic-ray interactions with interstellar matter, bremsstrahlung by cosmic-ray electrons, and inverse Compton scattering between soft interstellar photons and cosmic-ray electrons, produces a continuous energy spectrum without a cut-off in the TeV range.

Data from the EGRET satellite [36] and the HESS telescope [37] do not show any evidence for a gamma-ray emission line from the Galactic Centre in the 100 MeV to 10 GeV energy range and the 160 GeV to 30 TeV energy range, respectively. The diffuse gamma-ray flux measured by EGRET is larger than expected from background only. The excess could be due to secondary gamma-rays produced in WIMP annihilation [38]. However, the diffuse gamma-ray flux excess as observed by EGRET is not confirmed by the recently launched Fermi satellite, which has an increased angular resolution and sensitivity in a larger energy range (30 MeV to 300 GeV) with respect to EGRET [39].

Neutrinos

Neutrinos are electrically neutral fermions that only interact through the weak nuclear force. For a long time neutrinos were thought to have no mass, but by now experiments have compellingly shown that they do have a tiny mass. The absolute mass scale however is still unknown, although upper limits on the neutrino masses can be derived from cosmology and laboratory experiments (see section 1.3). Neutrinos can be produced in WIMP annihilation processes in a similar fashion to positrons. The ideal detection channel would be the direct $\chi\chi \rightarrow \nu\bar{\nu}$ process. Since WIMPs are non-relativistic, this would result in mono-energetic neutrinos with energies equal to the WIMP mass. However, this channel is helicity-suppressed for non-relativistic WIMPs that are scalar particles or Majorana fermions. In that case, neutrinos are mainly produced through secondary production channels, resulting in a continuous energy spectrum with a cut-off at the WIMP mass.

Neutrinos only interact weakly with other particles. Therefore their direction points back to the source, and they can escape from regions with high matter density. This offers a unique possibility to study WIMP annihilation in astrophysical sources such as the Sun and the Earth, and the Galactic Centre. The indirect detection principle using neutrinos is described in more detail in chapter 3.

Chapter 2

Supersymmetry

The most favoured WIMP candidate is the lightest neutralino, an elementary particle that follows from supersymmetry. Supersymmetry is regarded as a natural extension of the Standard Model of elementary particles and fields. In chapter 4, supersymmetry is used as a theoretical framework to calculate the neutrino flux that is expected from neutralino annihilation in astrophysical objects. This chapter gives a brief overview of supersymmetry, and introduces some nomenclature used in this thesis.

2.1 Supersymmetry

The group of all possible space-time symmetries of any quantum field theory is the Poincaré group (i.e. rotations, Lorentz boosts and translations in space and time). The algebra that describes the structure of the Poincaré group can be written as [40]

$$\begin{aligned}
[M_{\mu\nu}, M_{\rho\sigma}] &= i\,(\eta_{\mu\sigma} M_{\nu\rho} - \eta_{\mu\rho} M_{\nu\sigma} + \eta_{\nu\rho} M_{\mu\sigma} - \eta_{\nu\sigma} M_{\mu\rho}) \\
[M_{\mu\nu}, P_\rho] &= i\,(\eta_{\nu\rho} P_\mu - \eta_{\mu\rho} P_\nu) \\
[P_\mu, P_\nu] &= 0
\end{aligned} \tag{2.1}$$

where $M_{\mu\nu}$ is the generator of Lorentz transformations (i.e. rotations and boosts), P_μ is the generator of space-time translations, and $\eta_{\mu\nu} \equiv \mathrm{diag}(1, -1, -1, -1)$ is the metric tensor.

Supersymmetry considers the existence of a new symmetry in nature, i.e. a new type of operation under which the Lagrangian is invariant. The operator of this new symmetry involves a transformation between bosons and fermions [1]. In terms of the generator Q of this new operation, the supersymmetry transformation can generally be written as

$$Q\,|\,\mathrm{fermion}\,\rangle = |\,\mathrm{boson}\,\rangle \qquad \text{and} \qquad Q\,|\,\mathrm{boson}\,\rangle = |\,\mathrm{fermion}\,\rangle \tag{2.2}$$

[1] In this thesis only one new symmetry transformation is considered, i.e. *'N=1' supersymmetry*.

Necessarily, Q involves a spinor that carries spin 1/2. Therefore, supersymmetry can be considered as a space-time symmetry. This implies that the algebra involving Q and its Hermitian conjugate $\bar{Q}$ is an extension of the Poincaré algebra. By using left- and right-handed 2-component Weyl spinors Q_α and $\bar{Q}_{\dot{\alpha}}$ with indices $\alpha, \dot{\alpha} = 1$ or 2, it can be shown that the supersymmetry algebra, in addition to the Poincaré algebra given by equation (2.1), can be written as [40]

$$\begin{aligned}
\{Q_\alpha, Q_\beta\} &= 0 & [Q_\alpha, P_\mu] &= 0 \\
\{\bar{Q}_{\dot{\alpha}}, \bar{Q}_{\dot{\beta}}\} &= 0 & [\bar{Q}_{\dot{\beta}}, P_\mu] &= 0 \\
\{Q_\alpha, \bar{Q}_{\dot{\beta}}\} &= 2\,(\sigma^\mu)_{\alpha\dot{\beta}}\, P_\mu \\
[Q_\alpha, M_{\mu\nu}] &= \tfrac{i}{4}\,(\sigma_\mu\bar{\sigma}_\nu - \sigma_\nu\bar{\sigma}_\mu)_\alpha^{\ \beta}\, Q_\beta \\
[\bar{Q}^{\dot{\alpha}}, M_{\mu\nu}] &= \tfrac{i}{4}\,(\bar{\sigma}_\mu\sigma_\nu - \bar{\sigma}_\nu\sigma_\mu)^{\dot{\alpha}}_{\ \dot{\beta}}\, \bar{Q}^{\dot{\beta}}
\end{aligned} \tag{2.3}$$

In here, $\sigma^\mu = \bar{\sigma}_\mu \equiv (\mathbf{1}, \sigma^1, \sigma^2, \sigma^3)$ and $\sigma_\mu = \bar{\sigma}^\mu \equiv (\mathbf{1}, -\sigma^1, -\sigma^2, -\sigma^3)$, where σ^i are the Pauli matrices and $\mathbf{1}$ is the 2×2 identity matrix.

All single particle states are contained in the irreducible representations of the supersymmetry algebra, referred to as supermultiplets. Each supermultiplet contains both boson and fermion states. These so-called superpartners can be transformed into one another by some combination of Q and $\bar{Q}$. The structure of the supersymmetry algebra implies that each supermultiplet must contain the same number of boson and fermion degrees of freedom. Since Q and $\bar{Q}$ also commute with the generators of the Standard Model gauge group $SU(3)_C \otimes SU(2)_L \otimes U(1)_Y$, all particles in the same supermultiplet have the same gauge quantum numbers. This implies that Standard Model particles cannot be superpartners of one another in a supermultiplet. Therefore, supersymmetry predicts the existence of new particles: A spin 0 superpartner for each left-handed and right-handed quark and lepton field, generically called *squarks* and *sleptons*, and a spin 1/2 superpartner for each gauge and Higgs boson field, generically called *gauginos* and *higgsinos*. Furthermore, superpartners in the same supermultiplet must have the same mass, because $P^2 = P_\mu P^\mu$ is a Casimir operator of the supersymmetry algebra. Since none of these particles have been experimentally detected, it is generally believed that supersymmetry is broken at the electro-weak scale.

2.1.1 Motivation

Supersymmetry offers several solutions to some known problems and short-comings of the Standard Model that are summarised below.

Hierarchy problem

The mass of the Higgs boson is determined by its bare mass plus higher order quantum corrections due to interactions between the Higgs and other particles. However, for scalar particles, these corrections are quadratically divergent and their values become

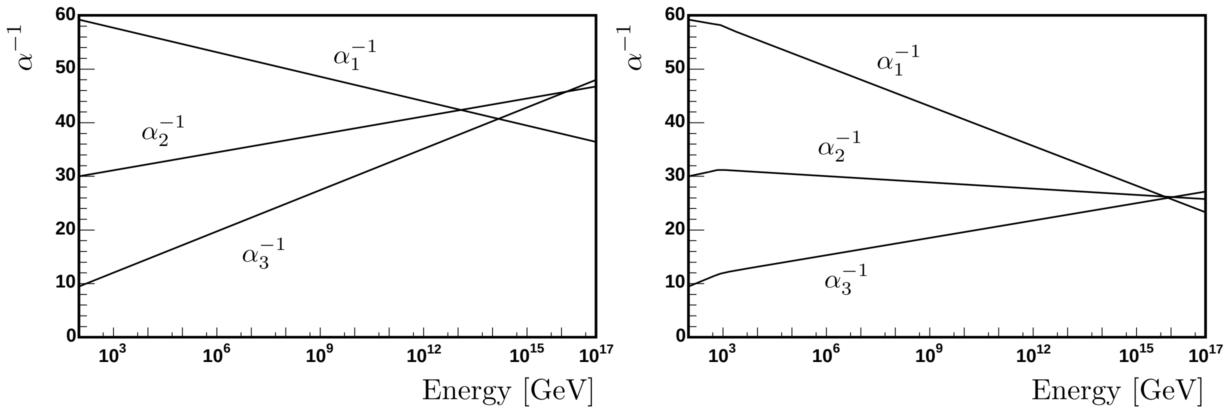

Figure 2.1: The energy dependence of $\alpha_1 \equiv \frac{5}{3}g'^{\,2}/4\pi$, $\alpha_2 \equiv g^2/4\pi$ and $\alpha_3 \equiv g_s^2/4\pi$ in the Standard Model (left) and in a minimal version of supersymmetry (right). Figure adapted from [41].

as large as the energy cut-off scale of the theory. On the other hand, precision measurements have shown that the Higgs vacuum expectation value should be around 250 GeV. This can only be accomplished by extreme fine-tuning of the mass parameters involved. This is usually taken as an indication for 'new' physics at these energy scales. If supersymmetry exists and the masses of the superpartners are of $\mathcal{O}$(TeV), their corrections to the Higgs mass would cancel the contributions of the Standard Model particles and one naturally ends up with a Higgs mass at the electro-weak scale.

Force unification

The coupling constants of the three gauge groups in the Standard Model, g' of $U(1)_Y$, g of $SU(2)_L$ and g_s of $SU(3)_C$, converge when they are evaluated at higher energy scales. However, they do not seem to extrapolate to a common unification scale, as shown in figure 2.1. The evolution with energy is governed by renormalisation group equations that are sensitive to the total particle content of the theory. If supersymmetry exists, the superpartners alter the renormalisation group equations and a common unification scale around $2 \cdot 10^{16}$ GeV can be achieved, suggesting a 'grand' unification of the three forces. In grand unified theories, fermions can generally be grouped into the same irreducible representation of the grand unified gauge group. This explains or offers hints to several features of the Standard Model, e.g. the relation between the values of the electric charge quantum number of quarks and leptons.

Symmetry unification

According to the Coleman-Mandula theorem [42], the symmetry group of any consistent 4-dimensional quantum field theory has to be a direct product between the Poincaré group and an internal symmetry group. This means that the only possible space-time symmetries are the elements of the Poincaré group, and they are strictly separated from gauge symmetries. However, there is one loop hole in this theorem [43]. A new conserved quantity is allowed if it is described not by a Lie algebra, but by a so-called graded Lie algebra that contains commutators as well as anti-commutators. This is the case for supersymmetry, and the only possible choice for the algebra is provided by equations (2.1) and (2.3).

Dark matter candidate

In the Standard Model, baryon and lepton numbers are conserved because the most general gauge-invariant and renormalisable Lagrangian does not contain any baryon or lepton number violating interactions. This is not the case for the supersymmetric Lagrangian. However, by combining the spin, baryon and lepton numbers S, B and L, a new quantum number called *R-parity* (R) can be defined :

$$R \equiv (-1)^{2S+3(B-L)} \tag{2.4}$$

If R-parity conservation is imposed, baryon and lepton number violating processes are forbidden. Furthermore, the definition is such that all Standard Model particles are R-parity even, while all superpartners are R-parity odd. Therefore, conservation of R-parity renders the lightest superpartner stable. If the lightest superpartner has the characteristics of a WIMP, it would be a natural dark matter candidate.

2.1.2 The Minimal Supersymmetric Standard Model

The Minimal Supersymmetric Standard Model (MSSM) is the minimal supersymmetric extension of the Standard Model. It contains the minimal number of supermultiplets needed to incorporate all Standard Model fields, and those interactions that are renormalisable, invariant under $SU(3)_C \otimes SU(2)_L \otimes U(1)_Y$ gauge transformations, and R-parity conserving. The MSSM contains the following features [44].

Particle content

To complete the MSSM particle spectrum, only two types of supermultiplets are introduced. Each left- and right-handed quark/lepton field and their corresponding squark/slepton superpartner fall into a so-called chiral supermultiplet, a combination of a 2-component Weyl fermion and a complex scalar. Each gauge boson and its corresponding gaugino fall into a so-called vector supermultiplet, a combination of a massless gauge boson and a massless 2-component Weyl fermion. Since the gauge bosons are contained in the adjoint representation of the gauge group, so are the gauginos. This implies that gauginos are Majorana fermions.

Supersymmetry breaking

Supersymmetry must be broken some how, but the underlying mechanism is not known. In the MSSM this is forced by adding explicit supersymmetry breaking terms to the Lagrangian. To avoid divergences in the Higgs mass, only so-called soft supersymmetry breaking (SSB) terms are considered: These include explicit mass terms for the gauginos and sfermions, mass and bilinear terms for the Higgs bosons, and trilinear scalar coupling terms between sfermions and Higgs bosons. To avoid large flavour changing neutral currents and CP-violating effects, the corresponding SSB parameters are constrained to be real and flavour conserving.

Electro-weak symmetry breaking

In the MSSM, two complex scalar Higgs $SU(2)_L$ doublets with opposite hypercharge are needed to break the electro-weak symmetry. The reason why a single Higgs doublet does not suffice in the MSSM (in contrast to the Standard Model) is twofold. Firstly, the fermion superpartners of a single Higgs doublet would introduce a gauge anomaly in the theory. The superpartners of a second Higgs doublet with opposite hypercharge cancel the contributions of the first Higgs doublet, keeping the MSSM anomaly-free. Secondly, two Higgs doublets with opposite hypercharge are needed to include mass terms in the MSSM Lagrangian for fermions of opposite weak isospin. Mass terms that include the Hermitian conjugate of a single Higgs doublet are not invariant under a supersymmetry transformation. Each Higgs doublet and its corresponding higgsino doublet are contained in a chiral supermultiplet.

In the MSSM, spontaneous electro-weak symmetry breaking occurs because the neutral components of the two Higgs doublets have non-zero vacuum expectation values while their charged counterparts have zero vacuum expectation values. Electro-weak symmetry breaking induces a mixing between fields that have different $SU(2)_L \otimes U(1)_Y$ quantum numbers but the same baryon, lepton and $SU(3)_C \otimes U(1)_{\rm em}$ quantum numbers. For the Standard Model fields, mixing leads to the usual Standard Model particles plus an additional CP-even Higgs scalar H^0, a CP-odd Higgs scalar A^0 and two charged Higgs scalars $H^\pm$. In case of the superpartners, there is mixing between left- and right-handed sfermions, and mixing between the electro-weak gauginos and higgsinos. The mixing in the latter case implies the existence of four *neutralinos* $\tilde{\chi}^0_{1-4}$, and two *charginos* $\tilde{\chi}^\pm_{1,2}$. The complete MSSM particle spectrum before and after electro-weak symmetry breaking is listed in table 2.1.

Neutralinos are mixtures of electro-weak gauginos and higgsinos due to electro-weak symmetry breaking. Interactions involving neutralinos are determined by the neutralino composition in terms of these fields. In the so-called neutralino gauge eigenstate basis $(\tilde{B}, \tilde{W}_3, \tilde{H}^0_d, \tilde{H}^0_u)$, the neutralino mass matrix M_χ that appears in the MSSM Lagrangian can be written as

$$M_\chi = \begin{bmatrix} m_{\tilde{B}} & 0 & -c_\beta\, s_{\theta_W}\, m_Z & s_\beta\, s_{\theta_W}\, m_Z \\ 0 & m_{\tilde{W}} & c_\beta\, c_{\theta_W}\, m_Z & -s_\beta\, c_{\theta_W}\, m_Z \\ -c_\beta\, s_{\theta_W}\, m_Z & c_\beta\, c_{\theta_W}\, m_Z & 0 & -\mu \\ s_\beta\, s_{\theta_W}\, m_Z & -s_\beta\, c_{\theta_W}\, m_Z & -\mu & 0 \end{bmatrix} \tag{2.5}$$

where $m_{\tilde{B}}$ and $m_{\tilde{W}}$ are the bino and wino SSB mass parameters, $s_{\theta_W} \equiv \sin(\theta_W)$ and $c_{\theta_W} \equiv \cos(\theta_W)$ in which θ_W is the electro-weak mixing angle, m_Z is the Z-boson mass,

Normal particles		Supersymmetric partners	
Symbol	Name	Symbol	Name
$\left.\begin{array}{l} q_{u,L} \\ q_{u,R} \end{array}\right\} \to q_u$	up-type quarks (×3) ($q_u = u, c, t$)	$\left.\begin{array}{l} \tilde{q}_{u,L} \\ \tilde{q}_{u,R} \end{array}\right\} \to \left\{\begin{array}{l} \tilde{q}_{u,1} \\ \tilde{q}_{u,2} \end{array}\right.$	up-type squarks (×3) ($\tilde{q}_u = \tilde{u}, \tilde{c}, \tilde{t}$)
$\left.\begin{array}{l} q_{d,L} \\ q_{d,R} \end{array}\right\} \to q_d$	down-type quarks (×3) ($q_d = d, s, b$)	$\left.\begin{array}{l} \tilde{q}_{d,L} \\ \tilde{q}_{d,R} \end{array}\right\} \to \left\{\begin{array}{l} \tilde{q}_{d,1} \\ \tilde{q}_{d,2} \end{array}\right.$	down-type squarks (×3) ($\tilde{q}_d = \tilde{d}, \tilde{s}, \tilde{b}$)
ν	neutrinos ($\nu = \nu_e, \nu_\mu, \nu_\tau$)	$\tilde{\nu}$	sneutrinos ($\tilde{\nu} = \tilde{\nu}_e, \tilde{\nu}_\mu, \tilde{\nu}_\tau$)
$\left.\begin{array}{l} l_{e,L} \\ l_{e,R} \end{array}\right\} \to l_e$	charged leptons ($l_e = e, \mu, \tau$)	$\left.\begin{array}{l} \tilde{l}_{e,L} \\ \tilde{l}_{e,R} \end{array}\right\} \to \left\{\begin{array}{l} \tilde{l}_{e,1} \\ \tilde{l}_{e,2} \end{array}\right.$	charged sleptons ($\tilde{l}_e = \tilde{e}, \tilde{\mu}, \tilde{\tau}$)
g	gluons (×8)	$\tilde{g}$	gluinos (×8)
$\left.\begin{array}{l} B \\ W_3 \\ H_u^0 \\ H_d^0 \end{array}\right\} \to \left\{\begin{array}{l} \gamma \\ Z^0 \\ h^0 \\ H^0 \\ A^0 \end{array}\right.$	photon Z-boson light scalar Higgs heavy scalar Higgs pseudoscalar Higgs	$\left.\begin{array}{l} \tilde{B} \\ \tilde{W}_3 \\ \tilde{H}_u^0 \\ \tilde{H}_d^0 \end{array}\right\} \to \tilde{\chi}^0_{1,2,3,4}$	bino wino higgsino higgsino → neutralinos
$\left.\begin{array}{l} W_1 \\ W_2 \\ H_u^+ \\ H_d^- \end{array}\right\} \to \left\{\begin{array}{l} W^\pm \\ H^\pm \end{array}\right.$	W-bosons charged Higgses	$\left.\begin{array}{l} \tilde{W}_1 \\ \tilde{W}_2 \\ \tilde{H}_u^+ \\ \tilde{H}_d^- \end{array}\right\} \to \tilde{\chi}^\pm_{1,2}$	wino wino higgsino higgsino → charginos

Table 2.1: Particle content of the MSSM.

$s_\beta \equiv \sin(\beta)$ and $c_\beta \equiv \cos(\beta)$ in which the angle β is related to the vacuum expectation values of the neutral components of the two Higgs doublets by $\tan(\beta) \equiv \langle H_u^0 \rangle / \langle H_d^0 \rangle$, and μ is the higgsino mass parameter. Since the neutralino mass matrix is Hermitian, it can be diagonalised by a unitary 4×4 matrix N according to $M_\chi^{\text{diag}} = N^\dagger M_\chi N$. The matrix N is thus the neutralino mixing matrix that relates the neutralino mass eigenstates $|\, \tilde{\chi}^0_i \,\rangle = (\tilde{\chi}^0_1, \tilde{\chi}^0_2, \tilde{\chi}^0_3, \tilde{\chi}^0_4)$ to the gauge eigenstates $|\, \tilde{\chi}^0_\alpha \,\rangle = (\tilde{B}, \tilde{W}_3, \tilde{H}^0_d, \tilde{H}^0_u)$ by

$$|\, \tilde{\chi}^0_i \,\rangle \;=\; \sum_{\alpha=1,2,3,4} N^*_{\alpha i} \,|\, \tilde{\chi}^0_\alpha \,\rangle \qquad \Leftrightarrow \qquad |\, \tilde{\chi}^0_\alpha \,\rangle \;=\; \sum_{i=1,2,3,4} N_{\alpha i} \,|\, \tilde{\chi}^0_i \,\rangle \tag{2.6}$$

The four gauge eigenstate fractions of neutralino mass eigenstate $|\, \tilde{\chi}^0_i \,\rangle$ are $|N^*_{\alpha i}|^2$ for α = 1,2,3,4.

2.2 Supergravity

Although the existence of supersymmetry has not been confirmed by experiment, it is clear that if it exists it has to be broken. Although the exact breaking mechanism is unknown, it is assumed to occur at a high energy scale and is induced by a 'hidden' sector that consists of new particle fields that interact only very weakly with the MSSM particle fields. This is motivated by the convergence of gauge couplings at a high energy scale, as shown in figure 2.1. Grand unified theories generally contain new heavy particles that can only interact very weakly with the Standard Model fields.

In the *gravity mediated supersymmetry breaking* scenario, it is assumed that supersymmetry breaking occurs in the hidden sector around the grand unification scale, and is mediated to the visible sector by gravitational interactions, leading to the soft supersymmetry breaking terms in the MSSM Lagrangian. This is motivated by the strength and the flavour independence of gravitational interactions, and the fact that supersymmetry can be linked to gravity through its algebra. Invariance under local Poincaré transformations gives rise to general relativity. Therefore, promoting supersymmetry from a global to a local symmetry necessarily implies gravity. The resulting theory is called *supergravity*. The massless gauge fields that correspond to local Poincaré invariance and to local supersymmetry are the spin 2 graviton and the spin 3/2 gravitino respectively. They are superpartners of each other, forming an additional supermultiplet. In supergravity, local supersymmetry is broken spontaneously around the grand unification scale. As a result, the Lagrangian remains invariant under local supersymmetric transformations but the vacuum state does not. This gives rise to a massless spin 1/2 Goldstone field, the so-called goldstino. This field is subsequently absorbed by the gauge field of the broken symmetry resulting in a massive gravitino with two additional degrees of freedom. This process is called the super-Higgs mechanism, due to its analogy with spontaneous electro-weak symmetry breaking in the Standard Model.

Like all quantum theories that include general relativity, supergravity is non-renormalisable as a quantum field theory. However, since the non-renormalisable terms always involve the gravitational coupling and so are suppressed by powers of the Planck mass ($\approx 10^{19}\,\text{GeV}$), supergravity can be regarded as an effective theory at lower energy scales.

Minimal supergravity

Although based on a simple principle, the MSSM is rather impractical due to its many parameters. The majority of the new parameters introduced in the MSSM Lagrangian is due to the various explicit SSB terms. In *minimal supergravity* (mSUGRA), it is assumed that the gauge couplings unify at the grand unification scale, as well as the SSB parameters [44]. Therefore, an mSUGRA model can be defined by only four parameters and a remaining sign, as summarised in table 2.2. Any MSSM parameter can be subsequently obtained at any energy scale by applying the corresponding renormalisation group equation.

An attractive aspect of mSUGRA is so-called radiative electro-weak symmetry breaking. Electro-weak symmetry is broken spontaneously at the electro-weak scale if the Higgs potential has an unstable minimum when the Higgs field is zero, and the potential is bounded from below. In the Standard Model, this is forced by an ad hoc choice of parameters in the Higgs potential. In particular, the Higgs mass parameter m_H^2 has to be negative. Instead in mSUGRA, spontaneous electro-weak symmetry breaking is generated dynamically through quantum corrections. In mSUGRA, the condi-

mSUGRA parameter	Symbol
The universal SSB scalar mass at the grand unification scale	$\mathbf{m_0}$
The universal SSB gaugino mass at the grand unification scale	$\mathbf{m_{1/2}}$
The universal SSB trilinear scalar coupling at the grand unification scale	$\mathbf{A_0}$
The ratio of the vacuum expectation values of the neutral components of the two Higgs doublets $\langle H_u^0 \rangle$ and $\langle H_d^0 \rangle$ at the electro-weak scale	$\mathbf{tan}(\boldsymbol{\beta})$
The sign of the higgsino mass parameter μ	$\mathbf{sign}(\boldsymbol{\mu})$

Table 2.2: The mSUGRA parameters.

tions for electro-weak symmetry breaking contain the SSB Higgs mass parameters $m^2_{H_u}$ and $m^2_{H_d}$. These are unified at m_0^2 at the grand unification scale. However, renormalisation group evolution drives the SSB Higgs mass parameter $m^2_{H_u}$ to negative values (or at least $m^2_{H_u} \ll m^2_{H_d}$) at the electro-weak scale, which therefore spontaneously breaks the electro-weak symmetry. This process is called radiative electro-weak symmetry breaking. Negative contributions to the evolution of $m^2_{H_u}$ are in particular due to the Yukawa coupling involving the heavy top quark. Consequently, the region in mSUGRA parameter phase space which exhibits radiative electro-weak symmetry breaking is significantly larger or smaller for a higher or lower top quark mass, respectively.

Chapter 3

Neutrinos from WIMP annihilation in astrophysical objects

Neutrino production is expected to occur in regions of high dark matter density, since the annihilation rate is proportional to the dark matter density squared. The dark matter density of the dark matter halo of our Galaxy peaks sharply at the Galactic Centre, making it an interesting region to search for dark matter. Furthermore, the dark matter density can be enhanced in massive astrophysical objects. Since the neutrino flux is inversely proportional to the distance to the dark matter source squared, astrophysical objects in the vicinity of Earth are particularly interesting objects to search for dark matter.

This chapter starts with a brief overview of the capture and annihilation of WIMPs in the Sun and the Earth. The subsequent production of neutrinos and what happens to them before they can be detected is described next. The neutrino energy spectra and angular distributions from WIMP annihilation in the Sun and the Earth are computated using the `WimpSim` simulation package [45]. Finally, neutrino production by WIMP annihilation in the dark matter halo is described, and an overview of current experimental limits is given.

3.1 WIMP capture and annihilation in the Sun and the Earth

WIMPs can pass through a massive celestial body because they only interact weakly with ordinary matter. However, if a WIMP does interact with a nucleus in the object and it loses sufficient kinetic energy so that its velocity after the collision is lower than the escape velocity of the object, the WIMP will be gravitationally bound to the object. The escape velocities at the surface of the Sun and the Earth are ~600 km/s and ~11 km/s, respectively [20, 46]. The average WIMP velocity in the dark matter halo of our Galaxy is about 270 km/s, as explained in section 1.4.2. In case the eccentricity of the resulting orbit is such that the WIMP can undergo additional collisions, it will eventually lose more and more kinetic energy and settle in the centre of the object. The WIMP density in the centre of the object will thus increase, thereby significantly increasing the WIMP annihilation probability. The time evolution of the number of WIMPs in the object $N_\chi(t)$ can be described by the differential equation [22]

$$\frac{dN_\chi}{dt} = R_{\text{cap}} - C_{\text{ann}} N_\chi^2 \tag{3.1}$$

where R_{cap} is the WIMP capture rate of the object, and the second term on the right is twice the WIMP annihilation rate $R_{\text{ann}}(t) \equiv \frac{1}{2}\, C_{\text{ann}} N_\chi^2$.

3.1.1 WIMP capture

The capture rate R_{cap} depends on the nature of the WIMP (mass and WIMP-nucleus elastic scattering cross section), the properties of the dark matter halo (density and velocity dispersion) and the composition of the accreting object (density and chemical composition). The capture rate is time-independent assuming the dark matter halo and the composition of the object remain constant in time. For the Sun and the Earth, the capture rates due to the SI and SD WIMP-nucleus cross sections can be approximated by [22]

$$\begin{aligned} R_{\text{cap}}^{\text{SD}} &= C^{\text{SD}} \frac{\rho_0\, \sigma_{\chi p}^{\text{SD}}}{m_\chi\, v_{\text{rms}}}\, S\left(\frac{m_\chi}{m_p}\right) \\ R_{\text{cap}}^{\text{SI}} &= C^{\text{SI}} \frac{\rho_0\, \sigma_{\chi p}^{\text{SI}}}{m_\chi\, v_{\text{rms}}} \sum_N A_N^2 \frac{\mu_{\chi N}^2}{\mu_{\chi p}^2}\, f_N\, \phi_N\, F_N(m_\chi)\, S\left(\frac{m_\chi}{m_N}\right) \end{aligned} \tag{3.2}$$

where in the SI case the sum is over all nucleus types N in the object, A_N and F_N are the mass number and nuclear form factor of nuclei of type N, f_N and ϕ_N are the mass fraction and average gravitational potential (relative to the surface) of nuclei of type N in the object (see table 3.1). S is a kinematic suppression factor which suppresses the capture rate if the WIMP mass differs from the mass of the nucleus. In the SD case, only WIMP scattering off hydrogen nuclei (protons) is considered. The numerical proportionality factors $C^{\text{SD/SI}}$ for the Sun and the Earth are approximately

$$\begin{aligned} C_{\text{Sun}}^{\text{SD}} &\approx 4.8 \cdot 10^{25}\ \text{s}^{-1} & \qquad C_{\text{Earth}}^{\text{SD}} &\approx 0 \\ C_{\text{Sun}}^{\text{SI}} &\approx 4.8 \cdot 10^{24}\ \text{s}^{-1} & \qquad C_{\text{Earth}}^{\text{SI}} &\approx 4.8 \cdot 10^{15}\ \text{s}^{-1} \end{aligned} \tag{3.3}$$

if the local dark matter halo density ρ_0 is given in units of 0.3 GeV/cm^3, the average dark matter velocity v_{rms} is given in units of 270 km/s, the WIMP mass is given in units of 1 GeV, and the SD/SI WIMP-proton cross sections $\sigma_{\chi p}^{\text{SD/SI}}$ are given in units of 10^{-40} cm^2 in equations (3.2). The capture rate in the Sun is higher than in the Earth, independent of the nature of the WIMP, due to the larger mass and volume of the Sun. The escape velocity of the Sun is almost two orders of magnitude larger than of the Earth, hence the Sun captures WIMPs much more efficiently than the Earth. In addition, the Earth consists mostly of nuclei with relatively high mass number A and $J = 0$ (see table 3.1). Therefore, capture of WIMPs in the Earth due to the SD

			Sun		Earth	
Nuclide	Mass number A	Nuclear spin J	f_N	ϕ_N	f_N	ϕ_N
Hydrogen	1	1/2	0.67	3.15	-	-
Helium	4	0	0.31	3.40	-	-
Oxygen	16	0	$8.8{\cdot}10^{-3}$	3.25	0.30	1.20
Manganese	24	0	$7.3{\cdot}10^{-4}$	3.22	0.15	1.20
Silicon	28	0	$8.0{\cdot}10^{-4}$	3.22	0.16	1.24
Iron	56	0	$1.4{\cdot}10^{-3}$	3.22	0.32	1.55

Table 3.1: Composition of the Sun and the Earth [46].

cross section is negligible. The Sun however consists mostly of hydrogen, hence both interactions have to be taken into account.

3.1.2 WIMP annihilation

The annihilation factor C_{ann} in equation (3.1) equals the WIMP annihilation cross section $\sigma_{\chi\chi}$ times the relative WIMP velocity v per unit volume, and depends on the WIMP distribution in the object. It can be approximated by [22]

$$C_{\text{ann}} \;=\; \frac{\sigma_{\chi\chi}\, v}{V} \tag{3.4}$$

where V is the effective volume of the object. The effective volumes of the Sun and the Earth, assuming their composition remains constant in time, are approximately

$$V_{\text{Sun}} \;\approx\; 5.8 \cdot 10^{30}\; m_\chi^{3/2}\;\;\text{cm}^3 \qquad\qquad V_{\text{Earth}} \;\approx\; 1.8 \cdot 10^{27}\; m_\chi^{3/2}\;\;\text{cm}^3 \tag{3.5}$$

with the WIMP mass in units of 1 GeV. The annihilation rate factor C_{ann} of the Sun is higher than in the Earth, independent of the nature of the WIMP.

Solving equation (3.1) for $N_\chi(t)$ results in

$$N_\chi \;=\; \sqrt{\frac{R_{\text{cap}}}{C_{\text{ann}}}}\;\tanh\left(\frac{t}{\tau}\right) \qquad \text{with} \qquad \tau \equiv (R_{\text{cap}}\, C_{\text{ann}})^{-\frac{1}{2}} \tag{3.6}$$

where τ can be seen as the equilibrium time scale between capture and annihilation in the object. The WIMP annihilation rate in the object can thus be written as

$$R_{\text{ann}} \;=\; \frac{R_{\text{cap}}}{2}\;\tanh^2\left(\frac{t}{\tau}\right) \tag{3.7}$$

WIMP type	WIMP annihilation channels
Scalar / Majorana fermion	$\chi\chi \rightarrow \tau^+\tau^-$, $b\,\bar{b}$, $t\,\bar{t}$, W^+W^- and Z^0Z^0
Other	$\chi\chi \rightarrow \nu_e\bar{\nu}_e$, $\nu_\mu\bar{\nu}_\mu$ and $\nu_\tau\bar{\nu}_\tau$

Table 3.2: WIMP types and annihilation channels considered in this thesis.

From equation (3.7) it can be seen that, for $t \gg \tau$, the annihilation rate depends only on the capture rate. In that case, it is the elastic scattering cross section and not the annihilation cross section that determines the annihilation rate. For both the Sun and the Earth, the relevant time scale is the age of the solar system, i.e. about $4.5 \cdot 10^9$ years. The capture rate of the Sun is nine orders of magnitude larger than that of the Earth, while the effective volume of the Sun is only three orders of magnitude larger than that of the Earth (cf. equations (3.3) and equations (3.5)). Hence the equilibrium time scale τ for the Sun is always smaller than for the Earth, i.e. equilibrium is always reached sooner in the Sun than in the Earth.

3.2 Neutrinos from WIMP annihilation

The flux of neutrinos of type ν_l at a detector from WIMP annihilation in a celestial object can be written as

$$\frac{d\Phi_{\nu_l}}{dE_{\nu_l}} = \frac{R_{\rm ann}}{4\pi D^2} \sum_X \left(\frac{\sigma_{\chi\chi\rightarrow X}}{\sigma_{\chi\chi}}\right)_X \left(\frac{dN_{\nu_l}}{dE_{\nu_l}}\right)_X \tag{3.8}$$

where $\nu_l = \{\nu_e\,,\,\bar{\nu}_e\,,\,\nu_\mu\,,\,\bar{\nu}_\mu\,,\,\nu_\tau\,,\,\bar{\nu}_\tau\}$, $R_{\rm ann}$ is the total annihilation rate in the object, and D is the distance to the object. The sum includes all WIMP annihilation channels $\chi\chi \rightarrow X$ that are capable of producing high-energy neutrinos, in which the ratio of the cross section $\sigma_{\chi\chi\rightarrow X}$ of annihilation channel X and the total annihilation cross section $\sigma_{\chi\chi}$ is the branching ratio of annihilation channel X, and $(dN_{\nu_l}/dE_{\nu_l})_X$ is the neutrino energy spectrum at the detector from annihilation channel X.

Various annihilation channels are capable of producing high-energy neutrinos. The most important ones are given in table 3.2, according to whether the WIMP is a scalar or Majorana fermion (e.g. the lightest neutralino in supersymmetry) or not (e.g. the first Kaluza-Klein excitation of the $U(1)_Y$-boson in the Universal Extra Dimensions scenario [17]).

The energy spectrum of a particular neutrino type will be influenced by neutrino mixing and interactions with matter when the neutrino propagates between the point of production in the astrophysical object and the detector. This is briefly discussed in the following.

3.2.1 Neutrino mixing

The neutrino interacts only through the weak nuclear force. It does so through its flavour eigenstates $|\,\nu_\alpha\,\rangle = (\nu_e, \nu_\mu, \nu_\tau)$, which are different from the mass eigenstates $|\,\nu_i\,\rangle = (\nu_1, \nu_2, \nu_3)$ that describe neutrino propagation [1]. This is analogous to the quark sector in the Standard Model. The flavour and mass eigenstates are linear superpositions of one another, and can be related by the unitary leptonic mixing matrix U:

$$|\,\nu_\alpha\,\rangle \;=\; \sum_{i=1,2,3} U^*_{\alpha i}\,|\,\nu_i\,\rangle \qquad \Leftrightarrow \qquad |\,\nu_i\,\rangle \;=\; \sum_{\alpha=e,\mu,\tau} U_{\alpha i}\,|\,\nu_\alpha\,\rangle \tag{3.9}$$

The matrix U can be parametrised as [47]

$$\begin{aligned} U \;=\; & \begin{bmatrix} 1 & 0 & 0 \\ 0 & c_{23} & s_{23} \\ 0 & -s_{23} & c_{23} \end{bmatrix} \times \begin{bmatrix} c_{13} & 0 & s_{13}e^{-i\delta} \\ 0 & 1 & 0 \\ -s_{13}e^{i\delta} & 0 & c_{13} \end{bmatrix} \times \begin{bmatrix} c_{12} & s_{12} & 0 \\ -s_{12} & c_{12} & 0 \\ 0 & 0 & 1 \end{bmatrix} \\ & \times \; \mathrm{diag}\left(e^{i\alpha_1/2},\; e^{i\alpha_2/2},\; 1\right) \end{aligned} \tag{3.10}$$

Inside this matrix $s_{ij} \equiv \sin(\theta_{ij})$ and $c_{ij} \equiv \cos(\theta_{ij})$, where θ_{ij} are the three mixing angles. Their measured values are $\theta_{12} = 33.2 \pm 4.9\,^\circ$, $\theta_{23} = 45.0 \pm 10.6\,^\circ$ and $\theta_{13} = 0.0 \pm 12.5\,^\circ$ [48]. The angles δ, α_1 and α_2 are the three CP-violating phases. The angles α_1 and α_2 are zero, unless neutrinos are Majorana fermions. The magnitudes of the CP-violating phases are still unknown.

Neutrino propagation in vacuum

As a neutrino propagates, the misalignment of neutrino flavour and mass eigenstates causes neutrino oscillations, i.e. a periodical change of flavour. This quantum mechanical phenomenon can have a macroscopic effect due to the smallness of the neutrino mass. The propagation of neutrinos can for these purposes be described by the Schrödinger equation. The time evolution of a flavour eigenstate $|\,\nu_\alpha(t)\,\rangle$ is therefore given by

$$|\,\nu_\alpha(t)\,\rangle \;=\; e^{-iHt}\,|\,\nu_\alpha(0)\,\rangle \tag{3.11}$$

where the evolution operator contains the Hamiltonian H. In the case of neutrino propagation through vacuum, H can be written as [47]

$$H \;=\; \frac{1}{2E}\,U\,\mathrm{diag}\,(0,\,\Delta m^2_{12},\,\Delta m^2_{13})\,U^\dagger \tag{3.12}$$

in which E is the neutrino energy, $\Delta m^2_{ij} = m^2_i - m^2_j$ is the difference between the neutrino masses squared, and U is the leptonic mixing matrix defined in equation (3.9). Using equation (3.12) and assuming CPT-invariance, the probability that a neutrino

[1] In this thesis it is assumed there are only three mass eigenstates.

with energy E oscillates from flavour α into β as it propagates a distance L in vacuum can be written as [47]:

$$P\left(\overset{(-)}{\nu}_\alpha \rightarrow \overset{(-)}{\nu}_\beta\right) = \delta_{\alpha\beta} - 4\sum_{i>j} \mathrm{Re}\left(U^*_{\alpha i}\, U_{\beta i}\, U_{\alpha j}\, U^*_{\beta j}\right) \sin^2\left(\Delta m^2_{ij}\,\frac{L}{4E}\right) \overset{(+)}{-} 2\sum_{i>j} \mathrm{Im}\left(U^*_{\alpha i}\, U_{\beta i}\, U_{\alpha j}\, U^*_{\beta j}\right) \sin\left(\Delta m^2_{ij}\,\frac{L}{2E}\right) \qquad (3.13)$$

where $\delta_{\alpha\beta} = 0, 1$ for $\alpha \neq \beta$ and $\alpha = \beta$ respectively. The oscillation probability is minimal/maximal if $\Delta m^2_{ij} L/E = 2\,k\,\pi$ for even/odd positive integers k, or equivalently, if $L/E \simeq 0.78\,k/\Delta m^2_{ij}$ with L given in units of km, E in units of GeV, and Δm^2_{ij} in units of eV^2. The experimental observation of neutrino oscillations implies that neutrinos have mass, as can be seen from equation (3.13). The absolute values and the hierarchy of the neutrino masses however cannot be determined by oscillation experiments, and are still unknown. The measured mass differences are $\Delta m^2_{12} = 8.1^{+1.0}_{-0.9} \cdot 10^{-5}\,\mathrm{eV}^2$ and $\Delta m^2_{13} = 2.2^{+1.1}_{-0.8} \cdot 10^{-3}\,\mathrm{eV}^2$ [48].

The standard oscillation scenario refers to the central values of the mixing angles and mass differences as quoted in this section, the so-called normal mass hierarchy (i.e. $m_{\nu_3} > m_{\nu_{1,2}}$), and all CP-violating angles are zero.

Neutrino propagation through matter

In the case of neutrino propagation through matter, interactions with the medium can induce coherent forward scattering of neutrinos due to flavour-conserving interactions with particles in the medium. This so-called Mikheyev-Smirnov-Wolfenstein (MSW) effect alters the Hamiltonian H in equation (3.12), and causes an additional mixing between neutrino flavours [49]. The probability of a flavour-conserving interaction between a neutrino and a nucleus in the medium is equal for all neutrino flavours, and therefore does not contribute to neutrino flavour transition in matter. However, (anti-)electron-neutrinos can also interact with atomic electrons in the medium. Hence for neutrino propagation through matter, the Hamiltonian in equation (3.12) contains an additional term,

$$H = \frac{1}{2E}\, U\, \mathrm{diag}\,(0,\, \Delta m^2_{12},\, \Delta m^2_{13})\, U^\dagger \pm \mathrm{diag}\,(\sqrt{2}\, G_F N_e,\, 0,\, 0) \qquad (3.14)$$

in which G_F is the Fermi coupling constant, and N_e is the number of electrons in the medium per unit volume. The relative sign is positive for neutrinos and negative for anti-neutrinos. The interaction term can be written as a mixing term by factorising out the part of the term proportional to the unit matrix which does not contribute to flavour change. The electron density at the centre of the Sun and the Earth is approximately $6 \cdot 10^{25}$ cm^{-3} and $4 \cdot 10^{24}$ cm^{-3} respectively. As can be derived from equation (3.14), these values imply that the interaction term dominates the Hamiltonian for the neutrino energy range of interest to neutrino telescopes ($E > 10$ GeV).

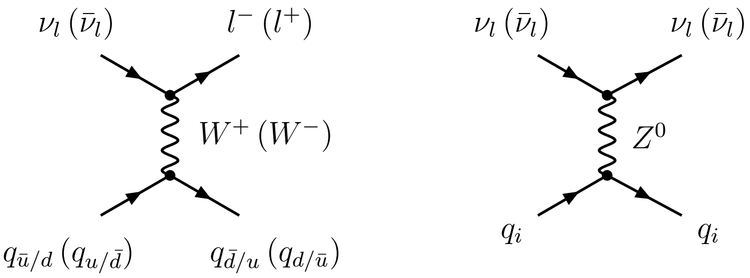

Figure 3.1: Lowest order Feynman diagrams contributing to the charged current (left) and neutral current (right) neutrino-nucleon interaction. $q_{\bar{u}/d}$ represents an up-type anti-quark or a down-type quark, q_i represents any quark or anti-quark.

3.2.2 Neutrino interactions

Neutrinos from WIMP annihilation that interact with a terrestrial detector do so predominantly with the atomic nuclei of the detector medium. This can occur through the exchange of a $W^{\pm}$ or a Z^0-boson, called the charged current (CC) and the neutral current (NC) interaction respectively. The lowest order Feynman diagrams that contribute to the neutrino-nucleon CC and NC interactions are shown in figure 3.1. In this figure, $q_{\bar{u}/d}$ represents an up-type anti-quark or a down-type quark, and q_i represents any (anti-)quark.

The neutrino-nucleon CC and NC cross sections σ_{CC} and σ_{NC} are shown as a function of neutrino energy E_ν for neutrinos (solid lines) and anti-neutrinos (dashed lines) in figure 3.2. The proton cross sections are shown in black, the neutron cross sections in red. As can be seen, the cross sections rise linearly with the neutrino energy for $E_\nu < 10^4$ GeV. The differences between the cross sections are due to the different quark content of the proton (uud) and the neutron (udd) as well as the electric charge of the interacting quarks.

3.3 Simulation of neutrinos from WIMP annihilation in the Sun and the Earth

In equation (3.8), the neutrino energy spectrum $(dN_{\nu_l}/dE_{\nu_l})_X$ from annihilation channel X at the detector depends on which particles are produced in the annihilation, and how these particles produce neutrinos. In addition, the energy spectrum of a particular neutrino type will be influenced by interactions and neutrino mixing when the neutrino propagates between the point of production in the astrophysical object and the detector. Neutrino telescopes are most sensitive to (anti-)muon-neutrinos, as will be explained in section 5.1. Monte Carlo simulations are used to compute the (anti-)muon-neutrino energy spectra of the main annihilation channels that are capable of producing muon-neutrinos. All annihilation channels considered in this thesis are summarised in table 3.2. These energy spectra will be used to derive the detection probability of the

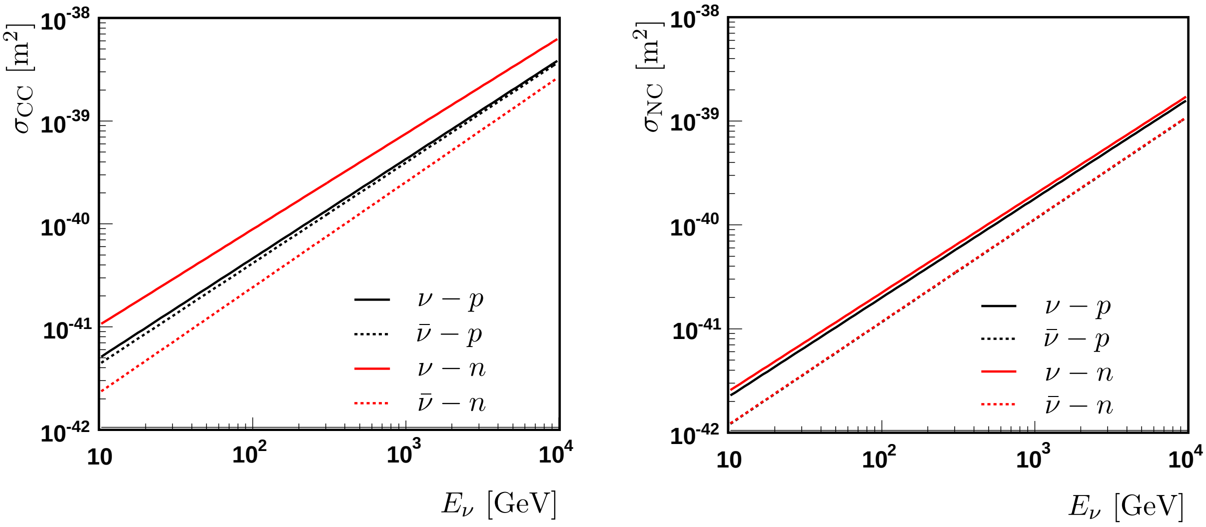

Figure 3.2: The charged and neutral current neutrino-nucleon cross sections $\sigma_{\rm CC}$ and $\sigma_{\rm NC}$ as a function of the neutrino energy E_ν, for neutrinos (solid lines) and anti-neutrinos (dashed lines) on a proton (black lines) and a neutron (red lines), assuming the CTEQ6-DIS parton distribution functions [50].

ANTARES neutrino telescope for specific annihilation channels in chapter 7.

3.3.1 Simulation procedure

The computation of the various energy spectra is done using the `WimpSim v2.09` simulation package [45], with which various WIMP annihilation processes in the Sun and the Earth can be simulated. Furthermore, the neutrino propagation process from the production point to the detector including neutrino mixing can be simulated. In this thesis, the standard neutrino oscillation scenario is taken into account (see section 3.2.1). Neutrino interactions during propagation through the Sun and the Earth are based on the `nusigma v1.15` parameterisation of the neutrino-nucleon cross section [50]. The composition of the Sun is based on the 'BS05(OP)' solar model [51]. The composition and matter density profile of the Earth are taken from [52]. The `PYTHIA v6.4` simulation package [53] is used to simulate the hadronisation and decay of all particles produced immediately after the WIMP annihilation.

3.3.2 Neutrino energy spectra

In the following, the neutrino energy spectra corresponding to all WIMP annihilation channels given in table 3.2 are shown in figures 3.3-3.7 and 3.9. The ν_μ and $\bar{\nu}_\mu$ energy spectra are shown in the left and right two panels of each figure (except figure 3.9). The energy spectra from annihilation in the Sun and the Earth are shown in the top and bottom two panels of each figure (except figure 3.9). Each panel shows the number of (anti-)muon-neutrinos produced per annihilation as a function of $z \equiv E_\nu/m_\chi$.

WIMP annihilation into fermions

The cross section of two WIMPs annihilating into any fermion anti-fermion pair, $\chi\chi \to f\bar{f}$, is proportional to the mass of the fermion squared. Therefore, this channel is dominated by annihilation into tau leptons, bottom quarks and, if kinematically possible (i.e. if $m_\chi > m_{\text{top}} \simeq 173$ GeV), top quarks. The energy spectra resulting from these three final states, evaluated at the detector for several WIMP masses m_χ, are shown in figures 3.3, 3.4 and 3.5 respectively.

As can be seen, the $\bar{\nu}_\mu$ energy spectrum from the Sun is always slightly harder than the ν_μ energy spectrum for any particular WIMP mass m_χ. This is caused by the ν_μ - nucleon cross section which is larger than the $\bar{\nu}_\mu$ - nucleon cross section (see figure 3.2). The higher probability to interact with matter implies that neutrinos are more likely to lose energy or be absorbed during their propagation through the Sun than anti-neutrinos, hence the resulting energy spectra are softer. In contrast, the ν_μ and $\bar{\nu}_\mu$ energy spectra from WIMP annihilation in the Earth are nearly identical for any WIMP mass m_χ for all three processes. This implies that neutrinos hardly interact when they travel from the centre of the Earth to the detector. This is expected from the matter density and radius of the Earth compared to the Sun. The matter density in the Earth (Sun) ranges from approximately 13 g/cm^3 (150 g/cm^3) at the centre to about 3 g/cm^3 (0 g/cm^3) at the surface. The radii of the Earth and the Sun are about $6.4 \cdot 10^6$ m and $7 \cdot 10^8$ m. respectively. As a consequence, the energy spectra from the Earth are always harder than from the Sun.

WIMP annihilation into $\tau^+\tau^-$

Amongst the three dominant fermion channels, the tau channel always gives the hardest ν_μ and $\bar{\nu}_\mu$ energy spectra for any WIMP mass m_χ. This is due to the lifetime and decay channels of the tau. The tau lifetime of about $3 \cdot 10^{-13}$ s is short enough for the tau to decay before it can interact with its surroundings. In contrast, muons are stopped before they can decay. The branching ratios of tau decay into a tau-neutrino and a lepton-neutrino pair, $\tau \to \mu\nu_\mu\nu_\tau$ and $\tau \to e\nu_e\nu_\tau$, are 17.5 % each. These decays give relatively hard neutrinos.

The tau channel is also unique in the fact that in tau decay, there are always more tau-neutrinos produced than electron- or muon-neutrinos. Neutrino mixing can have an observable effect in neutrino energy spectra if there is an asymmetry in neutrino flavours at the moment of production. For the Sun, the mixing effect is time dependent due to the eccentricity of the Earth's orbit. The distance between the centre of the Sun and the Earth, D, changes annually as $D \simeq 1.5 \cdot 10^{11} \pm 2.5 \cdot 10^9$ m. If the energy spectrum is averaged over one year, as is done for all energy spectra in this section, the mixing effect is averaged in time and hence in energy. However, $\overset{(-)}{\nu}_\tau \to \overset{(-)}{\nu}_\mu$ oscillations can still be seen for neutrino energies above ~300 GeV in the energy spectra from the Sun in figure 3.3. These oscillations are primarily due to Δm^2_{12}, as can be derived from equation (3.13). For the Earth, the tau-neutrino to muon-neutrino oscillations are visible only for neutrino energies smaller than ~100 GeV. As can be seen from the energy spectra for small WIMP masses in the bottom panels of figure 3.3, the first

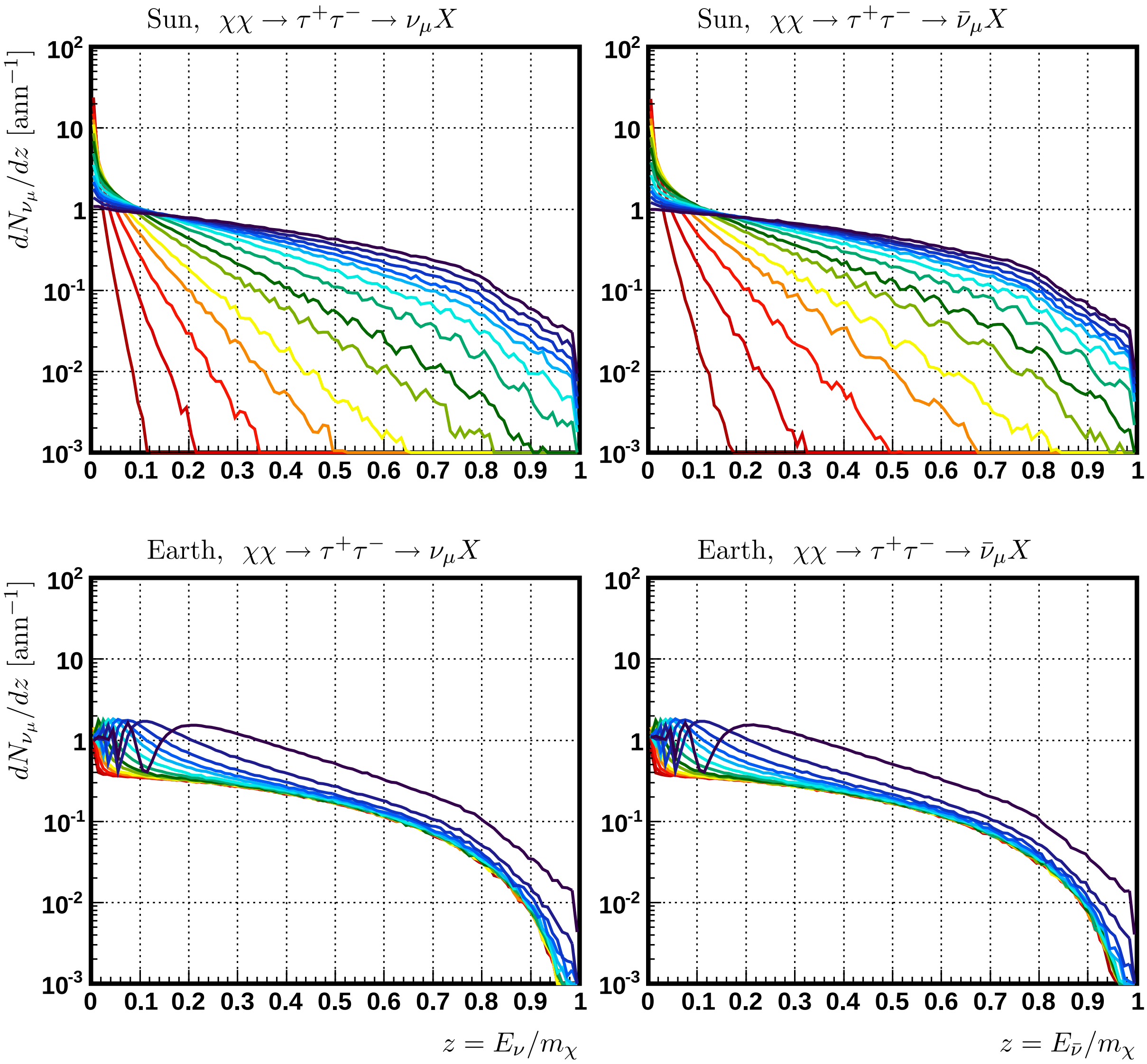

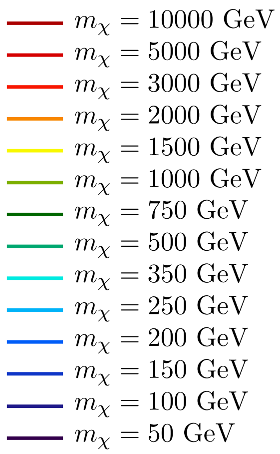

Figure 3.3:

The ν_μ and $\bar{\nu}_\mu$ energy spectra of the $\chi\chi \to \tau^+\tau^-$ process in the Sun and the Earth, evaluated at the detector for several WIMP masses m_χ.

oscillation peak lies at approximately 10 GeV. These oscillations are due to Δm^2_{23}, as can be derived from equation (3.13).

WIMP annihilation into $b\,\bar{b}$

For the annihilation processes considered in this section, the bottom quark channel always gives the softest ν_μ and $\bar{\nu}_\mu$ energy spectra for any WIMP mass m_χ. The soft spectra are a result of several effects. Firstly, the bottom quarks will hadronise into color-neutral B-hadrons and therefore lose energy. Due to their flavour content, these hadrons can only decay through the weak interaction. Therefore the lifetime of these hadrons is relatively long ($\sim 10^{-12}$ s). Hence they are stable enough to interact and lose energy before they decay, if the matter density at their point of production is large enough. The energy loss due to interactions is larger for more energetic hadrons because the lifetime scales with the Lorentz factor. On the other hand, their lifetime is short enough for them to decay before they are stopped, contrary to for instance kaons and pions, which are stopped before they can decay. The matter density in the centre of the Sun is large enough for B-hadrons above ∼50 GeV to lose a significant amount of energy during their propagation. For the Earth, only B-hadrons with energies above ∼500 GeV propagate far enough to lose a significant amount of energy before they decay. Finally, the decay into neutrinos produces three or more particles. The branching ratio of inclusive B-hadron decay into a neutrino-lepton pair plus other particles, i.e. $B \to l\,\nu_l\,X$, is 11 % for $l\,\nu_l = e\,\nu_e$ or $\mu\,\nu_\mu$, but only 2 % for $l\,\nu_l = \tau\,\nu_\tau$. As a result of these effects, the ν_μ and $\bar{\nu}_\mu$ energy spectra for the bottom quark channel are relatively soft.

As can be seen from in the bottom two panels of figure 3.4, the ν_μ and $\bar{\nu}_\mu$ energy spectra from the Earth are softer for higher WIMP masses due to the increased energy loss of B-hadrons in the centre of the Earth. Furthermore, the asymmetry in tau and muon/electron-neutrino production in B-meson decay manifests itself in the muon-neutrino energy spectra as a disappearance of soft muon-neutrinos due to neutrino mixing. The first oscillation peak due to Δm^2_{23} lies at approximately 10 GeV, as can be seen from the energy spectra for small WIMP masses in the bottom panels of figure 3.4.

WIMP annihilation into $t\,\bar{t}$

The muon-neutrino energy spectra from the top quark channel are similar to the bottom quark channel, but harder. This has two main reasons. Due to its relatively high mass, a top quark will immediately decay into a bottom quark and a W-boson before it can hadronise and lose energy. The bottom quark will hadronise and can produce soft neutrinos as explained in the previous paragraph. However, the W-boson can also decay directly into a neutrino and a charged lepton. The branching ratio of the W-boson into a neutrino-lepton pair is 11 % for each neutrino type (W-boson decay into hadrons can also produce neutrinos, but these are much softer). Hence the ν_μ and $\bar{\nu}_\mu$ energy spectra from the top quark channel are harder than from the bottom quark channel. They are however softer than the energy spectra from the tau channel since the tau can directly decay into neutrinos.

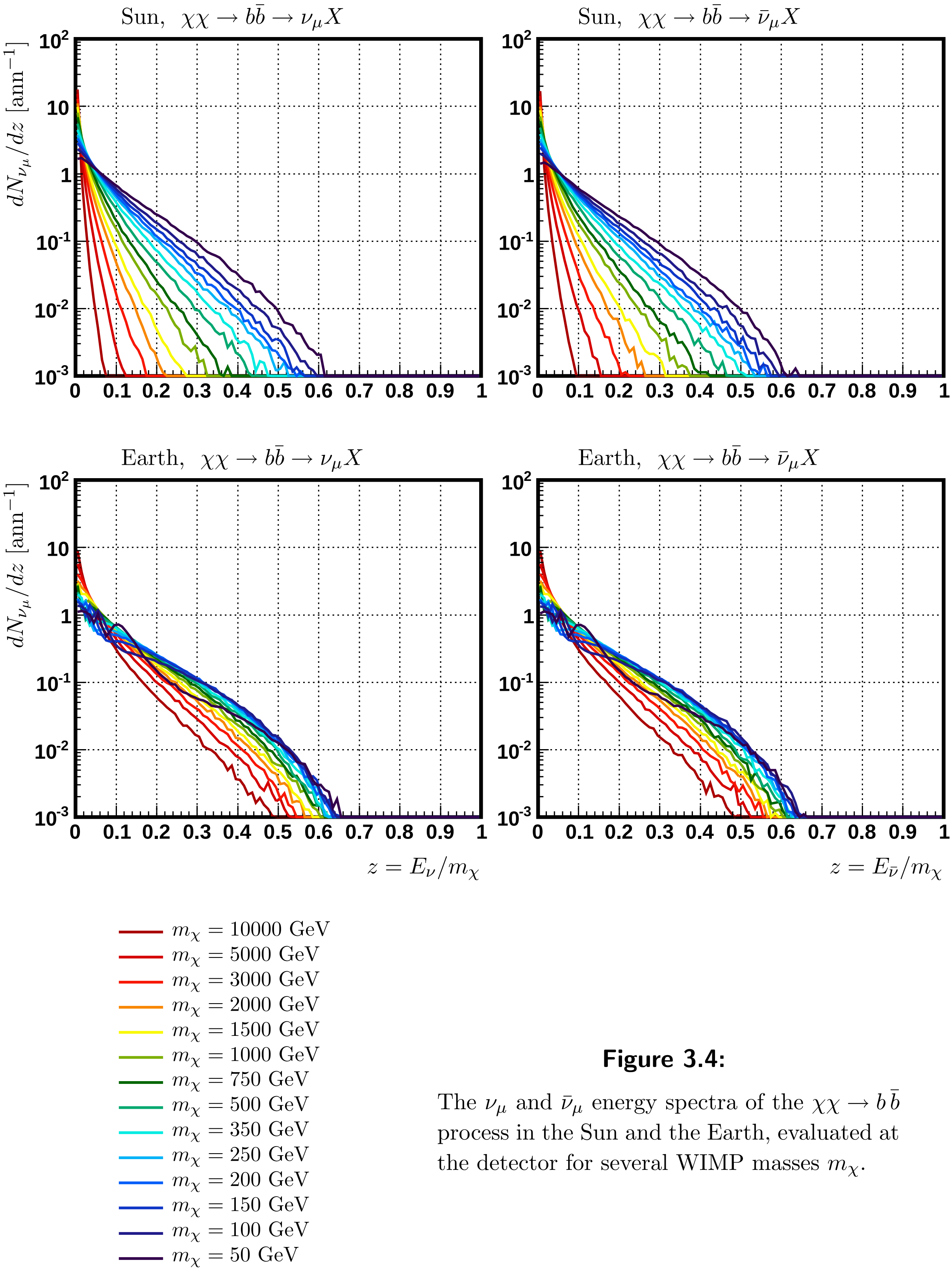

Figure 3.4:

The ν_μ and $\bar{\nu}_\mu$ energy spectra of the $\chi\chi \to b\,\bar{b}$ process in the Sun and the Earth, evaluated at the detector for several WIMP masses m_χ.

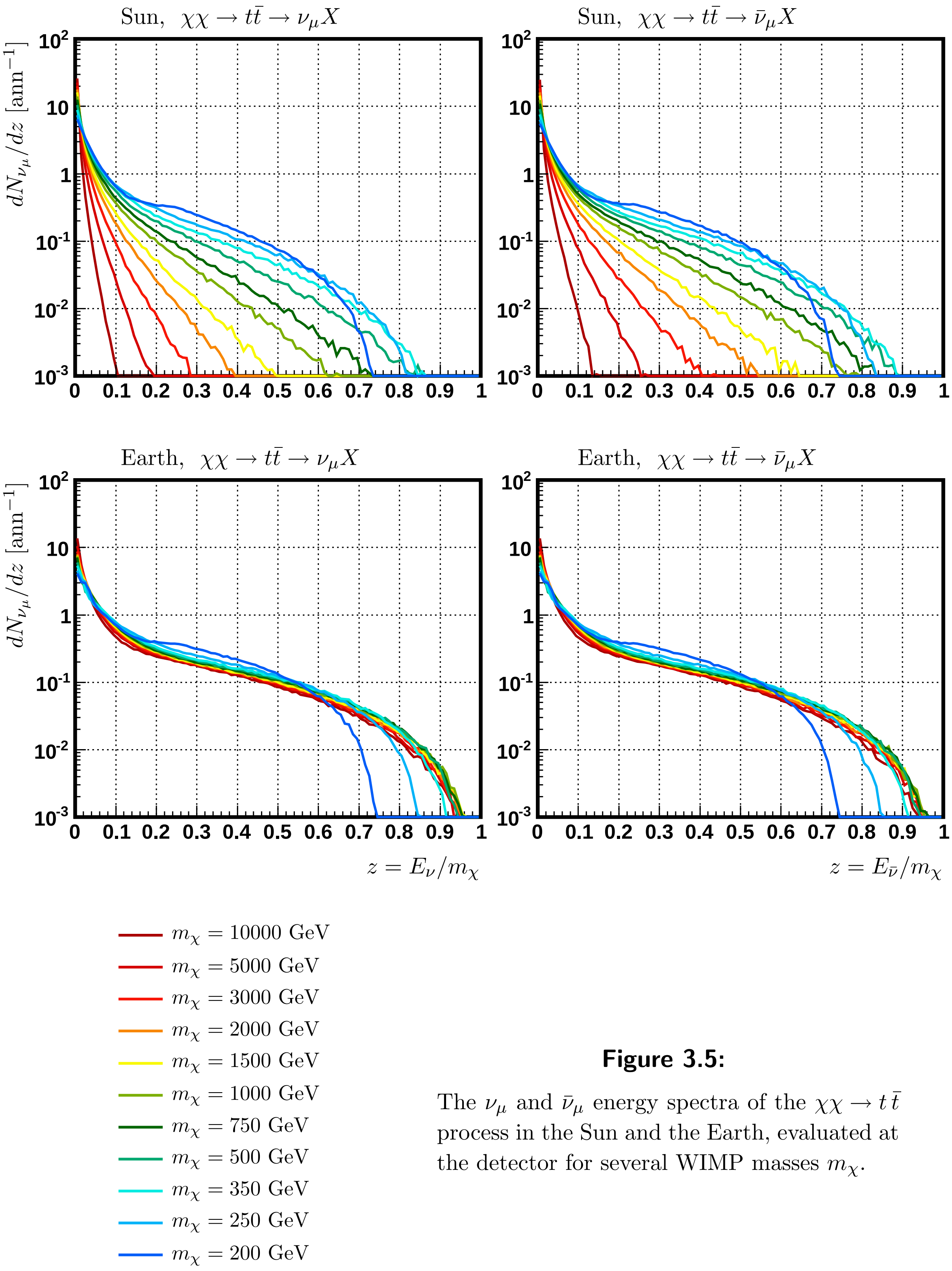

Figure 3.5:

The ν_μ and $\bar{\nu}_\mu$ energy spectra of the $\chi\chi \to t\,\bar{t}$ process in the Sun and the Earth, evaluated at the detector for several WIMP masses m_χ.

WIMP annihilation into weak vector bosons

WIMPs can also annihilate into a pair of weak vector bosons, i.e. $\chi\chi \to W^+W^-$ and $\chi\chi \to Z^0Z^0$. The energy spectra of muon-neutrinos from these two channels, evaluated at the detector for several WIMP masses m_χ, are shown in figure 3.6 and figure 3.7 respectively. As can be seen, these energy spectra are harder than those of the fermion channels. This is due to direct weak vector boson decay into neutrino(s), i.e. $W^+ \to l^+\,\nu_l$ and $Z^0 \to \nu_l\,\bar{\nu}_l$, where $\nu_l = \{\nu_e\,,\,\nu_\mu\,,\,\nu_\tau\}$. The corresponding branching ratios are 11 % and 6.7 %, for each neutrino type ν_l. The decays of weak vector bosons into hadrons can also produce neutrinos, but these will be softer.

WIMP annihilation into Higgs boson final states

WIMPs can possibly also decay into Higgs bosons, or a Higgs and a weak vector boson. Assuming the annihilation process is CP-invariant and WIMPs are non-relativistic, the possible annihilation channels are however restricted if the WIMP is a Majorana fermion. The CP-eigenvalue of a Majorana fermion is purely imaginary. Hence, in WIMP annihilation, the CP-eigenvalue of the initial state is odd since it has zero orbital angular momentum in the non-relativistic limit. Assuming CP-invariance, the CP-eigenvalue of the final state must be odd as well. As a consequence, WIMP annihilation into for instance two Higgs bosons is suppressed with the WIMP velocity squared, since the CP-eigenvalue of the Higgs boson is even [2]. Similarly, WIMP annihilation into a Higgs and a Z^0-boson is only possible if the orbital angular momentum of the final state is equal to one. Since the Higgs mass is a free parameter in the Standard Model and therefore possibly larger than the WIMP mass, these annihilation channels are not considered in this chapter.

WIMP annihilation into neutrinos

The probability that a (anti-)neutrino produced by $\chi\chi \to \nu_l\bar{\nu}_l$ annihilation in the Sun and the Earth will turn into a (anti-)muon-neutrino at the detector is shown as a function of the initial neutrino energy E_ν in figure 3.8. As can be seen from the bottom panels, neutrino interactions in the Earth are negligible as the total probability for all three neutrino flavours is equal to one. The probability for each neutrino flavour is only affected by neutrino mixing, which becomes significant below 100 GeV. This is caused by Δm^2_{23}, as can be derived from equation (3.13). Since the energy spectra for neutrinos and anti-neutrinos are identical, neutrino mixing due to the MSW effect is neglibible (see section 3.2.1). As can be seen from the top panels in figure 3.8, for the Sun the survival probability decreases with energy. Hence, neutrino interactions in the interior of the Sun clearly have a large effect. The decrease is larger for neutrinos than for anti-neutrinos due to the higher neutrino-nucleon cross section. The effects of mixing can also be clearly seen, since the probabilities for all three channels are approximately

[2] Supersymmetry, in which the dark matter candidate is usually the lightest neutralino, contains an additional CP-odd Higgs boson (see chapter 2). However, since the pseudoscalar Higgs is heavier than the neutralino, this annihilation channel is kinematically forbidden.

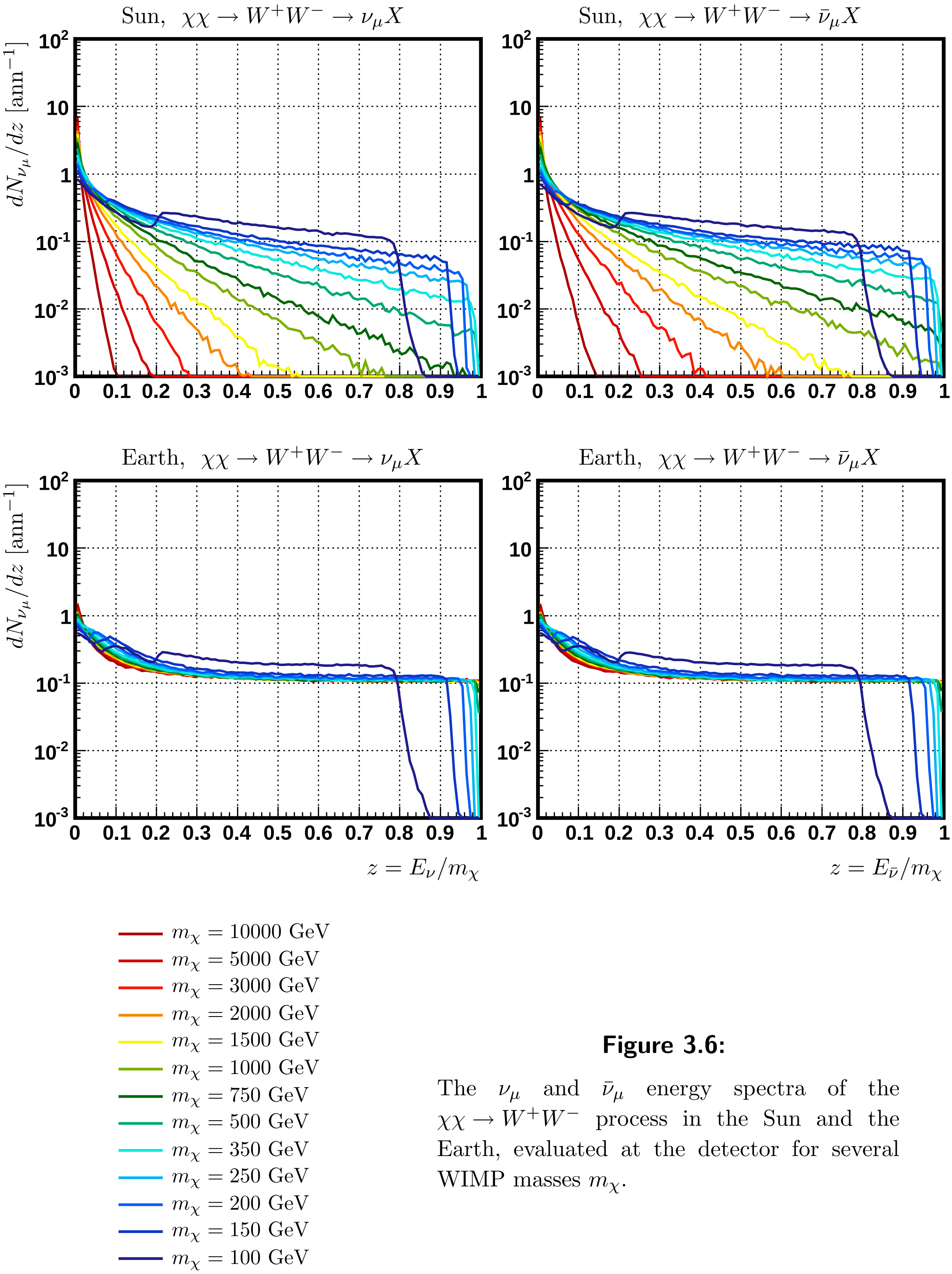

Figure 3.6:

The ν_μ and $\bar{\nu}_\mu$ energy spectra of the $\chi\chi \to W^+W^-$ process in the Sun and the Earth, evaluated at the detector for several WIMP masses m_χ.

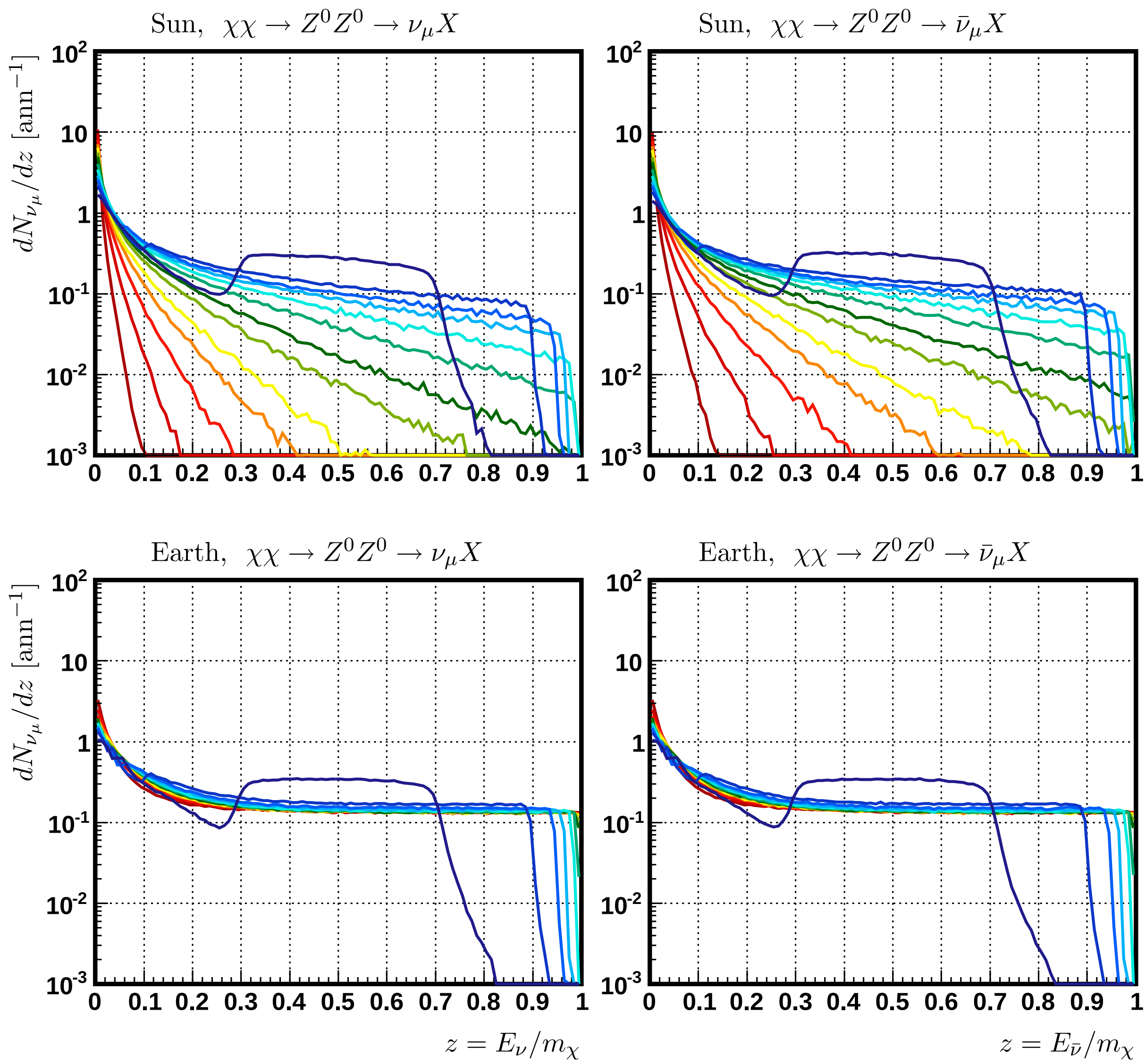

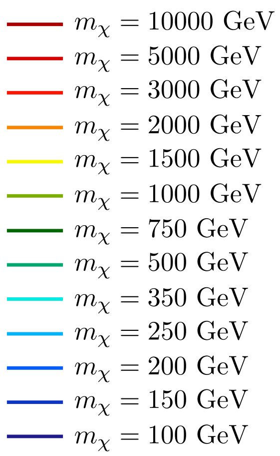

Figure 3.7:

The ν_μ and $\bar{\nu}_\mu$ energy spectra of the $\chi\chi \to Z^0Z^0$ process in the Sun and the Earth, evaluated at the detector for several WIMP masses m_χ.

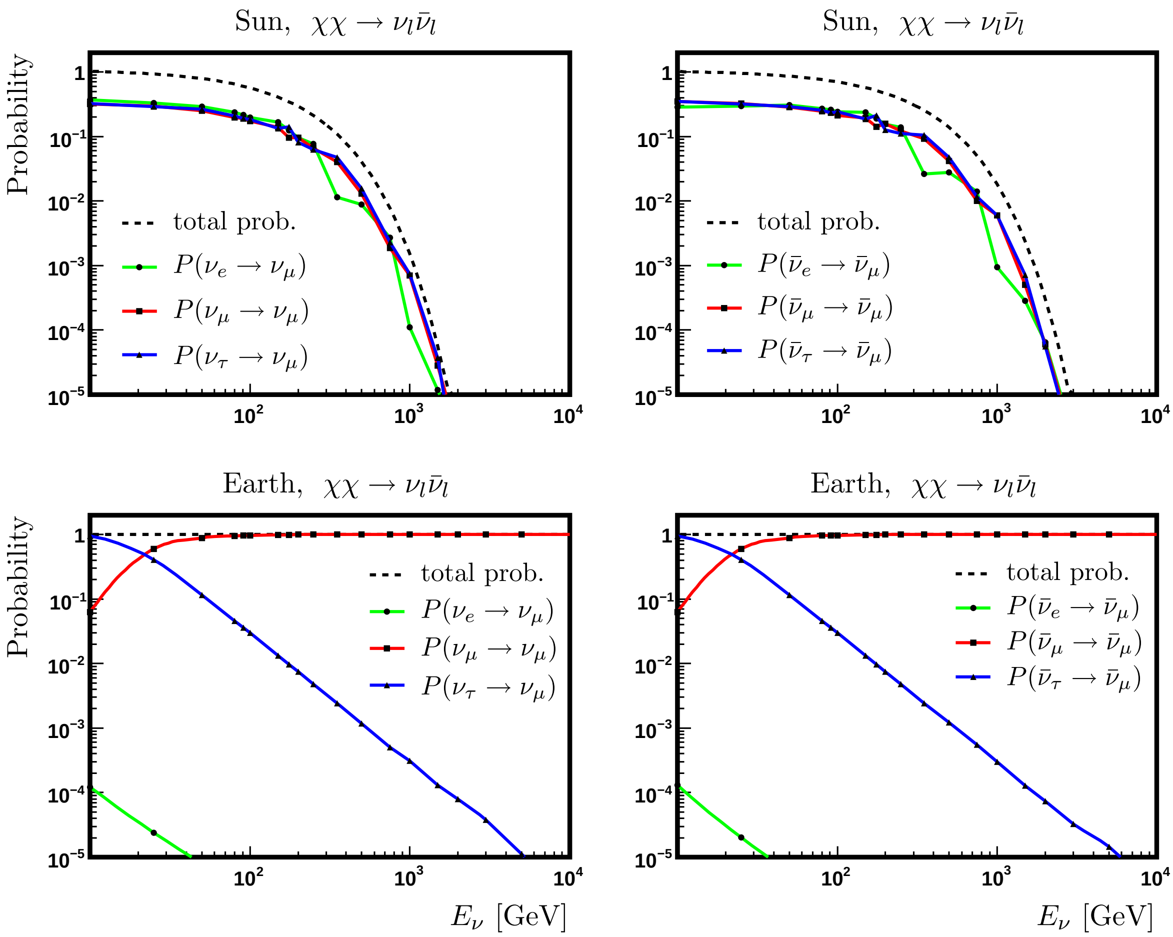

Figure 3.8: The probability that a (anti-)neutrino produced by $\chi\chi \to \nu_l\bar{\nu}_l$ annihilation in the Sun and the Earth will turn into a (anti-)muon-neutrino at the detector, as a function of the initial neutrino energy E_ν. The probabilities for neutrinos, $P\left(\nu_l \to \nu_\mu\right)$, and anti-neutrinos, $P\left(\bar{\nu}_l \to \bar{\nu}_\mu\right)$, are shown in the left and right panels respectively.

of the same order. The oscillations are different for neutrinos and anti-neutrinos due to the MSW effect.

The ν_μ and $\bar{\nu}_\mu$ energy spectra from $\chi\chi \to \nu_e\bar{\nu}_e$, $\chi\chi \to \nu_\mu\bar{\nu}_\mu$ and $\chi\chi \to \nu_\tau\bar{\nu}_\tau$ in the Sun at the detector are shown in figure 3.9 for several WIMP masses m_χ. The ν_μ and $\bar{\nu}_\mu$ energy spectra are shown in the left and right panels, respectively. The corresponding energy spectra for the Earth (not shown) are simple peaks at $E_\nu = m_\chi$. This is because interactions in the Earth are negligible, as was concluded previously. For the Sun, the energy spectra also have a peak at $E_\nu = m_\chi$ from the directly produced neutrinos, as can be seen from figure 3.9. There are however also a considerable number of soft muon-neutrinos due to interactions with solar material. The tau channel produces more soft neutrinos than the electron and muon channels due to the regeneration ability of the tau-neutrino. If a tau-neutrino interacts with a nucleus it produces a tau which will immediately decay, producing among other particles a new tau-neutrino. Electron-

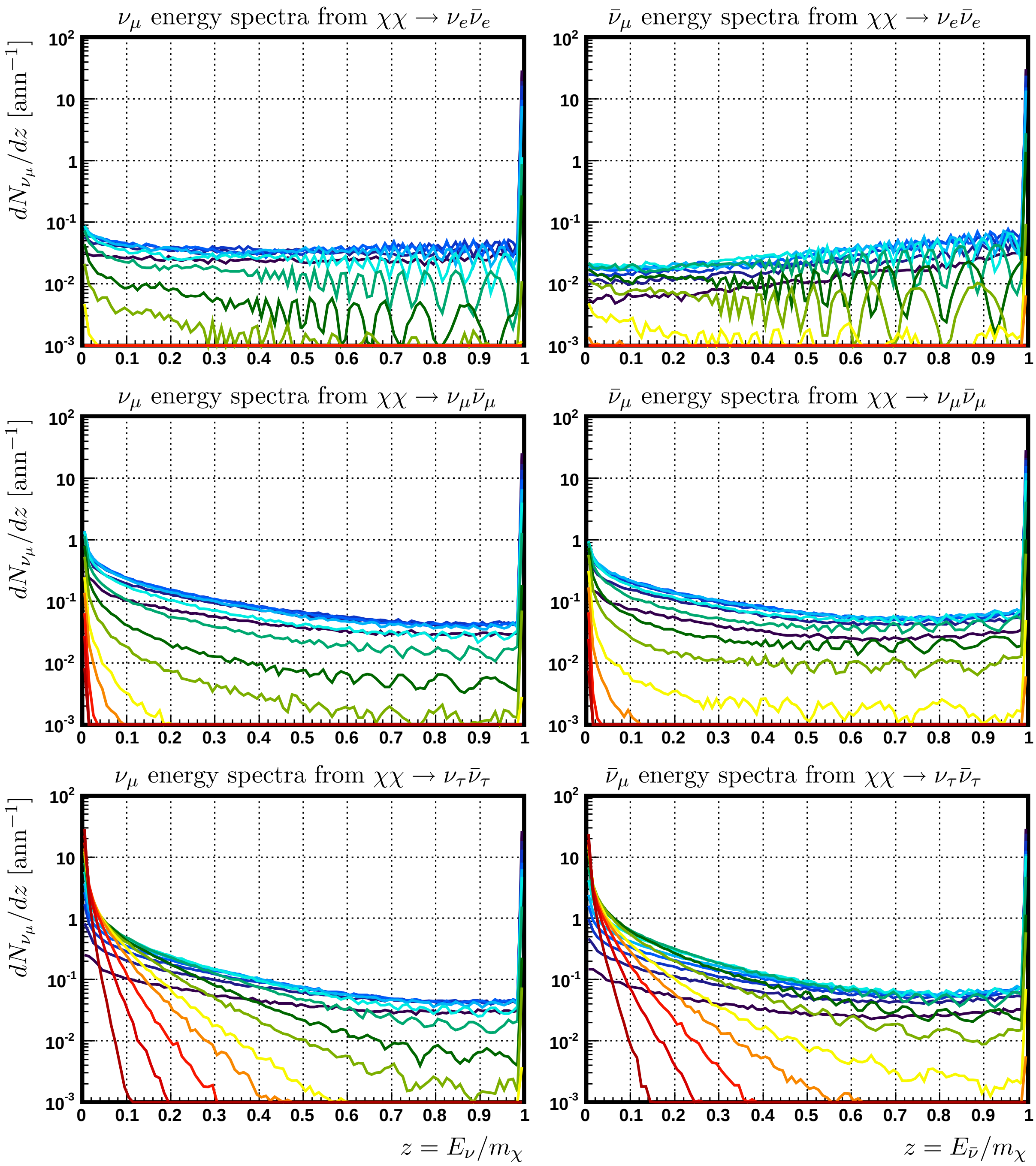

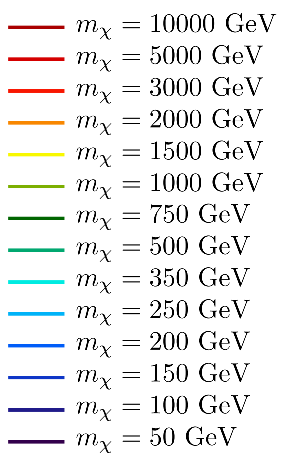

Figure 3.9:

The ν_μ and $\bar{\nu}_\mu$ energy spectra of the $\chi\chi \to \nu_e\bar{\nu}_e$, $\nu_\mu\bar{\nu}_\mu$ and $\nu_\tau\bar{\nu}_\tau$ processes in the Sun, evaluated at the detector for several WIMP masses m_χ.

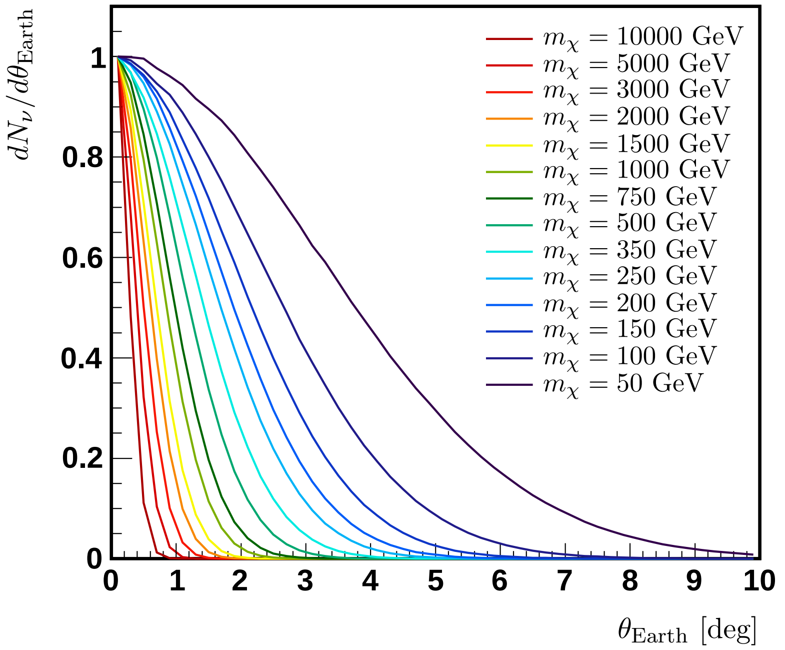

Figure 3.10:

The angular distribution of neutrinos from WIMP annihilation in the Earth $dN_\nu/d\theta_{\mathrm{Earth}}$ for several WIMP masses m_χ, where θ_{Earth} is the angle between the neutrino direction and the centre of the Earth at the detector. The distributions are normalised to 1 at $\theta_{\mathrm{Earth}} = 0°$ for comparison.

and muon-neutrinos do not have this regeneration ability since electrons and muons are stopped before they can decay. The effects of neutrino mixing can also be seen, and are similar to those in figure 3.3. The main interest for neutrino telescopes lies in the peaks at $E_\nu = m_\chi$. The mono-energetic nature of these neutrinos is particularly useful to distinguish these neutrinos from the background.

3.3.3 Angular distribution of neutrinos

WIMPs that have settled in the centre of the Sun or the Earth are in thermal contact with the core of the object. The WIMP number density N_χ will therefore be distributed according to a Gaussian distribution [54]

$$N_\chi(r) \;=\; N_\chi(0)\, e^{-r^2/(2\, r_\chi^2)} \qquad \text{with } \; r_\chi \;=\; \sqrt{\frac{3\, k_B\, T}{4\, \pi\, G_N\, \rho\, m_\chi}} \tag{3.15}$$

where r is the radius from the centre of the object, T and ρ are the temperature and density at the centre of the object, k_B is the Boltzmann constant, and G_N is the gravitational constant.

For the Sun, the temperature at the centre is of the order of 10^7 K. This implies that the angle from Earth between the neutrino direction and the centre of the Sun $\theta_{\mathrm{Sun}} < 0.005°$ for $m_\chi > 10$ GeV. Hence neutrino emission from WIMP annihilation in the Sun can be regarded as point-like.

At the centre of the Earth however, the temperature is approximately 6000 K and the density is a factor ten smaller than in the Sun. Therefore, the WIMP population in the Earth is distributed in a relatively larger volume, and neutrino emission from WIMP annihilation cannot be regarded as point-like. The angular distribution of neutrinos from WIMP annihilation in the Earth, $dN_\nu/d\theta_{\mathrm{Earth}}$, is shown in figure 3.10 for several WIMP masses m_χ, where θ_{Earth} is the angle between the neutrino direction and the centre of the Earth at the detector. The distributions are normalised to 1 at $\theta_{\mathrm{Earth}} = 0°$ for comparison.

3.4 Neutrinos from WIMP annihilation in the dark matter halo

The WIMP annihilation rate is proportional to the dark matter density squared. The fact that the density of the dark matter halo of our Galaxy peaks sharply at the Galactic Centre, makes it an interesting region to search for dark matter. The flux of neutrinos of type ν_l at a detector from WIMP annihilation in the dark matter halo along a direction that forms an angle ψ with respect to the Galactic Centre, can be written as [55]

$$\frac{d\Phi_{\nu_l}(\psi)}{dE_{\nu_l}} = \frac{\sigma_{\chi\chi} v}{4\pi m_\chi^2} \sum_X \left(\frac{\sigma_{\chi\chi\to X}}{\sigma_{\chi\chi}}\right)_X \left(\frac{dN_{\nu_l}}{dE_{\nu_l}}\right)_X \int_{\text{line of sight}} \rho_\chi^2 \, dl \tag{3.16}$$

where the coordinate $l(\psi)$ runs along the line of sight. v is the relative WIMP velocity. The sum includes all WIMP annihilation channels $\chi\chi \to X$ that are capable of producing neutrinos, in which the ratio of the cross section $\sigma_{\chi\chi\to X}$ of annihilation channel X and the total annihilation cross section $\sigma_{\chi\chi}$ is the branching ratio of annihilation channel X, and $(dN_{\nu_l}/dE_{\nu_l})_X$ is the neutrino energy spectrum at the detector from annihilation channel X.

All dark matter halo dependence of the neutrino flux is contained in the integral in equation (3.16). It is customary to define a normalised function $J(\psi)$, which contains the integral of the WIMP density squared along the line of sight, as

$$J(\psi) \equiv \frac{1}{\rho_0^2 D} \int_{\text{line of sight}} \rho_\chi^2 \, dl \tag{3.17}$$

where ρ_0 is the local dark matter halo density at the position of the Sun, and D is the distance between the Sun and the Galactic Centre. The average of $J(\psi)$ over a spherical region of solid angle $\Delta\Omega$ in the direction of ψ is defined as

$$\langle J(\psi)\rangle_\alpha \equiv \frac{1}{\Delta\Omega} \int_{\Delta\Omega} J(\psi) \, d\Omega \tag{3.18}$$

where the angle α corresponds to the half-aperture of a cone which spans a solid angle $\Delta\Omega$. The functions $J(\psi)$ and $\langle J(\psi)\rangle_\alpha$ for $\alpha = 1°, 2°, 3°, 4°, 5°$ are shown in figure 3.11, where the NFW profile is used for the radial density profile of the dark matter density [23], and $\rho_0 = 0.3$ GeV/cm^3 and $D = 8.5$ kpc (see section 1.4.2). As expected, $J(\psi)$ peaks in the direction of the Galactic Centre. For neutrino experiments $\Delta\Omega$ should correspond to the angular resolution of the detector, which is typically of the order of one degree.

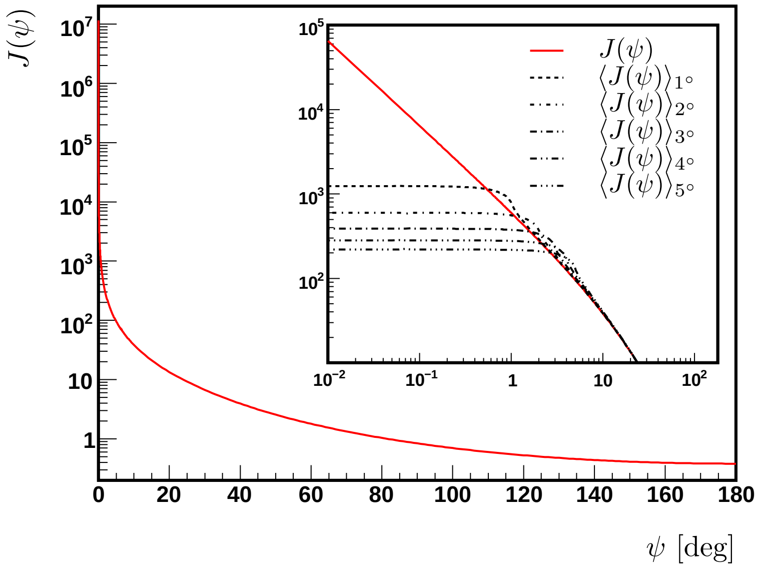

Figure 3.11:

The dimensionless functions $J(\psi)$ and $\langle J(\psi)\rangle_\alpha$ with $\alpha = 1°, 2°, 3°, 4°, 5°$ as a function of the angle ψ with respect to the Galactic Centre.

- $\rho(r)$ = NFW profile
- $\rho_0 = 0.3$ GeV/cm^3
- $D = 8.5$ kpc

The neutrino flux from WIMP annihilation channel $\chi\chi \to X$, from a solid angle $\Delta\Omega$ in the direction ψ, can then be written as

$$\left(\frac{d\Phi_{\nu_l}(\psi, \Delta\Omega)}{dE_{\nu_l}}\right)_X = C_{\text{halo}} \frac{\sigma_{\chi\chi\to X}\, v}{m_\chi^2} \left(\frac{dN_{\nu_l}}{dE_{\nu_l}}\right)_X \langle J(\psi)\rangle_\alpha\, \Delta\Omega \tag{3.19}$$

If ρ_0 is given in units of 0.3 GeV/cm^3, D in units of 8.5 kpc, m_χ in units of 1 GeV, and $\sigma_{\chi\chi\to X}\, v$ in units of 10^{-29} cm^3 s^{-1}, the proportionality factor C_{halo} in equation (3.19) is $\sim 9.4 \cdot 10^{-10}$ cm^{-2} s^{-1}.

3.5 Limits from neutrino experiments

Neutrino experiments hope to detect neutrinos from WIMP annihilation in astrophysical sources. However, no indication of WIMP annihilation from a specific source has been found yet. In that case, upper limits on the neutrino flux and corresponding muon flux can be set. To do so, the detection probability has to be calculated. Due to the neutrino detection principle, the detection probability is strongly dependent on the neutrino energy. It is customary for neutrino experiments to show their flux limits as a function of the WIMP mass. The neutrino energy spectra in this chapter can be used to calculate the detection probability for neutrinos from a specific annihilation channel and source as a function of the WIMP mass. The upper limits on the neutrino and muon flux can then be derived from the observed rate in the detector. This procedure will be discussed in more detail in chapter 7 for the ANTARES neutrino telescope.

A compilation of results derived from measurements made by other experiments is shown in figure 3.12. The figure shows the upper limit at 90 % C.L. on the neutrino-induced muon flux $\Phi_{\mu^-+\mu^+}$ from WIMP annihilation in the Earth, the Galactic Centre and the Sun as a function of the WIMP mass m_χ. This figure includes results from experiments that use scintillation techniques (Baksan [56] and MACRO [57]) and

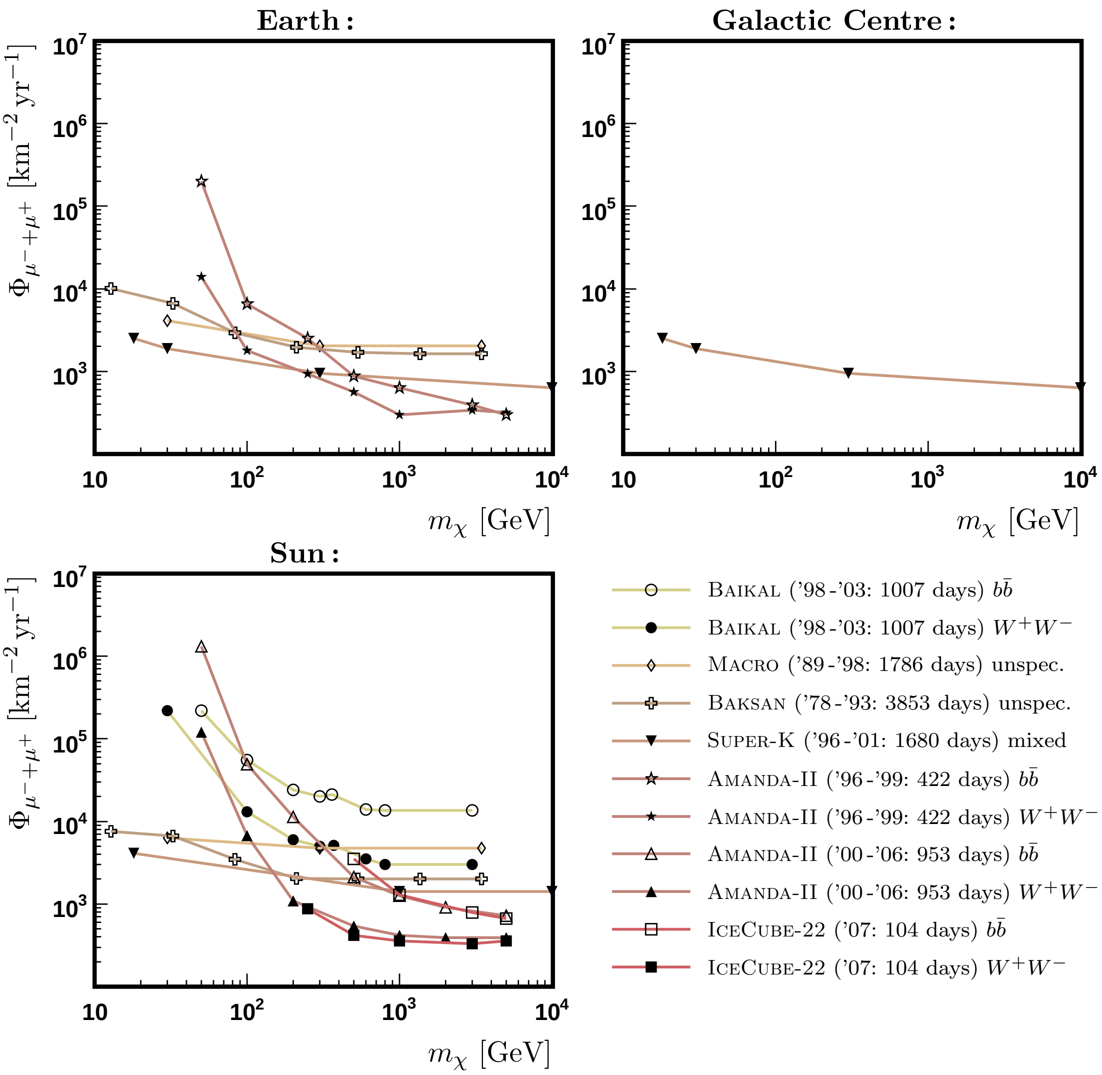

Figure 3.12: The upper limits at 90 % C.L. on $\Phi_{\mu^-+\mu^+}$ from WIMP annihilation in the Earth, the Sun and the Galactic Centre as a function of the WIMP mass m_χ. Results are from Baksan [56], MACRO [57], Super-Kamiokande [58], Baikal [59], AMANDA [60, 61] and IceCube [62].

water-Cherenkov techniques (Super-Kamiokande [58], Baikal [59] and AMANDA / Ice-Cube [60, 61, 62]). Limits are usually derived assuming the annihilation is dominated by one specific channel, as indicated in the legend [3]. Also indicated is the period of data-taking and total effective livetime that were used to derive each limit. For the Sun, the effective livetime for the AMANDA and IceCube experiments includes only days when the Sun was below the horizon.

[3] Results from Super-Kamiokande assume WIMP annihilation into 80 % $b\bar{b}$, 10 % $c\bar{c}$ and 10 % $\tau^+\tau^-$ final states. Results from Baksan and MACRO are published without specifying the annihilation channels.

Chapter 4

Neutrinos from neutralino annihilation in astrophysical objects

Since neutralinos are massive, stable, electrically neutral and colorless particles, the lightest neutralino is a WIMP and therefore a natural dark matter candidate. In this thesis, the lightest of the four neutralinos is referred to as *the* neutralino $\tilde{\chi}$. This chapter gives a general overview of neutralino dark matter in the context of mSUGRA. In particular, the implications for the indirect detection of neutralino annihilation in the Sun, the Earth and the Galactic Centre using neutrinos will be discussed.

All results presented in this chapter are obtained using the `DarkSUSY v5.0.5` package for supersymmetric dark matter calculations [63]. The evolution of the mSUGRA parameters from the grand unification scale to the electro-weak scale is done using the `ISASUGRA` routine of the `ISAJET v7.78` program [64]. Since mSUGRA has four real parameters and one discrete parameter, there are twelve possible 2-dimensional parameter phase space projections. In the literature, usually the m_0-$m_{1/2}$ projection for $\mathrm{sign}(\mu) = +$ is chosen for illustrative purposes. The same convention is used in this chapter. The other mSUGRA parameters are arbitrarily chosen as $\tan(\beta) = 45$ and $A_0 = 0$ GeV unless otherwise noted. The top quark mass is set at 172.7 GeV.

4.1 Neutralino dark matter

In most of mSUGRA parameter phase space, the lightest superpartner is the neutralino. This is illustrated in the left panel of figure 4.1, which shows the mass of the neutralino $m_{\tilde{\chi}}$ at the electro-weak scale in m_0-$m_{1/2}$ mSUGRA parameter space. The only exception is the plus-covered region where the lightest superpartner is usually the lightest scalar tau. The cross-covered region is excluded because radiative electro-weak symmetry breaking does not occur. In this region m_0 is too large with respect to $m_{1/2}$ to end up with a small enough $m_{H_u}^2$ at the electro-weak scale, which is needed for electro-weak symmetry breaking. The dot-covered region at low m_0 and $m_{1/2}$ is excluded by recent accelerator experiments [65]. The incidental white dots in the figure are caused by divergences in the iterative procedures in `ISASUGRA`.

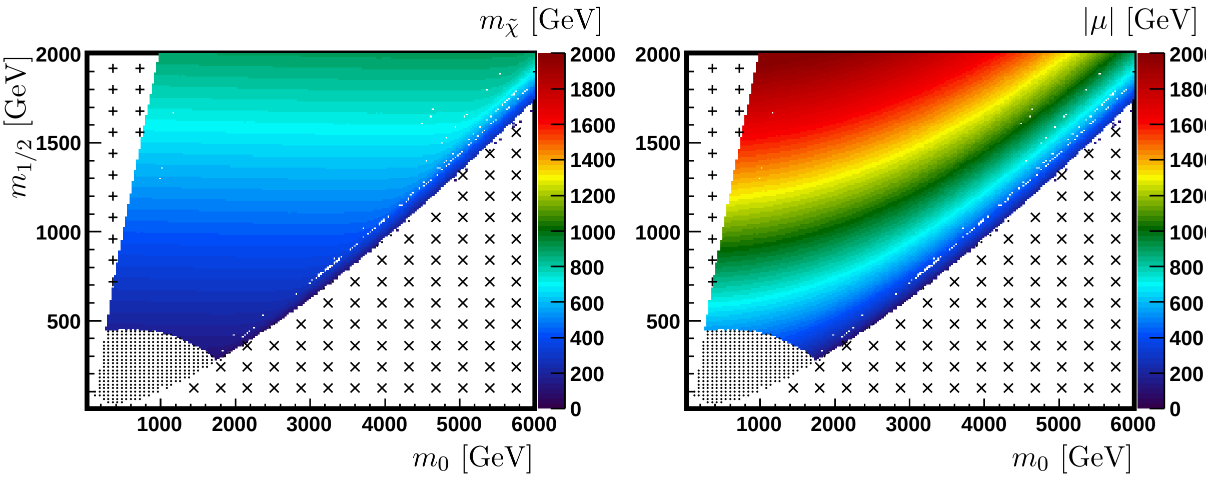

$\tan(\beta) = 45 \quad A_0 = 0$ GeV $\quad \mathrm{sign}(\mu) = +$

Figure 4.1: The neutralino mass $m_{\tilde{\chi}}$ and the magnitude of the higgsino mass parameter μ at the electro-weak scale in m_0-$m_{1/2}$ mSUGRA parameter space.

4.1.1 Neutralino mass

As can be seen from the left panel of figure 4.1, in most of mSUGRA parameter space the neutralino mass is only dependent on $m_{1/2}$, except close to the cross-covered region where electro-weak symmetry breaking does not occur. The latter region is the *Hyperbolic Branch* or *Focus Point* (HB/FP) region of mSUGRA parameter space. This can be explained by considering the neutralino mass matrix in equation (2.5). For m_0, $m_{1/2}$, $\mu \gg m_Z$, the four neutralino mass eigenstates are approximately $\tilde{B}$, $\tilde{W}_3$ and $\sqrt{1/2}(\tilde{H}_d^0 \pm \tilde{H}_u^0)$ with mass eigenvalues approximately equal to $m_{\tilde{B}}$, $m_{\tilde{W}}$, and $|\mu|$, respectively. The lightest mass eigenvalue determines which of the four eigenstates corresponds to the lightest neutralino. The magnitudes of $m_{\tilde{B}}$ and $m_{\tilde{W}}$ can be derived by applying the renormalisation group equations to the gaugino mass parameters. It can be shown that at any energy scale Q:

$$\frac{m_{\tilde{B}}(Q)}{\frac{5}{3}\, g'^{\,2}(Q)} \approx \frac{m_{\tilde{W}}(Q)}{g^2(Q)} \approx \frac{m_{\tilde{g}}(Q)}{g_s^2(Q)} \tag{4.1}$$

where the coupling constants g', g and g_s correspond to the three Standard Model gauge groups $U(1)_Y$, $SU(2)_L$ and $SU(3)_C$, respectively. By applying equation (4.1) at the electro-weak scale Q_{EW}, where $g'/g \equiv \tan(\theta_W)$ and $\cos(\theta_W) = m_W/m_Z \approx 0.88$, it can be derived that $m_{\tilde{W}}(Q_{\mathrm{EW}}) \approx 2\, m_{\tilde{B}}(Q_{\mathrm{EW}})$. Similarly, it can be derived that $m_{\tilde{B}}(Q_{\mathrm{EW}}) \approx 0.4\, m_{1/2}$, assuming the three coupling constants unify at $\frac{5}{3}\, g'^{\,2} = g^2 = g_s^2 \approx 0.5$ at the GUT scale as shown in figure 2.1. The magnitude of the higgsino mass parameter μ at the electro-weak scale can be derived from the radiative electro-weak symmetry breaking conditions, and is shown in m_0-$m_{1/2}$ mSUGRA parameter space in the right panel of figure 4.1. As can be seen, in most of mSUGRA parameter space $|\mu| > m_{\tilde{\chi}}$, except in the HB/FP-region. Thus, in most of mSUGRA parameter space

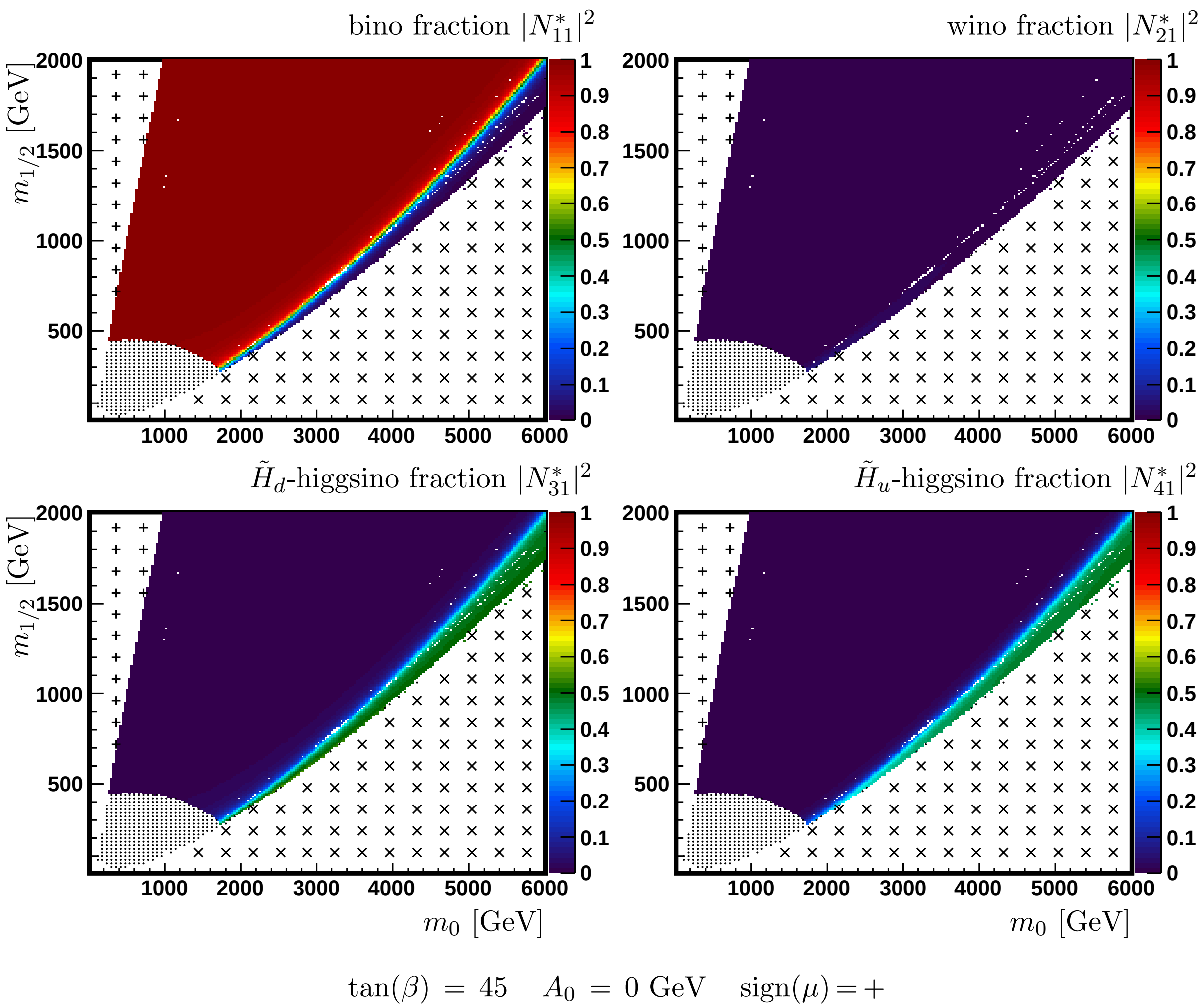

Figure 4.2: The neutralino gauge eigenstate fractions in m_0-$m_{1/2}$ mSUGRA parameter space. The four panels show the bino fraction $|N_{11}^*|^2$, the wino fraction $|N_{21}^*|^2$, the $\tilde{H}_d$-higgsino fraction $|N_{31}^*|^2$ and the $\tilde{H}_u$-higgsino fraction $|N_{41}^*|^2$ of the neutralino.

the neutralino is bino-like with $m_{\tilde{\chi}} \approx 0.4\, m_{1/2}$, except in the HB/FP-region where the neutralino becomes higgsino-like with $m_{\tilde{\chi}} \approx |\mu|$.

4.1.2 Neutralino composition

The neutralino composition in terms of its gauge eigenstates is shown in figure 4.2. Following equation (2.6), the four panels show the gauge eigenstate fractions $|N_{\alpha 1}^*|^2$ of the neutralino in m_0-$m_{1/2}$ mSUGRA parameter space: the bino fraction $|N_{11}^*|^2$ (top-left), the wino fraction $|N_{21}^*|^2$ (top-right), the $\tilde{H}_d$-higgsino fraction $|N_{31}^*|^2$ (bottom-left) and the $\tilde{H}_u$-higgsino fraction $|N_{41}^*|^2$ (bottom-right). As was concluded previously, the neutralino is indeed predominantly bino-like in most of mSUGRA parameter space, except in the HB/FP-region where it is predominantly higgsino-like.

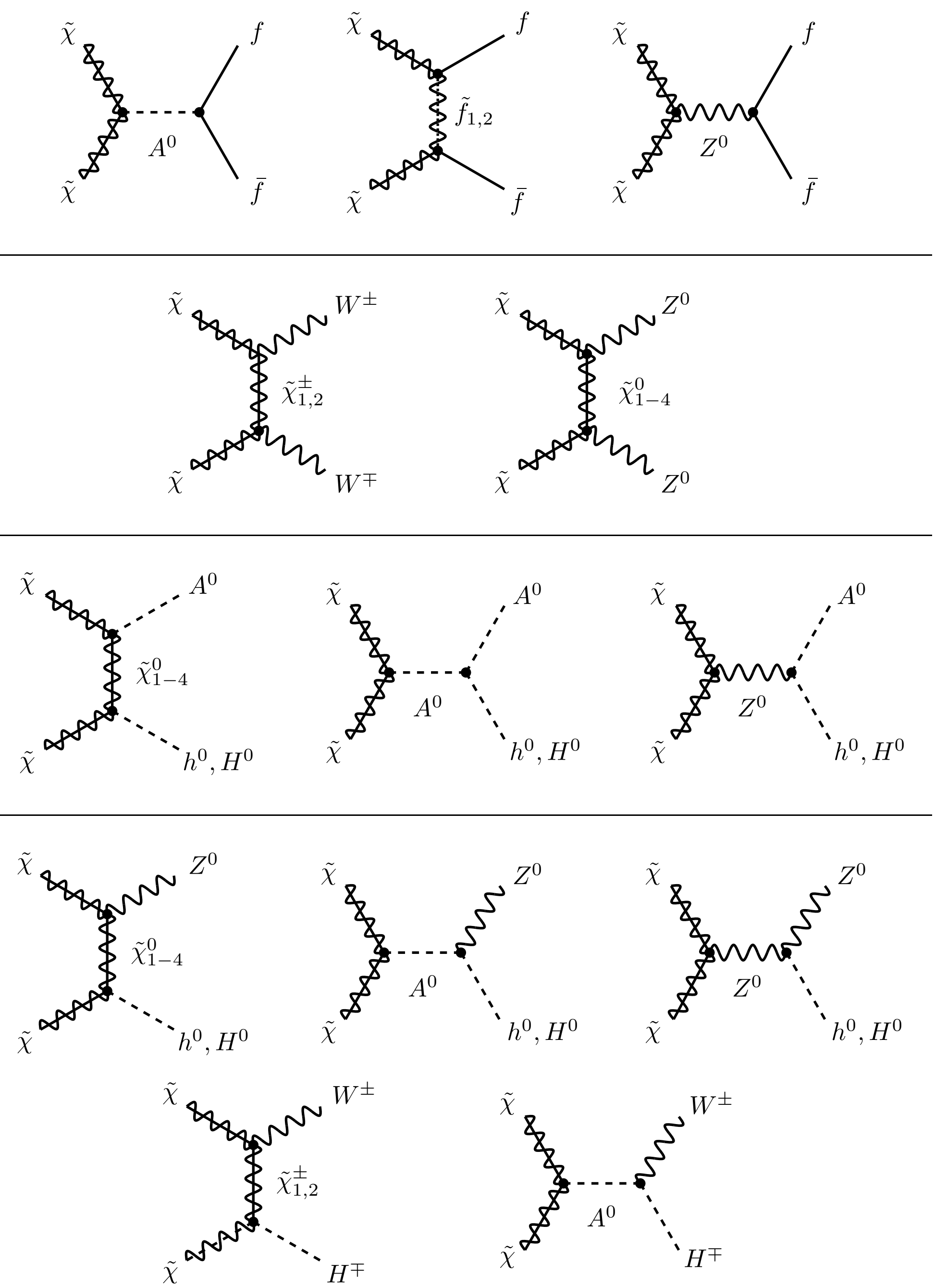

Figure 4.3: The leading order Feynman diagrams that contribute to neutralino annihilation in the non-relativistic limit [22]. Diagrams are categorised according to the final state: neutralino annihilation into fermion anti-fermion (top row), weak vector bosons (second row), Higgs bosons (third row), and weak vector / Higgs bosons (bottom rows).

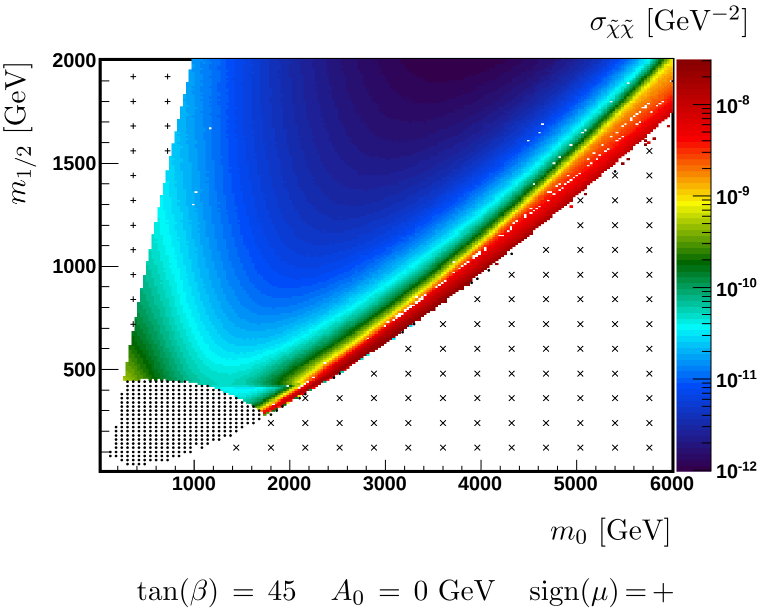

Figure 4.4: The total neutralino annihilation cross section $\sigma_{\tilde{\chi}\tilde{\chi}}$ in m_0-$m_{1/2}$ mSUGRA parameter space.

4.2 Neutralino annihilation

All leading order Feynman diagrams that contribute to neutralino annihilation from an s-wave initial state are shown in figure 4.3. The diagrams are categorised according to the final state. Some of these processes can be kinematically forbidden in parts of mSUGRA phase space, in particular those that have a charged Higgs $H^{\pm}$, scalar Higgs H^0 or pseudoscalar Higgs A^0 in the final state. The total neutralino annihilation cross section $\sigma_{\tilde{\chi}\tilde{\chi}}$ in m_0-$m_{1/2}$ mSUGRA parameter space for all leading order neutralino annihilation processes is shown in figure 4.4. As can be seen, the annihilation cross section is much larger for higgsino-like neutralinos than for bino-like neutralinos. This can be explained by analysing the dominant individual annihilation processes.

The six leading order processes that provide the largest contribution to the total annihilation cross section are $\tilde{\chi}\tilde{\chi} \to b\bar{b}$, $t\bar{t}$, W^+W^-, Z^0Z^0, $\tau^+\tau^-$, and Z^0h^0. The individual annihilation cross sections and corresponding branching ratios for these six processes are shown in figures 4.5 and 4.6, respectively. As can be seen, bino-like neutralinos annihilate preferably into fermions while higgsino-like neutralinos annihilate preferably into weak vector bosons. This can be explained by the fact that the B-boson of the $U(1)_Y$ gauge group does not couple to any other gauge boson nor to itself, and therefore neither does the bino. Hence, for pure bino-like neutralinos only the $\tilde{\chi}\tilde{\chi} \to f\bar{f}$ through t/u-channel squark exchange (see middle diagram, top row in figure 4.3) process contributes. The amplitude of this process is inversely proportional to the squark mass squared. Since the squark mass is generally relatively large, the annihilation cross section for this process is suppressed. Neutralinos that have a higgsino component however can couple to weak vector bosons or Higgs bosons. For higgsino-like neutralinos, the annihilation cross section is dominated by the $\tilde{\chi}\tilde{\chi} \to W^+W^-$ and Z^0Z^0 processes and, if kinematically possible, the $\tilde{\chi}\tilde{\chi} \to t\bar{t}$ process through s-channel Z^0-boson exchange. The annihilation cross sections for these processes are relatively large since they are not suppressed by large scalar masses as are the $\tilde{\chi}\tilde{\chi} \to f\bar{f}$ processes.

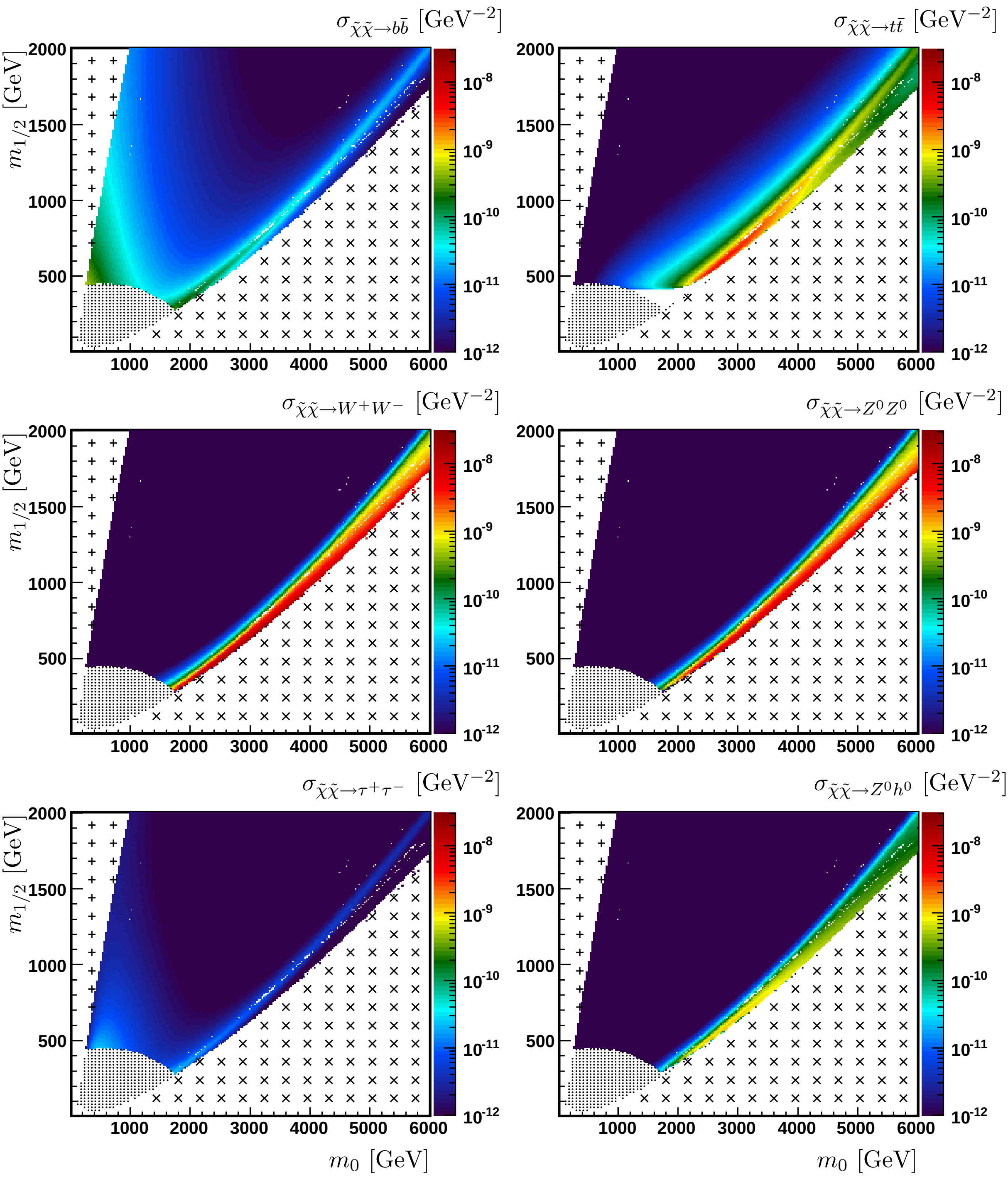

$\tan(\beta) = 45 \quad A_0 = 0$ GeV $\quad \text{sign}(\mu) = +$

Figure 4.5: The annihilation cross sections of the six dominant neutralino annihilation processes in m_0-$m_{1/2}$ mSUGRA parameter space. The six panels in the figure correspond to neutralino annihilation into $b\bar{b}$, $t\bar{t}$, W^+W^-, Z^0Z^0, $\tau^+\tau^-$, and Z^0h^0.

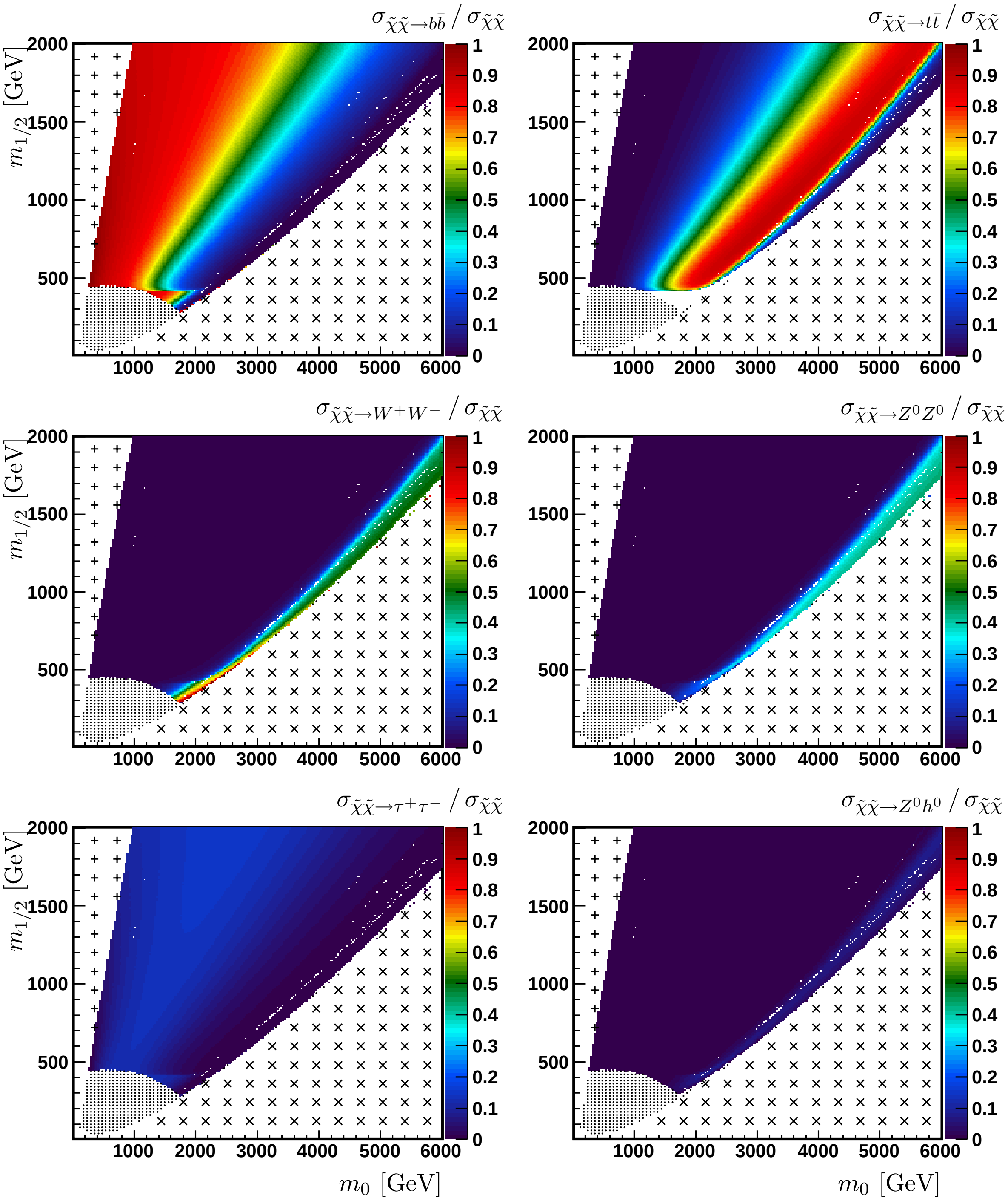

$\tan(\beta) = 45 \quad A_0 = 0$ GeV $\quad \mathrm{sign}(\mu) = +$

Figure 4.6: The branching ratios of the six dominant neutralino annihilation processes in m_0-$m_{1/2}$ mSUGRA parameter space. The six panels in the figure correspond to neutralino annihilation into $b\bar{b}$, $t\bar{t}$, W^+W^-, Z^0Z^0, $\tau^+\tau^-$, and Z^0h^0.

4.2.1 Helicity suppression of neutralino annihilation into fermions

The $b\bar{b}$ and (if kinematically possible) $t\bar{t}$ final states dominate neutralino annihilation to fermions in the non-relativistic limit, contrary to kinematic final state phase space considerations. The suppression of light fermion final states is due to the Majorana nature of neutralinos and the fact that they annihilate in the non-relativistic limit, as explained in section 1.5.2. These two conditions imply that the neutralino helicities in the initial state are equal, and hence the final state helicities as well. However, the Z^0-f-$\bar{f}$ coupling and the gaugino-fermion-sfermion couplings conserve chirality, so the final state fermions must have opposite chirality. The discrepancy between chirality and helicity manifests itself by a factor m_f in the amplitude, where m_f is the mass of the final state fermion. The A^0-f-$\bar{f}$ coupling and the higgsino-fermion-sfermion couplings contain an explicit factor m_f. Hence, the annihilation cross section for neutralino annihilation to fermions in the non-relativistic limit is proportional to m_f^2 [66]. Neutralino annihilation to fermions from a p-wave initial state does not suffer from helicity suppression, but is suppressed by the velocity of the neutralino squared, as shown in equation (1.18).

4.2.2 Present neutralino energy density

The present neutralino relic energy density parameter Ω_χ as defined in equation (1.9) is shown in m_0-$m_{1/2}$ mSUGRA parameter space in figure 4.7. As expected from equation (1.9), Ω_χ is inversely proportional to the total annihilation cross section (see figure 4.4). Since the Universe appears to be spatially flat, the cosmologically interesting region is the region in mSUGRA parameter space for which $\Omega_\chi < 1$. Cosmological measurements indicate that the present dark matter energy density $\Omega_{\mathrm{DM}} = 0.228 \pm 0.013$ at 68% C.L. (see table 1.1). The $\Omega_\chi = 1$ and $\Omega_\chi = 0.228$ contours are shown as a solid and a dotted line in figure 4.7, respectively. As can be seen, the cosmological measurements put very stringent constraints on the available m_0-$m_{1/2}$ mSUGRA parameter

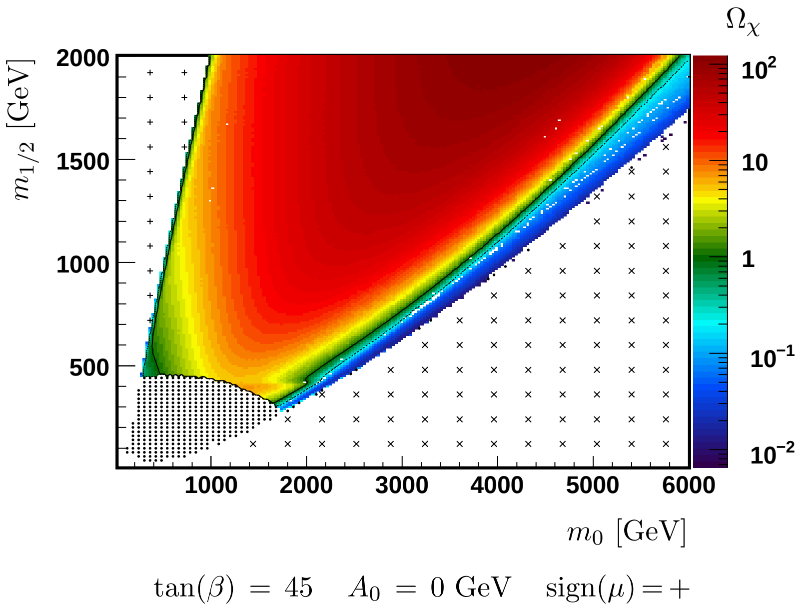

Figure 4.7: The present neutralino energy density parameter Ω_χ in m_0-$m_{1/2}$ mSUGRA parameter space. The $\Omega_\chi = 1$ and $\Omega_\chi = 0.228$ contours are shown as a solid and a dotted line, respectively.

space for fixed $\tan(\beta)$ and A_0. The allowed mSUGRA parameter space is limited to the HB/FP region where the neutralino is mixed bino-higgsino, and along the edge where the neutralino and the lightest stau become almost mass degenerate. Although the neutralino annihilation cross section in this region is too low to end up with the present dark matter energy density as determined by cosmological measurements, co-annihilation between the neutralino and the lightest stau (e.g. $\tilde{\chi}\tilde{\tau} \rightarrow Z^0\tau$) decreases the present neutralino energy density to the experimentally preferred value.

4.3 Neutrinos from neutralino annihilation in the Sun and the Earth

As discussed in section 1.5.2, the indirect detection of the neutrino flux resulting from WIMP annihilation in an astrophysical object is a possible way to confirm the existence of dark matter in the Universe. Potential dark matter sources are the centre of the Sun due to its relatively close proximity to Earth, and the Earth itself. In this section the neutrino flux from neutralino annihilation in the Sun and the Earth, as expected from mSUGRA, is presented.

4.3.1 Neutralino scattering

For astrophysical objects in which the neutralino capture and annihilation rates are in equilibrium, the annihilation rate is solely dependent on the capture rate (see equation (3.7)). The capture rate depends on the neutralino-nucleus cross section. In the non-relativistic limit, the neutralino-nucleus cross section has a spin-independent (SI) and a spin-dependent (SD) component (see section 1.5.1). The corresponding neutralino-proton cross sections in the $q = 0$ limit, $\sigma_{\chi p}^{\mathrm{SI}}$ and $\sigma_{\chi p}^{\mathrm{SD}}$, are defined in equations (1.17).

The three leading order Feynman diagrams that contribute to the total scattering cross section are shown in figure 4.8. Process (a) contributes only to the SI cross section, and process (c) contributes only to the SD cross section. Process (b) contributes to the

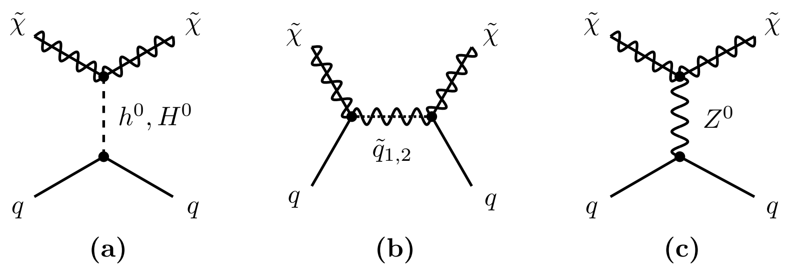

Figure 4.8: The leading order Feynman diagrams that contribute to neutralino-nucleus scattering [22]. In these processes, q represents a quark or an anti-quark.

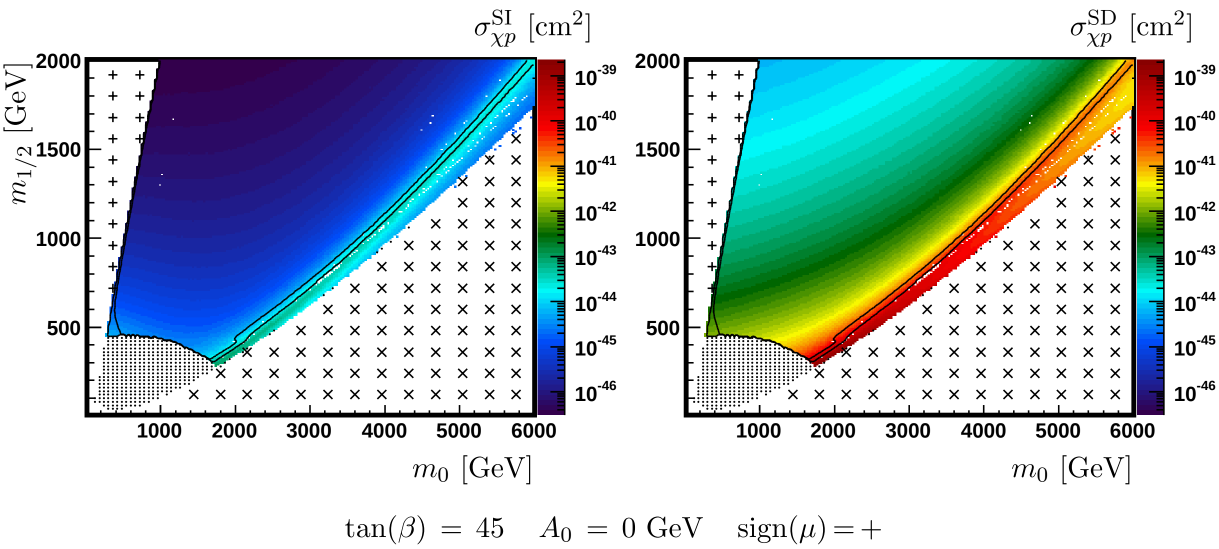

Figure 4.9: The SI and SD neutralino-proton cross sections in the $q = 0$ limit, $\sigma_{\chi p}^{\rm SI}$ and $\sigma_{\chi p}^{\rm SD}$, in m_0-$m_{1/2}$ mSUGRA parameter space.

SI cross section if the (anti-)quarks in the initial and final state have opposite helicity, while it contributes to the SD cross section if the (anti-)quarks in the initial and final state have equal helicity. Due to the relatively large squark masses, process (b) is suppressed with respect to the processes (a) and (c). For a pure bino-like neutralino, process (b) is the only process that contributes to both cross sections because the bino does not couple to weak vector bosons or Higgs bosons. Hence, if the neutralino has a higgsino component, processes (a) and (c) will dominate the SI and SD cross section, respectively.

The $\sigma_{\chi p}^{\rm SI}$ and $\sigma_{\chi p}^{\rm SD}$ in m_0-$m_{1/2}$ mSUGRA parameter space are shown in figure 4.9. As can be seen, the SD neutralino-proton cross section is larger than the SI neutralino-proton cross section. Both cross sections are suppressed for bino-like neutralinos, as expected from the Feynman diagrams in figure 4.8.

Both cross sections are shown as function of the neutralino mass in figure 4.10, for a larger scan of the mSUGRA parameters ($5 < \tan(\beta) < 50$). Only mSUGRA models in which the present neutralino relic energy density parameter $\Omega_\chi < 1$ are shown. All models are categorised into three groups, indicated by different colours:

- **Green:** mSUGRA models in which the present neutralino relic energy density parameter Ω_χ agrees with the experimentally determined $\Omega_{\rm DM} \pm 2\,\sigma$, i.e. $0.202 < \Omega_\chi < 0.254$ [10].
- **Blue:** mSUGRA models in which $0 < \Omega_\chi < 0.202$. The present neutralino relic energy density parameter in these models only partly explains the experimentally determined $\Omega_{\rm DM}$.
- **Red:** mSUGRA models in which $0.254 < \Omega_\chi < 1$. These models correspond to a spatially flat Universe, but have a present neutralino relic energy density parameter that is larger than the experimentally determined $\Omega_{\rm DM}$.

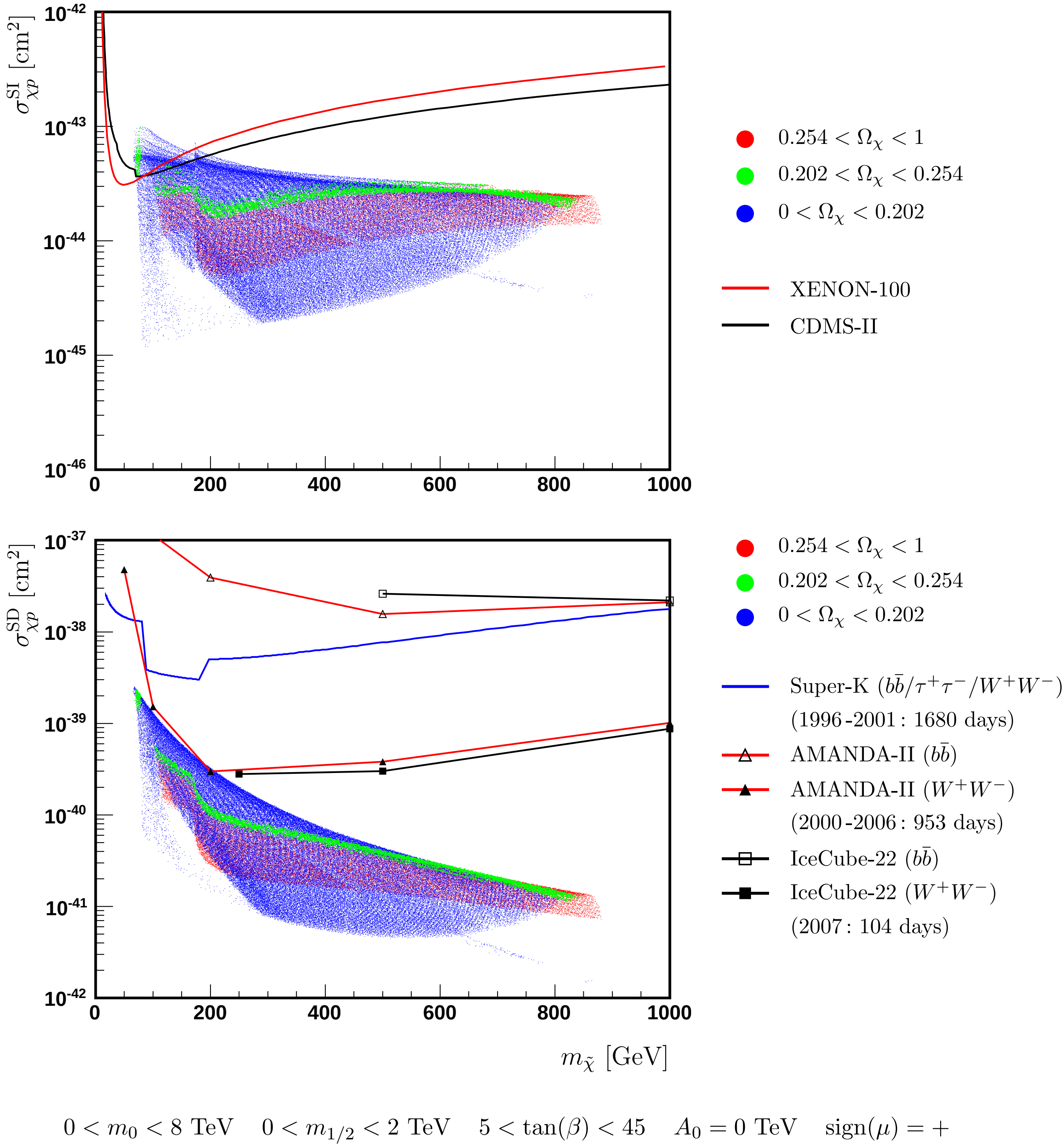

Figure 4.10: The SI and SD neutralino-proton cross sections $\sigma_{\chi p}^{SI}$ and $\sigma_{\chi p}^{SD}$ in mSUGRA as a function of the neutralino mass $m_{\tilde{\chi}}$. Only mSUGRA models in which $\Omega_\chi < 1$ are shown. Also shown are the upper limits at 90 % C.L. from CDMS [28] and XENON [29], and from Super-Kamiokande [58], AMANDA [61] and IceCube [62].

Also shown in figure 4.10 are the upper limits at 90 % C.L. for the SI WIMP-proton cross section from CDMS [28] and XENON [29]. As can be seen, the most recently obtained upper limits on the SI cross section are starting to constrain the mSUGRA parameter space. Projected sensitivities from these and other experiments indicate that a considerable part of the cosmologically interesting mSUGRA parameter space can be explored in the near future.

Figure 1.3 shows that direct detection experiments are currently not yet sufficiently sensitive to constrain mSUGRA parameter space. Their upper limits for the SD WIMP-proton cross section are still about two orders of magnitude above the SD neutralino-proton cross section in mSUGRA as shown in figure 4.10. However, there is an alternative way to set a limit on the WIMP-proton cross section. By using equation (3.8), a neutrino flux limit from an astrophysical object can be converted to a limit on the annihilation rate in that object. Assuming the capture and annihilation rates of WIMPs in the object are in equilibrium (see equation (3.7)) and the scattering is dominated by the SI or SD cross section only, the limit on the annihilation rate can be converted into a limit on the WIMP-nucleon cross section [67]. This procedure was followed by the Super-Kamiokande [58] and AMANDA/IceCube [61, 62] experiments. The resulting upper limits at 90 % C.L. on the SD WIMP-proton cross section are shown in figure 4.10. These limits are stronger than those obtained by direct detection experiments due to the relatively large amount of hydrogen in the Sun. In contrast, their limits on the SI WIMP-proton are less competitive than those obtained by direct detection experiments and are therefore not shown.

4.3.2 Neutralino capture and annihilation rate

The neutralino capture and annihilation rates R_{cap} and R_{ann} in the Sun and the Earth, as defined in equation (3.1), are shown in m_0-$m_{1/2}$ mSUGRA parameter space in fig-

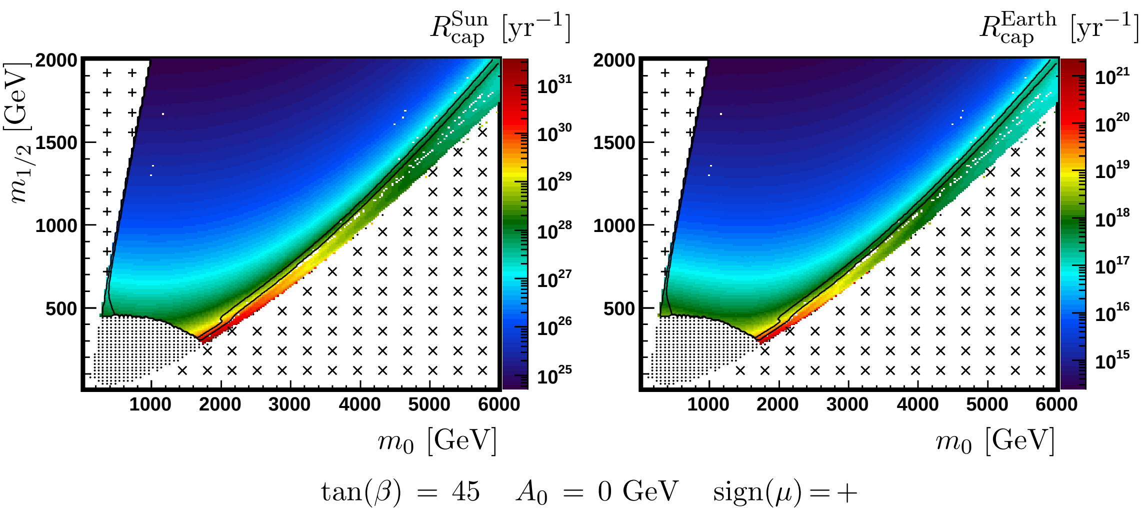

Figure 4.11: The neutralino capture rate R_{cap} in the Sun and the Earth in m_0-$m_{1/2}$ mSUGRA parameter space.

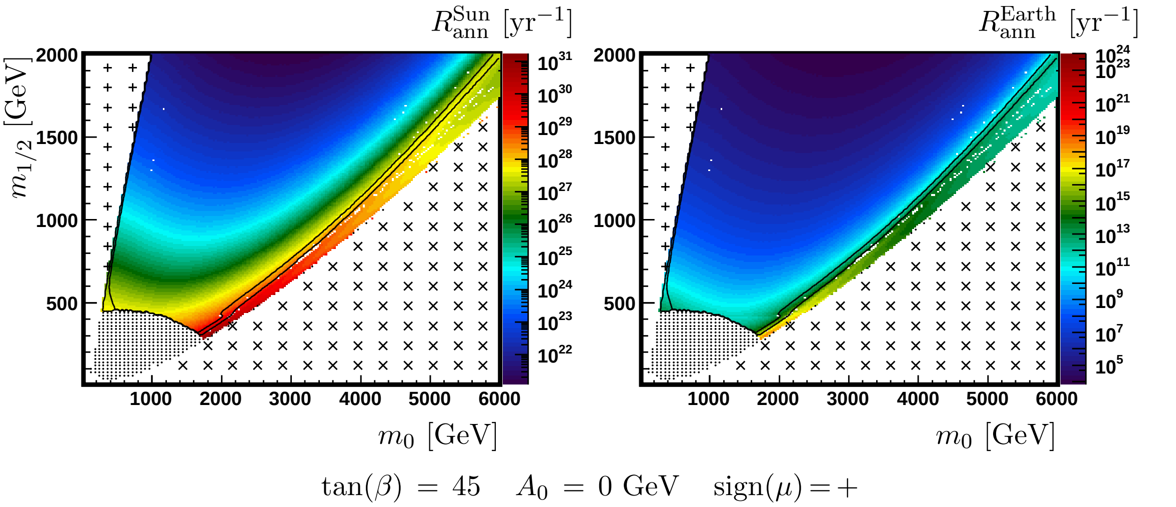

Figure 4.12: The neutralino annihilation rate R_{ann} in the Sun and the Earth in m_0-$m_{1/2}$ mSUGRA parameter space.

ures 4.11 and 4.12, respectively. The corresponding ratio of the equilibrium time scale τ, as defined in equation (3.6), and the age of the solar system ($4.5 \cdot 10^9$ yr) is shown in figure 4.13 for both objects.

As can be seen from figures 4.11 and 4.12, the neutralino capture and annihilation rates in the Sun are significantly higher than in the Earth. This is expected for any generic WIMP, due to the mass and volume of the Sun. As can be seen from figure 4.13, the ratio between the equilibrium time scale τ of the Sun and the age of the solar system is smaller than 1 in the region of mSUGRA parameter space where $\Omega_\chi < 1$. This implies that in the cosmologically interesting region of mSUGRA parameter space, the capture and annihilation rates of neutralinos in the Sun are currently in equilibrium. Therefore

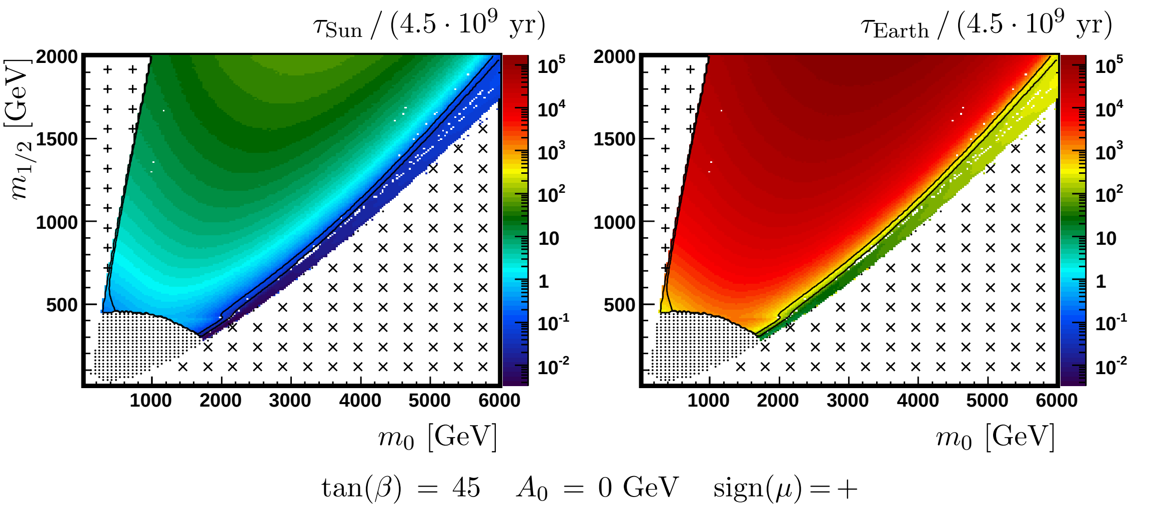

Figure 4.13: The ratio of the equilibrium time scale τ (see equation (3.6)) and the age of the solar system ($4.5 \cdot 10^9$ yr) in m_0-$m_{1/2}$ mSUGRA parameter space.

the neutralino annihilation rate in the Sun depends only on the neutralino-proton scattering cross section. The basis for equilibrium can be inferred from the substantial higgsino fraction of the neutralino in the cosmologically interesting region of mSUGRA parameter space (see figure 4.2). The higgsino fraction enhances the neutralino-proton cross section as well as the annihilation cross section, as shown in figures 4.4 and 4.9. The equilibrium timescale is proportional to the inverse of the square root of both cross sections (see equation (3.6)). The same holds for the Earth. However, the mass and volume of the Earth are not large enough so that the neutralino capture and annihilation rates are currently not in equilibrium.

4.3.3 Neutrino flux from neutralino annihilation

Neutralino annihilation in astrophysical objects can produce high-energy neutrinos in various ways. However, direct production of neutrinos is suppressed by the neutrino mass squared, due to the Majorana nature and non-relativistic velocity of the captured neutralinos as explained in section 4.2. Instead, neutrinos are expected to be produced in the decays of other particles produced in the annihilation of neutralinos. Using equation (3.8), the total flux of neutrinos of type ν_i at a detector from neutralino annihilation in an astrophysical object, for neutrino energies larger than $E_{\nu_i}^{\mathrm{min}}$, is defined as

$$\Phi_{\nu_i}(E_{\nu_i}^{\mathrm{min}}) \equiv \frac{R_{\mathrm{ann}}}{4\pi D^2} \sum_X \left(\frac{\sigma_{\chi\chi\to X}}{\sigma_{\chi\chi}}\right)_X \int_{E_{\nu_i}^{\mathrm{min}}}^{m_{\tilde{\chi}}} \left(\frac{dN_{\nu_i}}{dE_{\nu_i}}\right)_X dE_{\nu_i} \tag{4.2}$$

In this, R_{ann} is the annihilation rate in the object and D is the distance to the object. Equation (4.2) contains a sum over all annihilation channels $\chi\chi \to X$ that can produce high-energy neutrinos, which includes the relative branching ratio and neutrino energy spectrum of each annihilation channel. The six processes that provide the largest contribution to the total annihilation cross section, i.e. neutralino annihilation into $\tau^+\tau^-$, $b\bar{b}$, $t\bar{t}$, W^+W^-, Z^0Z^0, and Z^0h^0, are all capable of producing neutrinos. The relative branching ratios of these channels are shown in figure 4.6. The neutrino energy spectra for each of these channels (except Z^0h^0) are shown in figures 3.3 - 3.7, respectively. All ingredients are now available to calculate the neutrino flux from neutralino annihilation in the Sun and the Earth. For neutrino telescopes the most interesting neutrino type is the (anti-)muon-neutrino, as will be explained in chapter 5.

The total (anti-)muon-neutrino flux above 10 GeV from neutralino annihilation in the Sun, $\Phi_{\nu_\mu+\bar{\nu}_\mu}(E_{\nu_\mu}^{\mathrm{min}} = 10\,\mathrm{GeV})$, is shown in m_0-$m_{1/2}$ mSUGRA parameter space in the left panel of figure 4.14. Contrary to the Sun, neutrino emission from the centre of the Earth cannot be considered point-like as explained in section 3.2. Hence, the neutrino flux has to be integrated in a cone in the direction of the centre of the Earth. The half-aperture of the cone corresponding to this solid angle is typically of the order of a degree (see figure 3.10). As an example, the total neutrino flux above 10 GeV from neutralino annihilation in the Earth, integrated in a cone with a half-aperture of 3° in the direction of the centre of the Earth, is shown in m_0-$m_{1/2}$ mSUGRA parameter space in the right panel of figure 4.14.

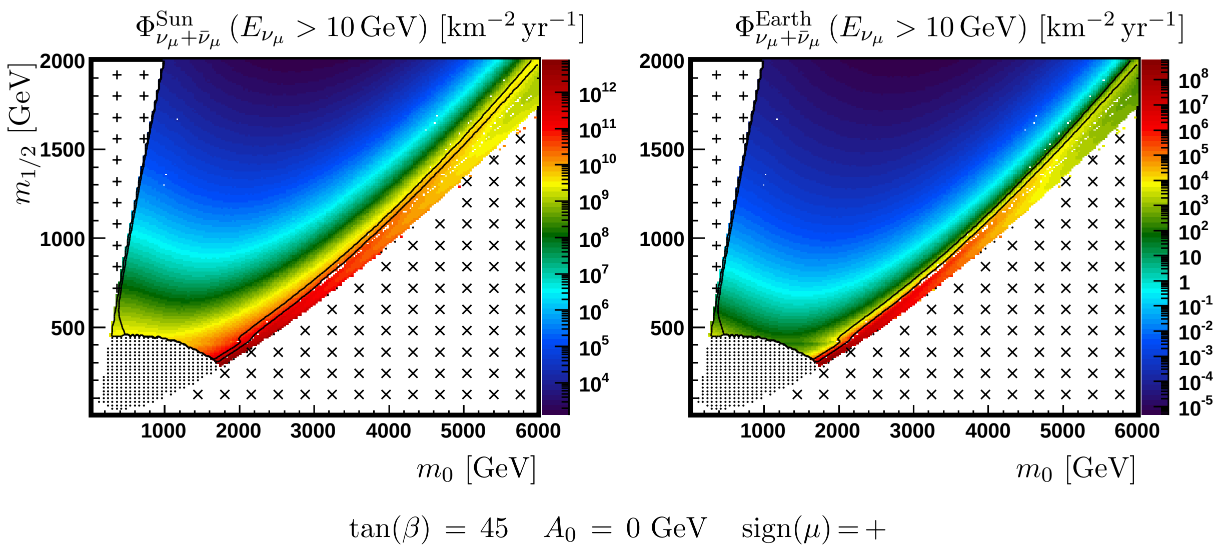

Figure 4.14: $\Phi_{\nu_\mu+\bar{\nu}_\mu}(E_{\nu_\mu} > 10\,\mathrm{GeV})$ from the Sun and the Earth in m_0-$m_{1/2}$ mSUGRA parameter space. In the case of the Earth, the flux is integrated in a cone with a half-aperture of 3° in the direction of the centre of the Earth.

The neutrino flux from both objects agrees with the annihilation rate (see figure 4.12) taking into account the average distance between the Sun and the Earth (~$1.5 \cdot 10^8$ km) and the radius of the Earth (~$6.4 \cdot 10^3$ km). Although the distance to the Sun is five orders of magnitude larger than to the centre of the Earth, the neutrino flux from the Sun is higher than from the Earth since the annihilation rate in the Sun is some thirteen orders of magnitude higher.

The total (anti-)muon-neutrino flux above 10 GeV from neutralino annihilation in Sun and the Earth is shown as a function of the neutralino mass $m_{\tilde{\chi}}$ in figure 4.15, for a larger scan of mSUGRA parameters ($5 < \tan(\beta) < 50$). In the case of the Earth, the flux is integrated in a cone with a half-aperture of 3° in the direction of the centre of the Earth. Only mSUGRA models in which the present neutralino relic density $\Omega_\chi < 1$ are shown. The colour coding is given in the legends. The neutrino flux from the Sun is correlated with the SD neutralino-proton cross section (see bottom panel in figure 4.10), since the Sun consists mostly of hydrogen. The neutrino flux is inversly proportional to the neutralino mass. This is due to the equilibrium between capture and annihilation of neutralinos in the Sun for mSUGRA models with $\Omega_\chi < 1$. Therefore, the annihilation rate is proportional to the capture rate, which is inversely proportional to the neutralino mass (see equation (3.2)). The neutrino flux for the Earth is correlated with the SI neutralino-proton cross section (see top panel in figure 4.10), since the composition of the Earth is dominated by nuclei with zero angular momentum. The decrease of the neutrino flux as a function of the neutralino mass is larger for the Earth than for the Sun, because capture and annihilation of neutralinos in the Earth are not in equilibrium for all mSUGRA models considered here. Therefore, the annihilation rate is proportional to the capture rate squared for the Earth (see equation (3.7)). The annihilation rate in the Earth is also inversely proportional to the effective volume of

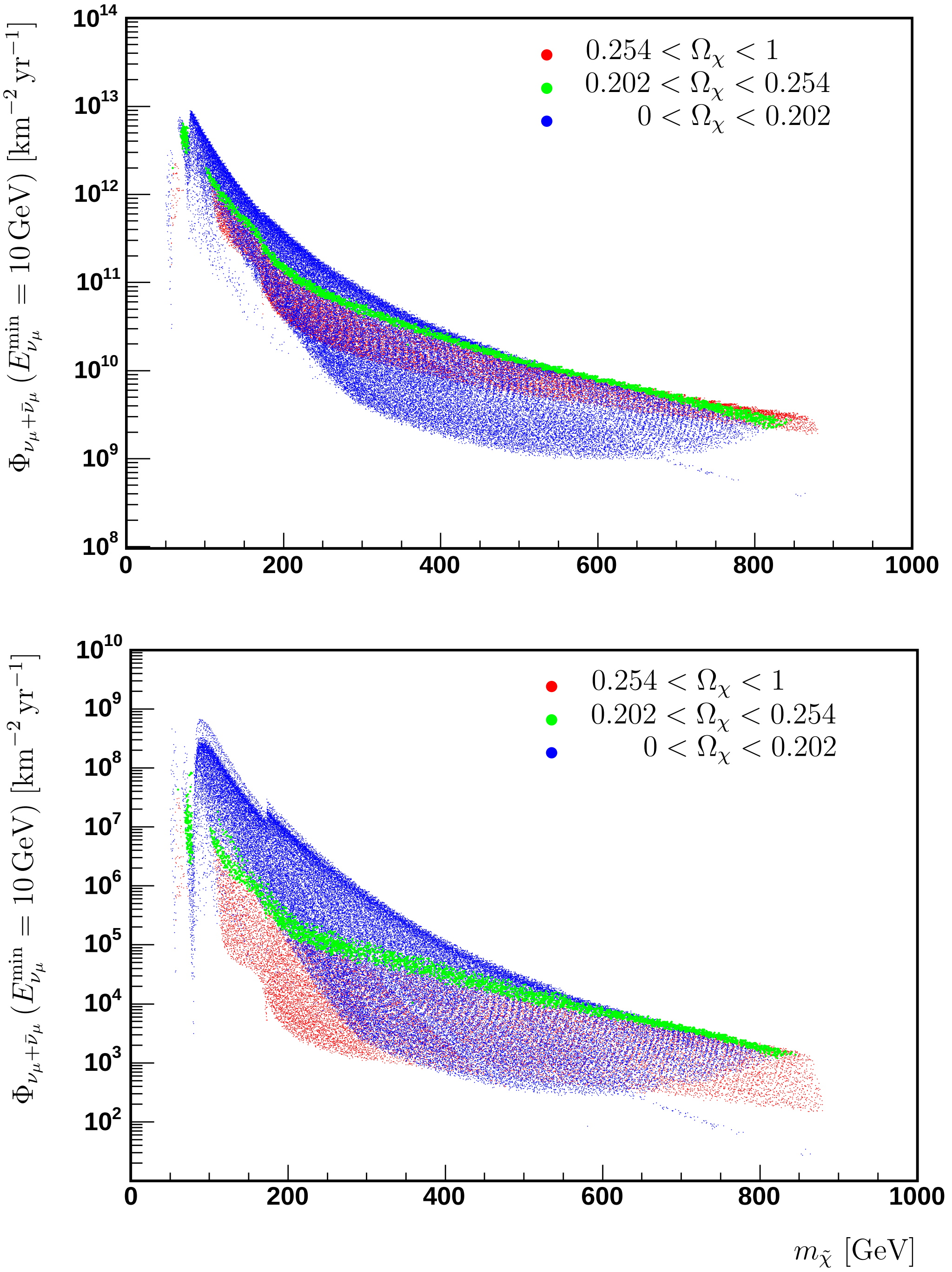

$m_0 < 8$ TeV $\quad m_{1/2} < 2$ TeV $\quad 5 < \tan(\beta) < 45 \quad A_0 = 0$ TeV $\quad \mathrm{sign}(\mu) = +$

Figure 4.15: $\Phi_{\nu_\mu+\bar{\nu}_\mu}\,(E^{\rm min}_{\nu_\mu} = 10\,{\rm GeV})$ from the Sun (top) and the Earth (bottom), versus the neutralino mass $m_{\tilde{\chi}}$. In the case of the Earth, the flux is integrated in a cone with a half-aperture of 3° in the direction of the centre of the Earth.

the Earth, which causes a further suppression for neutralinos of higher mass. Figure 4.15 also shows a discontinuity in the neutrino flux when the neutralino mass is equal to the top quark mass (~173 GeV). This is due to the harder (softer) energy spectra of the top quark channel with respect to the bottom quark (weak vector boson) channel.

4.3.4 Neutrino-induced muon flux from neutralino annihilation

Neutrino detection with a neutrino telescope is based on the interaction of a high energy muon-neutrino ($E_{\nu_\mu} \gtrsim 10$ GeV) with a nucleus in the detector. A charged current interaction will produce a relativistic muon, which can propagate a relatively long distance through the detector before it loses all its energy. During its propagation, the muon emits Cherenkov light which can be detected and used to reconstruct the muon direction and energy. The neutrino detection principle is described in more detail in sections 5.1, 7.1. In the following, the neutrino-induced muon flux from neutralino annihilation in the Sun and the Earth is presented. The derivation of the muon flux induced by a neutrino flux can be found in 7.8.3.

The total muon flux at a detector induced by muon-neutrinos from neutralino annihilation in an astrophysical object, for muon energies larger than E_μ^{min}, can be written as

$$\Phi_\mu(E_\mu^{\mathrm{min}}) \equiv \int_{E_\mu^{\mathrm{min}}}^{m_{\tilde{\chi}}} \frac{d\Phi_\mu}{dE_{\nu_\mu}}\, dE_{\nu_\mu} \tag{4.3}$$

where the differential muon flux is given by equation (7.28). For comparison amongst different experiments, it is customary to take $E_\mu^{\mathrm{min}} = 1$ GeV. The mean scattering angle between the muon and neutrino directions can be parameterised as $\theta_{\nu\mu} \simeq 0.7^\circ/E_{\nu_\mu}^{0.6}$ if E_{ν_μ} is given in units of TeV [68]. Therefore, the muon flux should be integrated over a spherical solid angle corresponding to a cone with a half-aperture of the order of one degree, centered on the object.

The total (anti-)muon flux above 1 GeV induced by (anti-)muon-neutrinos from neutralino annihilation in the Sun and the Earth, $\Phi_{\mu^++\mu^-}\,(E_\mu^{\mathrm{min}} = 1\,\mathrm{GeV})$, is shown in m_0-$m_{1/2}$ mSUGRA parameter space in figure 4.16. In both cases the muon flux is integrated in a cone with a half-aperture of 3° in the direction of the object. As can be seen from this figure, the muon flux above 1 GeV in a 3° cone can reach up to several thousand muons per km^2 per year for the Sun, for cosmologically interesting mSUGRA models. For the same mSUGRA models, the muon flux from neutralino annihilation in the Earth is smaller than one muon per km^2 per year.

The total (anti-)muon flux above 1 GeV induced by (anti-)muon-neutrinos from neutralino annihilation in the Sun and the Earth is shown as a function of the neutralino mass $m_{\tilde{\chi}}$ in figure 4.17, for a larger scan of mSUGRA parameters ($5 < \tan(\beta) < 50$). Only mSUGRA models in which the present neutralino relic density $\Omega_\chi < 1$ are shown. The colour coding is given in the legends. Also shown are upper limits at 90 % C.L. on $\Phi_{\mu^++\mu^-}\,(E_\mu^{\mathrm{min}} = 1\,\mathrm{GeV})$ from experiments that use scintillation techniques (Baksan [56] and MACRO [57]) and water-Cherenkov techniques (Super-Kamiokande [58], Baikal [59] and AMANDA / IceCube [60, 61, 62]). For the neutrino telescopes, the upper limits were derived assuming the annihilation is dominated by a specific channel,

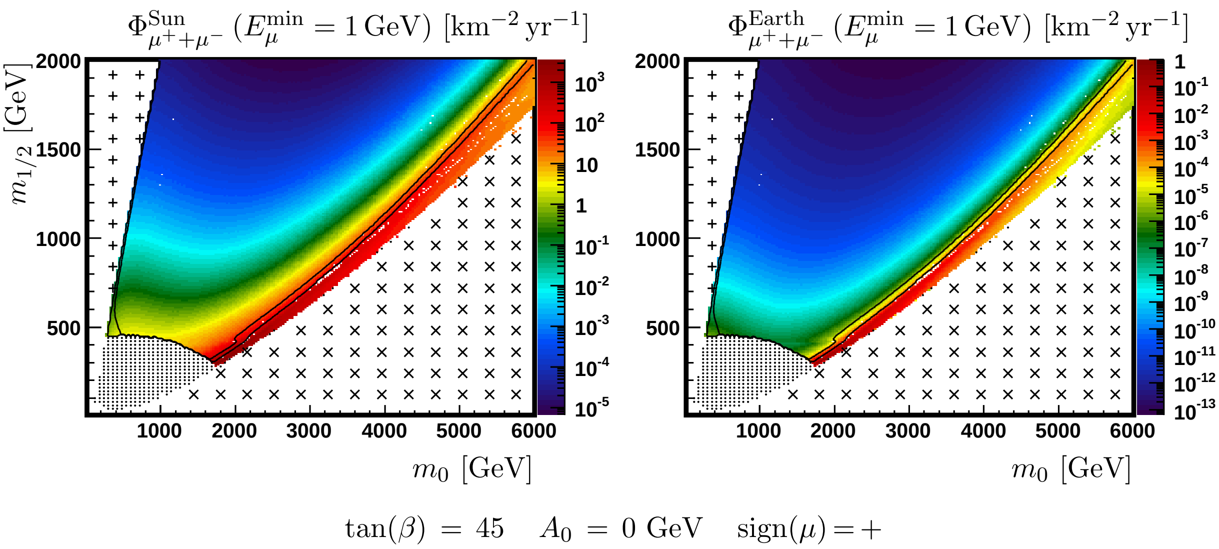

Figure 4.16: $\Phi_{\mu^++\mu^-}\,(E_\mu^{\rm min} = 1\,{\rm GeV})$ from the Sun and the Earth in m_0-$m_{1/2}$ mSUGRA parameter space. In both cases, the muon flux is integrated in a cone with a half-aperture of 3° in the direction of the object.

as indicated in the legend. In the case of Super-Kamiokande, neutralino annihilation into $b\bar{b}$ (80 %), $c\bar{c}$ (10 %) and $\tau^+\tau^-$ (10 %) is assumed. Also indicated are the period of data-taking and total effective livetime that were used to derive each limit. In the case of the Sun, the effective livetime for the AMANDA and IceCube experiments includes only days when the Sun was below the horizon.

As can be seen, the predicted muon flux from the Earth in mSUGRA lies four orders of magnitude below the currently best experimental limit, which is the 3-year AMANDA limit. Although this limit was derived when the AMANDA detector was still under construction, even a km^3-scale detector will not be sufficiently sensitive to reach the fluxes predicted by mSUGRA. For the Sun however, this is not the case. The most recently obtained upper limits by experiments that are currently taking data (Super-Kamiokande, IceCube) indicate that these experiments are reaching the sensitivity needed to detect neutrinos from neutralino annihilation as predicted by mSUGRA.

4.4 Neutrinos from neutralino annihilation in the dark matter halo

In the previous section, the neutrino flux from the Sun and the Earth in mSUGRA was discussed. Another potentially interesting source for neutralino annihilation is the Galactic Centre. In this section, the total (anti-)muon-neutrino flux from neutralino annihilation in the dark matter halo in the direction of the Galactic Centre, as defined in equation (4.2), is presented. The corresponding total (anti-)muon flux as defined in equation (4.3) is also shown. For the dark matter halo, the NFW profile with $\rho_0 = 0.3$ GeV/cm^3 as shown in figure 3.11 is assumed. For the distance between the Earth and the Galactic Centre, $D = 8.5$ kpc is assumed.

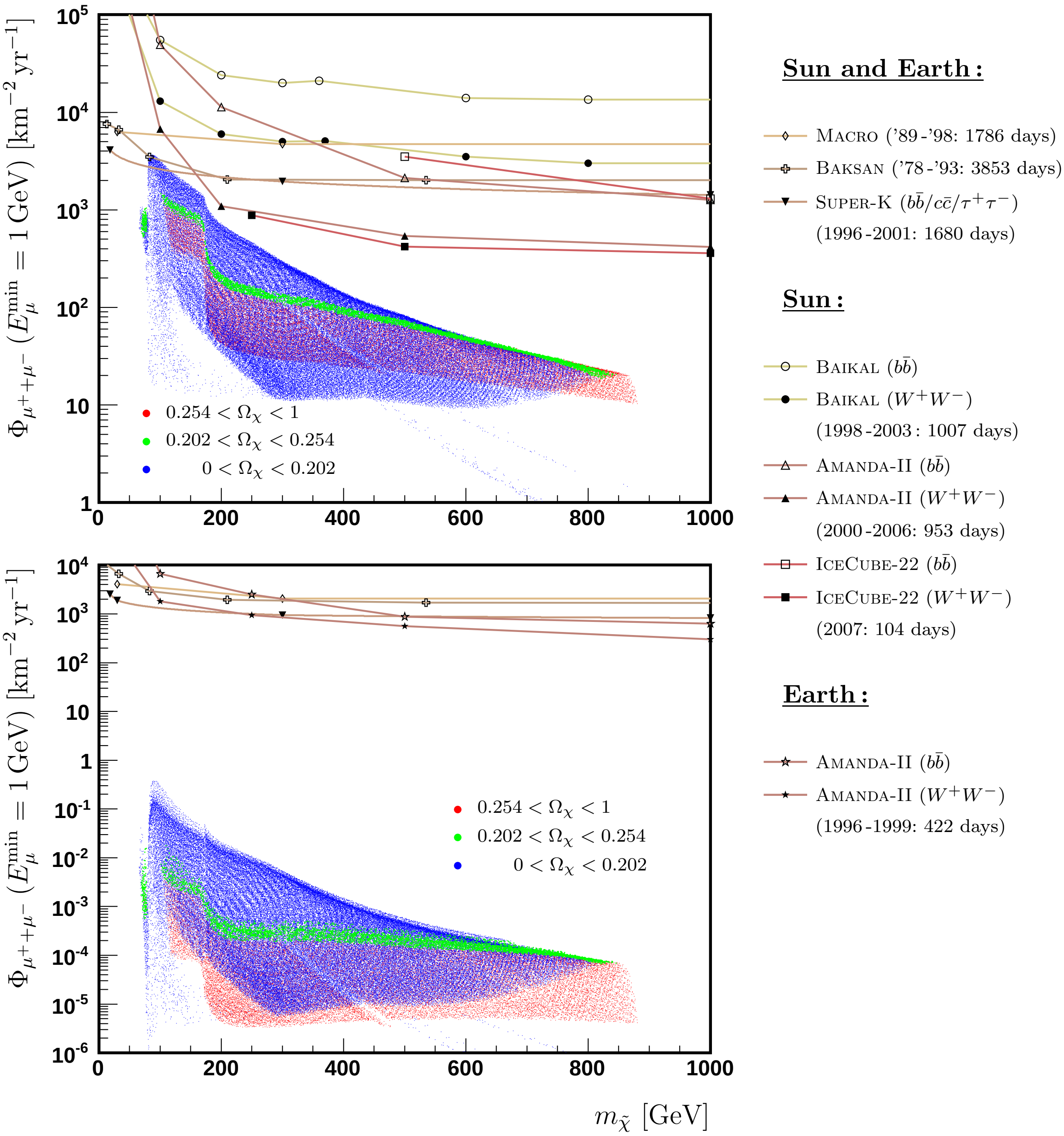

$0 < m_0 < 8$ TeV $\quad 0 < m_{1/2} < 2$ TeV $\quad 5 < \tan(\beta) < 45 \quad A_0 = 0$ TeV $\quad \mathrm{sign}(\mu) = +$

Figure 4.17: $\Phi_{\mu^++\mu^-}$ ($E_\mu^{\min} = 1\,\mathrm{GeV}$) from the Sun (top) and the Earth (bottom), versus the neutralino mass $m_{\tilde{\chi}}$. In both cases, the muon flux is integrated in a cone with a half-aperture of 3° in the direction of the object. Only mSUGRA models in which $\Omega_\chi < 1$ are shown. Also shown are the upper limits at 90 % C.L. from Baksan [56], MACRO [57], Super-Kamiokande [58], Baikal [59], AMANDA [60, 61] and IceCube [62].

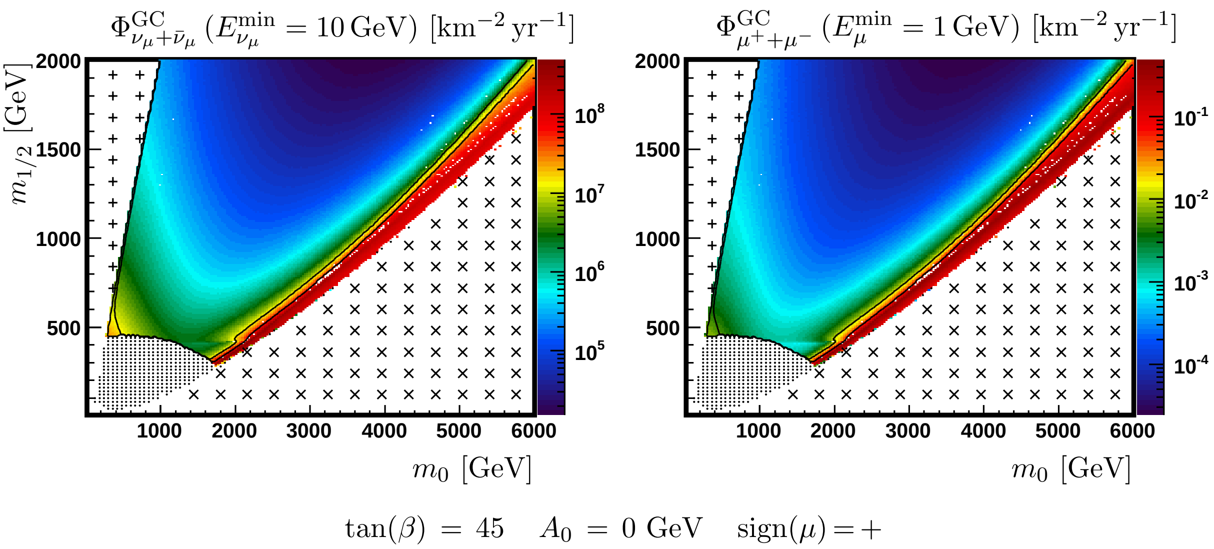

Figure 4.18: $\Phi_{\nu_\mu+\bar{\nu}_\mu}\,(E^{\rm min}_{\nu_\mu} = 10\,{\rm GeV})$ and $\Phi_{\mu^+ + \mu^-}\,(E^{\rm min}_{\mu} = 1\,{\rm GeV})$ from neutralino annihilation in the dark matter halo in m_0-$m_{1/2}$ mSUGRA parameter space. The fluxes are integrated in a cone with a half-aperture of 3° in the direction of the Galactic Centre.

The total (anti-)muon-neutrino flux above 10 GeV from neutralino annihilation in the dark matter halo, $\Phi_{\nu_\mu+\bar{\nu}_\mu}\,(E^{\rm min}_{\nu_\mu} = 10\,{\rm GeV})$, is shown m_0-$m_{1/2}$ mSUGRA parameter space in the left panel of figure 4.18. The flux is integrated in a cone with a half-aperture of 3° in the direction of the Galactic Centre. As can be seen, the neutrino flux is correlated with the total annihilation cross section (see figure 4.4), as expected from equation (3.16). The corresponding total (anti-)muon flux above 1 GeV, $\Phi_{\mu^+ + \mu^-}\,(E^{\rm min}_{\mu} = 1\,{\rm GeV})$, integrated in a cone with a half-aperture of 3° in the direction of the Galactic Centre, is shown in m_0-$m_{1/2}$ mSUGRA parameter space in the right panel of figure 4.18. As can be seen, the total muon flux above 1 GeV in a 3° cone is smaller than one muon per km^2 per year for cosmologically interesting mSUGRA models.

Both fluxes are shown as a function of the neutralino mass $m_{\tilde{\chi}}$ in figure 4.19 for a larger scan of mSUGRA parameters ($5 < \tan(\beta) < 50$). Only mSUGRA models in which the present neutralino relic density $\Omega_\chi < 1$ are shown. The colour coding is given in the legends. Also shown is the upper limit at 90 % C.L. from the Super-Kamiokande experiment [58]. As can be seen from the top panel, the neutrino flux does not decrease as steeply with the neutralino mass as it does for the Sun or the Earth (see figure 4.15). This is due to the absence of a neutralino capture process. From the bottom panel it can be concluded that neutrino telescopes are currently not sufficiently sensitive to detect neutrinos from neutralino annihilation in the dark matter halo as predicted by mSUGRA.

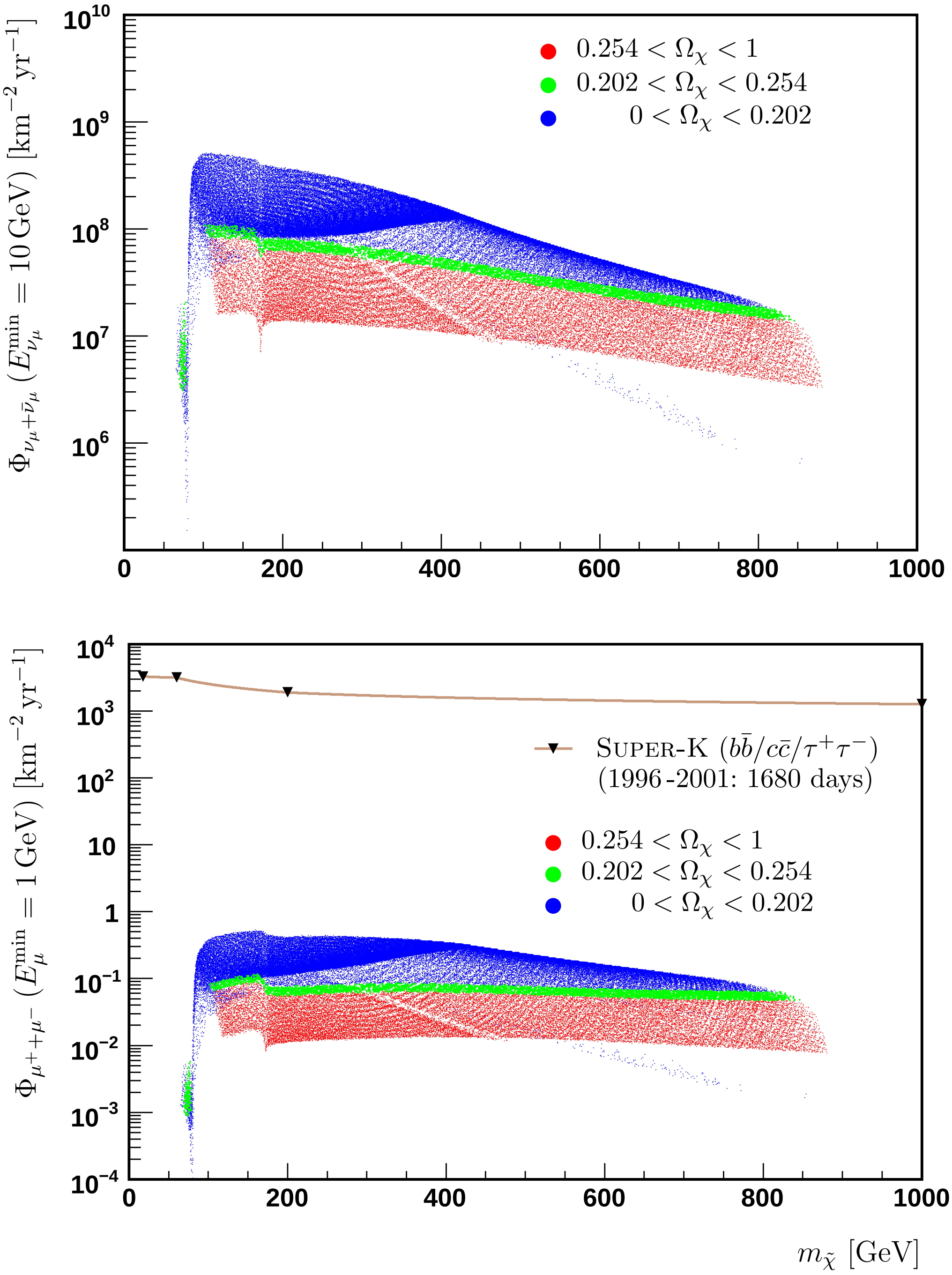

$m_0 < 8$ TeV $\quad m_{1/2} < 2$ TeV $\quad 5 < \tan(\beta) < 45 \quad A_0 = 0$ TeV $\quad \mathrm{sign}(\mu) = +$

Figure 4.19: $\Phi_{\nu_\mu+\bar{\nu}_\mu}\,(E_{\nu_\mu}^{\min} = 10\,\mathrm{GeV})$ (top) and $\Phi_{\mu^++\mu^-}\,(E_\mu^{\min} = 1\,\mathrm{GeV})$ (bottom) from neutralino annihilation in the dark matter halo, integrated over a spherical solid angle corresponding to a cone with a half-aperture of 3° in the direction of the Galactic Centre, versus the neutralino mass $m_{\tilde{\chi}}$. Only mSUGRA models in which $\Omega_\chi < 1$ are shown. Also shown are the upper limits at 90 % C.L. from Super-Kamiokande [58].

Chapter 5

The ANTARES neutrino telescope

In this chapter, the water-Cherenkov neutrino detection principle is discussed. This is followed by an overview of ANTARES, the world's first deep-sea neutrino telescope.

5.1 Neutrino detection

The water-Cherenkov neutrino detection principle as employed by neutrino telescopes is described in the following.

5.1.1 Neutrino signatures in a detector

The signatures of charged current (CC) and neutral current (NC) interactions between a neutrino and an atomic nucleus in a detector (see section 3.2.2) are shown in figure 5.1. For $E_\nu > 10$ GeV, the nucleus will disintegrate in the interaction and produce a hadronic shower (HS). The length of a hadronic shower in water is of the order of a few meters, since the nuclear interaction length in water is less than 1 m. In the case of an NC interaction, this is the only signal produced, as the outgoing neutrino will escape the detector medium without interacting a second time. In the case of a CC interaction, the signature depends on the flavour of the outgoing lepton which is determined by the flavour of the neutrino. In the case of an electron-neutrino, the outgoing electron will quickly lose its energy in the medium through the process of bremsstrahlung and pair production, resulting in an electromagnetic shower (ES). Since the radiation length in water is less than 1 m, the length of an electromagnetic shower in water is of the order of a few meters. In the case of a muon-neutrino, the outgoing muon has a much larger mass than an electron, which decreases the cross section for bremsstrahlung and pair production and therefore its energy loss. It also has a considerable lifetime of $2 \cdot 10^{-6}$ s. This enables a muon to travel a large distance before it has lost all its energy or it can decay. Finally, the tau-neutrino produces a tau which has an even larger mass than the muon, but it also has a much shorter lifetime of $3 \cdot 10^{-13}$ s. Hence it travels less far than a muon before it decays. The overall signature of a tau-neutrino depends on the decay of tau. Hadronic decay ($\sim 65\,\%$) results in a hadronic shower, $\tau^- \rightarrow \nu_\tau\, \bar{\nu}_e\, e^-$ ($\sim 18\,\%$) will produce an electromagnetic shower, and $\tau^- \rightarrow \nu_\tau\, \bar{\nu}_\mu\, \mu^-$ ($\sim 17\,\%$) produces

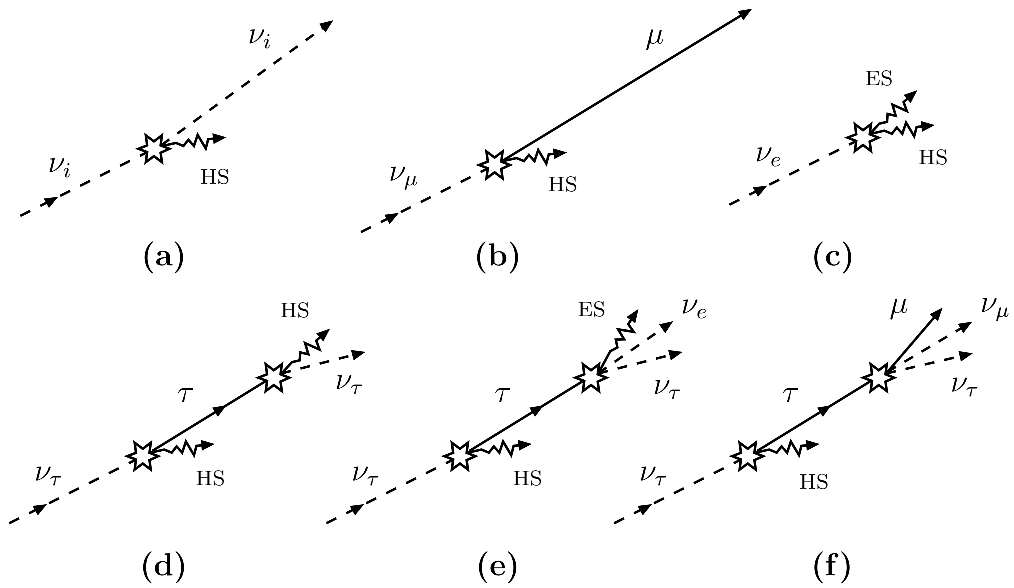

Figure 5.1: Neutrino interaction signatures: ν_i-nucleon NC interaction (a), ν_μ-nucleon CC interaction (b), ν_e-nucleon CC interaction (c), ν_τ-nucleon CC interaction followed by hadronic tau decay (d), by $\tau^- \to \nu_\tau\, \bar{\nu}_e\, e^-$ (e), and by $\tau^- \to \nu_\tau\, \bar{\nu}_\mu\, \mu^-$ (f).

a muon.

5.1.2 Neutrino-induced muons

In the case of a ν_μ-nucleon CC interaction, the mean scattering angle between the neutrino and the muon is determined to be small and can be parametrised by $\langle\theta_{\nu\mu}\rangle \simeq 0.7°/E_\nu^{0.6}$ with E_ν given in TeV [68], as shown in the left panel of figure 5.2. For energies of a TeV or higher, the mean scattering angle is one degree or less. The direction of the muon therefore gives a good indication of the direction of the incident neutrino.

Muons can travel a considerable distance before they lose all their kinetic energy and eventually decay. The mean distance a muon of a certain energy can travel is called the effective muon range, and depends on the muon energy loss due to interactions with atoms in the medium [70]. Below approximately 0.5 TeV, the traversing muon loses most of its energy through excitation and ionisation of the medium, resulting in a continuous energy loss of about 0.2 – 0.3 GeV/m independent of the muon energy. Above approximately 0.5 TeV, the energy loss is dominated by stochastic processes (i.e. bremsstrahlung, pair production and photo-nuclear processes) which generate electromagnetic and hadronic showers along the muon track. The energy loss due to these processes is approximately proportional to the energy of the muon. The resulting effective muon range is shown in the right panel of figure 5.2 for water ($A = 18$, $Z = 10$, $\rho = 1.03$ g/cm^3) and 'standard rock' ($A = 22$, $Z = 11$, $\rho = 2.65$ g/cm^3). The angular deviation of the muon with respect to its original direction caused by the above-mentioned

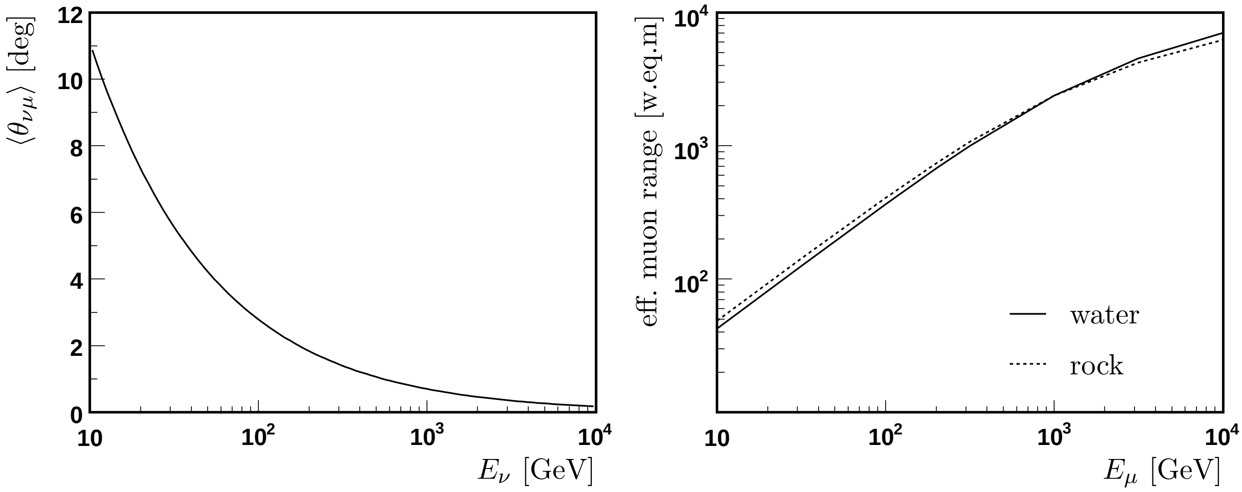

Figure 5.2: Left panel: The mean ν_μ-μ scattering angle $\langle\theta_{\nu\mu}\rangle$ after a ν_μ-nucleon CC interaction as a function of the neutrino energy E_ν.
Right panel: The effective muon range in water equivalent units in water (solid) and rock (dashed), as a function of the muon energy E_μ [69].

energy loss processes is less than one degree for $E_\mu > 10$ GeV [70].

5.1.3 The Cherenkov effect

If the charged particle such as a muon traverses a medium, there is another process besides excitation/ionisation through which it interacts continuously with the surrounding medium. The electromagnetic field of the traversing charged particle polarises the atoms of the medium. After the particle has passed, the atoms are restored to equilibrium by emitting electromagnetic radiation. If the particle was traveling with a velocity that exceeds the speed of light in the medium, coherence of the emitted radiation occurs at a characteristic emission angle θ_C, resulting in a light cone directed along the particle trajectory. This process is called the Cherenkov effect and is illustrated in figure 5.3. The Cherenkov angle θ_C can be expressed as [11]

$$\cos(\theta_\mathrm{C}) = \frac{1}{\beta n} \qquad \left(\beta > \frac{1}{n}\right) \tag{5.1}$$

where β is the particle velocity expressed as a fraction of the speed of light, and n is the refractive index of the medium. In particular, for relativistic particles in water ($n \approx 1.34$), the Cherenkov angle $\theta_\mathrm{C} \approx 42°$.

The muon energy loss due to the Cherenkov effect is three orders of magnitude smaller than for ionisation. The number of Cherenkov photons N emitted by a particle with unit charge per unit distance x and unit wavelength λ is [11]

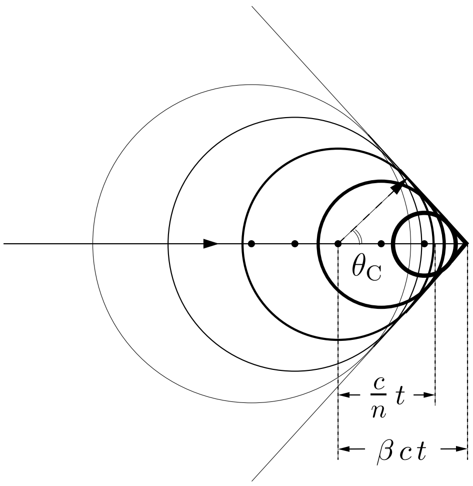

Figure 5.3:

Cherenkov emission by a relativistic charged particle traveling with a velocity $v > c/n$ through a medium with refractive index n.

$$\frac{d^2 N}{dx\, d\lambda} = \frac{2\pi\alpha}{\lambda^2}\left(1 - \frac{1}{\beta^2 n^2}\right) \tag{5.2}$$

where α is the fine-structure constant. Hence a relativistic muon in water emits about $3.5 \cdot 10^4$ Cherenkov photons per meter in the visible and UV wavelength regime (300 – 600 nm).

5.1.4 Light propagation

The group velocity of Cherenkov light in a medium v_g depends not only on the photon wavelength and the refractive index of the medium, but also on the wavelength dependence of the refractive index [71] :

$$v_{\mathrm{g}} = \frac{c}{n}\left(1 + \frac{\lambda}{n}\frac{dn}{d\lambda}\right) \equiv \frac{c}{n_{\mathrm{g}}} \tag{5.3}$$

where n_{g} is the group refractive index of the medium and c is the speed of light. In particular, for photons with a wavelength of 460 nm in sea water, the group refractive index is approximately 1.38.

Propagation of light through a medium is affected by absorption and scattering. The former effect reduces the intensity of the Cherenkov light while the latter effect influences the direction of the Cherenkov photons as a function of the propagation distance. Both phenomena depend on the photon wavelength. Photon absorption is characterised by the absorption length λ_{abs} of the medium, defined as the average distance through which a fraction of e^{-1} of the photons survives. Photon scattering in a medium is characterised by the scattering length λ_{scat} of the medium defined as the average distance through which a fraction of e^{-1} of the photons do not scatter, and by the scattering angle θ_{scat} of the photon single scattering process. These two quantities can be combined into a parameter with similar characteristics to λ_{abs}. This parameter is the effective scattering length, defined as $\lambda_{\mathrm{scat}}^{\mathrm{eff}} = \lambda_{\mathrm{scat}}/(1 - \langle\cos(\theta_{\mathrm{scat}})\rangle)$,

	Sea water (Mediterranean Sea) $\lambda = 473$ (375) nm	Water (Lake Baikal) $\lambda = 480$ nm	Ice (South Pole) $\lambda = 400$ nm
absorption length	60 ± 10 (26 ± 3) m	20 – 24 m	110 m
eff. scattering length	270 ± 30 (120 ± 10) m	200 – 400 m	20 m

Table 5.1: Light propagation parameters for (sea-)water and ice [72, 73].

where $\langle\cos(\theta_{\text{scat}})\rangle$ is the average cosine of the scattering angle. The light propagation parameters for (sea-)water and ice are summarised in table 5.1.

5.1.5 The neutrino telescope concept

As first suggested by the Russian physicist Moisei Aleksandrovich Markov in 1960 [74], a neutrino telescope consists of a three-dimensional array of photomultiplier tubes (PMTs) in a dark and transparent detector medium. The Cherenkov effect is used as a means to detect charged particles that are produced by neutrinos in the detector. The small neutrino interaction cross section requires the detector volume to be as large as possible. This condition, combined with the optical properties and the abundance of water on Earth, makes a volume of deep under water/ice (where sunlight cannot penetrate) the natural detector medium for a neutrino telescope.

Neutrino telescopes can be used to study the Universe using cosmic neutrinos. However, particles which can mimic the interaction signature but do not originate from a cosmic neutrino have to be taken into account. The different sources of these background particles are shown schematically in the left panel of figure 5.4. The two main backgrounds find their origin in high energy cosmic rays. The Earth experiences a constant isotropic flux of cosmic rays that consists of high-energy protons and atomic nuclei. These cosmic rays interact in the top of the atmosphere, thereby creating a cascade of secondary particles which can decay into muons or neutrinos. Muons produced in the cascade are referred to as *atmospheric muons*. They have sufficient energy to traverse the atmosphere and kilometers of water (see right panel in figure 5.2), and so are able to reach a deep water/ice neutrino detector despite its depth. The intensity of these muons is reduced through the energy loss process and so becomes strongly dependent on the amount of matter traversed. This leads to an angular distribution which is concentrated in the downward direction, as shown in the right panel of figure 5.4. Neutrinos produced in the cascade are referred to as *atmospheric neutrinos*. They are capable of traversing the entire Earth, making them individually indistinguishable from cosmic neutrinos. The flux of muons induced by atmospheric neutrinos is also shown in the right panel of figure 5.4. The atmospheric neutrino flux enhancement for horizontal directions is due to the increased path length in the upper atmosphere, which reduces the energy loss of particles in the cascade before they can decay into neutrinos.

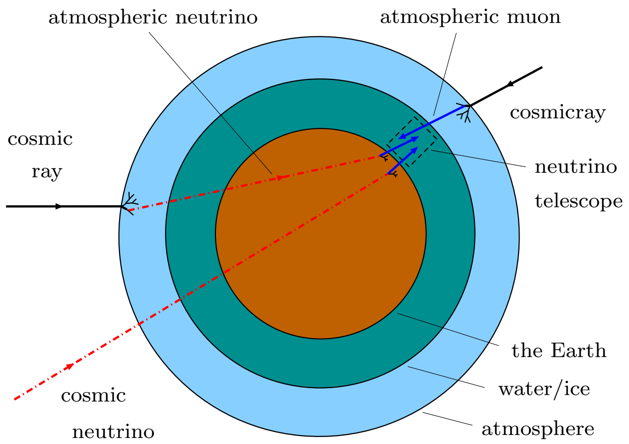

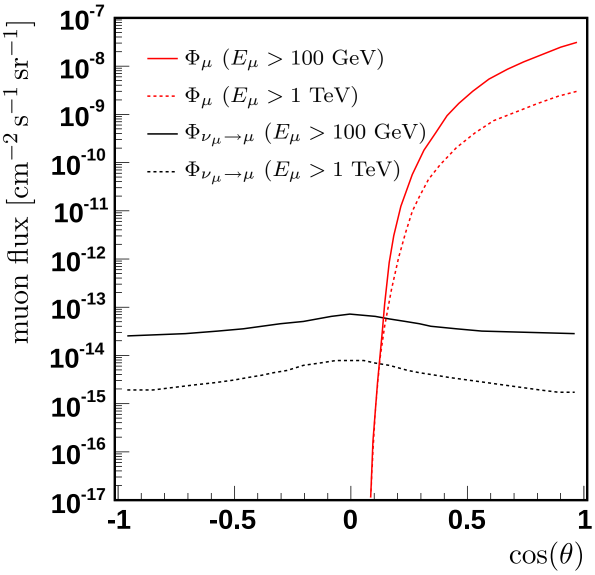

Figure 5.4: Left panel: Atmospheric muons and neutrinos. Right panel: the atmospheric muon flux and the muon flux induced by atmospheric neutrinos at a depth of 2.1 km.w.e., as a function of the cosine of the zenith angle of the muon [75].

5.1.6 Neutrino telescopes

After pioneering work by the DUMAND collaboration [76] between 1976 and 1995, the neutrino telescope concept has been realised by a number of experimental groups worldwide:

▷ Baikal

The Baikal Neutrino Telescope NT-200 [77] is located under water at a depth of 1.1 – 1.2 km in the southern part of Lake Baikal, Russia. The NT-200 comprises 192 optical modules arranged in pairs on 8 vertical strings that are placed in a heptagonal configuration. With a horizontal spacing between strings of about 20 m and a vertical spacing between optical module pairs that alternates between 5 and 7.5 m, the instrumented volume is about 10^5 m^3. Each optical module contains a 37 cm diameter PMT. The NT-200 has been fully operational since 1998, and was upgraded in 2005 by the addition of 3 strings, each 100 m away from the center of the main cluster of strings.

▷ AMANDA

The Antarctic Muon And Neutrino Detector Array (AMANDA) [78] is located in the ice sheet at a depth of about 1.5 – 2.0 km at the Geographic South Pole in Antarctica. The AMANDA-II detector consists of 677 optical modules arranged in 19 vertical strings layed out in concentric circles. The instrumented string length varies between 350 m and 1.1 km, resulting in an instrumented volume of approximately $1.5 \cdot 10^7$ m^3. Each

	Baikal NT-200	AMANDA-II	ANTARES	IceCube (DeepCore)
Location	$51°50'$ N $104°20'$ E	$90°$ S $0°$ W	$42°48'$ N $6°10'$ E	$90°$ S $0°$ W
Depth	1.1 – 1.2 km	1.5 – 2.0 km	2.0 – 2.5 km	1.5 (2.1) – 2.5 km
Height	72 m	$\sim$ 500 m	350 m	1000 m
Diameter	42 m	$\sim$ 200 m	$\sim$ 200 m	1000 m
Instrumented volume	10^5 m^3	$\sim 1.5 \cdot 10^7$ m^3	$\sim 1.1 \cdot 10^7$ m^3	$1.3 \cdot 10^9$ m^3
Number of PMTs	192	677	885	4800 (360)
PMT diameter	37 cm	20 cm	25 cm	25 cm
PMT grouping	pair	single	triplet	single
Number of strings	8	19	12	80 (6)
Vertical spacing	$\sim$ 6 m	$\sim$ 15 m	14.5 m	17 (7) m
Horizontal spacing	$\sim$ 20 m	$\sim$ 40 m	$\sim$ 60 m	125 ($\sim$ 60) m
Operational period	1998 – present	2000 – 2009	2008 – present	2011 – present

Table 5.2: Main detector parameters of existing neutrino telescopes.

optical module contains a 20 cm diameter PMT. AMANDA-II operated as an independent instrument from 2000 until 2006, and in conjunction with the partially completed IceCube detector (see below) in 2007 and 2008. AMANDA-II was decommissioned in April 2009.

▷ IceCube

As the successor of AMANDA, IceCube [79] is situated at the same location but at a greater depth of about 1.5 – 2.5 km. The IceCube detector comprises 4800 optical modules arranged on 80 vertical strings in a hexagonal configuration, and was completed in December 2010. With a 125 m horizontal spacing between strings and a 17 m vertical spacing between optical modules, the instrumented volume is 1.3 km^3. Each optical module contains a 25 cm diameter PMT. To lower the energy threshold of IceCube, the bottom-centre of the detector is more densely instrumented. This so-called DeepCore subdetector consists of an additional 6 strings, each of which contains 60 optical modules with a 7 m vertical spacing in the lower part.

▷ ANTARES

The Astronomy with a Neutrino Telescope and Abyss environmental RESearch (ANTARES) project [80] operates a detector at the bottom of the Mediterranean Sea. ANTARES will be described in more detail in the next section.

The main detector parameters of the telescopes are summarised in table 5.2. Other collaborations also aim to realise a neutrino telescope in the Mediterranean Sea. The NEutrino Mediterranean Observatory (NEMO) [81] and the Neutrino Extended Submarine Telescope with Oceanographic Research (NESTOR) [82] collaborations have both

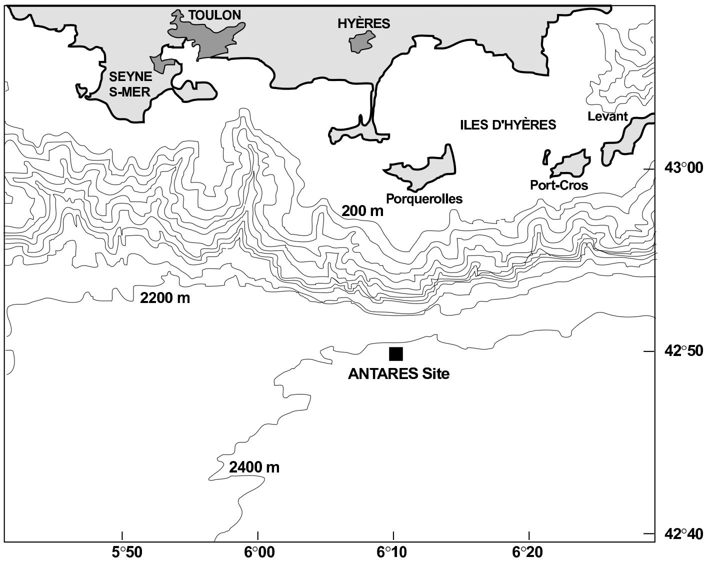

Figure 5.5:

The location of the ANTARES detector in the Mediterranean Sea. The distance between the ANTARES site and the city of Toulon, France, is about 40 km.

conducted detector design studies and tested prototype detector elements. Furthermore, a consortium formed around the institutes currently involved in the ANTARES, NEMO and NESTOR projects are pursuing the design, construction and operation of KM3NeT, a neutrino telescope with a volume of several cubic kilometres in the Mediterranean Sea. The consortium published its technical design report in 2010 [83] and is currently starting to prepare the construction of the KM3NeT telescope.

5.2 The ANTARES detector

The ANTARES detector is located at a depth of about 2.5 km in the Mediterranean Sea, approximately 40 km to the south-east, off the coast from Toulon, France. See figure 5.5. An electro-optical cable serves as the power and data transmission line between the detector and the ANTARES control station in La Seyne-sur-Mer.

5.2.1 Detector layout

The ANTARES detector can be described in terms of building blocks, each of which consist of smaller building blocks, and so on. The following description proceeds from the smallest building block to the largest building block:

1. The basic element is the Optical Module (OM) [84], as shown in figure 5.6. Each OM consists of a pressure-resistant glass sphere with a diameter of 43 cm and 15 mm wall-thickness, that contains a Hamamatsu R7081-20 PMT. The Hamamatsu R7081-20 is a hemispherical PMT with a diameter of 25 cm and an effective sensitive area of about 450 cm^2. It contains 14 amplification stages and has a nominal gain of $5 \cdot 10^7$ at a high voltage of 1760 V. The PMT is sensitive to single photons in the 300 – 600 nm wavelength range. The maximum quantum efficiency lies between 350 and 450 nm and is approximately 25 %. The charge resolution for a single photo-electron is about 30 % and the Transit Time Spread (TTS) through the PMT is

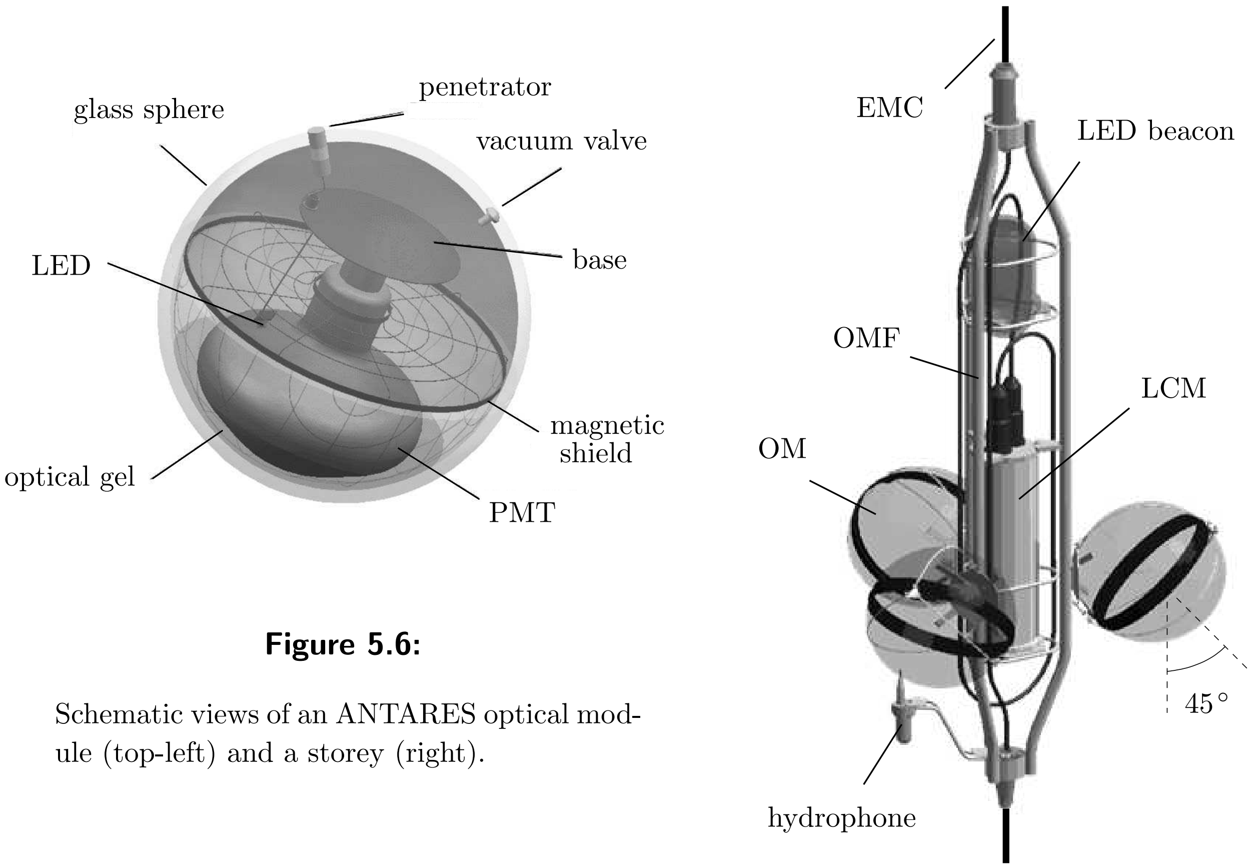

Figure 5.6:

Schematic views of an ANTARES optical module (top-left) and a storey (right).

approximately 2.6 ns FWHM. The dark count rate at the 0.25 photo-electron level is about 2 kHz. The PMT is surrounded by a μ-metal cage to minimise the influence of the Earth's magnetic field on its response. The high voltage is provided by the electronics board mounted on the PMT socket. This board also contains a LED calibration system. A transparent silicon rubber gel provides the optical contact between the PMT and the glass, and gives mechanical support. The glass hemisphere behind the PMT is painted black and contains a penetrator which provides the power and data transmission connection to the outside.

2. The OMs are grouped in triplets to form a storey or floor, as shown in figure 5.6. They are mounted at equidistant angles around a titanium Optical Module Frame (OMF), and point downwards at 45° with respect to the vertical. The OMs are connected to the Local Control Module (LCM). This titanium cylinder at the centre of the OMF houses data transmission electronics of the OMs, as well as various instruments for calibration and monitoring. A storey may also contain extra instruments that are mounted on the OMF, such as a LED beacon or an acoustic hydrophone.

3. Storeys are serially connected with Electro-Mechanical Cables (EMCs), which contain electrical wires for power distribution and optical fibres for data transmission. The distance between adjacent storeys is 14.5 m. Five storeys linked together constitute a sector, an individual unit in terms of power supply and data transmission. In

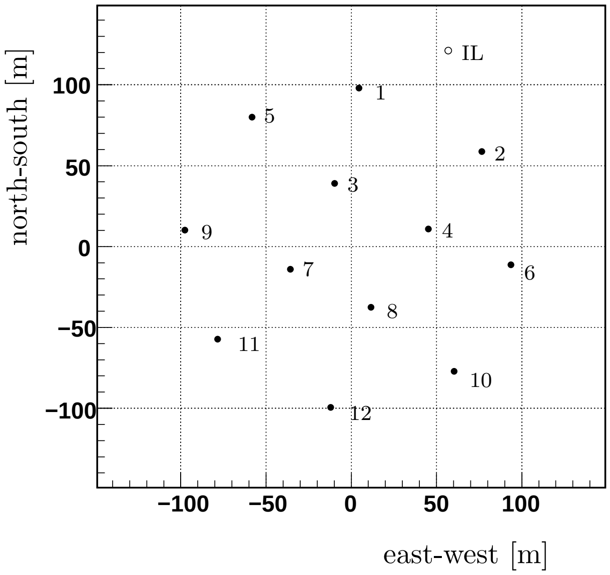

Figure 5.7:

Top view of the ANTARES detector. Detector lines are numbered according to the first time they were deployed and connected (see table 5.3).

each sector, one of the five LCMs is a Master LCM (MLCM). The data distribution between all LCMs in the sector and the SCM (see next point) is handled by the MLCM.

4. Five sectors linked together form an individual detector line. Each line is anchored to the seabed by a Bottom String Socket (BSS). The BSS contains a String Control Module (SCM), a String Power Module (SPM), calibration instruments and an acoustic release system. The acoustic release allows the complete detector line including BSS to be recovered, except for a dead-weight. The SPM houses the individual power supplies for all five sectors in the line. The SCM contains data transmission electronics to distribute data between each sector and the onshore control station. An extra ~100 m EMC is added between the BSS and the bottom storey of each line, to allow the development of the Cherenkov cone for upgoing particles. Each line is kept vertical by a buoy on top of the line.

5. The complete detector consists of 12 detector lines in an octagonal configuration, and a dedicated instrumentation line (IL), see figure 5.8. The IL and the top sector of Line 12 do not contain OMs. Instead, they are equipped with various instruments for acoustic neutrino detection and for monitoring of environmental parameters. The average horizontal distance between lines is approximately 60 m. The BSS of each line is connected to the Junction Box (JB), which is the distribution point for power and data between the detector lines and the ~40 km long Main Electro-Optical Cable (MEOC) to the onshore control station in La Seyne-sur-Mer.

To summarize, the ANTARES detector contains 885 PMTs [1], arranged in triplets on 12 vertical strings. The total instrumented volume of the detector is about $1.1 \cdot 10^7$ m^3.

[1] $(12 \times 5 \times 5 \times 3) - (5 \times 3) = 885$ OMs.

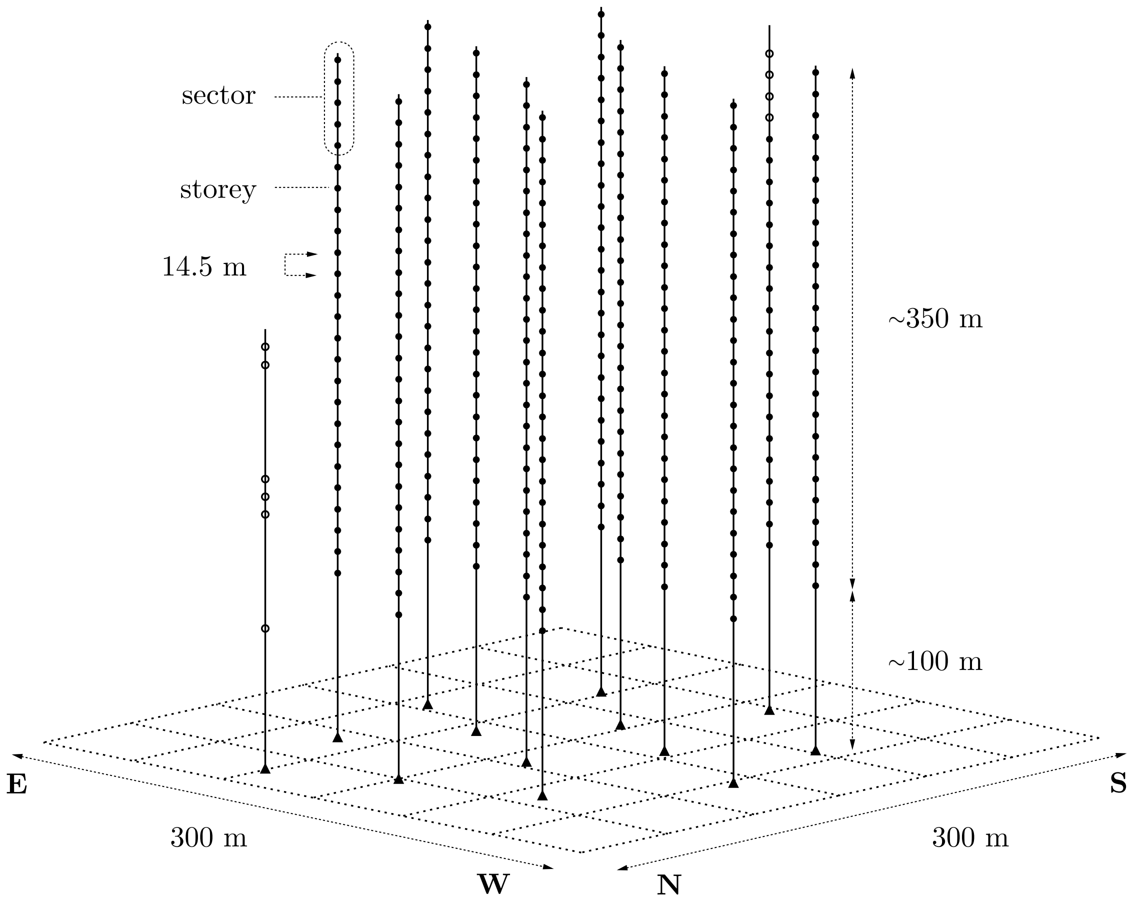

Figure 5.8: The ANTARES detector is composed of 12 detector lines of 25 storeys each, plus an instrumentation line (IL) of 6 storeys. Line 12 has 24 stories of which the top 4 do not contain optical modules.

5.2.2 Data acquisition

The transport of data and control signals between the PMTs and the onshore control station and vice versa is handled by the Data AcQuisition (DAQ) system. The DAQ system involves several steps, as described in the following [85].

Signal digitisation

A photon that hits the photocathode of a PMT can induce an electrical signal on the anode of the PMT. The probability for this to happen is characterised by the quantum efficiency of the PMT. If the amplitude of the signal exceeds a certain voltage threshold, the signal is read out and digitised by a custom designed front-end chip, the Analogue Ring Sampler (ARS) [86], located in the LCM. The voltage threshold is set to a fraction of the single photo-electron average amplitude to suppress the PMT dark current, typically 0.3 photo-electrons. The time at which the signal crosses the threshold is timestamped by the ARS with respect to a reference time, provided by a local clock. All clocks in the detector are synchronised with a 20 MHz onshore master clock. A Time-to-Voltage Converter (TVC) is used to measure the time of the signal within the 50 ns interval between two subsequent clock pulses. The TVC provides a voltage which is digitised with an 8-bit analogue-to-digital converter to achieve a timestamp accuracy of about 0.2 ns. Each ARS contains two TVCs which operate in flip-flop mode to eliminate electronic dead-time. Additionally, the charge of the analogue signal is integrated and digitised by the ARS over a certain time period. The integration gate is typically set to 35 ns to integrate most of the PMT signal and to limit the contribution from electronic noise. The combined time and charge information of a digitised PMT signal is called a hit, and is stored in 6 bytes. Each PMT is read out by two ARS chips that operate in a token ring to minimise electronic dead-time. All 6 ARS chips in an LCM are read out by a Field Programmable Gate Array (FPGA). The FPGA arranges the hits produced in a certain time window into so-called dataframes, and buffers these in a 64 MB Synchronous Dynamic Random Access Memory (SDRAM). The length of the time window is set to a value much larger than the time it takes for a muon to traverse the complete detector, typically 13.1072 ms ($2^{19} \cdot 25$ ns) or 104.8576 ms ($2^{22} \cdot 25$ ns).

Data transmission

Each LCM contains a Central Processing Unit (CPU) which is connected to the onshore computer system. Each CPU runs two programs that manage the data transfer to shore. The DaqHarness program handles the transfer of dataframes from the SDRAM to the onshore control station. The ScHarness program handles the transfer of calibration and monitoring data, referred to as slow control data. Communication between all offshore CPUs and the onshore control station is done via optical fibres using the Transmission Control Protocol and Internet Protocol (TCP/IP). A schematic representation of the data stream in a single detector line is shown in figure 5.9. Each LCM CPU in a sector has a bi-directional Fast Ethernet link (100 Mb/s) via an electro-optical (e/o) converter to the MLCM. In the MLCM, these links are e/o converted and passed to an electronic data router (switch). The switch merges the 5 bi-directional Fast Ethernet links (4 LCM and 1 MLCM CPU) into two uni-directional Gigabit Ethernet links (1 Gb/s), one for incoming control signals and one for outgoing data. The gigabit signals are e/o converted using an optical wavelength which is unique for each MLCM in a detector line. The incoming and outgoing optical links of the 5 MLCMs in a detector line are routed to the SCM, where they are (de)multiplexed into a single optical fibre using Dense Wavelength-Division Multiplexing (DWDM). The optical fibre from each SCM runs through the JB and the MEOC to the onshore control station, where they are (de)multiplexed into separate MLCM channels using wavelengths identical to those in the corresponding SCM. The uni-directional optical MLCM channels from all demultiplexers are linked to an onshore switch via e/o converters. Finally, the switch is connected to a computer farm which accommodates the detector control and the data processing systems.

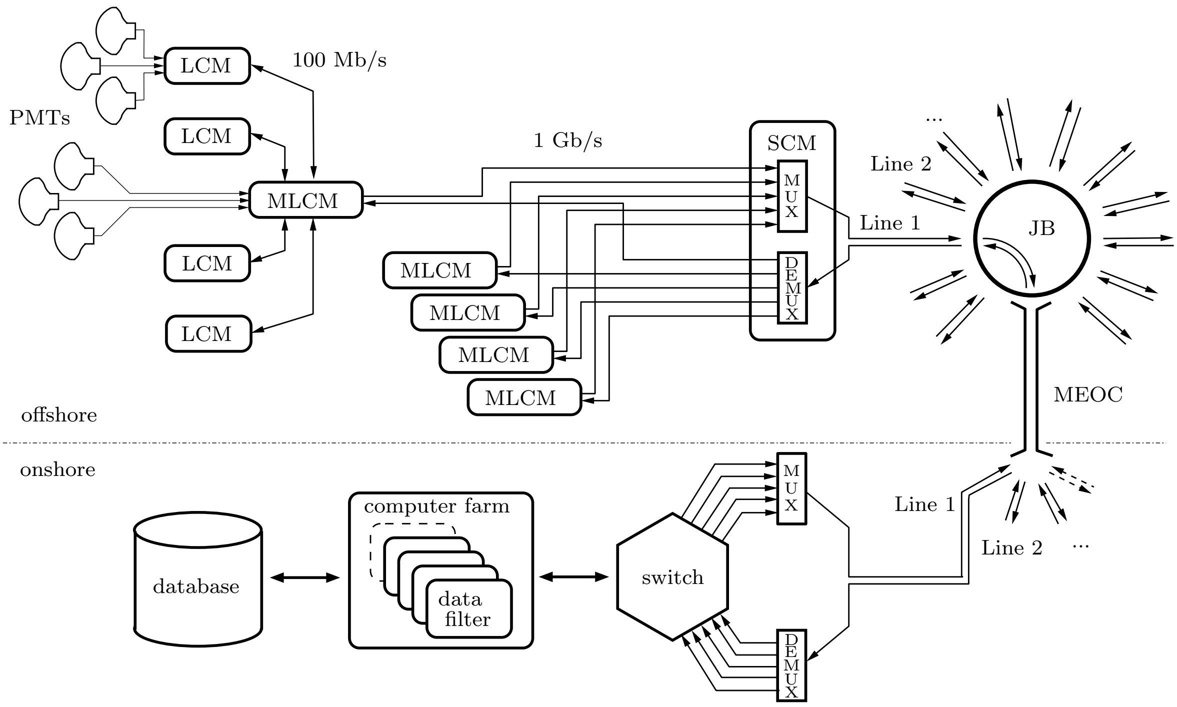

Figure 5.9: Flow diagram of the data stream in a single ANTARES detector line.

Data filtering and storage

The DAQ system is designed according to the so-called all-data-to-shore concept. This entails that no offshore signal selection is done except for the ARS threshold criterion, and all detected hits are transferred to shore. However, since the vast majority of detected signals is due to the optical background in the detector (see section 5.2.5), the data are filtered in the onshore computing farm to reduce the data storage demands. This is done by sending all dataframes that belong to the same time window to a common processor in the onshore computer farm. The set of dataframes is referred to as a timeslice, which consequently contains all hits that were detected in the same time window. Each timeslice is handled by a different processor, each of which accommodates a `dfilter` program. The `dfilter` program collects all dataframes corresponding to the same timeslice, and applies a trigger algorithm to search for signals that can be attributed to a charged particle which traversed the detector. Hence data filtering is done using software rather than hardware, which has advantages in terms of flexibility and detection sensitivity. Different trigger algorithms can be applied in parallel to search for specific signatures, as will be explained in the next chapter. The output from every datafilter is passed to the `dwriter` program that formats the data using the ROOT software package [87] and stores them in a database for offline analysis. Similarly, the slow control data are collected and processed by the `scDataPolling` program, and written to the database by the `dbwriter` program.

Detector line	Connection date	Not operational
Line 1	March 2nd 2006	
Line 2	September 21st 2006	
Line 3	January 27th 2007	
Line 4	January 29th 2007	March 3rd 2008 – May 28th 2008
Line 5	January 29th 2007	
Line 6	December 5th 2007	October 27th 2009 – November 3rd 2010
Line 7	December 6th 2007	
Line 8	December 6th 2007	
Line 9	December 7th 2007	July 2nd 2009 – November 3rd 2010
Line 10	December 6th 2007	January 7th 2009 – November 6th 2009
Line 11	May 25th 2008	
Line 12	May 28th 2008	March 12th 2009 – November 13th 2009
IL	December 4th 2007	November 3rd 2010 – present

Table 5.3: Operational timeline of the ANTARES detector.

5.2.3 Detector status

The ANTARES detector has been fully operational since May 28th 2008. Prior to its completion, ANTARES has taken data in intermediate configurations. An overview is given in table 5.3. Data taking started in 2006 with the connection of Line 1 on March 2nd and Line 2 on September 21st. On January 29th 2007, after the connection of Lines 3 – 5, ANTARES surpassed the Baikal telescope as the largest neutrino telescope on the Northern Hemisphere. The detector doubled in size on December 7th 2007 with the connection of Lines 6 – 10 and the IL. Finally, ANTARES was completed on May 28th 2008 with the connection of Lines 11 and 12. As can also be seen from table 5.3, some detector lines that showed significant problems during operation have been recovered, repaired, redeployed and reconnected. The detector was not operational between June 25th 2008 and September 5th 2008 due to a fault in the MEOC.

5.2.4 Detector calibration

The precision with which the direction and energy of charged particles traversing the detector can be determined, depends on the accuracy with which the photon arrival times at the PMTs and the location of the PMTs in the detector are measured. ANTARES is designed to achieve an angular resolution smaller than 0.3° for muons above 10 TeV [88]. To realize this resolution, the ANTARES detector comprises several independent calibration systems that are able to measure and monitor the absolute and relative timing of PMT signals and the location of all PMTs.

Time calibration

The relative timing of the photon arrival times on the PMTs are needed to reconstruct the neutrino direction. Hence the offset of each local clock, caused by the optical path length to shore, has to be known. The offsets are obtained by an internal clock calibration system. A calibration signal sent by the onshore master clock is echoed back along the same optical path by each LCM, to measure the relative offset of each LCM with an accuracy of 0.1 ns. A second calibration system based on a blue (470 nm) LED inside each OM is used to calibrate the time offset between the PMT photocathode up to the readout electronics. The internal LED system is used in dedicated data-taking runs to monitor the relative variation of the PMT transit time. Finally, a calibration system based on optical beacons in the detector is used to calibrate the relative time offsets between PMTs. The system comprises four blue (470 nm) LED beacons located on storeys 2, 9, 15 and 21 of each detector line, and two green (532 nm) LASER beacons on the BSS of Lines 7 and 8. A small PMT in each LED beacon and a photodiode in each LASER beacon measure the time of emission. Dedicated data-taking runs in which one or several beacons are flashed are performed regularly (typically once per week), to monitor the relative time offsets between the PMTs and the influence of water on the light propagation.

Measurements obtained by the internal LED and optical beacon systems have shown that the contribution of the detector electronics to the photon arrival time resolution is less than 0.5 ns [88]. Therefore the time resolution is dominated by the TTS of the PMTs ($\sigma_{\mathrm{TTS}} \simeq 1.3$ ns), and the light scattering and chromatic dispersion by the sea water ($\sigma_{\mathrm{sea}} \simeq 1.5$ ns, for an optical path length of 40 m). Absolute timing is needed to correlate the reconstructed neutrino direction with specific sources in the Universe. This is achieved by synchronising the onshore master clock to the Global Positioning System (GPS) time with an accuracy of 100 ns [85].

Position calibration

Each detector line is anchored to a BSS on the seabed and kept vertical by the buoyancy of the individual OMs and a top buoy. Nevertheless, due to the sea current and the flexibility of the EMCs, the sideways displacement of a detector line can be considerable and real time positioning of each line is needed. This is achieved through two independent systems : an acoustic positioning system and a tiltmeter-compass system.

The acoustic positioning system consists of a three dimensional array of acoustic emitters and receivers (hydrophones). The high frequency emitters (40 – 60 kHz) are located on the BSS of each line. An additional independent autonomous emitter is located approximately 145 m from the detector. Five hydrophones are located on storeys 1, 8, 14, 20 and 25 of each detector line. Dedicated acoustic runs are performed every 2 minutes, during which the transit times between each emitter and the receivers are recorded alternately. The distances between emitters and receivers are calculated using the sound velocity which is monitored by several sound velocity profilers located throughout the detector. The calculated distances are then used to triangulate the position of each acoustic receiver relative to the acoustic emitters with an accuracy of 10 cm [89].

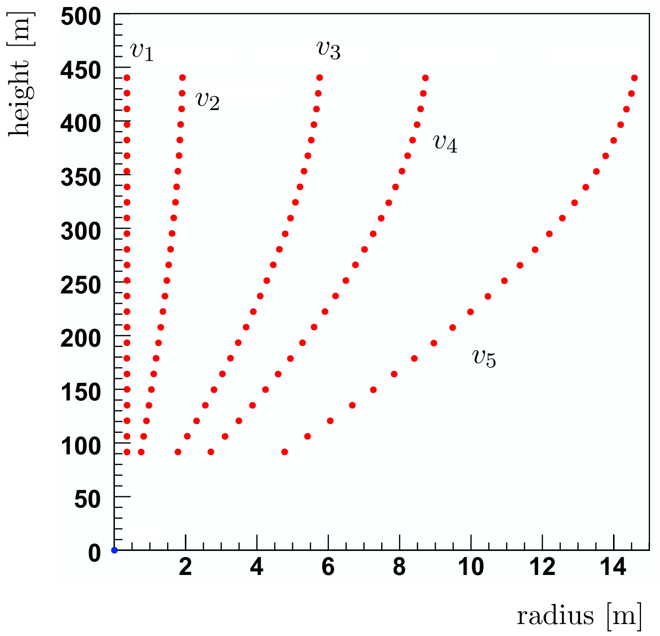

Figure 5.10:

Reconstructed detector line shape at different sea current velocities [90] :

- $v_1 = 0.01$ cm/s
- $v_2 = 7$ cm/s
- $v_3 = 12.6$ cm/s
- $v_4 = 16$ cm/s
- $v_5 = 20$ cm/s

The tiltmeter-compass system comprises a tiltmeter and a compass in each LCM. The two perpendicular tilt angles of a storey, the pitch and roll angles along the North-South and East-West axes, are monitored by a tiltmeter with an accuracy of 0.2°. The heading angle of a storey with respect to the North-South axis is monitored with a compass with an accuracy of 1°. The tiltmeter-compass data are also read out every 2 minutes.

The shape of each detector line is reconstructed by performing a global χ^2 fit using information from both systems. The line shape is used to calculate the relative position of each PMT in the detector line with respect to the BSS. The reconstructed detector line shape for various sea current velocities is shown in figure 5.10. The absolute position of the BSS of each line is determined during the connection of a line to the JB with a Remotely Operated Vehicle (ROV). This is done by acoustic positioning and pressure measurements by the ROV, and the GPS location of the ship.

5.2.5 Optical background

Naturally, sea water contains two independent sources of visible light which have to be taken into account in the neutrino telescope concept : the radioactive isotope of potassium, ^{40}K, and bioluminescence.

Monitoring of the sea water salinity at the ANTARES shows that it is constant at about 3.9 %. This implies that sea water consists for approximately 400 ppm of potassium. About 0.012 % of potassium consists of the long-lived radioactive isotope ^{40}K, which has a half-life of 1.3 billion years. It can decay to ^{40}Ca through beta decay (89 % of the time) and to ^{40}Ar through electron capture and emission of an energetic photon (11 % of the time). In the beta decay, the maximum electron energy of 1.3 MeV lies above the Cherenkov threshold in water. In the electron capture, the photon energy of 1.46 MeV is sufficiently high to Compton scatter an electron above the Cherenkov

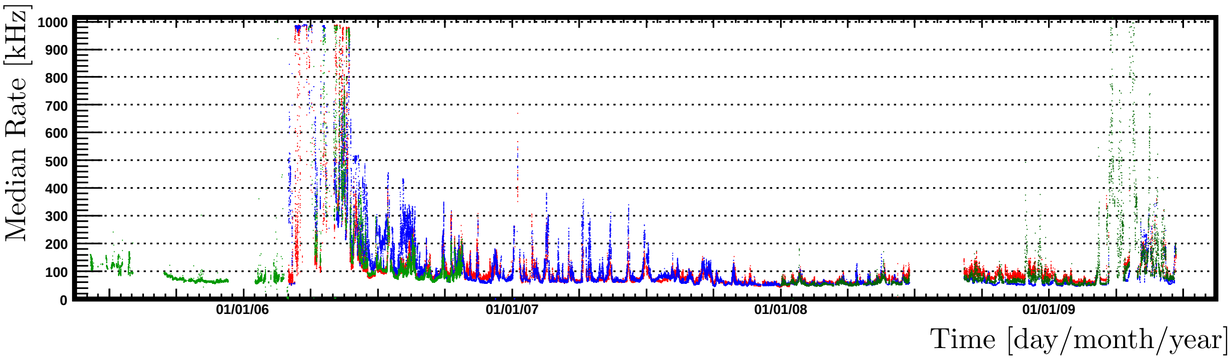

Figure 5.11: Median rate of measured single photon counts for a number of representative PMTs in ANTARES, as measured between 2005 and 2009.

threshold. A dedicated Monte Carlo simulation indicates that the counting rate for each PMT in the ANTARES detector due to ^{40}K events is constant at 34 ± 7 kHz [91]. Furthermore, if a ^{40}K event occurs within a few meters of a storey, a coincident signal may be detected by two of the three PMTs on the storey. An mean coincidence rate of 16 ± 2 Hz is observed. This agrees with the expected rate of 19 ± 3 Hz, obtained by Monte Carlo simulation [92].

The median rate of measured single photon counts for a number of representative PMTs in ANTARES, as measured between 2005 and 2009, is shown in figure 5.11. As can be seen, the PMT counting rate is higher than what is expected from ^{40}K alone, and is highly time dependent. It is assumed that the surplus and time variations are due to bioluminescence, light produced by organisms living in the water. The amount of bioluminescent light detected in ANTARES is expected to be correlated to the number of luminescent organisms in the water, and hence depends on the magnitude of the sea current velocity. This is indeed observed [93]. Furthermore, occasionally the actual PMT counting rates can increase up to several MHz for short periods of time. These so-called bursts can last for seconds and are thought to be produced by organisms hitting the PMTs.

Chapter 6

Data filtering in ANTARES

The all-data-to-shore concept used in ANTARES entails that all hits that pass the ARS threshold criterion are sent to shore. Since the vast majority of all detected hits is due to the optical background, the data is filtered onshore to alleviate the data storage demand. This chapter gives a brief description of the trigger algorithms that are used to search for muon signatures in the online data stream. In particular, the Galactic Centre trigger as used during data-taking is described.

6.1 Trigger

The `dfilter` program uses a trigger algorithm to analyse all hits in a single timeslice [94]. In general, the goal of a trigger algorithm is to verify if the timeslice contains hits which could have originated from a traversing muon. Hits that originate from the same muon are correlated to the muon and to each other in terms of time, position and charge. The ARS information in every hit is first decoded using calibration data. The muon hypothesis can be tested in various ways. Hence, several algorithms with different characteristics regarding efficiency, purity and speed have been developed.

In the following, the standard trigger algorithm as used during data-taking is described. This is followed by the source tracking trigger, which can be used for any continuous neutrino source with a known direction. The source tracking trigger is currently used during data-taking to follow the Galactic Centre. Since both algorithms are based on the same causality criterion, this are discussed first.

6.1.1 Causality

Hits that originate from the same muon are causally related in space and time. Consider a pair of hits detected in PMT_i and PMT_j and assume they are produced by two Cherenkov photons emitted by a single muon. The maximum time difference between the hits is caused by a muon that passes through one of the two PMTs. If the time difference is larger, the hits cannot be attributed to the same muon whereas if it is smaller they can (e.g. the time difference is zero if the hits are caused by a muon that traverses the symmetry plane between the two PMTs). Hence, a pair of hits that is caused by a single muon has to fulfil the causality criterion

$$-\frac{|\vec{x}_i - \vec{x}_j|}{v_{\mathrm{g}}} \;\leq\; t_i - t_j \;\leq\; \frac{|\vec{x}_i - \vec{x}_j|}{v_{\mathrm{g}}} \tag{6.1}$$

where v_{g} is the group velocity of light in water given by equation (5.3), and the factor $|\vec{x}_i - \vec{x}_j|$ represents the three-dimensional distance between the two PMTs.

The causality criterion given by equation (6.1) is valid for muons traveling in any direction. However, if the muon direction is fixed, the causality relation between a pair of hits can be refined further. This so-called directional causality criterion can be quantified by considering a muon traveling through a detector while emitting Cherenkov photons that are detected by the PMTs, as shown in figure 6.1. The arrival time t_i of a Cherenkov photon γ_i on PMT$_i$, emitted by a muon travelling in the z-direction at the speed of light, with respect to an arbitrary reference time t_0 corresponding to the time when the muon was at $z = 0$ can be expressed as

$$t_i \;=\; t_0 \;+\; \frac{1}{c}\left(z_i - \frac{r_i}{\tan(\theta_{\mathrm{C}})}\right) \;+\; \frac{1}{v_{\mathrm{g}}}\frac{r_i}{\sin(\theta_{\mathrm{C}})} \tag{6.2}$$

where θ_{C} is the Cherenkov angle and r_i is the distance of closest approach between the muon and PMT$_i$. To verify if a pair of hits could have originated from the same muon, the difference in arrival times between the two hits has to be considered. By using equation (6.2), the difference in arrival times between two hits in PMT$_i$ and PMT$_j$ can be expressed as

$$t_i - t_j \;=\; \frac{z_i - z_j}{c} \;+\; \frac{r_i - r_j}{c}\left(\frac{c}{v_{\mathrm{g}}}\frac{1}{\sin(\theta_{\mathrm{C}})} \;-\; \frac{1}{\tan(\theta_{\mathrm{C}})}\right) \tag{6.3}$$

$$\approx\; \frac{z_i - z_j}{c} \;+\; \frac{r_i - r_j}{c}\,\tan(\theta_{\mathrm{C}}) \tag{6.4}$$

where the approximation in the second line is exact if one assumes $n_{\mathrm{g}} = n$. Since the muon direction is fixed but its transverse position is not, the only unknown factor in equation (6.4) is $(r_i - r_j)$. The maximum time difference occurs when the muon passes through one of the two PMTs, i.e. when $r_i = 0$ or $r_j = 0$. In that case, $r_i - r_j = \pm R_{ij}$, where R_{ij} represents the transverse distance between PMT$_i$ and PMT$_j$ with respect to the muon direction. Hence, given that a muon travels in the z-direction with the speed of light, a pair of hits can be caused by that same muon if

$$-\frac{R_{ij}}{c}\,\tan(\theta_{\mathrm{C}}) \;\leq\; (t_i - t_j) \;-\; \frac{z_i - z_j}{c} \;\leq\; \frac{R_{ij}}{c}\,\tan(\theta_{\mathrm{C}}) \tag{6.5}$$

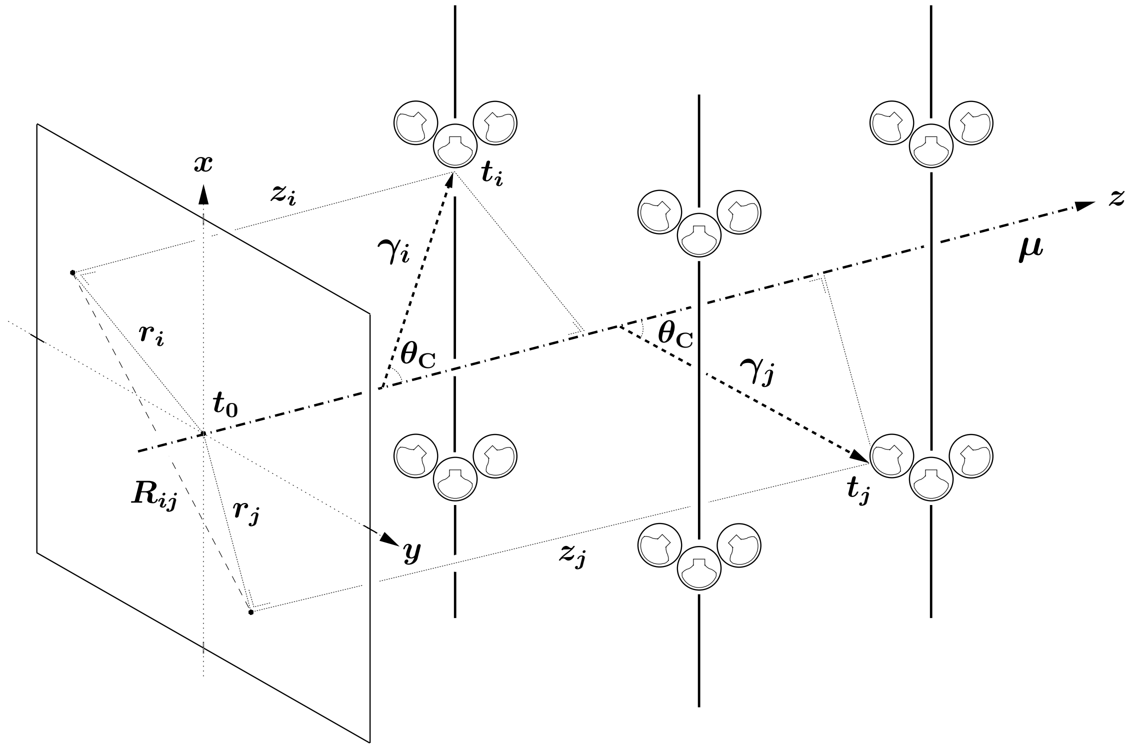

Figure 6.1: Schematic view of a muon traversing a part of the ANTARES detector.

6.1.2 Standard trigger

The standard trigger as used during data-taking is based on the so-called `trigger3N` algorithm [94]. In this algorithm, all hits in a single timeslice are analysed according to the following steps. The default values of the various parameters in the algorithm are shown in parentheses [95].

1. A subsample of specific hits is created from all hits in the timeslice. A hit is selected by its charge and by the time difference with any other hit detected by a different PMT on the same storey. The selection principle is based on the assumption that the optical background processes are not correlated and produce only single photons. Hence, background hits are assumed to have a charge corresponding to a single photo-electron. A hit with a larger charge is more likely to originate from a muon since it corresponds to multiple photons detected within the ARS integration gate of the same PMT. The charge selection is determined by the parameter `highThreshold` (3 p.e.), which is the minimum charge of a hit in units of photo-electrons. Similarly, two hits that are detected in coincidence by more than one PMT on the same storey are more likely to originate from a muon. The maximum time difference between two hits that are regarded as a coincident pair is determined by the parameter `maxLocalTime` (20 ns). Hits that satify these criteria are referred to as L1 hits, hits that do not are called L0 hits.

2. The L1 hits are subjected to the causality criterion, given by equation (6.1), that identifies pairs of hits which could have originated from a single muon. The allowed

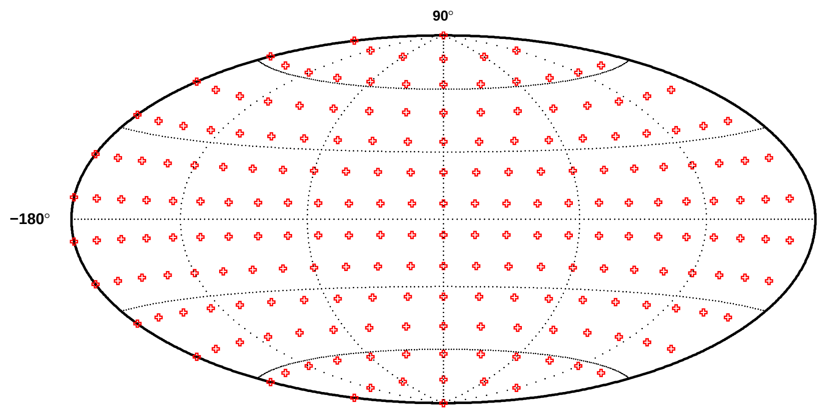

Figure 6.2: Hammer-Aitoff projection (see Appendix B) of the default grid of 210 directions used in the standard trigger algorithm (`omega`=10).

time window between hits is increased with the parameter `maxExtraTime` (20 ns), to take into account calibration uncertainties and some light scattering in the water. The largest group of hits within a certain time window which are all causally related to each other is called a cluster. The number of hits in a cluster is referred to as the cluster size. To reduce processing time, the clustering starts by requiring that the maximum time difference in the causality criterion is limited to `maxEventTime` (2.2 μs). This corresponds to the time it takes for a relativistic muon to traverse the entire detector. For each cluster of sufficient size, the causality criterion is applied to every pair of L1 hits in the cluster. Each cluster for which the cluster size equals or exceeds `numberOfHits` (5 L1 hits) is selected for the next step.

3. For each selected cluster, all L1 hits are subjected to the directional causality criterion given by equation (6.5). This is done to suppress accidental clusters due to the random optical background. The allowed time window in the directional causality criterion is increased with the parameter `maxExtraTime` to allow for some light scattering and calibration uncertainties. Since the direction of the muon is not known, an isotropic grid of directions which covers the full 4π solid angle is generated. The directional causality criterion is applied with respect to every direction on the grid. The direction spacing on the grid is determined by the parameter `omega` (10). The default value corresponds to a grid of 210 directions with an average grid spacing of 13°. See figure 6.2.

Furthermore, the directional causality criterion is made more restrictive by imposing a limit on the transverse distance R_{ij} between two L1 hits. This restriction is based on the absorption of light in water and the geometrical spread of the Cherenkov cone. The intensity of the Cherenkov light emitted by a muon decreases as a function of the transverse distance to the muon as

$$I(r) \propto \frac{1}{r}\, e^{-r/(\sin(\theta_C)\, \lambda_{\mathrm{abs}})} \tag{6.6}$$

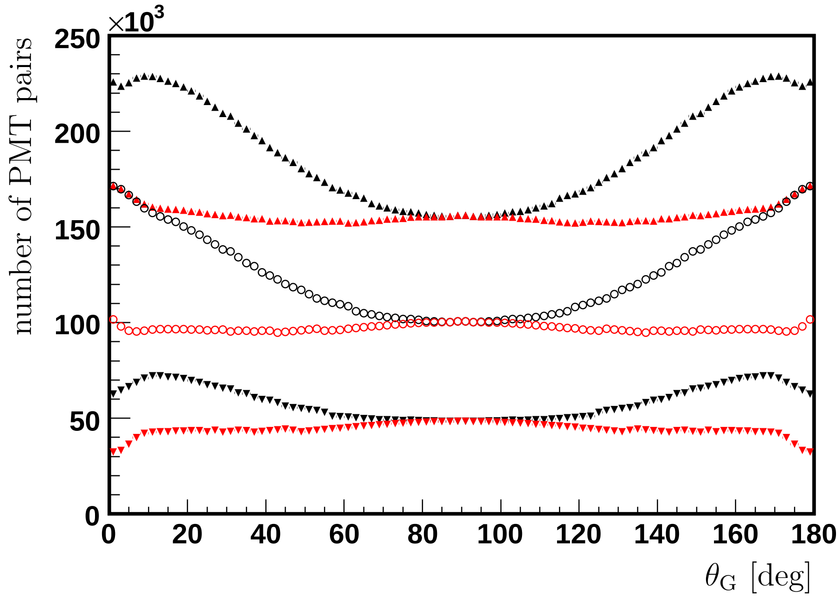

Figure 6.3: The number of PMT pairs that can be causally correlated according to the directional causality criterion, before (in black) and after (in gray) multiplication of the maximum transverse distance with the factor $(1 - \frac{1}{4}\cos^2(\theta_G))$, as a function of θ_G for three different maximum transverse distances (▲ = 120 m, ○ = 90 m, ▼ = 60 m).

where λ_{abs} is the absorption length in water. The maximum accepted transverse distance between a pair of L1 hits is determined by the parameter `roadWidth` (90 m). This corresponds to about two absorption lengths in water (see table 5.1). However, due to the PMT distribution in ANTARES, the number of PMT pairs that can be causally correlated according to the directional causality criterion is greater for vertical directions than for horizontal directions. To compensate for this effect, the maximum transverse distance is multiplied with a factor $(1 - \frac{1}{4}\cos^2(\theta_G))$, where θ_G is the zenith angle of the grid direction [96]. The effect of this last restriction is demonstrated in figure 6.3, which shows the number of PMT pairs that can be causally correlated according to the directional causality criterion, before and after correction by the factor $(1 - \frac{1}{4}\cos^2(\theta_G))$, as a function of θ_G.

If, for any direction in the grid, a cluster still has at least `numberOfHits` L1 hits which are all causally related to each other according to the restricted directional causality criterion, the cluster is selected for the final step.

4. Selected clusters which (partially) overlap in time within `maxEventTime` are merged into a single cluster. Each cluster is then formatted in the form of a so-called PhysicsEvent for subsequent storage on disk. A PhysicsEvent contains the L1 hits which comprised the selected cluster as well as all L0 hits within plus or minus `maxEventTime` around the cluster. These are referred to as triggered hits and snapshot hits respectively. This is done to include any hits caused by the muon that did not pass the L1 criteria in step 1. All PhysicsEvents that are obtained through the standard trigger are tagged as `TRIGGER_3N` for offline analysis.

6.1.3 Source tracking trigger

The source tracking trigger can be used to monitor a continuous neutrino source with a given position in the Universe. Presently it is used during data-taking to follow the Galactic Centre. The source tracking trigger is based on the so-called `triggerMX` algorithm [94], in which all hits in a single timeslice are analysed according to the following steps. The default values of the various parameters in the algorithm are shown in parentheses [95].

1. The GPS time of the timeslice is used to calculate the direction of the source that is followed in the ANTARES local coordinate system. In the local cartesian coordinate system, the x-axis points to the east, the y-axis points to the north and the z-axis points vertically upward. The direction of the source in the local frame is given by its zenith angle $\theta_{\rm S}$, defined as the angle with respect to the positive z-axis, and its azimuth angle $\phi_{\rm S}$, defined as the counter-clockwise angle in the horizontal plane with respect to the positive x-axis. See also figure B.2 in Appendix B. Given the location of the source on the celestial sphere (i.e. its declination and right ascension), the source direction $(\theta_{\rm S}, \phi_{\rm S})$ in the local frame can be calculated by considering the time and the location of ANTARES on Earth. The procedure is described in more detail in Appendix B.

   The direction of a source in the local frame is a periodical function of time due to the rotation of the Earth. For objects outside the solar system, the time period is equal to one sidereal day. To illustrate, the directions in the local frame of several sources with different declinations are shown in figure 6.4. Sources with positive/negative declinations are indicated by solid/open symbols. The only two sources that always point in the same two directions in the sky are the celestial poles. The movement of the other sources with time is indicated by the markers, which are each separated by one hour. As can be seen, a source with a declination larger than $47°12'$ is always located above the ANTARES horizon, as expected from the geographic latitude $\lambda_{\rm ANT} = 42°48'$ of ANTARES. Sources at these declinations rotate counter-clockwise around the celestial north pole, since the Earth rotates in a counter-clockwise direction. Similarly, sources with a declination smaller than $-47°12'$ are always located below the ANTARES horizon, and rotate clockwise around the celestial south pole. Sources with declinations between $\pm\lambda_{\rm ANT}$ traverse the entire azimuthal range. For these sources, the direction of time runs opposite to the azimuthal direction, i.e. E $\rightarrow$ S $\rightarrow$ W $\rightarrow$ N $\rightarrow$ E. For any source, the minimum and maximum zenith angle always occur when its azimuth angle corresponds to the northward or southward direction.

2. A set of L1 hits is created from all hits in the timeslice, as explained in step 1 in section 6.1.2. All hits in the timeslice are subjected to the directional causality criterion given by equation (6.5) with respect to the trigger direction (θ, ϕ) of the source that is followed. Since the neutrino-induced muon points away from the source, the trigger direction is opposite to the source direction, i.e. $(\theta, \phi) = (\pi - \theta_{\rm S}, \pi + \phi_{\rm S})$. The maximum transverse distance for every hit pair with respect to the trigger

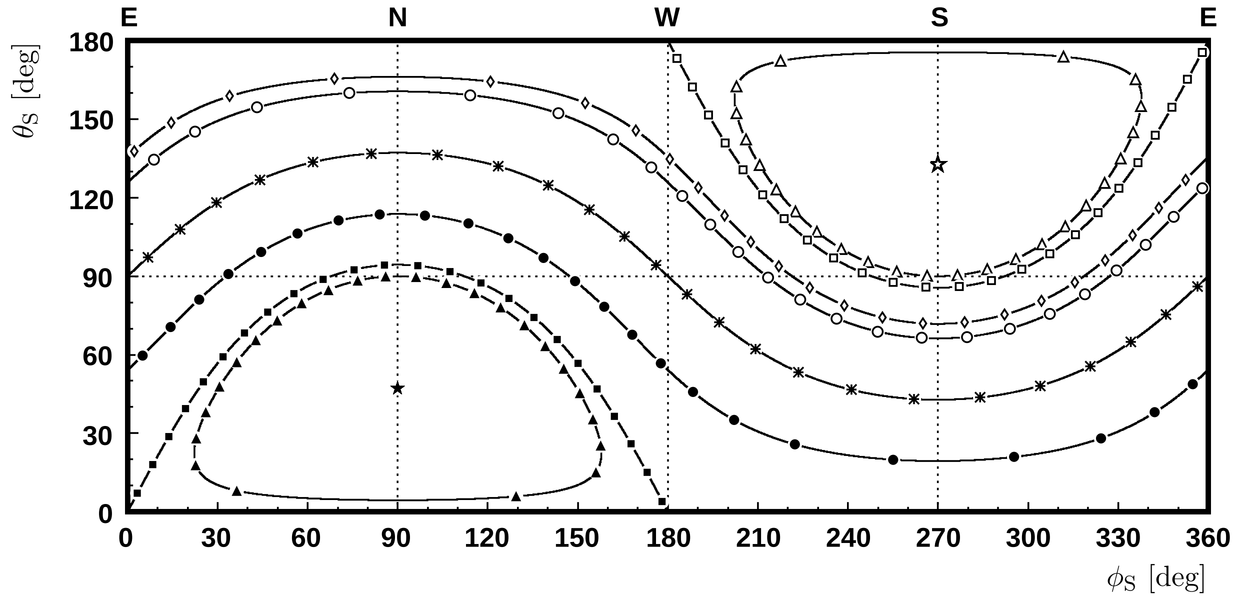

Source declination:

★	$+90°$	⇔	North Celestial Pole
▲	$+47° 12'$	⇔	$90° - \lambda_{\mathrm{ANT}}$
■	$+42° 48'$	⇔	λ_{ANT}
●	$+23° 26'$	⇔	Sun, summer solstice
✱	$0°$	⇔	Celestial Equator
○	$-23° 26'$	⇔	Sun, winter solstice
◇	$-29°$	⇔	Galactic Centre
□	$-42° 48'$	⇔	$-\lambda_{\mathrm{ANT}}$
△	$-47° 12'$	⇔	$\lambda_{\mathrm{ANT}} - 90°$
☆	$-90°$	⇔	South Celestial Pole

The geographic latitude of the ANTARES detector, λ_{ANT}, is $42°48'$.

Figure 6.4:

The time-dependent direction of sources with various declinations in the local ANTARES coordinate system. Sources with positive/negative declinations are indicated by solid/open symbols. The markers are each separated by one hour to indicate the movement of a source with time.

direction, R_{max}, is determined by the parameter `roadWidthL0` (85 m). Similar to the standard trigger, the maximum transverse distance is multiplied by a factor of $(1 - \frac{1}{4}\cos^2(\theta))$ to compensate for the asymmetric PMT distribution with respect to the zenith angle θ in ANTARES. Since the zenith angle θ is a time-dependent quantity, R_{max} is time-dependent as well. The allowed time window in the directional causality criterion is increased with the parameter `maxExtraTime`. A cluster is defined as the largest group of hits that are all causally related to each other according to the restricted directional causality criterion, and which includes at least 1 L1 hit. Each cluster for which the number of hits besides the L1 hit equals or exceeds the parameter `numberOfL0s` (5 L0 hits) is selected for the next step. Hence selected clusters correspond to a minimum of 6 detected photons per cluster.

3. Clusters which have a relatively small cluster size are subjected to a track fit procedure, to further suppress accidental clusters due to the random optical background. The critical cluster size is determined by the parameter `factoryLimit` (4). All clusters of size equal to or less than `factoryLimit` + `numberOfL0s` + 1 are subjected

to the following track fit procedure.

In the track fit, it is assumed that all hits are due to Cherenkov photons emitted by a muon travelling at the speed of light in the trigger direction. In general, a track can be described by 5 independent parameters (i.e. 3 positional and 2 directional parameters). By assuming the direction of the muon, there are 3 degrees of freedom left. These can be chosen as the two-dimensional position (x_0, y_0) and the time t_0 where and when the muon crosses an arbitrary plane in the detector perpendicular to the muon direction. In that case, the expected arrival time t_i of a photon on PMT$_i$ with position (x_i, y_i, z_i) is given by equation (6.2), where $r_i^2 \equiv (x_i - x_0)^2 + (y_i - y_0)^2$. See also figure 6.1. By considering the difference between the expected arrival times t_i and t_j of two hits on different PMTs, a linear relation between the three track parameters can be derived [97]

$$\begin{aligned}(\xi_j'^{\,2} - \xi_i'^{\,2}) \; - \; 2\,(\xi_j' - \xi_i')\,\xi_0' \;&=\; (x_j^2 - x_i^2) \; - \; 2\,(x_j - x_i)\,x_0 \\ &\quad + (y_j^2 - y_i^2) \; - \; 2\,(y_j - y_i)\,y_0\end{aligned} \tag{6.7}$$

where

$$\xi_j' \;\equiv\; (\,c\,t_j - z_j - z_0\,)\,/\,\tan(\theta_\mathrm{C}) \tag{6.8}$$

$$\xi_0' \;\equiv\; c\,t_0\,/\,\tan(\theta_\mathrm{C}) \tag{6.9}$$

By considering equation (6.7) all consecutive hit pairs in the cluster (including the combination between the final and the first hit), the following matrix equation can be derived

$$\underbrace{2\begin{bmatrix} (x_2 - x_1) & (y_2 - y_1) & (\xi_1' - \xi_2') \\ (x_3 - x_2) & (y_3 - y_2) & (\xi_2' - \xi_3') \\ \vdots & \vdots & \vdots \\ (x_1 - x_n) & (y_1 - y_n) & (\xi_n' - \xi_1') \end{bmatrix}}_{\Updownarrow \; \mathbf{H}} \times \underbrace{\begin{bmatrix} x_0 \\ y_0 \\ \xi_0' \end{bmatrix}}_{\Updownarrow \; \boldsymbol{\theta}} = \underbrace{\begin{bmatrix} x_2^2 - x_1^2 + y_2^2 - y_1^2 + \xi_1'^2 - \xi_2'^2 \\ x_3^2 - x_2^2 + y_3^2 - y_2^2 + \xi_2'^2 - \xi_3'^2 \\ \vdots \\ x_1^2 - x_n^2 + y_1^2 - y_n^2 + \xi_n'^2 - \xi_1'^2 \end{bmatrix}}_{\Updownarrow \; \mathbf{y}} \tag{6.10}$$

i.e. the $n \times 3$ matrix $\mathbf{H}$ and the $n \times 1$ matrix $\mathbf{y}$ are related by the 1×3 matrix $\boldsymbol{\theta}$ which contains the track parameters, where n is the cluster size. The track fit of a cluster is found by solving the corresponding matrix equation, which is linear with respect to the track parameters. However, the exact analytical solution does not exist since the system is over-determined (a cluster contains more than 3 hits). Nevertheless, since all 3 columns of matrix $\mathbf{H}$ are linearly independent, minimising

$$\chi^2 \;\equiv\; (\mathbf{y} - \mathbf{H}\,\boldsymbol{\theta})^\mathrm{T}\,\mathbf{V}^{-1}\,(\mathbf{y} - \mathbf{H}\,\boldsymbol{\theta}) \tag{6.11}$$

leads to the unique and optimal analytical solution

$$\hat{\boldsymbol{\theta}} \equiv (\mathbf{H}^{\mathrm{T}}\,\mathbf{V}^{-1}\,\mathbf{H})^{-1}\,\mathbf{H}^{\mathrm{T}}\,\mathbf{V}^{-1}\,\mathbf{y} \tag{6.12}$$

where $\mathbf{V}$ is the covariance matrix which contains the (co)variances in time and position between the different hits in the cluster. It is assumed the covariance matrix is diagonal, and the uncertainties in time and position of each hit are equal. They are determined by the parameter `sigma` (10 ns).

The distribution of possible χ^2 values in equation (6.11) corresponds to a χ^2 function with a given number of degrees of freedom (i.e. the cluster size minus the number of track parameters). Since the properties of this function are known, the quality of the fit can be assessed by calculating the χ^2 probability of the fit. The χ^2 probability is defined as the probability that for a correct model and normally distributed errors the χ^2 value exceeds or equals the observed value, given the number of degrees of freedom. If the χ^2 probability of the track fit is larger than `prob` (0.01), the cluster is selected for the next step.

4. Clusters which (partially) overlap in time within `maxEventTime` (see section 6.1.2) are merged into a single cluster. Each cluster is then formatted in the form of a PhysicsEvent for subsequent storage to disk. A PhysicsEvent contains all hits in the cluster as well as all L0 hits within a time window around the cluster, which is also determined by the `maxEventTime` parameter. In general, all PhysicsEvents that are produced by the source tracking trigger are tagged as `TRIGGER_1D_MIXED` or `TRIGGER_1D_MIXED_WITH_PREFIT` for offline analysis. For the Galactic Centre trigger, PhysicsEvents are also tagged as `TRIGGER_GC`.

5. A final selection is made based on the surface area density, which is related to the number of triggered hits per unit area of the PhysicsEvent. The area to be considered is the so-called convex hull of all triggered hits in the PhysicsEvent projected on the transverse plane with respect to the trigger direction. In general, the convex hull of a point set is defined as the polygon with the smallest area and perimeter that contains all points in the set [98]. PhysicsEvents which are caused by a muon have a relatively large surface area density due to the distance dependence of the Cherenkov light intensity given by equation (6.6). For accidental PhysicsEvents, which are composed of hits due to the random optical background, the opposite is true since the time window in the directional causality criterion is proportional to the transverse distance between two hits. Examples of two PhysicsEvents, one triggered by a muon and the other by random optical background, are shown in figure 6.5. The plot shows the triggered hits of both events in the transverse plane as solid and open stars respectively. The PMT positions and the maximum transverse area (i.e. a circle with diameter R_{max}) are shown as black dots and as a black circle for reference. The convex hull of each event is represented by the solid polygon surrounding all triggered hits. As can be seen, the number of triggered hits inside the convex hull is larger for the muon event than for the background event.

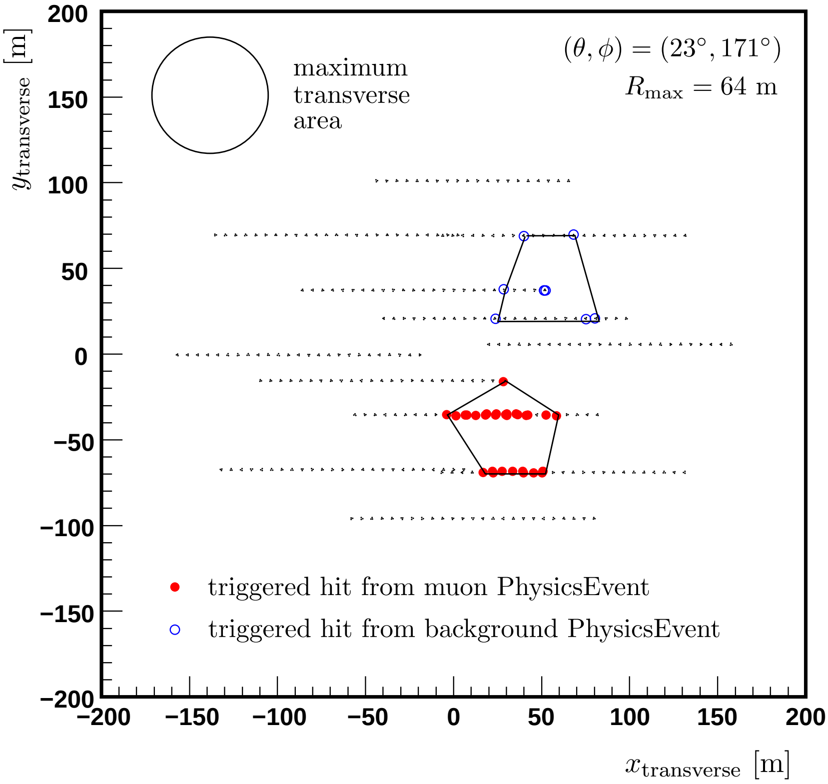

Figure 6.5: Examples of two PhysicsEvents, one triggered by a muon and the other by random optical background. The plot shows the triggered hits of both events in the transverse plane with respect to the source direction used in the trigger, $(\theta, \phi) = (23°, 171°)$, as solid and open circles respectively. The PMT positions and the maximum transverse area (i.e. a circle with diameter $R_{\rm max}$) are shown as black dots and as a black circle for reference. The convex hull of each event is shown as a solid polygon.

The surface area density of a PhysicsEvent is then defined as the dimensionless quantity

$$\varrho \equiv \sum_{i=0}^{n} a_i \cdot \frac{1}{A_{\text{c-hull}}} \cdot \frac{\pi \, (R_{\rm max}/2)^2}{n_{\rm min}} \tag{6.13}$$

where $A_{\text{c-hull}}$ is the convex hull of all triggered hits in the PhysicsEvent projected on the transverse plane. The contrast between muon events and random background events is further enhanced by taking into account the total charge of all triggered hits, $\sum_{i=0}^{n} a_i$, where a_i is the amplitude of triggered hit i in units of photo-electrons and n is the total number of triggered hits in the PhysicsEvent. The surface area density is transformed into a dimensionless quantity by multiplying by the maximum transverse area, $\pi(R_{\rm max}/2)^2$, and dividing by the minimum number of triggered

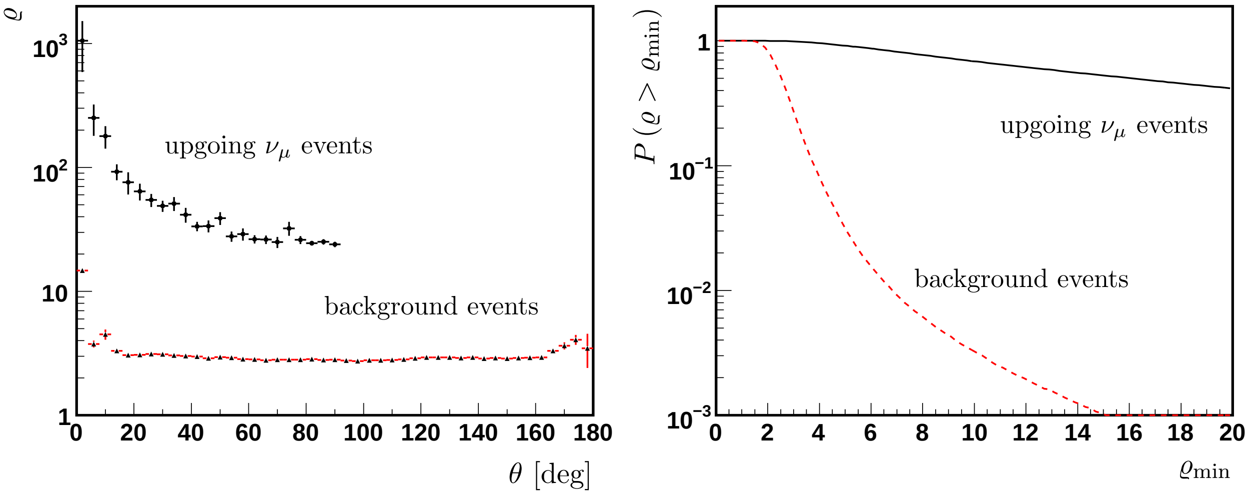

Figure 6.6: Left panel: The surface area density ϱ of upgoing muon-neutrino events and events due to random optical background, as a function of the zenith angle θ of the trigger direction. The default `triggerMX` algorithm was used, the random background was derived from data run 37218 (see next section, table 6.1). Right panel: The corresponding probability that $\varrho > \varrho_{\min}$ as a function of $\varrho_{\min}$.

single photon electrons, $n_{\min} \equiv$ `numberOfL0s` $+ 1$. The definition in equation (6.13) also takes into account the asymmetric PMT distribution in ANTARES, since the maximum transverse distance between two triggered hits, $R_{\max}(\theta)$, is a function of the zenith angle of the trigger direction θ.

The surface area density of upgoing muon-neutrino events and events due to random optical background is shown in the left panel of figure 6.6, as a function of the zenith angle θ of the trigger direction. In both cases the default values for all trigger parameters were used. The random background was derived from data run 37218 (see next section, table 6.1). The corresponding probability that $\varrho > \varrho_{\min}$ is shown in the right panel of figure 6.6, as a function of $\varrho_{\min}$. As can be seen in the left panel, the surface area density is still dependent on the trigger direction, even after normalising it with the θ-dependent maximum transverse area. Nevertheless, the surface area density ϱ for signal events is significantly larger than for random optical background events.

For a PhysicsEvent the minimum surface area density to pass the final selection step of the algorithm is determined by the parameter `qhullThreshold` (6.0). As can be seen in the right panel of figure 6.6, the random background can be suppressed by about two orders of magnitude by selecting only events with $\varrho > 6$, while less than 15 % of all upgoing muon-neutrino events are rejected.

Detector configuration	Line 1-5		Line 1-12	
Data run	**28712**	**29105**	**35428**	**37218**
Date	11/07/2007	16/08/2007	15/09/2008	18/11/2008
Baseline rate	63.1 kHz	84.1 kHz	84.9 kHz	63.2 kHz
Burst fraction	7 %	40 %	44 %	17 %
Active PMT fraction	90.3 %	83.3 %	84.9 %	80.5 %

Table 6.1: Data runs used to simulate the random optical background. The baseline rate corresponds to the average PMT counting rate of all PMTs that were active during the run. The burst fraction corresponds to the fraction of time for which the PMT counting rates were more than 20 % higher than the baseline rate. The active PMT fraction is the average ratio of active PMTs over total number of PMTs during the run. More details can be found in Appendix A.

6.2 Trigger performance

The performance of a trigger algorithm can be summarised in terms of efficiency to detect a muon, susceptibility to random optical background and processing speed. In this section, the performance of the standard trigger and the source tracking trigger are assessed using a full simulation of the detector response to atmospheric muons and muon-neutrinos, including random optical background. The atmospheric muon and muon-neutrino generation is done using `MUPAGE v3r4` [99] and `Genhen v5r2` [100], respectively. The particle propagation and PMT response are simulated using `KM3 v3r6` [101] and `Geasim v4r10` [102], for muons and hadronic showers respectively. The random optical background is simulated according to the actual PMT counting rates as measured during data-taking. The data runs used for this purpose are given in table 6.1, more details are given in Appendix A. The simulation of the ARS response and the trigger algorithms is done using `TriggerEfficiency` and `TriggerProcessor` [103]. The simulated ARS thresholds are all assumed to be equal and set at 0.3 photo-electrons. In the decoding of the ARS data, the default values for all calibration parameters are used. The detector lines are assumed to be perfectly vertical in all simulation steps described above.

6.2.1 Accidental trigger rate

The susceptibility of a trigger algorithm to random optical background can be quantified by the accidental trigger rate. The accidental trigger rate of an algorithm is defined as the rate of events found by the algorithm which are caused by random background hits. A first estimate can be made by considering the rate of clusters found by the algorithm which are caused by accidental coincidences of random background hits, without taking into account the causality of individual hit pairs. The accidental cluster rate can be estimated by considering the k-fold coincidence rate R_k among n different sources

$$R_k \;=\; \frac{k}{\Delta t} \cdot \binom{n}{k} \cdot (R_1\,\Delta t)^k \cdot (1 \,-\, R_1\,\Delta t)^{n-k} \tag{6.14}$$

if $R_1\,\Delta t \ll 1$, where Δt is the coincidence time window and R_1 is the counting rate of each of the sources. For instance, the accidental L1 rate R_{L1} due to hits that are detected within a local coincidence window Δt_l by more than one PMT on the same storey is

$$R_{\mathrm{L1}} \;=\; \frac{2}{\Delta t_l} \cdot \binom{3}{2} \cdot (R_{\mathrm{L0}}\,\Delta t_l)^2 \cdot (1 \,-\, R_{\mathrm{L0}}\,\Delta t_l) \;+\; \frac{3}{\Delta t_l} \cdot \binom{3}{3} \cdot (R_{\mathrm{L0}}\,\Delta t_l)^3 \tag{6.15}$$

where R_{L0} is the PMT counting rate. Hence, for $\Delta t_l = \pm 20$ ns and $R_{\mathrm{L0}} = 100$ kHz, the accidental L1 rate R_{L1} is 1.2 kHz per storey. Using equation (6.15), the rate of accidental clusters with at least 5 L1 hits within a cluster time window Δt_c in ANTARES, $R_{\mathrm{L1}\times 5}$, can be written as

$$\begin{aligned} R_{\mathrm{L1}\times 5} \;=\; \sum_{k=5}^{295} R_k \;&=\; \frac{5}{\Delta t_c} \cdot \binom{295}{5} \cdot (R_{\mathrm{L1}}\,\Delta t_c)^5 \cdot (1 \,-\, R_{\mathrm{L1}}\,\Delta t_c)^{290} \\ &\quad+ \frac{6}{\Delta t_c} \cdot \binom{295}{6} \cdot (R_{\mathrm{L1}}\,\Delta t_c)^6 \cdot (1 \,-\, R_{\mathrm{L1}}\,\Delta t_c)^{289} \\ &\quad+ \;\ldots \end{aligned} \tag{6.16}$$

since the total number of storeys equipped with PMTs in ANTARES is 295. Similarly, the rate of accidental clusters with at least 1 L1 hit and 5 L0 hits within a cluster time window Δt_c in ANTARES, $R_{\mathrm{L1+L0}\times 5}$, is

$$\begin{aligned} R_{\mathrm{L1+L0}\times 5} \;&=\; 295 \cdot R_{\mathrm{L1}} \cdot \sum_{k=5}^{885} R_{\mathrm{L0}\times\mathrm{k}} \\ &=\; 295 \cdot R_{\mathrm{L1}} \cdot \frac{5}{\Delta t_c} \cdot \binom{885}{5} \cdot (R_{\mathrm{L0}}\,\Delta t_c)^5 \cdot (1 \,-\, R_{\mathrm{L0}}\,\Delta t_c)^{880} \\ &\quad+ 295 \cdot R_{\mathrm{L1}} \cdot \frac{6}{\Delta t_c} \cdot \binom{885}{6} \cdot (R_{\mathrm{L0}}\,\Delta t_c)^6 \cdot (1 \,-\, R_{\mathrm{L0}}\,\Delta t_c)^{879} \\ &\quad+ \;\ldots \end{aligned} \tag{6.17}$$

since the total number of PMTs in ANTARES is 885.

The accidental cluster rates of the `trigger3N` and `triggerMX` algorithms are given by equation (6.16) and equation (6.17) respectively, and are shown in figure 6.7 for different cluster time windows. The cluster time window Δt_c that should be considered

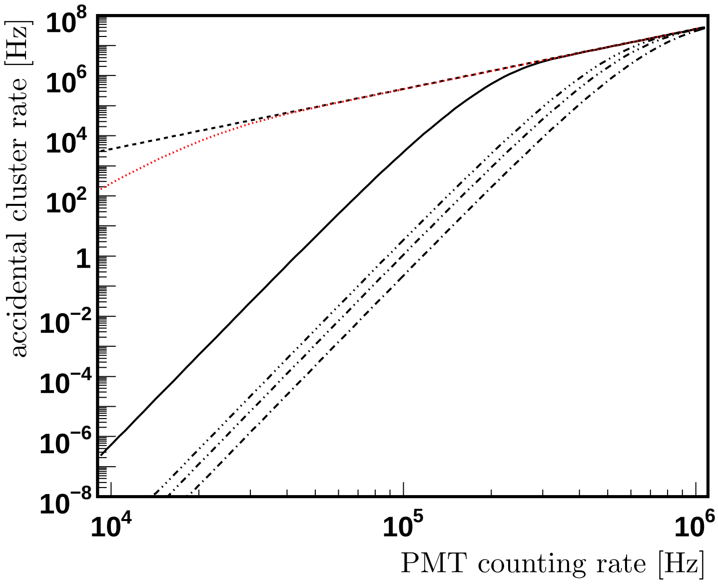

Figure 6.7: Accidental cluster rates in ANTARES, due to accidental coincidences of random background hits without taking into account causality, for $\Delta t_l = \pm 20$ ns.

depends on the maximum transverse distance that is used (see equation (6.5)), e.g. a maximum transverse distance of 90 m corresponds to a cluster time window of 270 ns. As expected from equation (6.15) and equation (6.16), the $R_{\mathrm{L1}\times 5}$ rates rise with the tenth power of the PMT counting rate, until they reach the total R_{L1} rate summed over all storeys which rises with the square of the PMT counting rate. For $R_{\mathrm{L0}} = 100$ kHz and $\Delta t_c = \pm 270$ ns, the accidental cluster rates $R_{\mathrm{L1}\times 5}$ and $R_{\mathrm{L1+L0}\times 5}$ are about 1 Hz and 350 kHz respectively. By imposing the causality criterion on each hit pair in a cluster, the cluster rate will decrease by about two orders of magnitude or so. The accidental trigger rate of the `trigger3N` algorithm therefore becomes lower than the (irreducible) trigger rate due to atmospheric muons (see section 6.2.3), for $R_{\mathrm{L0}} < 200$ kHz. In contrast, the accidental cluster rate of the `triggerMX` algorithm is still significantly higher. Hence the additional track fit and surface area density requirements in the `triggerMX` algorithm.

The accidental trigger rate of the `triggerMX` algorithm is shown in figure 6.8 as a function of the zenith angle θ (left panels) and azimuth angle ϕ (right panels) of the trigger direction, for different optical background conditions and detector configurations (see table 6.1). The corresponding data rate is indicated on the right axes, assuming an average PhysicsEvent size of 2.5 kB [1]. The zenith angle distribution is averaged over azimuth, and vice versa. The average accidental trigger rates are indicated by markers, the statistical errors are shown in different shades of grey. As can be seen, the accidental trigger rate for background conditions according to data runs 29105 and 35428 is more than an order of magnitude higher than for background conditions according to data runs 28712 and 37218, for the 5 and 12 detector line configuration respectively. The

[1]The size of a PhysicsEvent is mainly determined by the size of the snapshot and hence the parameter `maxEventTime`, and the average PMT counting rate R_{L0}. For `maxEventTime` $= 2.2$ μs and $R_{\mathrm{L0}} = 100$ kHz, the average number of hits in a PhysicsEvent is about 400. In that case, the PhysicsEvent size is about 2.5 kB, since each hit constitutes 6 bytes.

Line 1-5 detector configuration:

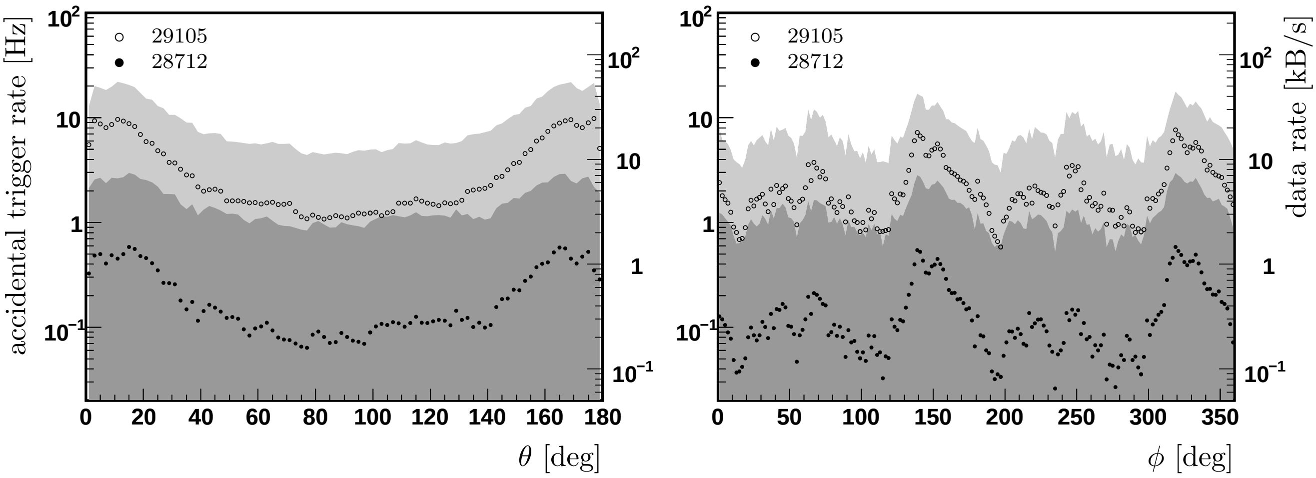

Line 1-12 detector configuration:

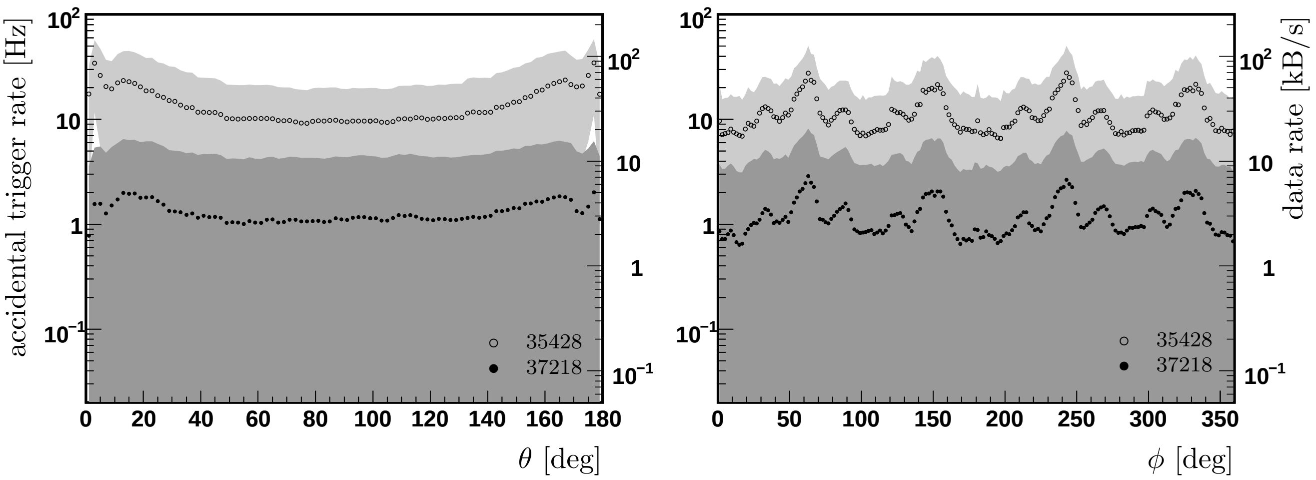

Figure 6.8: The accidental trigger rate of the `triggerMX` algorithm as a function of the zenith and azimuth angles of the trigger direction, θ and ϕ, for different optical background conditions and detector configurations (see table 6.1). The corresponding data rate is indicated on the right axes, assuming an average PhysicsEvent size of 2.5 kB.

top left panel shows that the accidental trigger rate is approximately symmetric with respect to $\theta = 90°$, as expected. Although the maximum transverse distance used in the algorithm is corrected with the factor $(1 - \frac{1}{4}\cos^2(\theta))$, the accidental trigger rate is still dependent on the zenith angle of the source. In general, it is enhanced for vertical directions. Furthermore, the accidental trigger rate is dependent on the azimuth angle of the source, as can be seen from the top right panel. The peak locations and the 180° periodicity of the azimuthal distribution indicate a significant correlation between azimuth angles of the source direction and horizontal directions for which neighbouring detector lines are aligned. For instance, the peaks at $\phi \approx 63°$, 243° and $\phi \approx 153°$, 333°

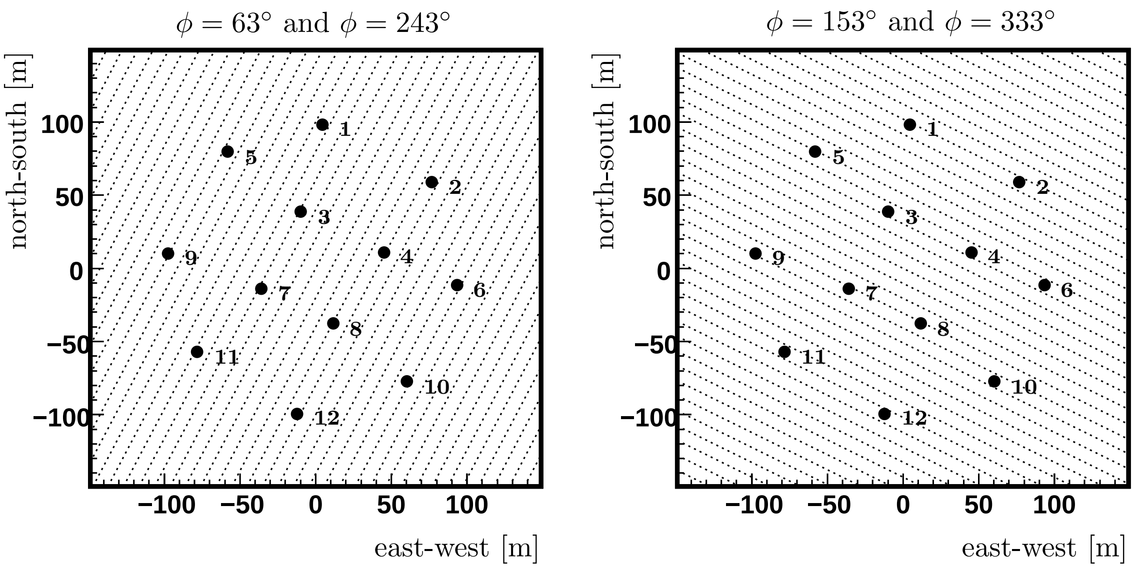

Figure 6.9: Azimuth angles for which the accidental trigger rate of the `triggerMX` algorithm is enhanced, due to alignment of neighbouring detector lines and the source direction used in the trigger algorithm.

correspond to the horizontal directions shown in the left and right panels of figure 6.9 respectively.

6.2.2 Processing speed

The performance of the trigger algorithm in terms of processing speed can be quantified by considering the time needed to process a single timeslice of data on a single CPU. The results in this section are obtained by running the trigger algorithms on a computer farm composed of *Intel Xeon E5335* 2.0 GHz CPUs and by considering a timeslice length of 104.8576 ms.

The CPU processing time per timeslice of the `trigger3N` algorithm is listed in

Detector configuration	Line 1-5		Line 1-12	
Data run	**28712**	**29105**	**35428**	**37218**
CPU time / timeslice	111 ± 4 ms	169 ± 14 ms	371 ± 14 ms	248 ± 8 ms
minimum number of CPUs	2	2	4	3

Table 6.2: The CPU processing time per timeslice of the `trigger3N` algorithm on an *Intel Xeon E5335* 2.0 GHz CPU, for different optical background conditions and detector configurations (see table 6.1). The duration of a timeslice is 104.8576 ms.

Line 1-5 detector configuration:

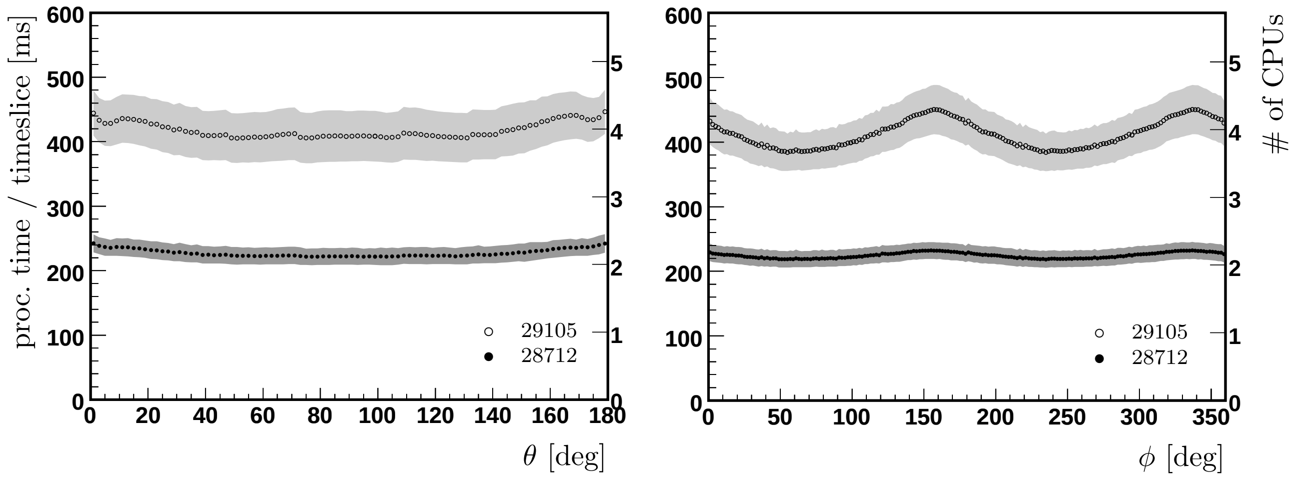

Line 1-12 detector configuration:

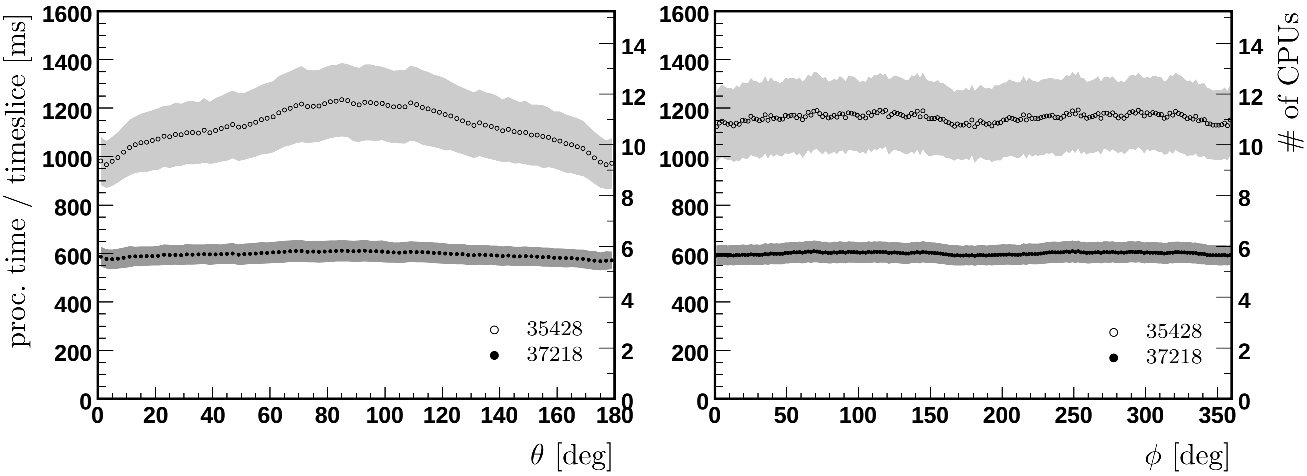

Figure 6.10: The CPU processing time per timeslice of the `triggerMX` algorithm on an *Intel Xeon E5335* 2.0 GHz CPU as a function of the zenith and azimuth angles of the trigger direction, θ and ϕ, for different optical background conditions and detector configurations (see table 6.1). The duration of a timeslice is 104.8576 ms. The corresponding total number of CPUs needed for real time data processing is indicated on the right axes.

table 6.2, for different optical background conditions and detector configurations (see table 6.1). Hence, 2 CPUs are sufficient for real time processing all data from ANTARES in its 5 detector line configuration, while 3 - 4 CPUs suffice for the complete ANTARES detector, for the background conditions considered here.

The CPU processing time per timeslice of the `triggerMX` algorithm is shown in figure 6.10 as a function of the zenith angle θ (left panels) and the azimuth angle ϕ (right panels) of the trigger direction. The corresponding total number of CPUs needed for real time data processing is indicated on the right axes. The zenith angle distributions

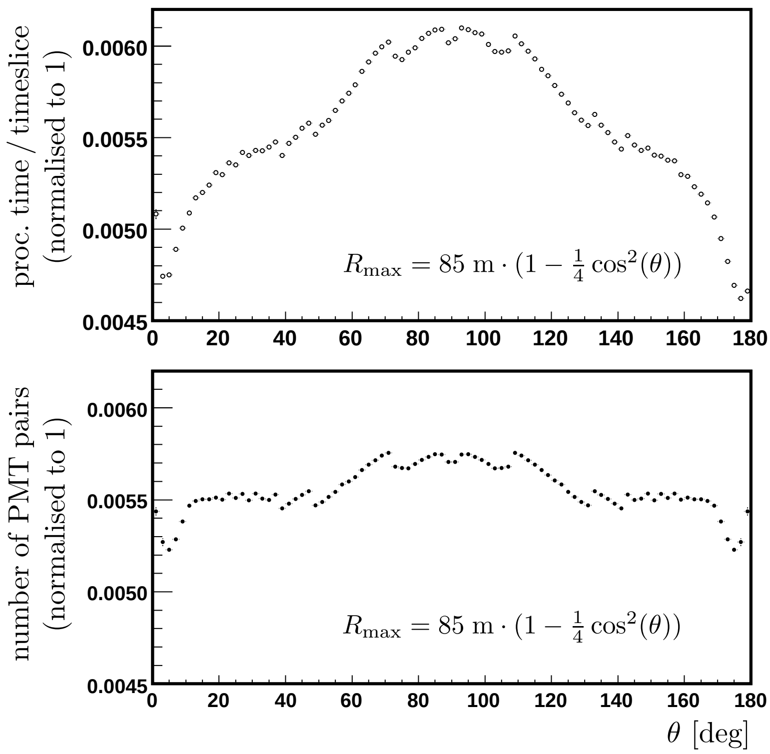

Figure 6.11:

Top panel: The CPU processing time per timeslice of the `triggerMX` algorithm as a function of the zenith angle θ, normalised to 1. Background conditions according to data run 35428 are assumed (see figure 6.10).

Bottom panel: The number of PMT pairs that can be causally correlated according to the directional causality criterion used in the `triggerMX` algorithm as a function of the zenith angle θ (see figure 6.3), normalised to 1.

are averaged over azimuth, and vice versa. The average processing times are indicated by markers, the statistical errors are shown in different shades of grey.

As can be seen from the top panels of figure 6.10, for the 5 detector line configuration, the time needed to process a single 104.8576 ms timeslice containing background hits according to data runs 28712 and 29105 is about 250 and 450 ms respectively. Hence, less than 5 CPUs are needed to process all data in real time for these background conditions. For the 12 detector line configuration, the time needed to process a single timeslice containing background hits according to data runs 35428 and 37218 is about 1200 and 600 ms respectively. Therefore, 14 CPUs are sufficient to process all data from ANTARES in real time for the background conditions considered here. For the 5 detector line configuration, the processing time has a small dependence on the azimuth angle of the source. This can be attributed to the asymmetrical layout of the 5 detector line configuration with respect to the azimuth. The processing time has a maximum at $\phi \approx 153°$, $333°$, which corresponds to the azimuth angle with the largest number of PMT pairs which can be causally correlated according to the directional causality criterion in the 5 detector line configuration (see figure 6.9). Similarly, the processing time of the `triggerMX` algorithm has a small dependency on the zenith angle of the source, despite the correction factor $(1 - \frac{1}{4}\cos^2(\theta))$ in the maximum transverse distance used in the algorithm. The correlation between the processing time and the number of PMT pairs that can be causally correlated according to the directional causality criterion in the 12 detector line configuration (see figure 6.3) is shown as a function of zenith angle θ in more detail in figure 6.11, in which both quantities are normalised to 1 for comparison. The number of possible PMT pairs was calculated for the complete ANTARES detector, whereas in the calculation of the processing time

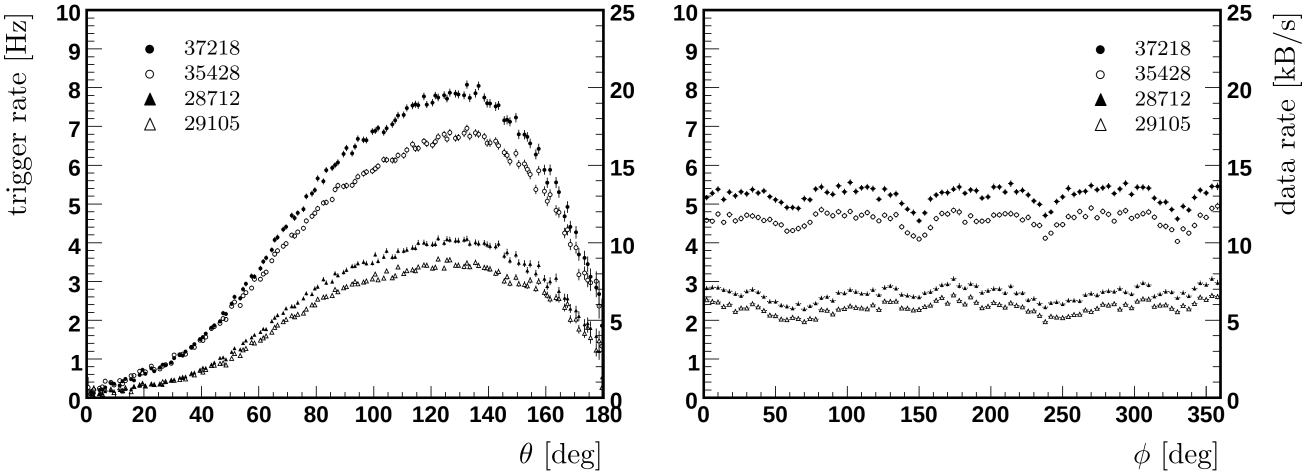

Figure 6.12: Trigger rate of the `triggerMX` algorithm due to atmospheric muons as a function of the zenith and azimuth angles of the trigger direction, θ and ϕ, for different optical background conditions and detector configurations (see table 6.1). The corresponding data rate is indicated on the right axes, assuming an average PhysicsEvent size of 2.5 kB.

the number of active PMTs during run 35428 was taken into account.

6.2.3 Atmospheric muons

The trigger rate due to atmospheric muons constitutes an irreducible data rate in the ANTARES data acquisition system. The trigger rates of the `trigger3N` and `triggerMX` algorithms for different optical background conditions and detector configurations (see table 6.1) are deduced using a simulated sample of atmospheric muons generated with the `MUPAGE v3r4` generator [99]. In the generation, only bundles with $95° \leq \theta_\mu \leq 180°$ and muon multiplicity smaller than 100 are considered, and a muon bundle energy threshold of 1 GeV is assumed.

For the `trigger3N` algorithm, the atmospheric muon trigger rates in the 5 and 12 detector line configuration are about 1.7 Hz and 4.3 Hz, respectively. These trigger rates correspond to a continuous data rate of 4.3 kB/s and 10.8 kB/s respectively, assuming an average PhysicsEvent size of 2.5 kB.

For the `triggerMX` algorithm, the atmospheric muon trigger rates are shown in figure 6.12 as a function of the zenith angle θ (left panel) and azimuth angle ϕ (right panel) of the trigger direction, for different optical background conditions and detector configurations. The corresponding data rate is indicated on the right axes, assuming an average PhysicsEvent size of 2.5 kB. The zenith angle distribution is averaged over azimuth, and vice versa. The statistical errors on the average trigger rates are indicated by the error bars. Additionally, the Monte Carlo expectation has considerable systematic errors due to various uncertainties in the simulation method, which are not indicated in figure 6.12. A detailed study of the uncertainties in the knowledge of the environmental parameters (i.e. the light absorption and scattering length in water) and the uncertainties on the description of the detector (i.e. the angular dependence of the detection efficiency of an optical module and the PMT effective area) leads to an overall systematic error of $^{+35\,\%}_{-30\,\%}$ after reconstruction [104]. Furthermore, uncertainties on the primary cosmic ray composition and hadronic interaction models result in an additional systematic error of about 50 %. As can be seen from figure 6.12, the trigger rate due to atmospheric muons is considerable higher for downward going trigger directions than for upward going directions, whereas it is approximately independent of the azimuth angle of the trigger direction. Furthermore, the trigger rate is slightly lower for high background rates (data runs 29105 and 35428) than for low background rates (data runs 28712 and 37218). This can be attributed to the smaller active PMT fraction and larger electronic deadtime induced by the higher background rates in the former data runs.

6.2.4 Trigger efficiency

The performance of the trigger algorithm in terms of its ability to detect a muon can be quantified by the trigger efficiency, defined as the probability that an event is accepted by the trigger algorithm. The trigger efficiency is derived using a simulated sample of atmospheric neutrinos generated with the `Genhen v5r6` generator [100]. In the generation, only (anti-) muon-neutrinos with $0° \leq \theta_\nu \leq 90°$ and $10\text{ GeV} \leq E_\nu \leq 10^7\text{ GeV}$ are considered, and an energy spectrum proportional to $E_\nu^{-1.4}$ is assumed. For the `triggerMX` algorithm, the neutrino direction is used as the trigger direction. The trigger efficiency is calculated with respect to events in which at least 5 PMTs in different LCMs detected a hit. Only the 12 detector line configuration is considered in this section.

The trigger efficiency of the `trigger3N` and `triggerMX` algorithms is shown in figure 6.13 as a function of various event properties: the number of different detector lines and LCMs in the event which detected a hit induced by the muon (top panels), and the total number of signal hits in the event (bottom panel). As can be seen from this figure, the trigger efficiency of the source tracking trigger is higher than for the standard trigger. This is due to the less stringent cluster size requirement of the former. For both algorithms the trigger efficiency is slightly lower for higher background rates, as expected.

The trigger efficiency of the `trigger3N` and `triggerMX` algorithms is shown in figure 6.14 as a function of the characteristics of the neutrino, for background conditions according to data run 37218. The top panels show the trigger efficiency as function of the neutrino energy E_ν for three different zenith angle ranges. The middle and bottom panels show the trigger efficiency as function of the zenith angle θ_ν and the azimuth angle ϕ_ν, for four different energy ranges. As can be seen, the trigger efficiency of both algorithms rises quickly with the neutrino energy (note the logarithmic scale of the horizontal axes in the top panels) until it settles down at about 60 percent at the highest neutrino energies considered here. In general, the `triggerMX` algorithm is more efficient in accepting neutrinos than the `trigger3N` algorithm, especially in the lower energy regime. The trigger efficiency of both algorithms has a moderate dependence

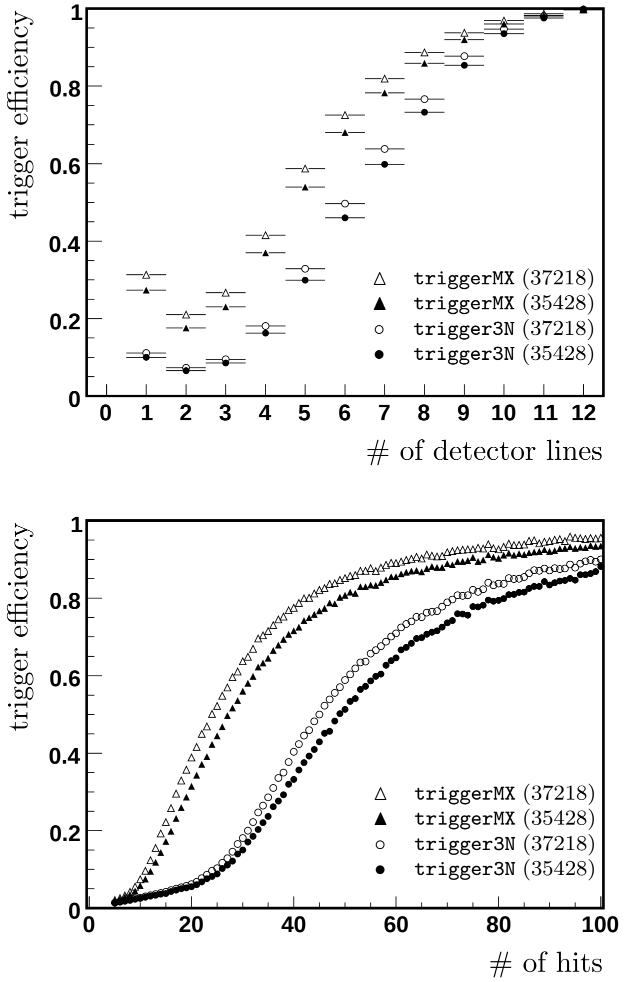

Figure 6.13:

The trigger efficiency of the `trigger3N` and `triggerMX` algorithms as a function of various event properties: the number of detector lines and LCMs in the event which detected a hit caused by the neutrino-induced muon (top panels), and the total number of signal hits in the event (bottom panel), for different background conditions.

on the zenith angle of the neutrino. Upgoing neutrinos are accepted more easily than horizontal neutrinos, especially in the lower energy regime. The trigger efficiency of both algorithms is approximately independent of the azimuth angle of the neutrino. A simulation using background conditions according to data run 35428 leads to similar but slightly lower results than are shown in figure 6.14.

The trigger efficiency dependence of both algorithms on the neutrino energy is shown in more detail in figure 6.15, which shows the trigger efficiency of both algorithms as a function of the energy, averaged over all upgoing neutrino directions, for high and low background rates (left panel). For comparison, the ratio of the trigger efficiencies of both algorithms is shown in the right panel. As can be seen, the `triggerMX` algorithm is more efficient than the `trigger3N` algorithm, especially in the lower energy regime. At $E_\nu = 10$ GeV, the trigger efficiency of the standard trigger is more or less zero while for the source tracking trigger it is still around 20 percent. The gain in efficiency is about a factor of 3 at $E_\nu = 100$ GeV, after which the gain slowly decreases with energy until both algorithms become more or less equally efficient at 60 percent for the highest energies considered here. These conclusions hold for both background conditions considered in this section.

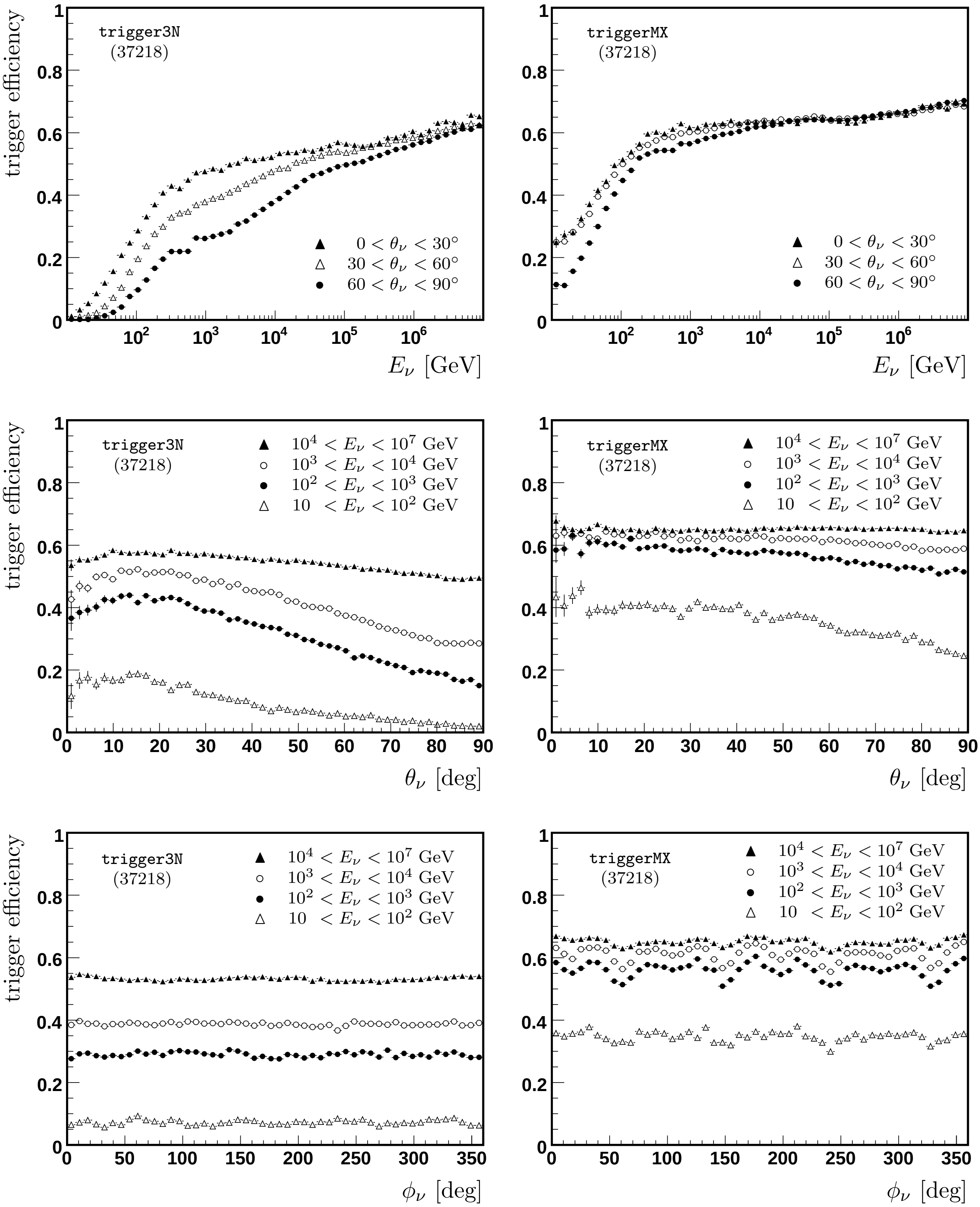

Figure 6.14: The trigger efficiency of the `trigger3N` and `triggerMX` algorithms (left and right panels), as a function of the neutrino energy E_ν (top panels), the neutrino zenith angle θ_ν (middle panels) and the neutrino azimuth angle ϕ_ν (bottom panels), for background conditions according to data run 37218.

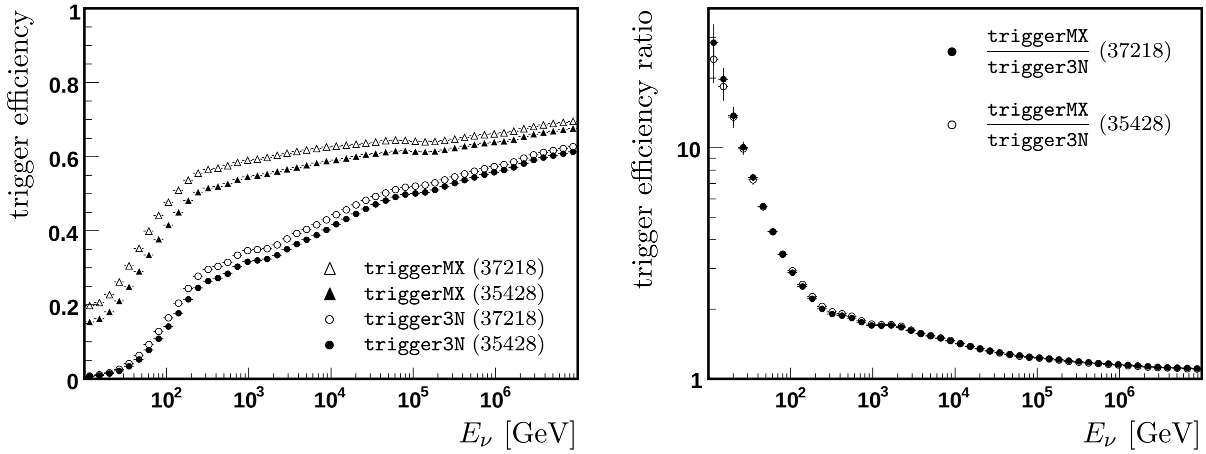

Figure 6.15: The trigger efficiency of the `trigger3N` and `triggerMX` algorithms as a function of the neutrino energy E_ν, averaged over all upgoing neutrino directions for different optical background conditions (left panel). The corresponding ratio of the trigger efficiencies of both algorithms is shown in the right panel.

6.2.5 Hit efficiency and purity

The quality of a trigger algorithm in terms of the number of signal and background hits in the events that are accepted by the trigger algorithm can be quantified by the hit efficiency and purity of its triggered events. These are defined as

$$\begin{aligned} \text{hit efficiency} &= \frac{\text{total \# of triggered signal hits}}{\text{total \# of signal hits}} \\ \text{hit purity} &= \frac{\text{total \# of triggered signal hits}}{\text{total \# of triggered hits}} \end{aligned} \tag{6.18}$$

In these definitions, a signal hit is defined as a hit which is directly or indirectly caused by a neutrino-induced (anti-)muon, i.e. a hit caused by an unscattered or scattered photon, which originates from the muon or from an electromagnetic shower induced by the muon. A triggered hit is defined as any hit, signal or background, which is accepted by the trigger algorithm. In this section, the hit efficiency and purity of the `trigger3N` and `triggerMX` algorithms are calculated using the same simulated sample of atmospheric neutrinos as described in the previous section. Only events in which at least 5 PMTs in different LCMs detected a signal hit and which were accepted by the trigger algorithm are considered.

The hit efficiency and purity of the `trigger3N` and `triggerMX` algorithms for high and low background rates are shown in the top and bottom panels of figure 6.16 respectively, as a function of the neutrino energy E_ν (left panels), the number of signal hits in the event (top right panel), and the total number of triggered hits in the event (bottom

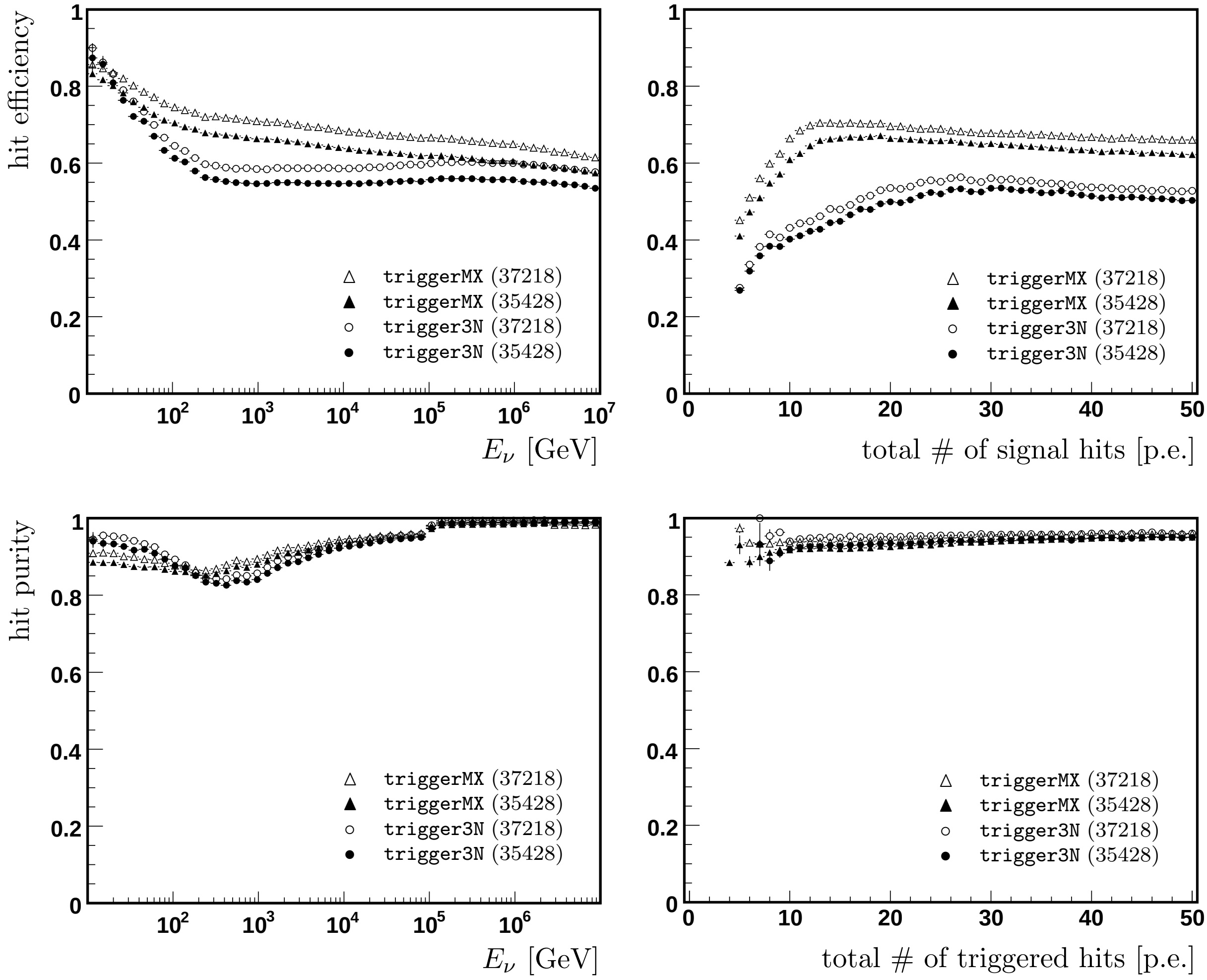

Figure 6.16: The hit efficiency and purity of the `trigger3N` and `triggerMX` algorithms for high and low background rates as a function of the neutrino energy E_ν (left panels), the number of signal hits in the event (top right panel), and the total number of triggered hits in the event (bottom right panel).

right panel). As can be seen from the top left panel, more than 80 percent of all signal hits are found by both algorithms in the low energy regime. The hit efficiency of the `trigger3N` algorithm rapidly decreases to about 60 percent in the high energy regime. So does the hit efficiency of the `triggerMX` algorithm, but it does so more gradually. The latter is particularly higher for events with a small number of signal hits, as is evident from the top right panel. The bottom panels show that the hit purity is more than 80 percent for both algorithms, for all neutrino energies considered here. In the high energy regime the hit purity increases to more than 95 percent, indicating that the majority of the triggered hits originate from the muon. To conclude, although the fraction of signal hits that is triggered decreases slowly with energy, those hits that are triggered are very likely signal hits. As can be seen from all panels in figure 6.16, the hit efficiency and purity decrease slightly for higher background rates.

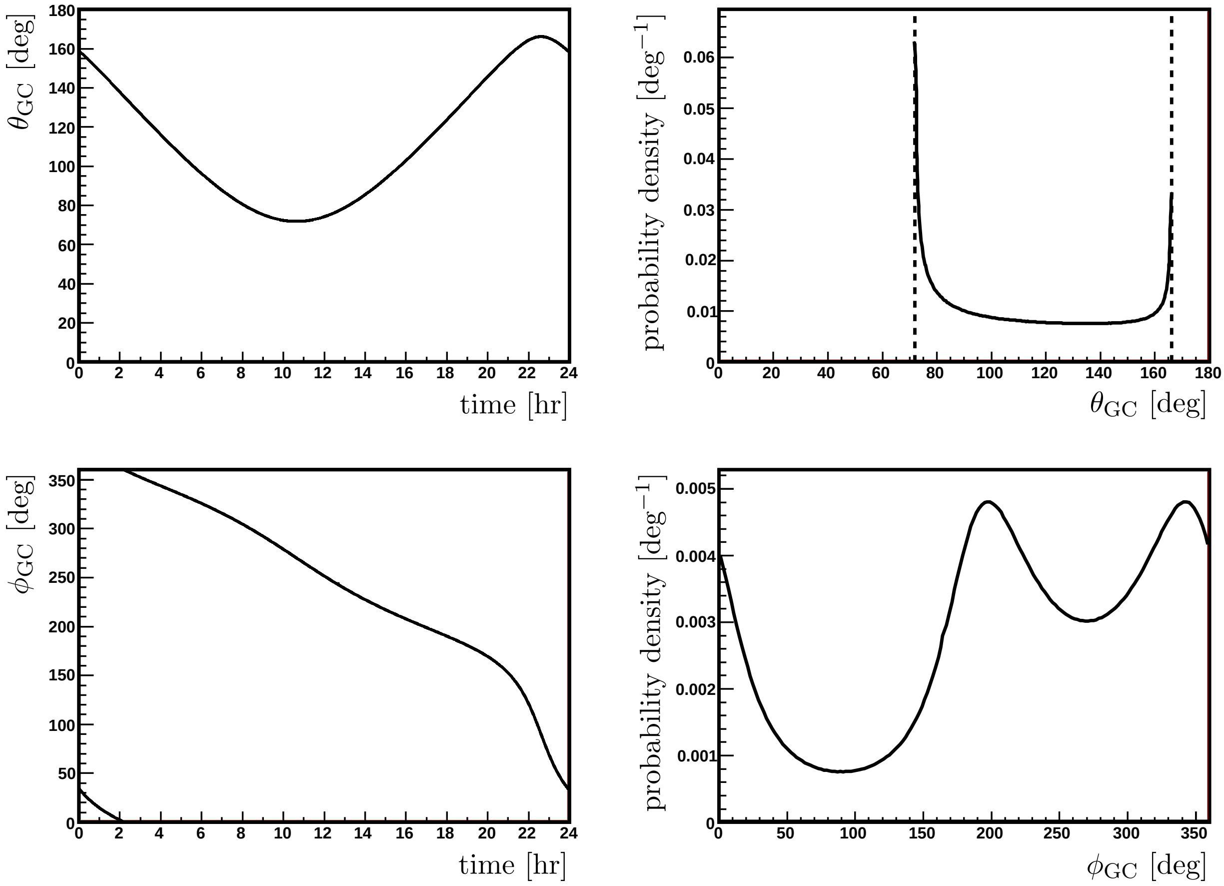

Figure 6.17: Left panels: The zenith and azimuth angles of the Galactic Centre at ANTARES, θ_{GC} and ϕ_{GC}, as a function of time for an arbitrary day (01/01/2007). The corresponding probability densities of both angles during a sidereal day are shown in the right panels.

6.3 The Galactic Centre trigger

The source tracking trigger is currently used during data-taking to follow the Galactic Centre (GC). The time of the timeslice is used to calculate the direction of the GC at the ANTARES site as explained in Appendix B, which is used to process the timeslice using the `triggerMX` algorithm. The zenith and azimuth angles of the GC at ANTARES are shown as a function of time for an arbitrary day (01/01/2007) in the left panels of figure 6.17. Both angles are periodical functions of time due to the rotation of the Earth, with a time period equal to one sidereal day. Hence both angles follow the same path as shown in the left panels of figure 6.17 for any day, except for a translation in time. The corresponding probability densities of both angles during a sidereal day are shown in the right panels of figure 6.17. The zenith angle range of the GC at ANTARES is [71.8°, 166.2°], as expected from the latitude of the ANTARES site and the declination of the GC (see figure 6.4).

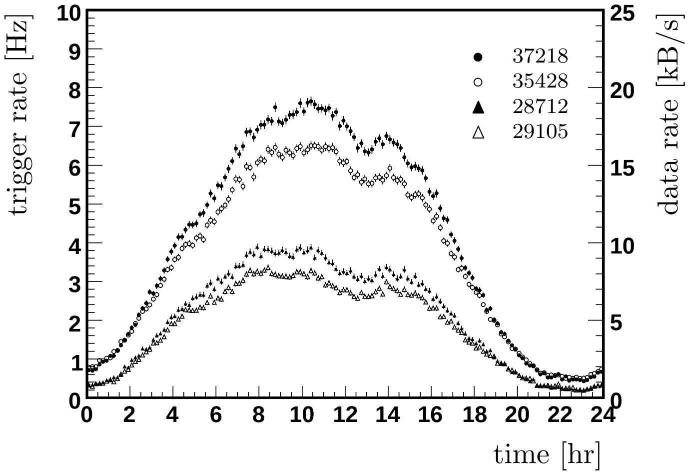

Figure 6.18:

The trigger rate of the GC trigger due to atmospheric muons as a function of time on 01/01/2007. The corresponding data rate is indicated on the right axis, assuming an average PhysicsEvent size of 2.5 kB.

6.3.1 Performance

In this section, the behaviour of the GC trigger is evaluated as a function of time. All results in this section refer to the first day of 2007. The direction of the GC on this day is shown in figure 6.17. Different optical background conditions and detector configurations are considered, see table 6.1.

Atmospheric muons

The trigger rate of the GC trigger due to atmospheric muons is shown in figure 6.18 as a function of time on 01/01/2007. The corresponding data rate is indicated on the right axis, assuming an average PhysicsEvent size of 2.5 kB. The statistical errors on the average trigger rate are indicated by the error bars. There is also a significant systematic error, as explained in section 6.2.3. As can be seen, the trigger rate is significantly enhanced around $t = 10$ hr 39 min, when the GC zenith angle is around its minimum (i.e. above the horizon), as expected from figure 6.12.

Accidental trigger rate

The accidental trigger rate of the GC trigger due to random background hits is shown in the top panels of figure 6.19 as a function of time on 01/01/2007. The corresponding data rate is indicated on the right axes, assuming an average PhysicsEvent size of 2.5 kB. The average accidental trigger rates are indicated by markers, the statistical errors are shown in different shades of grey. As can be seen, the accidental trigger rate for high background conditions (data runs 29105 and 35428) is more than an order of magnitude higher than for low background conditions (data runs 28712 and 37218). The accidental trigger rate is significantly enhanced around $t = 21$ hr and $t = 23$ hr 6 min. On this particular day, these times correspond to $(\theta_{\mathrm{GC}}, \phi_{\mathrm{GC}}) = (156°, 153°)$ and $(165°, 63°)$ respectively. Hence, the accidental trigger rate is enhanced because both zenith angles are close to the maximum zenith angle ($t = 22$ hr 36 min), and in addition the azimuth angles correspond to the horizontal directions in which multiple neighbouring detector lines are aligned (see figure 6.9).

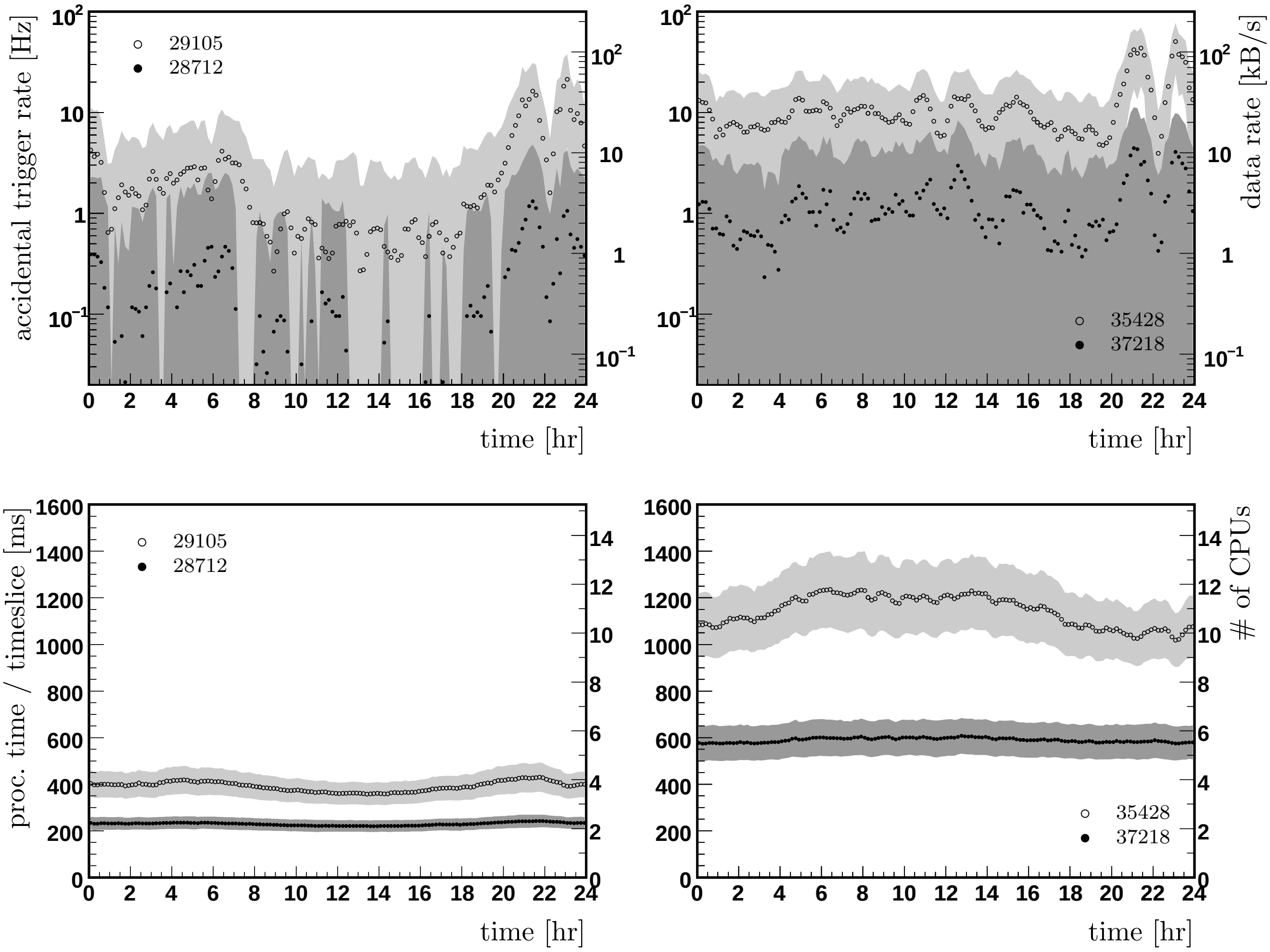

Figure 6.19: Top panels: The accidental trigger rate of the GC trigger as a function of time on 01/01/2007. The corresponding data rate is indicated on the right axes, assuming an average PhysicsEvent size of 2.5 kB.

Bottom panels: The CPU processing time per timeslice of the GC trigger on an *Intel Xeon E5335* 2.0 GHz CPU as a function of time on 01/01/2007, for a 104.8576 ms timeslice window. The corresponding total number of CPUs needed for real time data processing is indicated on the right axes.

Processing time

The CPU processing time per timeslice of the GC trigger on an *Intel Xeon E5335* 2.0 GHz CPU is shown in the bottom panels of figure 6.19 as a function of time on the same day, for a 104.8576 ms timeslice window. The corresponding total number of CPUs needed for real time data processing is indicated on the right axes. As can be seen, 14 CPUs are sufficient to process all data from ANTARES in real time for the background conditions considered here.

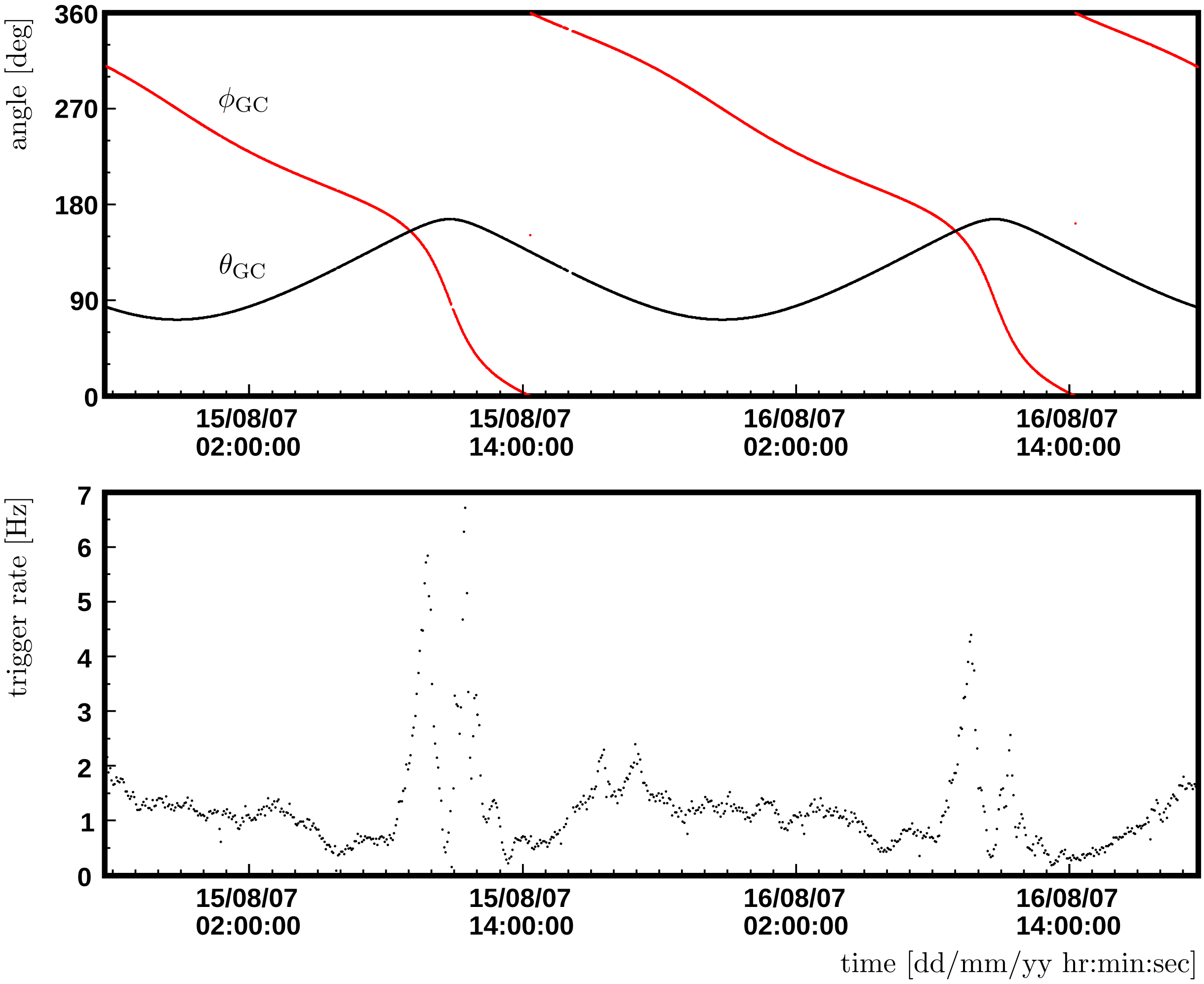

Figure 6.20: Bottom panel: The GC trigger rate during a 48 hr data-taking period when ANTARES was operational in its 5 detector line configuration (data runs 29098 until 29112). Top panel: The zenith angle $\theta_{\rm GC}$ and azimuth angle $\phi_{\rm GC}$ of the GC at ANTARES during the same period.

6.3.2 Data analysis

In this section, a comparison between the Monte Carlo expectations from the previous section and data taken with the GC trigger is made. Two 48 hr data-taking periods are chosen, when the GC trigger was active and the ANTARES detector was operational in its 5 and 12 detector line configuration: 15-16/08/07 and 23-24/12/08. The GC trigger rate and the direction of the GC at ANTARES during these periods are shown in figure 6.20 and figure 6.21 respectively.

The periodic behaviour of the GC trigger is obvious from both figures. As can be seen from figure 6.20, there is a significant enhancement in the GC trigger rate around $t = 11$ hr on both days. The enhancement and the double peak structure are due to random background, as expected from figure 6.19: During these periods the GC zenith angle is around its maximum and the GC azimuth angle correspond to one

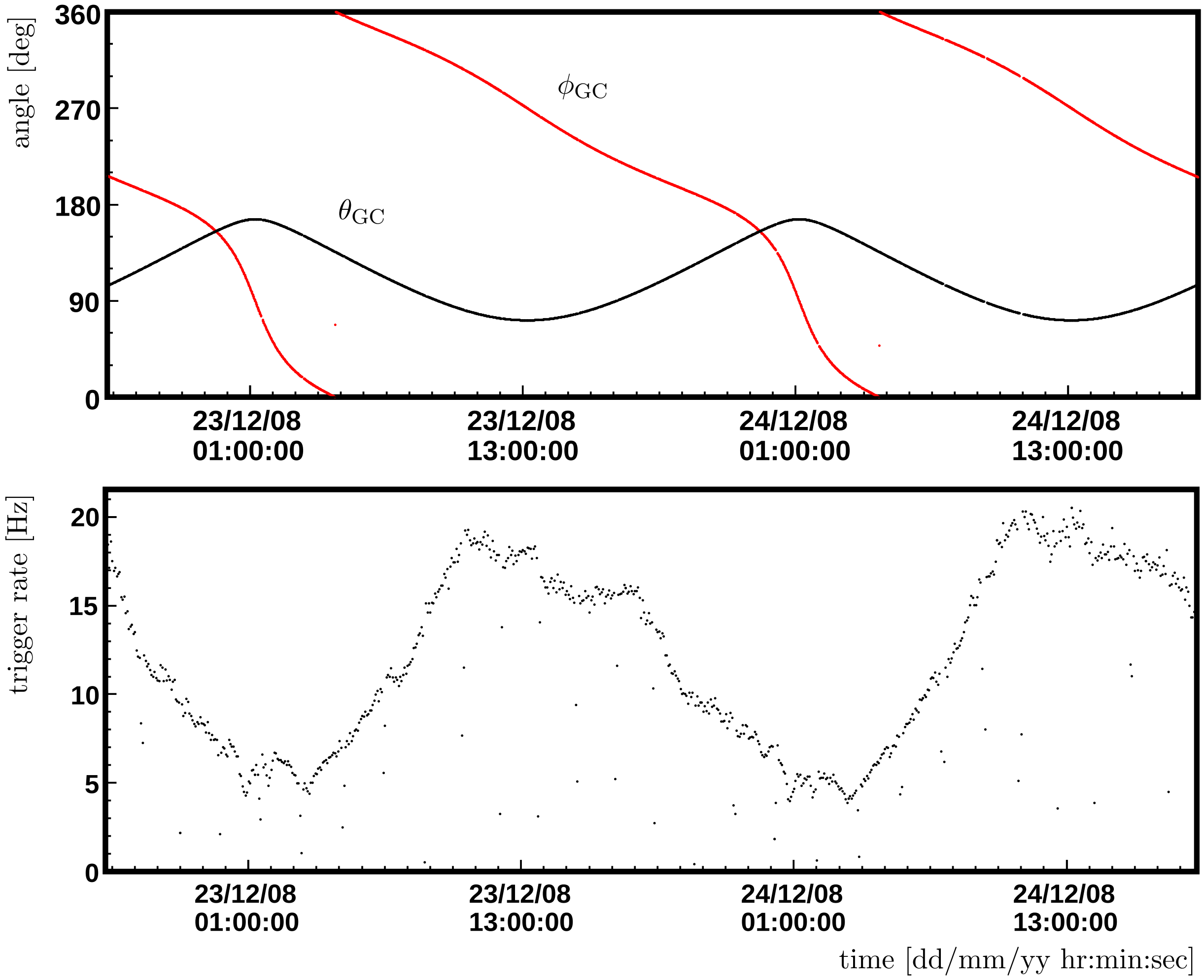

Figure 6.21: Bottom panel: The GC trigger rate during a 48 hr data-taking period when ANTARES was operational in its 12 detector line configuration (data runs 38052 until 38122). Top panel: The zenith angle θ_{GC} and azimuth angle ϕ_{GC} of the GC at ANTARES during the same period.

of the two horizontal directions shown in figure 6.9. A smaller enhancement in the GC trigger rate can be distinguished over a longer time interval 12 hours earlier/later around $t = 23$ hr, when the GC zenith angle is around its minimum. This is due to atmospheric muons, as expected from figure 6.18. Similar features in the GC trigger rate can be distinguished in figure 6.21. However, in this period the GC trigger rate is much higher when the GC is above the horizon than when it was at its maximum zenith angle. Hence, the atmospheric muon contribution to the GC trigger rate is much higher than the contribution due to random background during this data-taking period. Nonetheless, the magnitude of the GC trigger rate during both data-taking periods agree with the Monte Carlo expectations from atmospheric muons and random background, taking into account the uncertainties in the Monte Carlo simulation.

Chapter 7

Search for WIMP dark matter in the Sun and the GC with ANTARES

In this chapter, data from the ANTARES neutrino telescope are used to search for an excess of neutrinos from the Sun and the Galactic Centre, as an indication for the presence of dark matter. First, the analysis approach and the data selection are explained. Next, the necessary simulation methods and the offline data-processing steps are described. After a comparison between simulation results and data, final selection criteria are defined and the corresponding detection efficiency is calculated. Finally, data from the ANTARES neutrino telescope is analysed. The outcome is combined with the detection efficiency to draw a conclusion regarding the neutrino and muon flux from WIMP annihilation in the Sun and the Galactic Centre.

7.1 Analysis approach

A neutrino that undergoes a charged current interaction in the vicinity of a neutrino telescope produces a muon which can be detected as detailed in chapter 5. The relationship between the neutrino flux arriving at the surface of the Earth, Φ_ν, and the detection rate in a neutrino telescope, R_{det}, can be expressed as [105]

$$R_{\text{det}} = \iiint \frac{d^2\Phi_\nu(E,\hat{r})}{dE\,d\Omega}\, P_{\text{Earth}}(E,\hat{r})\, \rho(\vec{x})\, N_A\, \sigma_{\text{CC}}(E)\, P_{\text{det}}(E,\hat{r},\vec{x})\, dE\, d\Omega\, d\vec{x} \tag{7.1}$$

where E and $\hat{r}$ are the energy and direction of the neutrino flux and $\vec{x}$ is the position of the neutrino interaction. The integrand is composed of the following terms:

$\dfrac{d^2\Phi_\nu(E,\hat{r})}{dE\,d\Omega}$ **:** the differential neutrino flux arriving at the surface of the Earth $[\text{GeV}^{-1}\,\text{sr}^{-1}\,\text{m}^{-2}\,\text{s}^{-1}]$,

$P_{\text{Earth}}(E,\hat{r})$ **:** the probability of neutrino transmission through the Earth without any interactions,

$\rho(\vec{x})\,N_A$: the number of nucleons per unit volume [m^{-3}], expressed as the product of the nucleon molar density $\rho(\vec{x})$ and Avogadro's number N_A,

$\sigma_{\mathrm{CC}}(E)$: the total charged current neutrino-nucleon cross section [m^2],

$P_{\mathrm{det}}(E,\hat{r},\vec{x})$: the detection probability. This quantity depends on the outcome of the neutrino-nucleon interaction, the propagation and light emission of the muon in the vicinity of the detector, the instrumental characteristics of the detector, as well as the efficiency of all subsequent data-processing steps.

Equation (7.1) can be used to calculate the expected event rate for any given neutrino flux, provided all above-mentioned quantities are known. This is true for all terms, except for the detector-specific detection probability P_{det}. To evaluate this term, a detailed Monte Carlo simulation of the complete detection process is necessary. The simulation scheme is described in the following section. This is followed by a definition of the effective volume and neutrino effective area, which are measures for the detection efficiency. Finally, equation (7.1) will be applied to the neutrino flux from WIMP annihilation in an astrophysical object.

7.1.1 Simulation scheme

A Monte Carlo simulation of a process which can be represented by an intricate multi-dimensional integral such as equation (7.1) involves the evaluation of this integral by means of Monte Carlo integration. In this mathematical technique, random numbers are used to numerically evaluate an integral. Consider for instance the n-dimensional integral of some function $f(\boldsymbol{x})$, where $\boldsymbol{x} = (x_1, x_2, ..., x_n)$, over a part of the phase space $V = \{\boldsymbol{x}\,|\,a_1 < x_1 < b_1,\ a_2 < x_2 < b_2,\ \ldots,\ a_n < x_n < b_n\}$:

$$\int_{a_1}^{b_1}\int_{a_2}^{b_2}\cdots\int_{a_n}^{b_n} f(x_1, x_2, \ldots, x_n)\,dx_1\,dx_2\ldots dx_n \;\equiv\; \int_V f(\boldsymbol{x})\,d\boldsymbol{x} \tag{7.2}$$

This integral can be approximated by [106]

$$\int_V f(\boldsymbol{x})\,d\boldsymbol{x} \;\approx\; \frac{V_p}{N_{\mathrm{gen}}}\sum_{i=1}^{N_{\mathrm{gen}}}\frac{f(\boldsymbol{x}_i)}{p(\boldsymbol{x}_i)} \quad \text{with} \quad V_p \;\equiv\; \int_V p(\boldsymbol{x})\,d\boldsymbol{x} \tag{7.3}$$

where $\boldsymbol{x}_i$ are randomly sampled points from V which are distributed according to the probability density function $p(\boldsymbol{x})$, and N_{gen} is the generated number of points.

Hence the detection rate given by equation (7.1) can be approximated as

$$R_{\mathrm{det}} \;\approx\; \frac{V_E\,V_\Omega\,V_{\vec{x}}}{N_{\mathrm{gen}}}\sum_{i=1}^{N_{\mathrm{gen}}}\frac{d^2\Phi_\nu(E_i,\hat{r}_i)}{dE\,d\Omega}\,\frac{P_{\mathrm{Earth}}(E_i,\hat{r}_i)\;\rho(\vec{x}_i)N_A\;\sigma_{\mathrm{CC}}(E_i)\;P_{\mathrm{det}}(E_i,\hat{r}_i,\vec{x}_i)}{p_E(E_i)\;p_\Omega(\hat{r}_i)\;p_{\vec{x}}(\vec{x}_i)} \tag{7.4}$$

where V_E, V_Ω, $V_{\vec{x}}$ and $p_E(E)$, $p_\Omega(\hat{r})$, $p_{\vec{x}}(\vec{x})$ are the individual phase space terms and probability distribution functions which correspond to the sampling of the energy, direction and interaction point of the neutrino, respectively. $P_{\rm det}(E_i, \hat{r}_i, \vec{x}_i)$ is now discretely determined for each simulated event $(E_i, \hat{r}_i, \vec{x}_i)$. It has the value 1 for events that are detected and 0 for events that are not.

Typically, the neutrino direction and interaction point are sampled uniformly while the neutrino energy is sampled according to a power law spectrum, i.e. $p_E(E) \propto E^{-\gamma}$. In this case, the phase space terms are:

$$\begin{aligned} V_E &\equiv \int E^{-\gamma}\, dE &&= \begin{cases} (E_{\rm max}^{1-\gamma} - E_{\rm min}^{1-\gamma})/(1-\gamma) & \text{if} \quad \gamma \neq 1 \\ \ln(E_{\rm max}/E_{\rm min}) & \text{if} \quad \gamma = 1 \end{cases} \\ V_\Omega &\equiv \int d\Omega &&= (\phi_{\rm max} - \phi_{\rm min}) \cdot (\cos(\theta_{\rm max}) - \cos(\theta_{\rm min})) \\ V_{\vec{x}} &\equiv \int d\vec{x} &&\equiv V_{\rm gen} \end{aligned} \tag{7.5}$$

and equation (7.4) can be written as

$$R_{\rm det} \approx \frac{1}{N_{\rm gen}} \sum_{i=1}^{N_{\rm gen}} \frac{d^2\Phi_\nu(E_i, \hat{r}_i)}{dE\, d\Omega}\, w_i(E_i, \hat{r}_i, \vec{x}_i)\, P_{\rm det}(E_i, \hat{r}_i, \vec{x}_i) \tag{7.6}$$

where the so-called event weight w_i which belongs to a specific set of values $\{E_i, \hat{r}_i, \vec{x}_i\}$ is defined as

$$w_i(E_i, \hat{r}_i, \vec{x}_i) \equiv V_E\, V_\Omega\, V_{\rm gen}\, P_{\rm Earth}(E_i, \hat{r}_i)\, \rho(\vec{x}_i) N_A\, \sigma_{\rm CC}(E_i)\, E_i^\gamma \tag{7.7}$$

7.1.2 Detection efficiency

The simulation scheme described in the previous subsection can be used to evaluate the detection probability $P_{\rm det}$ of the detector. Note that this quantity depends, among other things, on the efficiency of the reconstruction algorithm and any subsequent selection criteria that are applied in the simulation. Since these steps are done offline for data, there is freedom to tune the detection probability according to the objective of the analysis. This freedom will be exploited in section 7.5 for background rejection.

To compare different neutrino detectors, it is customary to express all distances in water equivalent units (i.e. $\vec{x}\,[\text{w.eq.m}] \equiv \vec{x}\,[m] \cdot \rho(\vec{x})/\rho_{\rm w}$, where $\rho_{\rm w}$ is the nucleon molar density of water), and to combine the detection probability $P_{\rm det}$ with other terms in equation (7.1) in order to construct two quantities which are typically used as a measure for the overall detector efficiency of a neutrino detector. The so-called *effective volume* $V_{\rm eff}$ [w.eq.m^3] is defined as

$$V_{\rm eff}(E, \hat{r}) \equiv \int P_{\rm det}(E, \hat{r}, \vec{x})\, d\vec{x} \approx \frac{V_{\rm gen}}{N_{\rm gen}} \sum_{i=1}^{N_{\rm gen}} P_{\rm det}(E_i, \hat{r}_i, \vec{x}_i) \tag{7.8}$$

The area with which the neutrino flux must be multiplied to determine the detection rate is called the *neutrino effective area* $A_{\text{eff},\nu}$ [w.eq.m^2]. It is defined as

$$\begin{aligned} A_{\text{eff},\nu}(E,\hat{r}) &\equiv \int P_{\text{Earth}}(E,\hat{r})\,\rho(\vec{x})\,N_A\,\sigma_{\text{CC}}(E)\,P_{\text{det}}(E,\hat{r},\vec{x})\,d\vec{x} \\ &\approx \frac{V_{\text{gen}}}{N_{\text{gen}}}\sum_{i=1}^{N_{\text{gen}}} P_{\text{Earth}}(E_i,\hat{r}_i)\,\rho_{\text{w}} N_A\,\sigma_{\text{CC}}(E_i)\,P_{\text{det}}(E_i,\hat{r}_i,\vec{x}_i) \end{aligned} \tag{7.9}$$

Equation (7.1) can therefore be rewritten as

$$\begin{aligned} R_{\text{det}} &= \iiint \frac{d^2\Phi_\nu(E,\hat{r})}{dE\,d\Omega}\,P_{\text{Earth}}(E,\hat{r})\,\rho(\vec{x})\,N_A\,\sigma_{\text{CC}}(E)\,P_{\text{det}}(E,\hat{r},\vec{x})\,dE\,d\Omega\,d\vec{x} \\ &= \iint \frac{d^2\Phi_\nu(E,\hat{r})}{dE\,d\Omega}\,P_{\text{Earth}}(E,\hat{r})\,\rho_{\text{w}}\,N_A\,\sigma_{\text{CC}}(E)\,V_{\text{eff}}(E,\hat{r})\,dE\,d\Omega \\ &= \iint \frac{d^2\Phi_\nu(E,\hat{r})}{dE\,d\Omega}\,A_{\text{eff},\nu}(E,\hat{r})\,dE\,d\Omega \end{aligned} \tag{7.10}$$

7.1.3 Neutrinos from WIMP annihilation in astrophysical objects

The relationship between a general neutrino flux at the surface of the Earth and the resulting detection rate in a neutrino telescope is given by equation (7.1), or equivalently equation (7.10). Similarly, the relationship between the neutrino flux at the surface of the Earth from WIMP annihilation in an astrophysical object, $\Phi_\nu^{\circledS}$, and the resulting detection rate in a neutrino telescope, $R_{\text{det}}^{\circledS}$, can be written as

$$R_{\text{det}}^{\circledS}(m_\chi,\hat{r}) = \int_0^{m_\chi} \frac{d\Phi_\nu^{\circledS}(m_\chi,E,\hat{r})}{dE}\,A_{\text{eff},\nu}(E,\hat{r})\,dE \tag{7.11}$$

where m_χ is the WIMP mass, $\hat{r}$ is the opposite direction of the object (i.e. the direction of a neutrino originating from the object) at the telescope, and

$\dfrac{d\Phi_\nu^{\circledS}(m_\chi,E,\hat{r})}{dE}$ **:** the differential neutrino flux at the surface of the Earth from WIMP annihilation in the object [GeV^{-1} m^{-2} s^{-1}],

$A_{\text{eff},\nu}(E,\hat{r})$ **:** the neutrino effective area [m^2] given by equation (7.9).

The integral over the neutrino energy in equation (7.11) is limited to $E < m_\chi$, the maximum attainable energy by a neutrino from the annihilation of two WIMPs.

Each particular annihilation channel $\chi\chi \rightarrow X$ has its own particular differential neutrino flux, which may be different for neutrinos and anti-neutrinos due to interaction with material in the object. The energy spectra of all dominant WIMP annihilation processes for several WIMP masses are shown in section 3.2. As is customary in indirect dark matter detection experiments, the analysis in this thesis focuses on a typical hard spectrum, from $\chi\chi \rightarrow W^+W^-$, and a typical soft spectrum, from $\chi\chi \rightarrow b\,\bar{b}$ (see figure 3.12). By defining the normalised energy spectrum of the neutrino flux from a specific annihilation channel $\chi\chi \rightarrow X$ as

$$p_E^{\circledS}(m_\chi, E) \;\equiv\; \frac{1}{\Phi_\nu^{\circledS}(m_\chi)}\,\frac{d\Phi_\nu^{\circledS}(m_\chi, E, \hat{r})}{dE} \quad \text{with} \quad \Phi_\nu^{\circledS}(m_\chi) \;\equiv\; \int_0^{m_\chi} \frac{d\Phi_\nu^{\circledS}(m_\chi, E, \hat{r})}{dE}\, dE \tag{7.12}$$

the corresponding detection rate can be written as

$$R_{\text{det}}^{\circledS}(m_\chi, \hat{r}) \;=\; \Phi_\nu^{\circledS}(m_\chi) \int_0^{m_\chi} A_{\text{eff},\nu}(E, \hat{r})\; p_E^{\circledS}(m_\chi, E)\; dE \tag{7.13}$$

The direction of any astrophysical object at the neutrino telescope, $\hat{r}(t)$, is a function of time due to the rotation of the Earth. If the object is relatively close by, the annual rotation of the Earth around the Sun has to be taken into account as well. By using equation (7.13), the number of detected muons N_{det} in a time interval Δt, caused by neutrinos from $\chi\chi \rightarrow X$ in an astrophysical object, can be written as

$$n_{\text{det}}^{\circledS}(m_\chi, \Delta t) \;=\; \Delta t \int R_{\text{det}}^{\circledS}(m_\chi, \hat{r})\; p_{\hat{r}}^{\circledS}(\Delta t, \hat{r})\; d\hat{r} \tag{7.14}$$

where $p_{\hat{r}}^{\circledS}(\Delta t, \hat{r})$ is the directional probability density function for neutrinos from the object during Δt. Hence, by using equation (7.13) in equation (7.14) and by defining

$$A_{\text{eff},\nu}^{\circledS}(m_\chi, \Delta t) \;\equiv\; \int\!\!\int_0^{m_\chi} A_{\text{eff},\nu}(E, \hat{r})\; p_E^{\circledS}(m_\chi, E)\, dE\; p_{\hat{r}}^{\circledS}(\Delta t, \hat{r})\, d\hat{r} \tag{7.15}$$

the relationship between the integrated neutrino flux from $\chi\chi \rightarrow X$ in an astrophysical object and the number of detected muons in a time interval Δt can be written as

$$\Phi_\nu^{\circledS}(m_\chi) \;=\; \frac{n_{\text{det}}^{\circledS}(m_\chi, \Delta t)}{A_{\text{eff},\nu}^{\circledS}(m_\chi, \Delta t)} \cdot \frac{1}{\Delta t} \tag{7.16}$$

In the following, equation (7.15) will be used to evaluate the ANTARES neutrino effective area for WIMP annihilation in the Sun and the Galactic Centre, for the $\chi\chi \rightarrow W^+W^-$ and the $\chi\chi \rightarrow b\,\bar{b}$ annihilation processes. After comparing the expected number of muons from simulations to the detected number of muons in ANTARES data, equation (7.16) will be used to draw a conclusion about the integrated neutrino flux from WIMP annihilation in both astrophysical objects and for both annihilation channels.

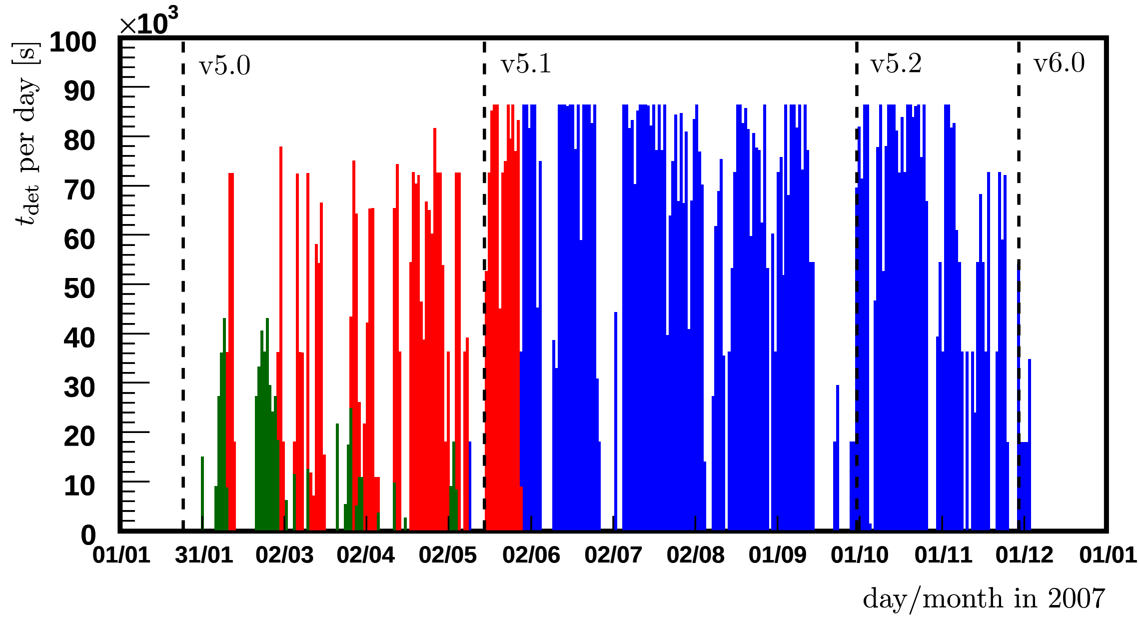

Figure 7.1:
The effective livetime t_{det} per day of the total data sample considered in this analysis, as a function of time. The labels 'v$x.x$' denote the calibration sets used for offline data-processing (see section 7.4).

GREEN[1] :	`highThreshold`	= 10 p.e.
	`allSampling`	= 2
RED :	`highThreshold`	= 10 p.e.
	`allSampling`	= 1
BLUE :	`highThreshold`	= 3 p.e.
	`allSampling`	= 1

7.2 Data selection

The analysis in this chapter is based on ANTARES data taken in 2007, when the detector was operational in its 5-line configuration, see section 5.2.3. Only data which were processed with the `trigger3N` algorithm (see section 6.1.2) are considered. During this period, two distinct `highThreshold` settings were used in the algorithm : 10 and 3 photo-electrons.

The following data quality criteria are applied to all physics data runs :

- All 'basic' data consistency criteria as defined in [107] are satisfied.
- The active PMT fraction (see Appendix A) is larger than 80 %.
- The baseline rate (see Appendix A) is lower than 120 kHz.
- The burst fraction (see Appendix A) is less than 40 %.
- The run setup name does not contain the word 'SCAN' (i.e. the data run is not a trial run with variable parameter settings).
- The database contains dynamic alignment information for the data run period.

[1]The `allSampling` parameter determines the inverse fraction of timeslices that is sent to shore during data taking (e.g. the efficiency of a data run with `allSampling`=2 in terms of livetime is 50 %).

data run type	$t_{\rm det}$		corrected $t_{\rm det}$
`highThreshold` = 10 p.e.	4080668 s	(~47.23 days)	~37.78 days
`highThreshold` = 3 p.e.	10215442 s	(~118.23 days)	~94.59 days
all	14296110 s	(~165.46 days)	~132.37 days

Table 7.1: The total effective livetime of all selected data runs, $t_{\rm det}$, before and after correcting for the additional deadtime caused by the online data filtering software.

The effective livetime $t_{\rm det}$ per day of all 935 physics data runs satisfying these criteria is shown as a function of time in figure 7.1. In this figure, the inefficiency in terms of livetime is mainly due to short periods of increased bioluminescence. The total effective livetime of all selected data runs, $t_{\rm det}$, is summarised in table 7.1. An implementation error in the online data filtering software caused an additional 20 % deadtime during the complete 5-line data taking period. This is taken into account in the right column of table 7.1.

The directional probability density function of the Galactic Centre at ANTARES for all selected data runs, $p_{\hat{r}}^{\rm GC}(t_{\rm det}, \hat{r})$, is scaled with $t_{\rm det}$. The resulting differential effective livetime is integrated over ϕ (θ) and shown as a function of θ (ϕ) in the left (right) panel of figure 7.2 (see right panels in figure 6.17). Similarly, the directional probability density function of the Sun at ANTARES for all selected data runs, $p_{\hat{r}}^{\rm Sun}(t_{\rm det}, \hat{r})$, is scaled with $t_{\rm det}$. Since the diurnal path of the Sun across the sky changes during the

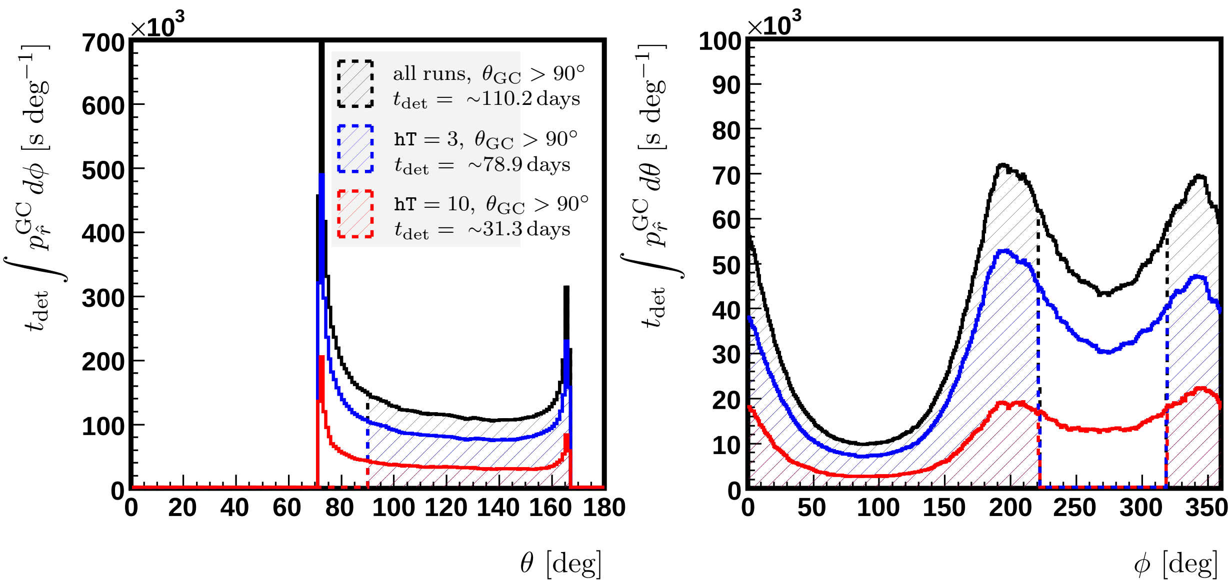

Figure 7.2: The directional probability density function of the Galactic Centre at ANTARES for all selected data runs, normalised to $t_{\rm det}$.

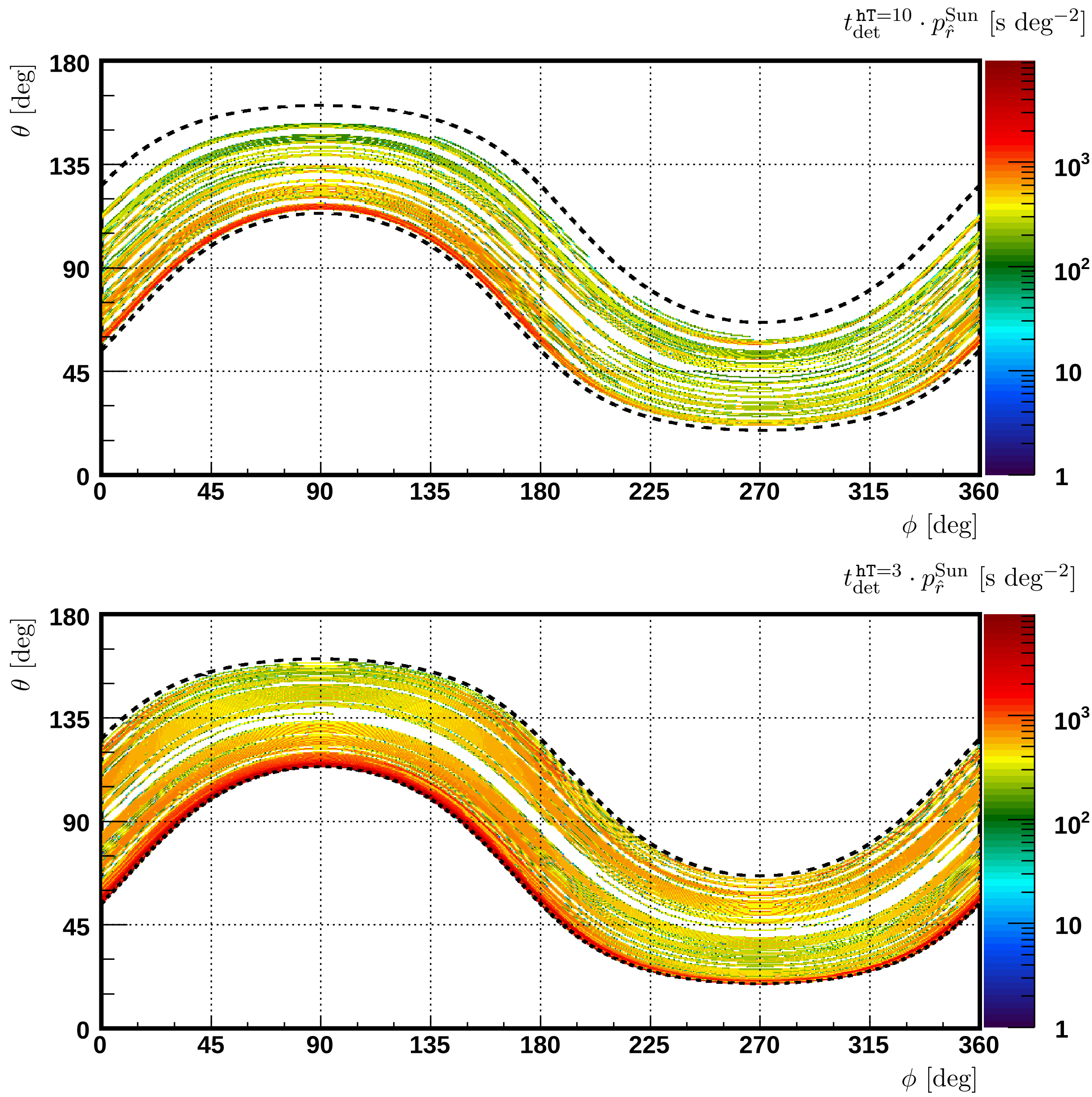

Figure 7.3: The directional probability density function of the Sun at ANTARES, for all selected `highThreshold` = 10 p.e. and 3 p.e. data runs (top and bottom panel, respectively), normalised to $t_{\rm det}$ of the corresponding data run type sample. The solar direction during the winter and summer solstice is indicated by the upper and lower dashed line, respectively)

year due to the combined effect of the Earth's tilted rotational axis with respect to the plane of the solar system and the Earth's annual rotation around the Sun, the resulting differential effective livetime is shown as a function of ϕ and θ in figure 7.3. The selected `highThreshold` = 10 p.e. and 3 p.e. data run type periods are shown separately. For comparison, the solar direction during the winter and summer solstice is indicated by the upper and lower dashed line, respectively.

7.3 Detector simulation

To determine the required effective areas as outlined in section 7.1.1, a full simulation of the detector response to (anti-)muon-neutrinos and atmospheric muons is performed, including random optical background. The simulation procedure is outlined in the following. In all simulation steps, the detector lines are assumed to be perfectly vertical. The positions of the detector lines are obtained from the BSS positions measured in situ.

Neutrino and atmospheric muon generation

- The (anti-)muon-neutrino generation is done using `Genhen v5r2` [100]. Only charged current interactions are simulated. This is done with the `LEPTO` simulation package, using the `CTEQ6-D` parton distribution functions. The neutrinos are generated as an isotropic upgoing flux, where the zenith angles range from 0° to 90°. The neutrino energies are simulated according to a power law spectrum $p_E(E) \propto E^{-1.4}$, between 10 and 10^7 GeV. To estimate the background from atmospheric neutrinos (section 7.5), the events are reweighted according to the *Bartol* parameterisation [108].
- For the atmospheric muons, two independent simulations are performed using programs which adopt a different simulation strategy: `Corsika v6r3` [109] and `MUPAGE v3r4` [99]. The Corsika method comprises a full simulation of interactions of cosmic rays. The interaction products are propagated through the atmosphere to the sea level using the `QGSJET.01c` hadronic interaction model [110]. Muon propagation through the water to the instrumented detector volume is done using the `MUSIC` program [111]. Five different primary nuclei are considered: *p*, *He*, *N*, *Mg* and *Fe*. The cosmic rays are generated as an isotropic downgoing flux, where the zenith angle ranges between 95° and 180°. The cosmic ray energy is simulated according to a power law spectrum $p_E(E) \propto E^{-2}$, between 1 and 10^5 TeV/nucleon. To estimate the background from atmospheric muons (section 7.5), the Corsika events are reweighted according to the *NSU* parameterisation of the primary cosmic ray flux [112]. In contrast, the MUPAGE method is based on a parameterised description of the underwater muon flux. The single and multiple muons at the instrumented detector volume are generated as an isotropic downgoing flux, where the zenith angle ranges between 95° and 180°.

Particle propagation, photon emission and photon propagation

Particle propagation through the instrumented detector volume, photon emission by these (charged) particles and photon propagation to the PMTs, is simulated using `KM3 v3r6` [101] and `Geasim v4r10` [102], for muons and hadronic showers respectively. The particle propagation is based on the `MUSIC` program. The photon absorption length and its wavelength dependence is taken from a fit based on results from in situ measurements (e.g. $\lambda_{\text{abs}}(470 \text{ nm}) = 55$ m). Effects due to photon scattering are derived from the `partic-0.0075` model. The PMT angular efficiency is taken from a fit based on results from a dedicated measurement (`dic08` [113]).

Type	SRB location and number of generated events
ν_μ	/in2p3/mc/neutrino/mu/dic08/r12_c00_s01/5L_07/ARS_thr_meas/ Total number of generated events: $9 \cdot 10^{11}$
$\bar{\nu}_\mu$	/in2p3/mc/neutrino/mu/dic08/r12_c00_s01/5L_07/ARS_thr_meas/ Total number of generated events: $4 \cdot 10^{11}$
μ (Corsika)	/in2p3/mc/muon/corsika/qgsjet/dic08/r12_c00_s01/5L_07/ARS_thr_meas/ Total number of generated events: $\sim 7.5 \cdot 10^9$
μ (MUPAGE)	/in2p3/mc/muon/mupage/dec08/r12_c00_s01/5L_07/ARS_thr_meas/ Total number of generated events (muon multiplicity 1-100): $\sim 1.6 \cdot 10^9$ Total number of generated events (muon multiplicity 101-1000): $\sim 1 \cdot 10^5$

Table 7.2: Simulation samples used in this analysis.

PMT and ARS response, random optical background and data filtering

The simulation of the PMT and ARS response, the addition of random background hits and the simulation of the `trigger3N` algorithm as used during data-taking is done using `TriggerEfficiency` [103].

- The charge resolution of every PMT is simulated according to a Gaussian distribution with a relative gain of 1 with respect to the (integer) number of photons that hit the PMT, and a width of 0.3 p.e.. The time resolution of every PMT is simulated according to a Gaussian distribution with a width of 1.5 ns (σ_{TTS}).
- The rate of random optical background hits is simulated according to the observed PMT counting rates during data-taking (see Appendix A). This is achieved by using the PMT counting rate in every 300$^{\text{th}}$ timeslice of every selected data run. The charge of the random hits is generated according to the observed charge distribution, with a maximum charge of 20 p.e..
- For every ARS individually, the simulated ARS L0 threshold is set equal to the measured value during data-taking (0.45 ± 0.10 p.e.). For all ARS chips, the simulated deadtime is 250 ns, and the charge integration gate is 40 ns. For the TVC and AVC calibration, the default calibration parameters are used. In the TVC calibration, the so-called 'walk' effect is taken into account. Afterpulses are not simulated.
- Corresponding to the trigger settings during data-taking, in the trigger simulation the ARS L1 thresholds are set at 10 and 3 p.e.. Hence there are two independent trigger simulations for each simulation sample. For all other trigger parameters, the default values as given in section 6.1.2 are applied.

In this analysis, the official ANTARES simulation production that follows this procedure is used. The results can be found in the ANTARES SRB data management system as summarised in table 7.2.

Calibration set	First data run	Last data run
`2007:L5:V5.0`	25700	27754
`2007:L5:V5.1`	27755	29814
`2007:L5:V5.2`	29836	30416
`2007:L10:V6.0`	30417	30452

Table 7.3: Offline time and charge calibration sets used in this analysis, and their validity range in terms of data run numbers.

7.4 Offline data-processing

All selected data runs and all simulation results are processed using the `CalReal v2r5` calibration and reconstruction package [114].

7.4.1 Calibration

To calibrate the time, position and charge information of each hit in every PhysicsEvent in a (simulated) data file, a set of offline calibration parameters is needed. In the calibration procedure, the calibration of time and charge and the calibration of position are handled separately.

For data, the time and charge calibration parameters are typically updated every couple of months. In the `CalReal` program, an automatic procedure selects the most appropriate calibration set corresponding to the data file [115]. The time and charge calibration sets used in this analysis are given in table 7.3. In contrast, the position calibration parameters are updated every 6 minutes, providing there is sufficient data from the acoustic positioning system and the tiltmeter-compass system (see section 5.2.4). In this so-called dynamic alignment procedure, the shapes of all detector lines are reconstructed. In this analysis, `alignreco v0.993` is used for the dynamic alignment [116].

For simulated data, as in the simulation of the online trigger, the default time and charge calibration parameters are used. For the position calibration, it is assumed the detector is perfectly vertical, as is assumed in all previous simulation steps in section 7.3. This simplification is motivated by the data quality criteria regarding bioluminescence. Since the amount of bioluminescent light detected is correlated with the magnitude of the sea current velocity (see section 5.2.5), discarding data which show high bioluminescence activity effectively means ignoring periods in which the detector is not vertical (see figure 5.10).

7.4.2 Reconstruction

Assuming the muon is relativistic, its track can be described by five independent parameters: its position $\vec{x}$ and its direction $\hat{r}$. The goal of the reconstruction is, given a set of detected photons, to find the most likely values of these parameters. Depending on the definition of 'most likely', this can be done in a variety of ways. In this analysis, the reconstruction of the muon track in the detector is done using the `AartStrategy` algorithm in `CalReal v2r5` (i.e. Strategy '99') [75, 117].

Given the position and direction of the muon track, the expected arrival time of a Cherenkov photon at a PMT is given by equation (6.2). The difference between the measured arrival time and the expected arrival time of a detected photon is referred to as the time residual Δt of the photon with respect to the muon track. In general, the aim of a reconstruction algorithm is to find the muon track parameters for which the time residuals of the detected photons are minimal. In the `AartStrategy` algorithm, this is achieved by maximising the likelihood function $L(\vec{x}, \hat{r})$:

$$L(\vec{x}, \hat{r}) \;\equiv\; \prod_{i=1}^{N_{\text{det}}} P(\Delta t_i,\, a_i \,|\, \vec{x}, \hat{r}) \tag{7.17}$$

for a set of n_{det} detected photons, where $P(\Delta t_i,\, a_i \,|\, \vec{x}, \hat{r})$ is the probability density function of the time residual Δt_i of an individual photon with charge a_i. Parameterisations for $P(\Delta t_i,\, a_i \,|\, \vec{x}, \hat{r})$ have been derived from simulations, depending on the charge of the photon-hit. They take into account the probability that the photon is due to Cherenkov emission from the muon track, as well as the probability that the photon scatters during propagation or that is due to Cherenkov emission from secondary particles or random optical background. The `AartStrategy` algorithm attempts to find the maximum of $L(\vec{x}, \hat{r})$ by using the `e04dgf` minimisation [1] routine from the `NAGLIB` numerical algorithm library [118]. Since the minimisation is done iteratively, an initial estimate of the track parameters is necessary. Furthermore, since $L(\vec{x}, \hat{r})$ typically has many local maxima, a reasonable initial track estimate is essential to find the global maximum. Hence, the `AartStrategy` algorithm comprises four consecutive track fitting and hit selection procedures. The initial estimate is a linear track fit that assumes the hits occur on the muon track. This followed by two intermediate track fits, in which the likelihood function has a less refined form than the 'full' likelihood function given by equation (7.17), making them less sensitive to local minima. These are repeated an additional eight times, using four rotated and four translated versions of the linear track fit. Finally, from these nine results, the track fit with the maximum likelihood per degree of freedom (i.e. the number of hits in the fit minus the number of track parameters, 5) is used as input for the final track fit using the 'full' likelihood function.

The logarithm of the likelihood per degree of freedom of the final fit can be used to assess the quality of the final fit. Additionally, if different initial track estimates result in the same final fit, it is more likely that the global maximum is found. Hence, the quality of the final fit is defined as [75]

$$\Lambda \;\equiv\; \frac{\log(L(\vec{x}_{\text{final}}, \hat{r}_{\text{final}}))}{N_{\text{dof}}} + 0.1(N_{\text{comp}} - 1) \tag{7.18}$$

where N_{dof} is the number of degrees of freedom of the final fit, and N_{comp} is the number of times the same final fit is obtained from the nine different initial track estimates.

[1] The maximum of $L = \prod P$ is found by minimising $-\log(L) = -\sum P$.

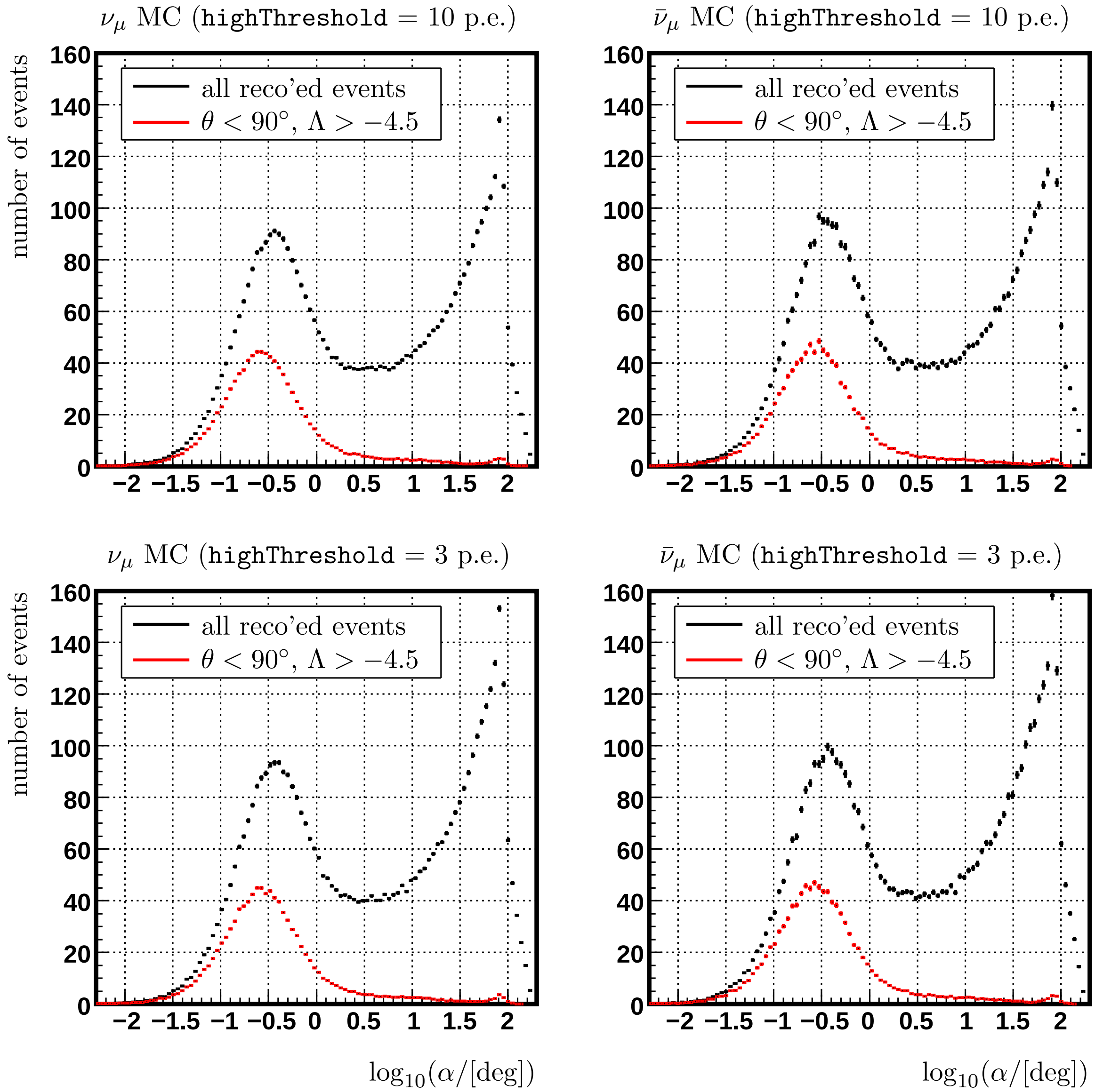

Figure 7.4: The reconstruction error α of the final track fit of the `AartStrategy` algorithm in each of the four simulated (anti-)muon-neutrino samples ($p_E(E) \propto E^{-1.4}$). In black the distribution for all reconstructed events. In red, the distribution for all events reconstructed as upgoing and with $\Lambda > -4.5$.

The performance of a reconstruction algorithm can be verified by the reconstruction error α, defined as the angle between the muon direction and the reconstructed track direction. The reconstruction error α of the final fit of the `AartStrategy` algorithm in each of the four simulated (anti-)muon-neutrino samples ($p_E(E) \propto E^{-1.4}$) is shown in figure 7.4. The distributions of the reconstruction error of all reconstructed events and upward-reconstructed events with $\Lambda > -4.5$ are shown in black and red, respectively. As can be seen, badly reconstructed tracks can be removed by a selection based on Λ.

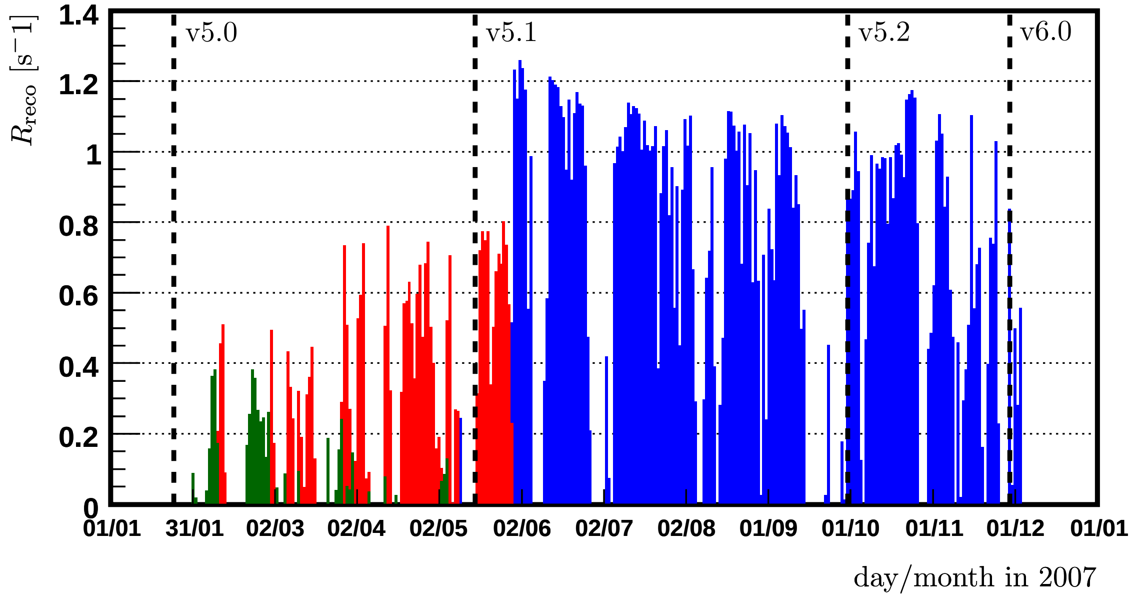

Figure 7.5:
The reconstructed track $R_{\rm reco}$ in the data sample, as a function of time. The labels 'v$x.x$' denote the calibration sets used for offline data-processing.

GREEN :	`highThreshold`	$= 10$ p.e.
	`allSampling`	$= 2$
RED :	`highThreshold`	$= 10$ p.e.
	`allSampling`	$= 1$
BLUE :	`highThreshold`	$= 3$ p.e.
	`allSampling`	$= 1$

The reconstructed track rate $R_{\rm reco}$ in the data sample is shown as a function of time in figure 7.5. The total number of reconstructed events in all 935 selected data runs is ~$1.4 \cdot 10^7$.

7.5 Background rejection

As is shown in the right panel of figure 5.4, the atmospheric muon flux prohibits a simple search for neutrinos in the GeV/TeV energy range in the downward direction. Similarly, the atmospheric neutrino flux has to be taken into account in any search for extra-terrestrial neutrinos in the upward direction. In this section, a comparison is made between the reconstructed data sample and these two types of background. Reconstruction criteria are derived to take these backgrounds into account.

7.5.1 Data - Monte Carlo comparison

As shown in the previous section, the fit quality parameter Λ can be used to reject badly reconstructed tracks. Hence, it is useful to compare the fit quality parameter Λ of the reconstructed tracks in the data sample and the simulated background samples. This can be seen in figure 7.6, which shows the zenith angle θ of the reconstructed tracks in

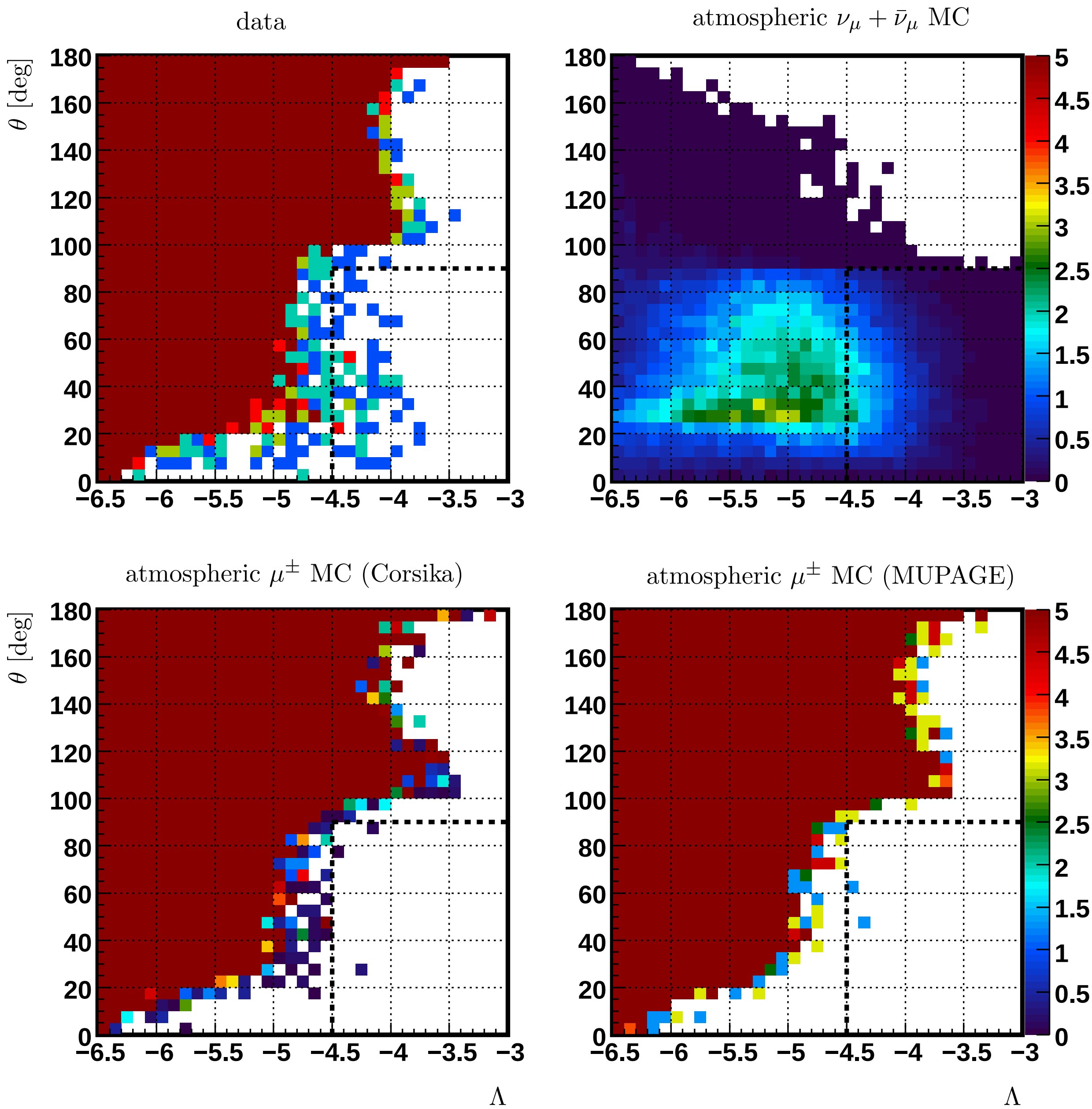

Figure 7.6: The zenith angle θ of the reconstructed tracks in the data sample and the simulated background samples as a function of the fit quality parameter Λ. The z-axis gives the number of tracks per bin. For comparison, the simulated background samples are normalised to the effective livetime of the data sample, and the maximum number of tracks per bin is set at 5.

the data sample (top left panel) and the simulated background samples (top right and bottom panels) as a function of the fit quality parameter Λ. For comparison, the simulated background samples are normalised to the effective livetime of the data sample, and the maximum number of tracks per bin is set at 5. As can be seen from the bottom

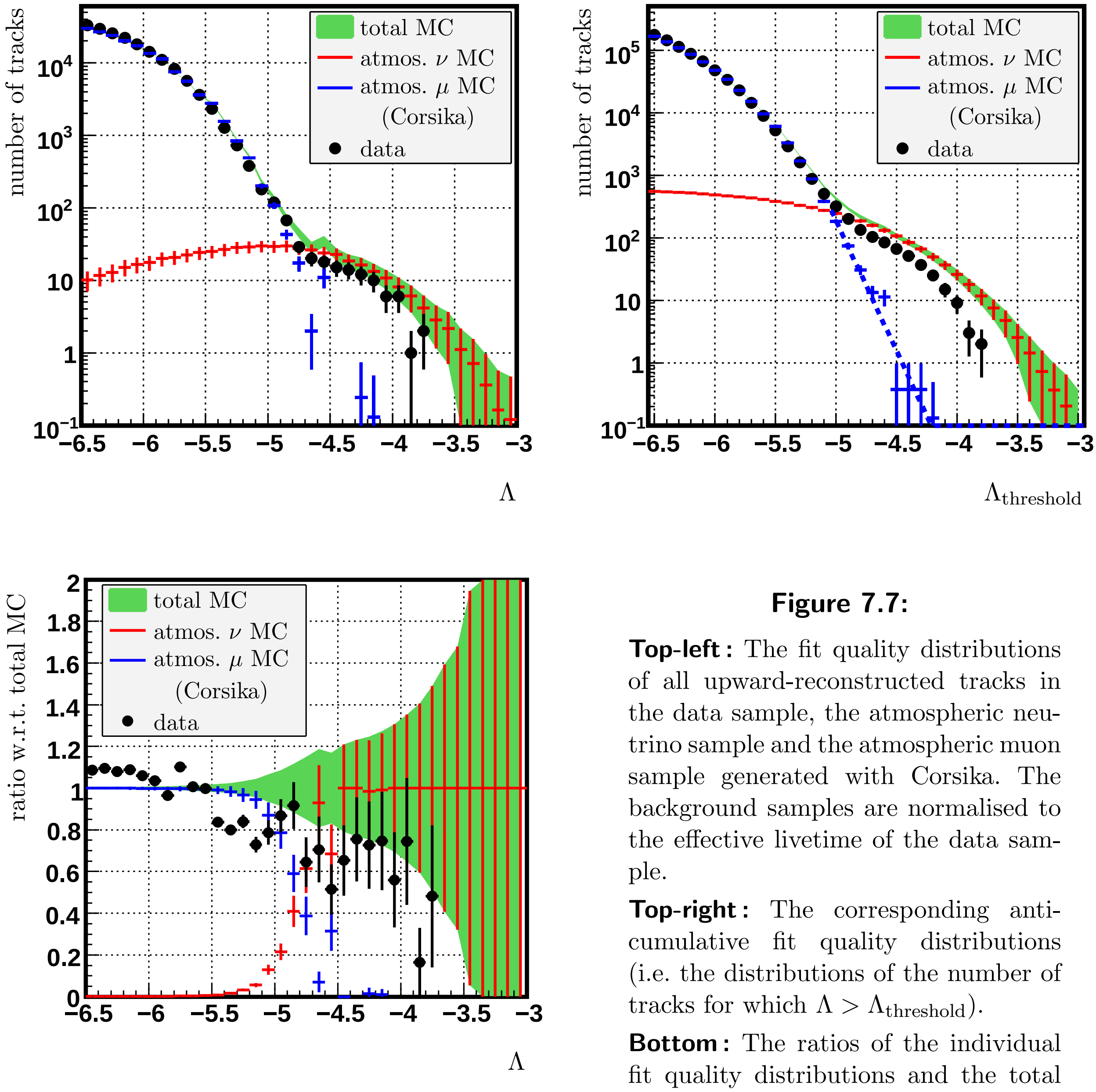

Figure 7.7:

Top-left : The fit quality distributions of all upward-reconstructed tracks in the data sample, the atmospheric neutrino sample and the atmospheric muon sample generated with Corsika. The background samples are normalised to the effective livetime of the data sample.

Top-right : The corresponding anti-cumulative fit quality distributions (i.e. the distributions of the number of tracks for which $\Lambda > \Lambda_{\text{threshold}}$).

Bottom : The ratios of the individual fit quality distributions and the total MC fit quality distribution.

All panels : statistical errors only.

panels of figure 7.6, a significant amount of the atmospheric muon flux is misreconstructed in the upward direction. The majority of these misreconstructed atmospheric muons has $\Lambda \lesssim -5$. In contrast, about 50 % of the upward-reconstructed atmospheric neutrinos has $\Lambda \gtrsim -5$. The upward-reconstructed tracks in the data sample are similar to the sum of both background samples. Considering only upward-reconstructed tracks, a more detailed comparison between data and simulated background samples is made in the following.

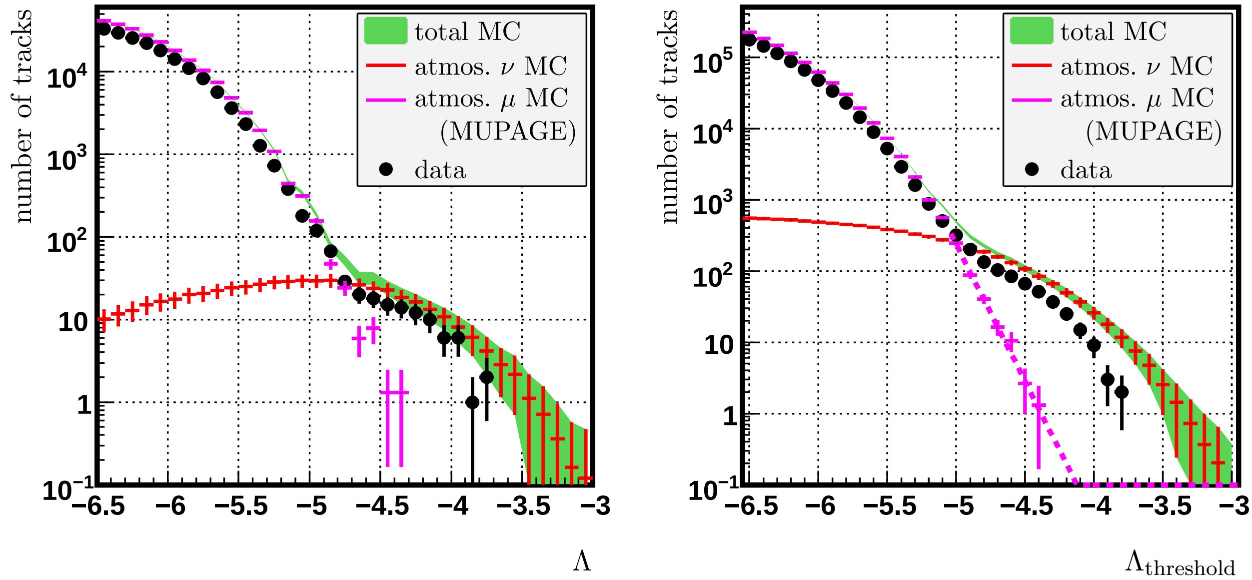

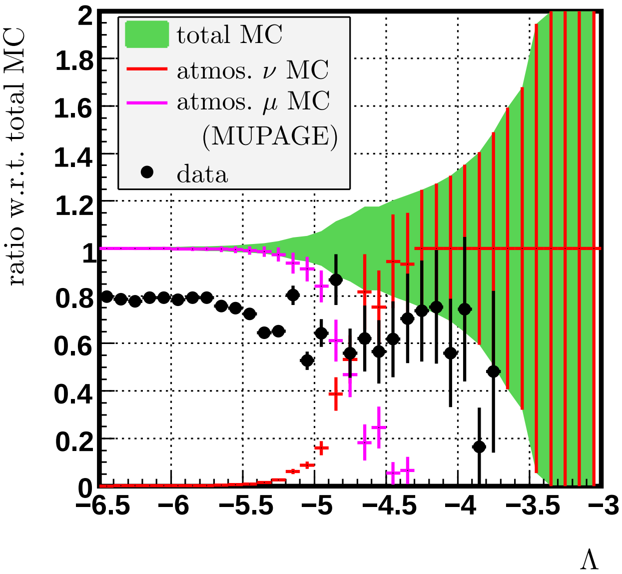

Figure 7.8:

Top-left : The fit quality distributions of all upward-reconstructed tracks in the data sample, the atmospheric neutrino sample and the atmospheric muon sample generated with MUPAGE. The background samples are normalised to the effective livetime of the data sample.

Top-right : The corresponding anti-cumulative fit quality distributions (i.e. the distributions of the number of tracks for which $\Lambda > \Lambda_{\text{threshold}}$).

Bottom : The ratios of the individual fit quality distributions and the total MC fit quality distribution.

All panels : statistical errors only.

The fit quality distributions of all upward-reconstructed tracks in the data sample, the atmospheric neutrino samples and the atmospheric muon sample generated with Corsika (MUPAGE) are shown in the top-left panel of figure 7.7 (7.8). The simulated background samples are normalised to the effective livetime of the data sample. The corresponding anti-cumulative fit quality distributions, i.e. the distributions of the number of tracks for which $\Lambda > \Lambda_{\text{threshold}}$, are shown in the top-right panels. For comparison, the ratios of the individual fit quality distributions and the total MC fit quality distribution can be found in the bottom panels. Only statistical errors are shown. As can be seen from figure 7.7, the atmospheric muon flux originating from the *NSU* primary cosmic ray flux gives an acceptable prediction of the number of upward-reconstructed tracks with $\Lambda \lesssim -5$ in the data sample. The atmospheric muon flux generated with MUPAGE as shown in figure 7.8 gives an over-estimate of ~20 %. The *Bartol* parameterisation of the atmospheric neutrino flux as shown in both figures over-estimates the number of upward-reconstructed tracks with $\Lambda \gtrsim -5$ in the data sample with ~20 %. However, given the statistical errors and the uncertainties on the absolute atmospheric muon and neutrino flux (~30 % each), it can be concluded that the overall fit quality distribution of the upward-reconstructed tracks in the data sample is reasonably well described by the sum of the simulated background samples.

7.5.2 Reconstruction criteria

As can be seen from the top-right panels in figures 7.7 and 7.8, the atmospheric neutrino flux starts to dominate the sample of upward-reconstructed tracks in the data for $\Lambda \gtrsim -5$. Above this value, the anti-cumulative fit quality distributions of the atmospheric muon samples are fitted with an exponential function, as shown in both panels. From these exponential fits it can be concluded that for upward-reconstructed tracks with $\Lambda > -4.5$ the atmospheric muon contribution is about two orders of magnitude smaller than the atmospheric neutrino contribution.

To reject the atmospheric muon background and to ensure an unambiguous determination of the azimuthal angle, the following reconstruction criteria are applied [2] :

1 : The reconstructed track has to be directed upward, $\theta < 90°$.

2 : The reconstructed track must have a fit quality $\Lambda > -4.5$.

3 : The reconstructed track has to have hits on at least three detector lines.

The effects of successive application of these criteria on the number of reconstructed tracks in the data and simulation samples is summarised in table 7.4. The simulated background is normalised to the effective livetime of the data sample. The distributions of the reconstructed zenith angle θ and the reconstructed azimuthal angle ϕ of all selected tracks in the data and simulation samples are shown in the top-left and top-right panels of figure 7.9. The bottom panels show the ratio of the data distribution and the total atmospheric neutrino distribution.

[2] Assuming the likelihood function near the fitted maximum can be described by a 5-dimensional Gaussian distribution, the covariance matrix of the fit can be derived using the second order partial derivative of the likelihood with respect to the track parameters at the fitted maximum. Thus, the error on the track direction can be calculated, which can be used to reject badly reconstructed tracks. However, since the derivation of the covariance matrix is not included in the implementation of the `AartStrategy` algorithm in `CalReal v2r5`, this option is not used in this analysis.

	no selection	$\theta < 90°$	$\Lambda > -4.5$	$n_{\text{lines}} \geq 3$
atmos. μ MC (Corsika)	$\sim 1.11 \cdot 10^7$	$\sim 9.69 \cdot 10^5$	5	0.4
atmos. μ MC (MUPAGE)	$\sim 1.49 \cdot 10^7$	$\sim 1.28 \cdot 10^6$	5	2
atmos. $\nu_\mu + \bar{\nu}_\mu$ MC	718	661	112	107
data	$\sim 1.38 \cdot 10^7$	$\sim 7.67 \cdot 10^5$	69	66

Table 7.4: The effects of successive application of the reconstruction criteria on the number of reconstructed tracks in the data and simulation samples. The latter are normalised to the effective livetime.

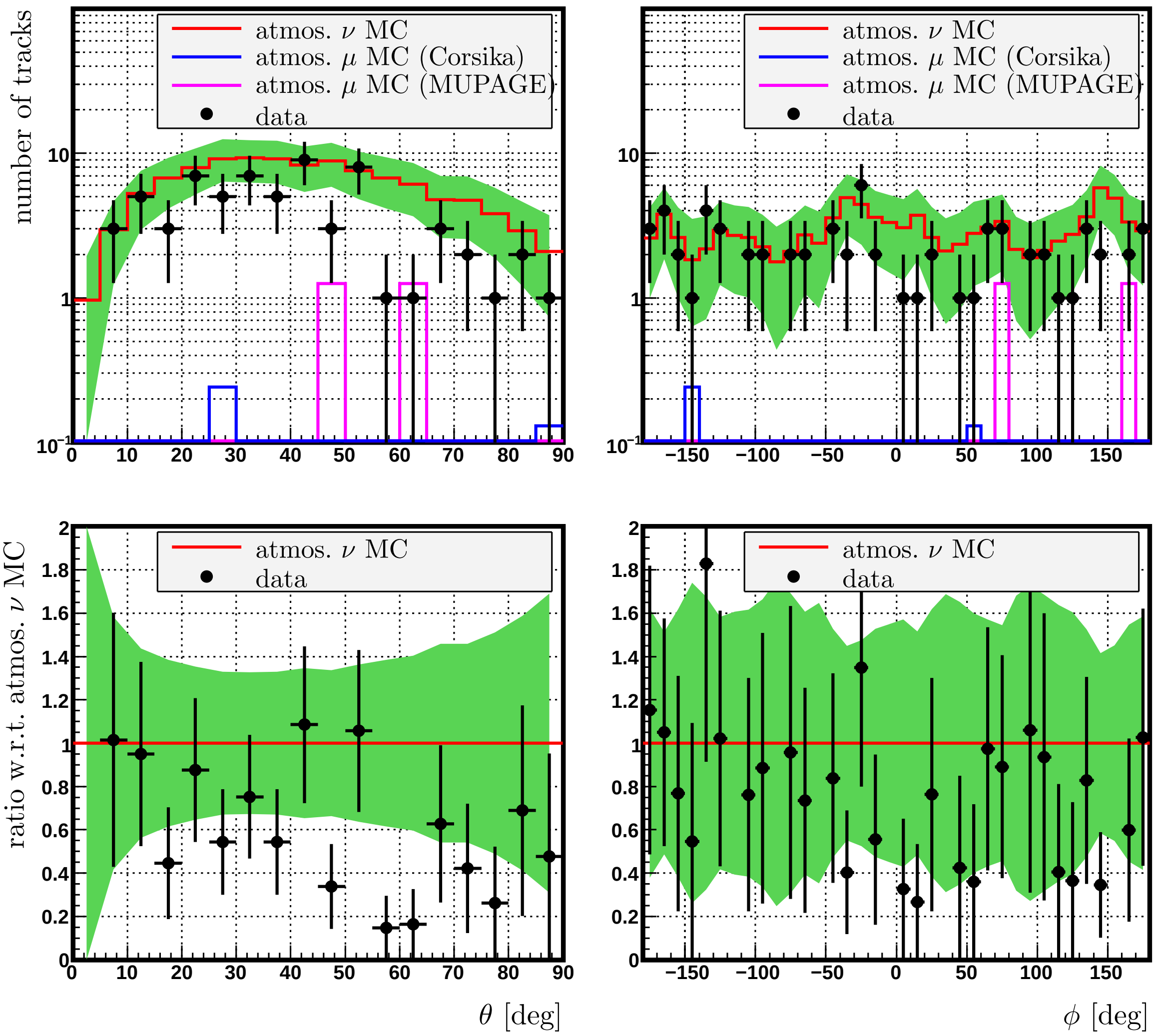

Figure 7.9: The distributions of the zenith angle θ (top-left panel) and the azimuthal angle ϕ (top-right panel) of all selected tracks in the data and simulation samples. The latter are normalised to the effective livetime. The bottom panels show the ratio of the data distribution and the total atmospheric neutrino distribution. The statistical errors in the data and atmospheric neutrino simulations are shown in all panels.

As can be seen from this figure, the selected tracks in the data are reasonably well described by the atmospheric neutrino flux after application of the reconstruction criteria, taking into account the statistical errors and the uncertainties on the absolute atmospheric neutrino flux. The impurity in the reconstructed data sample caused by atmospheric muons is of the order of 1 %.

7.5.3 Analysis strategy

The agreement between the selected tracks in the data and the simulated atmospheric neutrino samples indicates that a distinct signal from WIMP annihilation has not been found in the data considered in this analysis. Given the apparent absence of neutrino candidates in data apart from what is expected from the atmospheric neutrino flux, the aim of this analysis is to derive an upper limit on the neutrino flux from WIMP annihilation in the Sun and the Galactic Centre. The calculation of the limit is based on a search for an excess of neutrinos in the direction of these astrophysical objects with respect to the number of neutrinos expected from the (diffuse) atmospheric neutrino flux. Energy reconstruction is not used in the derivation of the limits, due to the energy spectrum of the simulated atmospheric neutrinos that pass all reconstruction criteria. This energy spectrum is shown, normalised to the effective livetime of the data sample, in figure 7.10. As can be seen, the energy of the majority of the selected atmospheric neutrinos is of the same order as the neutralino mass expected from mSUGRA (see figure 4.1). Therefore the reconstructed energy provides no additional information to distinguish signal from background. The search method will be presented in section 7.7.

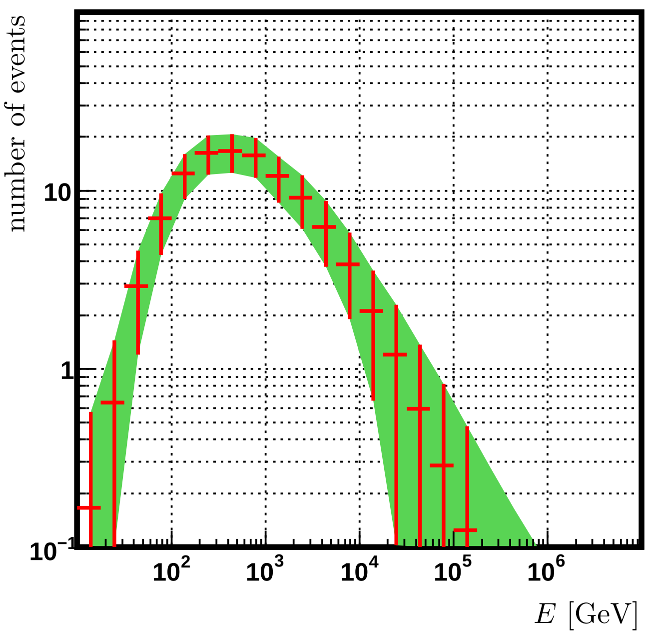

Figure 7.10:

The simulated atmospheric neutrino energy spectrum, normalised to the effective livetime.

7.6 Detector performance

The performance of a neutrino telescope in terms of neutrino detection can be characterised by its detection efficiency and pointing accuracy. The former can be quantified by the neutrino effective area as discussed in section 7.1.2. In this section, equation (7.15) will be used to derive the ANTARES neutrino effective area for $\chi\chi \rightarrow W^+W^-$ and the $\chi\chi \rightarrow b\,\bar{b}$ annihilation in the Sun and the Galactic Centre, taking into account the data-taking conditions and all data-selection criteria considered in this analysis.

7.6.1 Pointing accuracy

The pointing accuracy can be quantified by the angular resolution. The muon angular resolution is defined as the median angle of the reconstruction error (see section 7.4.2). Similarly, the neutrino angular resolution is defined as the median of the angle between the neutrino direction and the reconstructed track direction. As can be seen from figure 7.4, the angular resolution not only depends on the instrumental characteristics of the detector but also on all required data-processing and selection steps. The angular resolution of the ANTARES detector, taking into account the data-taking conditions and all data-selection criteria considered in this analysis, is derived from the simulated neutrino samples and is shown as a function of the neutrino energy in figure 7.11. The muon and neutrino angular resolutions are indicated by blue and red lines, respectively. As can be seen from this figure, the angular resolution is smaller for the muon than for the neutrino. This is due to the scattering angle between the neutrino and the induced muon. The median of this scattering angle is shown as a black line in figure 7.11. Both angular resolutions improve with neutrino energy due to the decrease of the scattering

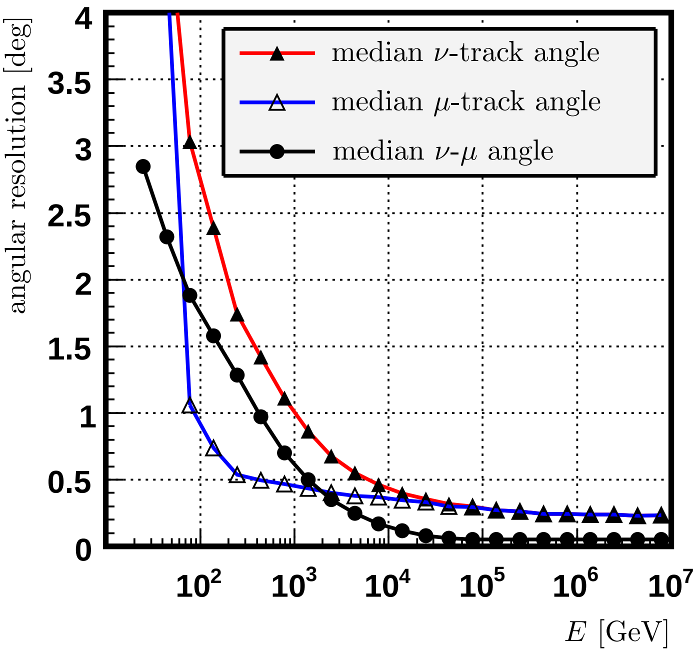

Figure 7.11:

The angular resolution of the ANTARES detector for the data-taking period considered in this analysis, taking into account all subsequent data-processing and selection steps, as a function of the neutrino energy E. In blue (red): the muon (neutrino) angular resolution. In black: the median scattering angle between the neutrino and the muon.

angle and the improvement of the muon detection probability for higher energies. The latter is due to the increase of the muon range with energy (see figure 5.2).

7.6.2 Detection efficiency

The detection efficiency of a neutrino telescope not only depends on the instrumental characteristics of the detector, but also on all required data-processing and selection steps.

The effective volume V_{eff} and neutrino effective area $A_{\mathrm{eff},\nu}$

The effective volume V_{eff} and neutrino effective area $A_{\mathrm{eff},\nu}$ of the ANTARES detector are derived from the simulated neutrino samples by using equations (7.8) and (7.9). In this way the data-taking conditions and all data-selection criteria considered in this analysis are taken into account. The weighted averages of the effective volume and the neutrino effective area with respect to the effective livetimes of each of the two distinct `highThreshold` data-taking periods are shown as a function of the neutrino energy in figure 7.12, averaged over all neutrino directions. For comparison, the instrumented detector volume of ANTARES is indicated by a dashed line in the left panel. As can be seen from this figure, the effective volume is slightly larger for anti-neutrinos than for neutrinos for $E \lesssim 10^5$ GeV, while the opposite is true for the neutrino effective area. This is caused by differences in the interactions of neutrinos and anti-neutrinos with

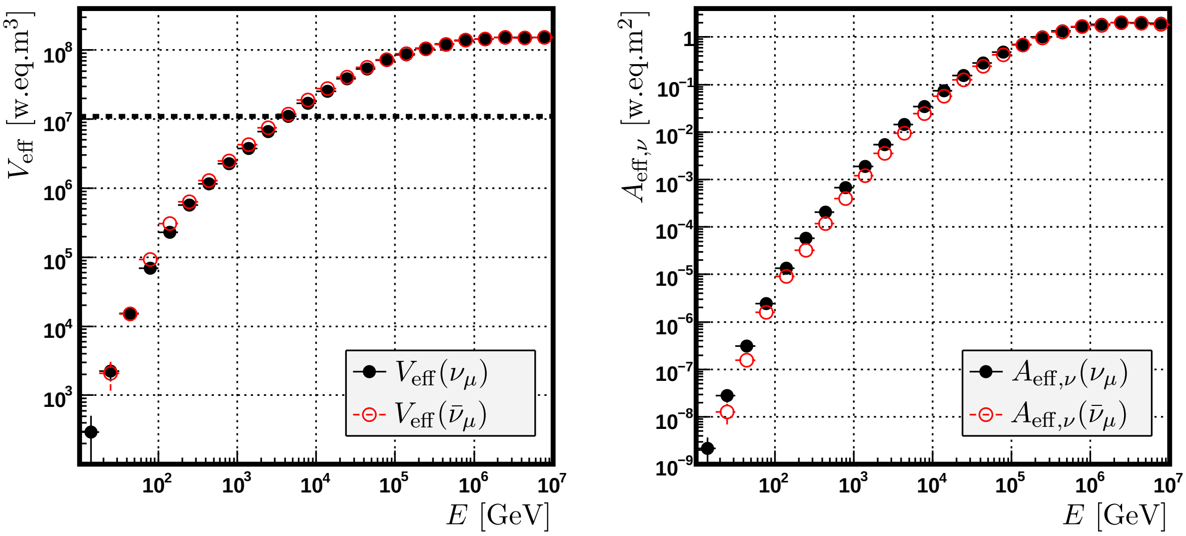

Figure 7.12: The effective volume V_{eff} and neutrino effective area $A_{\mathrm{eff},\nu}$ of the ANTARES detector for the data-taking conditions and all data-selection criteria considered in this analysis, averaged over all directions, as a function of the neutrino energy E. For comparison, the instrumented detector volume of ANTARES is indicated by a dashed line in the left panel.

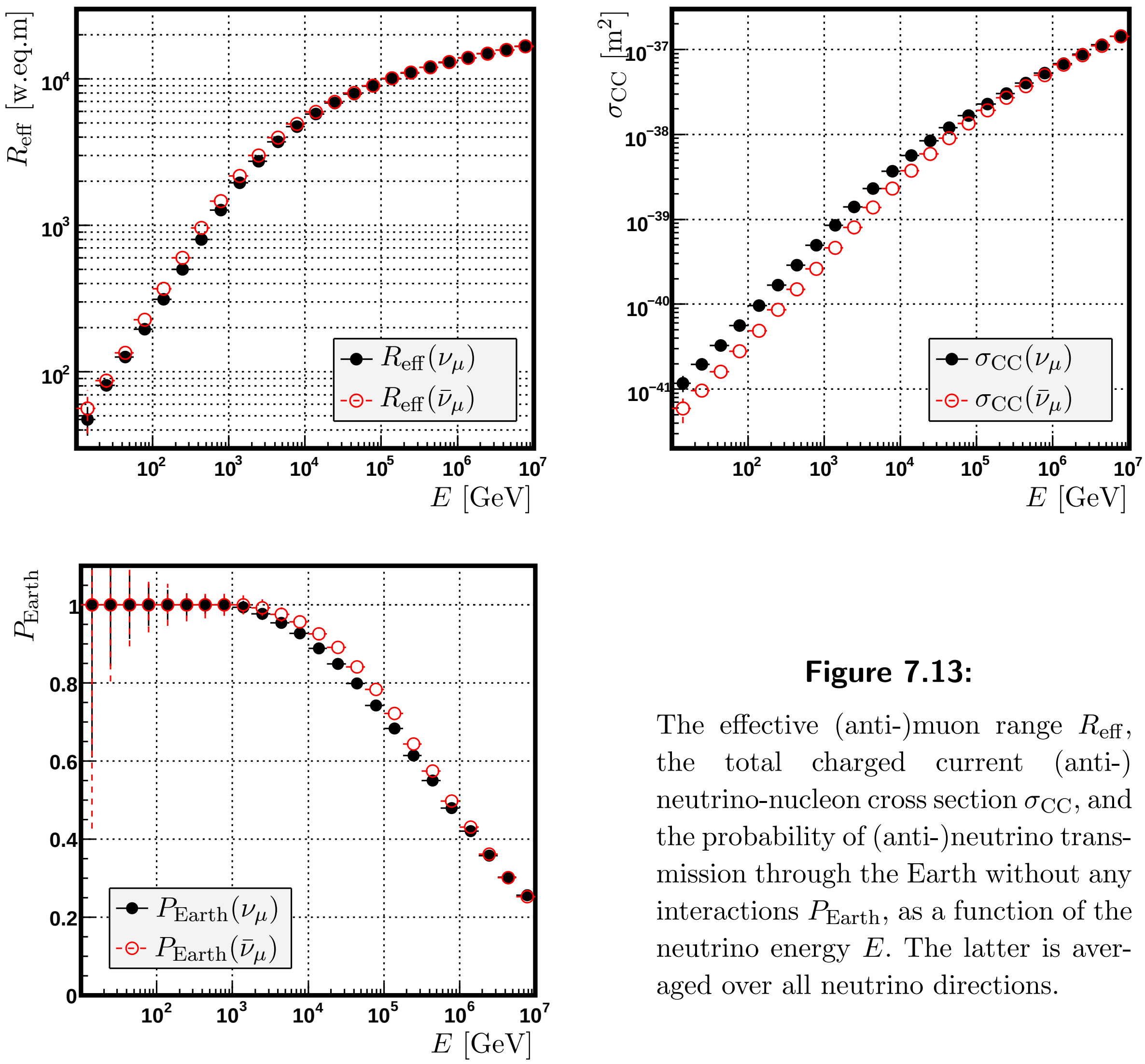

Figure 7.13:

The effective (anti-)muon range R_{eff}, the total charged current (anti-) neutrino-nucleon cross section σ_{CC}, and the probability of (anti-)neutrino transmission through the Earth without any interactions P_{Earth}, as a function of the neutrino energy E. The latter is averaged over all neutrino directions.

nucleons. The average energy of a muon, induced by a neutrino-nucleon interaction, is smaller for $E \lesssim 10^5$ GeV than the average energy of an anti-muon, induced by an anti-neutrino of the same energy. Therefore the average muon propagation distance (i.e. the effective muon range) for a particular neutrino energy is also smaller, as shown in the top-left panel of figure 7.13. The effect of a smaller effective muon range is a reduced effective volume. In contrast, the total charged current neutrino-nucleon cross section is larger for neutrinos than for anti-neutrinos, as shown in the top-right panel of figure 7.13. Although this also decreases the transmission probability through the Earth, as shown in the bottom panel of figure 7.13, the neutrino effective area is slightly larger for neutrinos than for anti-neutrinos.

The neutrino effective area for $\chi\chi \to b\,\bar{b}$ and $\chi\chi \to W^+W^-$ in the Sun and the GC

The effective area for neutrinos from $\chi\chi \to X$ annihilation in an astrophysical object, corresponding to a certain data-taking period Δt, $A_{\mathrm{eff},\nu}(m_\chi, \Delta t)$, is given by equation (7.15). Hence, to derive the neutrino effective area of the ANTARES detector for $\chi\chi \to b\,\bar{b}$ and $\chi\chi \to W^+W^-$ in the Sun and the Galactic Centre for the data-taking period considered in this analysis, two additional ingredients besides the (general) neutrino effective area $A_{\mathrm{eff},\nu}(E,\hat{r})$ are required:

- The normalised neutrino energy spectra from $\chi\chi \to b\,\bar{b}$ and $\chi\chi \to W^+W^-$ in the Sun and the Galactic Centre, $p_E^{\mathrm{Sun}}(m_\chi, E)$ and $p_E^{\mathrm{GC}}(m_\chi, E)$. These are derived in chapter 3 for the Sun and the Earth and are shown in figures 3.4 and 3.6. In this analysis, the energy spectra from WIMP annihilation in the dark matter halo are assumed to be identical to those from WIMP annihilation in the Earth, since the neutrinos from WIMP annihilation in the Earth do not interact during their propagation between the centre of the Earth and the detector.

- The directional probability density functions of the Sun and the Galactic Centre at ANTARES for the data-taking period considered in this analysis, $p_{\hat{r}}^{\mathrm{Sun}}(\Delta t, \hat{r})$ and $p_{\hat{r}}^{\mathrm{GC}}(\Delta t, \hat{r})$. These are derived in section 7.2 and shown in figures 7.2 and 7.3, scaled with the effective livetime.

The neutrino effective areas for $\chi\chi \to b\,\bar{b}$ and $\chi\chi \to W^+W^-$ in the Sun and the Galactic Centre, $A_{\mathrm{eff},\nu}^{\mathrm{Sun}}(m_\chi)$ and $A_{\mathrm{eff},\nu}^{\mathrm{GC}}(m_\chi)$, are derived by combining the (general) neutrino effective area $A_{\mathrm{eff},\nu}(E,\hat{r})$ for the data-taking conditions and all data-selection criteria considered in this analysis, with $p_{\hat{r}}(\Delta t, \hat{r})$ of the Sun and the Galactic Centre for the data-taking period and $p_E(m_\chi, E)$ for $\chi\chi \to b\,\bar{b}$ and $\chi\chi \to W^+W^-$ in the Sun and the Galactic Centre, in equation (7.15). The results are shown as a function of the WIMP mass $m\chi$ in figure 7.14 for the Sun and figure 7.15 for the Galactic Centre. The insets show the neutrino effective areas for small WIMP masses.

A number of conclusions can be drawn from these figures. As can be seen, the neutrino effective areas for $\chi\chi \to W^+W^-$ are always larger than the neutrino effective areas for $\chi\chi \to b\,\bar{b}$. This is due to the neutrino energy spectrum of the $\chi\chi \to W^+W^-$ process which is harder than that of the $\chi\chi \to b\,\bar{b}$ process (see figures 3.4 and 3.6). The neutrino effective areas of the Sun are always smaller than those of the Galactic Centre. This is due to energy loss in the Sun caused by interactions of the neutrinos with solar material during their propagation through the interior of the Sun. This softens the neutrino energy spectra as can be seen by comparing the top and bottom panels of figures 3.4 and 3.6. Since the general neutrino effective area is larger for neutrinos than for anti-neutrinos in the WIMP energy regime (see right panel of figure 7.12), this is also true for the neutrino effective areas of the Galactic Centre. For the Sun, this is also the case for small WIMP masses, while for large WIMP masses the neutrino energy spectra are suppressed due to energy loss and absorption of neutrinos in the Sun. Therefore, the anti-neutrino effective areas of the Sun are larger than the neutrino effective areas for large WIMP masses. The suppression of the neutrino effective area is stronger for the $\chi\chi \to W^+W^-$ process, since the neutrino energy spectra are harder for this process.

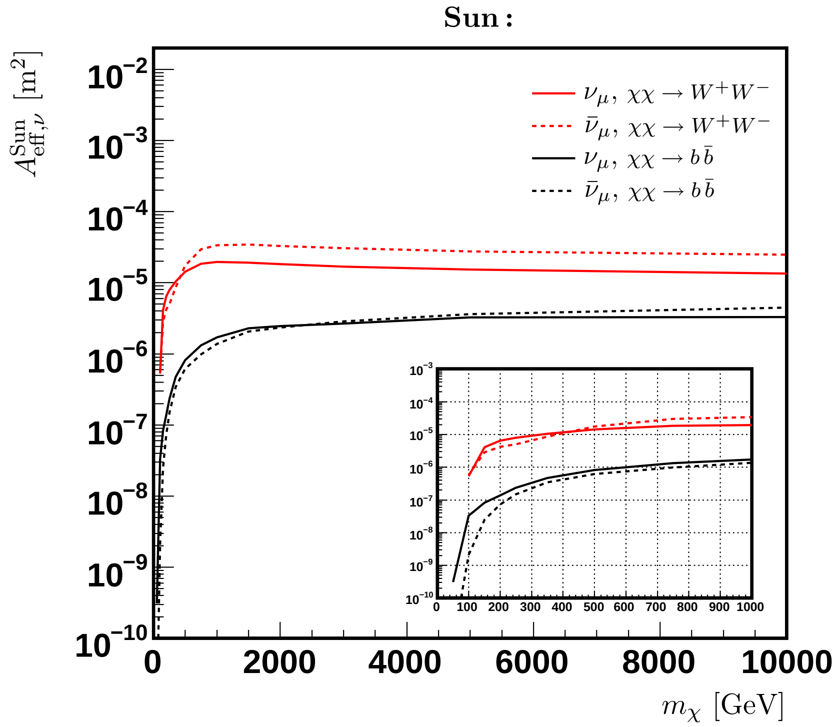

Figure 7.14:

The neutrino effective area of the ANTARES detector for $\chi\chi \to b\,\bar{b}$ and $\chi\chi \to W^+W^-$ in the Sun, $A^{\mathrm{Sun}}_{\mathrm{eff},\nu}$, for the data-taking period and all data-selection criteria considered in this analysis, as a function of the WIMP mass m_χ. The low mass region is shown in the inset.

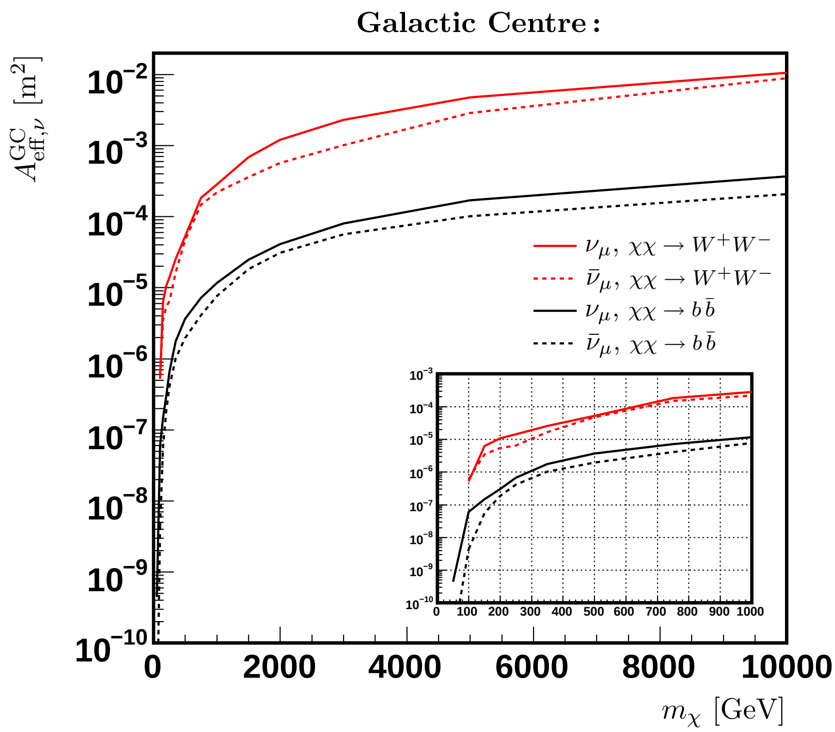

Figure 7.15:

The neutrino effective area of the ANTARES detector for $\chi\chi \to b\,\bar{b}$ and $\chi\chi \to W^+W^-$ in the Galactic Centre, $A^{\mathrm{GC}}_{\mathrm{eff},\nu}$, for the data-taking period and all data-selection criteria considered in this analysis, as a function of the WIMP mass m_χ. The low mass region is shown in the inset.

7.7 Search for neutrinos from the Sun and the GC

In this section, the direction of the selected neutrino candidates is compared with the direction of the Sun and the Galactic Centre at the moment of detection, to search for a possible excess of neutrinos with respect to the diffuse atmospheric neutrino flux.

7.7.1 Search method

The pointing accuracy of a neutrino telescope is limited by its angular resolution. In the search for neutrinos from the Sun and the Galactic Centre, this is taken into account by considering all detected neutrino candidates in a cone around the direction of the objects. The number of detected events in the cone, n_{det}, is regarded as the sum of the number of signal events in the cone due to WIMP annihilation in the object and the number of background events in the cone. Given the relatively small number of detected events, it is assumed that the number of detected events in a cone can be described by a Poisson distribution with a mean given by the sum of the mean number of signal events, μ_{s}, and the mean number of background events in the cone, μ_{b}.

The comparison between data and Monte Carlo simulations indicates that the detected number of events is consistent with the predicted number of events due to the atmospheric neutrino flux. Therefore, the aim of the search is not to claim a discovery but to derive an upper limit on the number of signal events in the cone. This will be used to calculate the upper limit on the integrated neutrino flux.

Upper limit on the number of signal events $\hat{\mu}_{\mathrm{s}}$

For a given number of detected events n_{det} and an expected number of background events μ_{b}, the upper limit on the number of signal events in the cone, $\hat{\mu}_{\mathrm{s}}(n_{\mathrm{det}}, \mu_{\mathrm{b}})$, can be calculated at a certain confidence level α. In frequentist statistics, the upper limit and the confidence level are defined such that if the number of signal events μ_{s} is equal to (or larger than) the upper limit $\hat{\mu}_{\mathrm{s}}$, the probability that a repetition of the experiment will detect a number of events n which is as small or smaller than n_{det} is equal to (or smaller than) $1-\alpha$:

$$P(n \leq n_{\mathrm{det}} \,|\, \mu_{\mathrm{s}} \geq \hat{\mu}_{\mathrm{s}}) \;=\; \sum_{n=0}^{n_{\mathrm{det}}} \frac{(\hat{\mu}_{\mathrm{s}}+\mu_{\mathrm{b}})^n}{n!}\, e^{-(\hat{\mu}_{\mathrm{s}}+\mu_{\mathrm{b}})} \;\leq\; 1-\alpha \tag{7.19}$$

As is customary in neutrino experiments, the Feldman-Cousins method is used to calculate $\hat{\mu}_{\mathrm{s}}$ [119]. In this analysis, a confidence level of $\alpha = 90\,\%$ is implied.

The average upper limit from an ensemble of repeated experiments in which the expected number of signal events is zero is referred to as the signal sensitivity $\bar{\mu}_{\mathrm{s}}(\mu_{\mathrm{b}})$. It is defined as the sum of the upper limits for every possible value of n_{det}, weighted by their Poisson probability of occurrence [119]:

$$\bar{\mu}_{\mathrm{s}}(\mu_{\mathrm{b}}) \;\equiv\; \sum_{n_{\mathrm{det}}=0}^{\infty} \hat{\mu}_{\mathrm{s}}(n_{\mathrm{det}}, \mu_{\mathrm{b}})\, \frac{\mu_{\mathrm{b}}^{n_{\mathrm{det}}}}{n_{\mathrm{det}}!}\, e^{-\mu_{\mathrm{b}}} \tag{7.20}$$

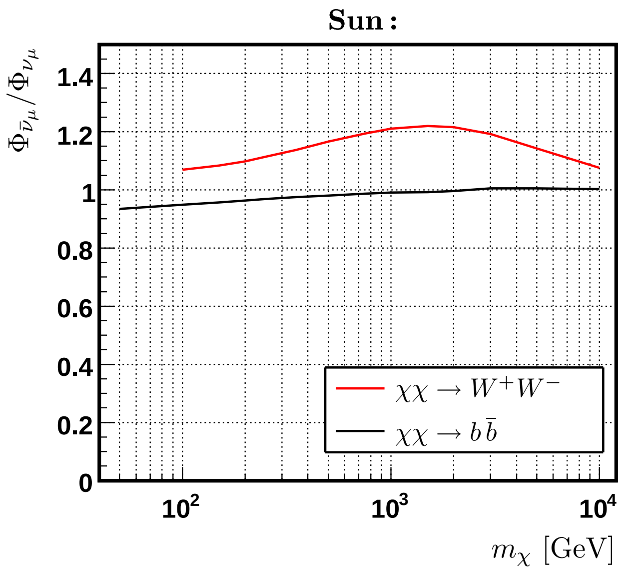

Figure 7.16:

The ratio between the integrated anti-neutrino flux $\Phi_{\bar{\nu}_\mu}$ and the integrated neutrino flux Φ_{ν_μ} at the surface of the Earth from $\chi\chi \to W^+W^-$ and $\chi\chi \to b\,\bar{b}$ annihilation in the Sun, as a function of the WIMP mass m_χ.

Upper limit on the integrated neutrino flux $\hat{\Phi}_\nu$

In general, the integrated neutrino and anti-neutrino fluxes from WIMP annihilation in an astrophysical object, Φ_{ν_μ} and $\Phi_{\bar{\nu}_\mu}$, and the total number of detected events from this flux, $n_\text{s} \equiv n_{\nu_\mu} + n_{\bar{\nu}_\mu}$, are related by equation (7.16) :

$$n_\text{s} \;=\; \left(\Phi_{\nu_\mu}\, A_{\text{eff},\nu_\mu} \;+\; \Phi_{\bar{\nu}_\mu}\, A_{\text{eff},\bar{\nu}_\mu}\right)\, t_\text{det} \tag{7.21}$$

where A_{eff,ν_μ} and $A_{\text{eff},\bar{\nu}_\mu}$ are the weighted averages of the (anti-)neutrino effective area with respect to the effective livetimes of each of the two distinct `highThreshold` data-taking periods, and t_det is the total effective livetime. The relationship between the total neutrino flux $\Phi_\nu \equiv \Phi_{\nu_\mu} + \Phi_{\bar{\nu}_\mu}$ and the total number of detected events n_s can be derived by considering the ratio of the integrated anti-neutrino flux and the integrated neutrino flux, $\gamma \equiv \Phi_{\bar{\nu}_\mu}/\Phi_{\nu_\mu}$:

$$n_\text{s} \;=\; \Phi_{\nu_\mu}\left(A_{\text{eff},\nu_\mu} \;+\; \gamma A_{\text{eff},\bar{\nu}_\mu}\right) t_\text{det} \;=\; \Phi_\nu\, \bar{A}_{\text{eff},\nu}\, t_\text{det} \tag{7.22}$$

where

$$\bar{A}_{\text{eff},\nu} \;\equiv\; \frac{A_{\text{eff},\nu_\mu} \;+\; \gamma A_{\text{eff},\bar{\nu}_\mu}}{1 \;+\; \gamma} \tag{7.23}$$

The flux ratio γ can be obtained from the WIMP annihilation simulations discussed in section 3.3.1. The flux ratios for $\chi\chi \to W^+W^-$ and $\chi\chi \to b\,\bar{b}$ annihilation in the Sun are shown as a function of the WIMP mass m_χ in figure 7.16. As can be seen, the expected anti-neutrino flux from $\chi\chi \to W^+W^-$ is larger than the corresponding neutrino flux, and vice versa for $\chi\chi \to b\,\bar{b}$. These effects are due to the (anti-)neutrino interaction cross section with matter and by the MSW effect in the Sun, respectively. The flux ratios for WIMP annihilation at the Galactic Centre are equal to one (not shown), as expected.

The upper limit on the integrated neutrino flux, $\hat{\Phi}_\nu$, is defined by scaling the integrated neutrino flux with the ratio of the upper limit on the number of signal events $\hat{\mu}_\mathrm{s}$ and the expected number of signal events n_s [120]. Hence, by using equation (7.22) :

$$\hat{\Phi}_\nu \;\equiv\; \Phi_\nu \frac{\hat{\mu}_\mathrm{s}}{n_\mathrm{s}} \;=\; \frac{\hat{\mu}_\mathrm{s}}{\bar{A}_{\mathrm{eff},\nu}\, t_\mathrm{det}} \tag{7.24}$$

The neutrino flux sensitivity refers to the average upper limit on the integrated neutrino flux for an ensemble of experiments in which the expected number of signal events is zero. It is defined similar to the upper limit on the integrated neutrino flux equation (7.24) :

$$\bar{\Phi}_\nu \;\equiv\; \Phi_\nu \frac{\bar{\mu}_\mathrm{s}}{n_\mathrm{s}} \;=\; \frac{\bar{\mu}_\mathrm{s}}{\bar{A}_{\mathrm{eff},\nu}\, t_\mathrm{det}} \tag{7.25}$$

7.7.2 Cone size optimisation

Since the angular resolution of a neutrino telescope depends on the neutrino energy, the cone size can be optimised. In this analysis, the cone size is optimised as a function of the WIMP mass m_χ, for a specific WIMP annihilation process in an astrophysical object. The optimisation procedure is based on the maximisation of the signal-to-background ratio $\mu_\mathrm{s}/\mu_\mathrm{b}$ in the cone with the intent to minimise the upper limit on the integrated neutrino flux from WIMP annihilation in the object, $\hat{\Phi}_\nu$. Following equation (7.25), the neutrino effective area including cone selection efficiency and the signal sensitivity of the cone are used as measures for μ_s and μ_b, respectively.

Signal efficiency

The neutrino effective area $\bar{A}_{\mathrm{eff},\nu}(m_\chi)$ given by equations (7.15) and (7.23), including the additional constraint that $\bar{A}_{\mathrm{eff},\nu}(m_\chi)$ is zero if the angle between the neutrino direction from the object $\hat{r}$ and the reconstructed muon direction $\hat{r}_\mathrm{reco}$ is larger than the half-aperture of the cone θ_cone, is used as a measure for the expected number of signal events in the cone :

$$\bar{A}_{\mathrm{eff},\nu}(m_\chi, \theta_\mathrm{cone}) \;\equiv\; \begin{cases} \bar{A}_{\mathrm{eff},\nu}(m_\chi) & \text{if} \quad \arccos(\hat{r}\cdot\hat{r}_\mathrm{reco}) < \theta_\mathrm{cone} \\ 0 & \text{if} \quad \arccos(\hat{r}\cdot\hat{r}_\mathrm{reco}) > \theta_\mathrm{cone} \end{cases} \tag{7.26}$$

The neutrino effective area $\bar{A}_{\mathrm{eff},\nu}(m_\chi, \theta_\mathrm{cone})$ for $\chi\chi \to W^+W^-$ and the $\chi\chi \to b\,\bar{b}$ annihilation in the Sun and the Galactic Centre is shown as a function of the half-aperture of the cone θ_cone in figure 7.17, for various values of the WIMP mass m_χ. As can be seen from this figure, $\bar{A}_{\mathrm{eff},\nu}(m_\chi, \theta_\mathrm{cone})$ increases with cone size until it stabilises at a value close to $A_{\mathrm{eff},\nu}(m_\chi)$ shown in figures 7.14 and 7.15. This is due to the cone selection efficiency, which decreases for smaller cone sizes.

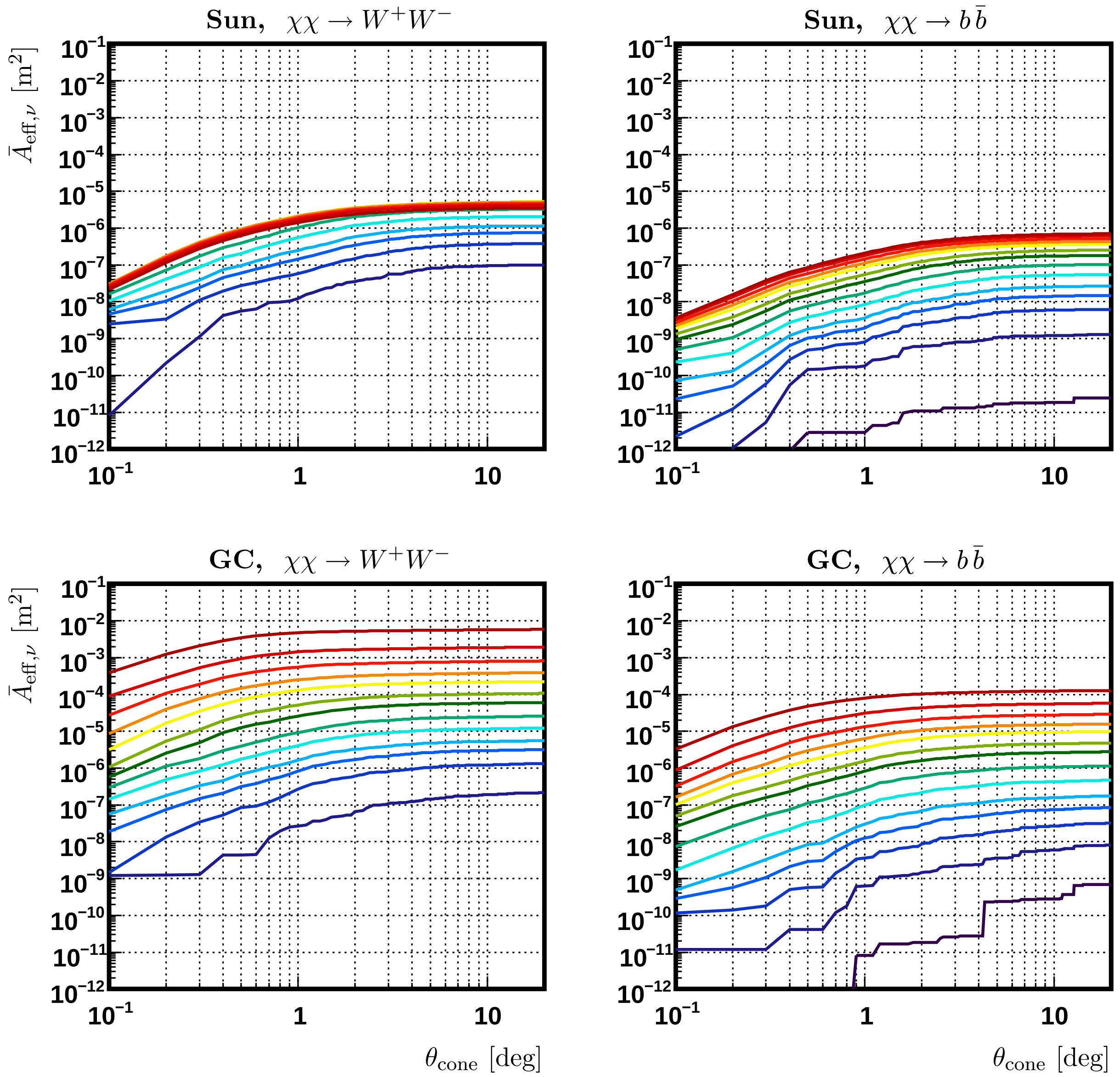

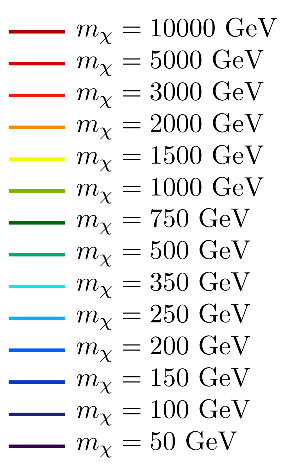

Figure 7.17:

The neutrino effective area $\bar{A}_{\mathrm{eff},\nu}(m_\chi, \theta_{\mathrm{cone}})$ for $\chi\chi \to W^+W^-$ and $\chi\chi \to b\,\bar{b}$ annihilation in the Sun and the Galactic Centre, as a function of the half-aperture of the cone θ_{cone} for various values of the WIMP mass m_χ.

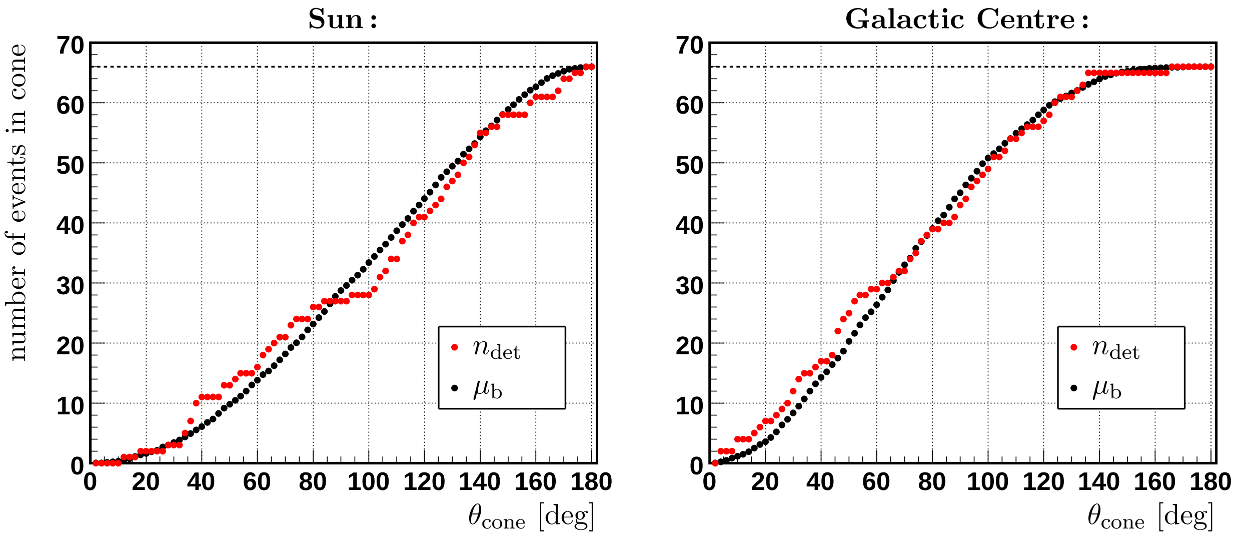

Figure 7.18: The number of detected events in a cone around the Sun and the Galactic Centre, n_{det}, and the number of randomised data events in the cone, μ_{b}, as a function of the half-aperture of the cone θ_{cone}.

Cone sensitivity

The signal sensitivity of the cone $\bar{\mu}_{\text{s}}(\mu_{\text{b}})$ as defined in equation (7.20) is used as a measure for the expected background in the cone. By using the signal sensitivity instead of the upper limit on the number of signal events, the optimisation procedure does not depend on the detected number of events in the cone. This choice ensures that the analysis is not biased by the data.

The background in the cone can be estimated from the atmospheric neutrino simulations and from data. In the latter case, a background sample is created by randomising the reconstructed directions and the detection times of the selected neutrino candidates, normalised to the number of selected neutrino candidates. In this way the analysis is not biased due to the use of the selected neutrino candidates themselves, i.e. the 'blindness' of the analysis is preserved. In this analysis, the randomised data set is used to derive the signal sensitivity, while the atmospheric neutrino simulations are used to cross-check the result.

The number of detected events in a cone around the Sun and the Galactic Centre, n_{det}, and the number of randomised data events in the cone, μ_{b}, are shown as a function of the half-aperture of the cone θ_{cone} in figure 7.18. As can be seen from this figure, n_{det} and μ_{b} are always larger for the GC than for the Sun for a particular cone size. This is due to the zenith angle distribution of the GC, which lies predominantly below the ANTARES horizon. Hence, the number of atmospheric neutrinos in a cone around the GC is expected to be larger than for the Sun, since the Sun is only below the horizon for ~50 % of the time (see figures 7.2 and 7.3).

The expected background in a cone around the Sun and the Galactic Centre derived from the randomised data set is compared to the expected background in the cone de-

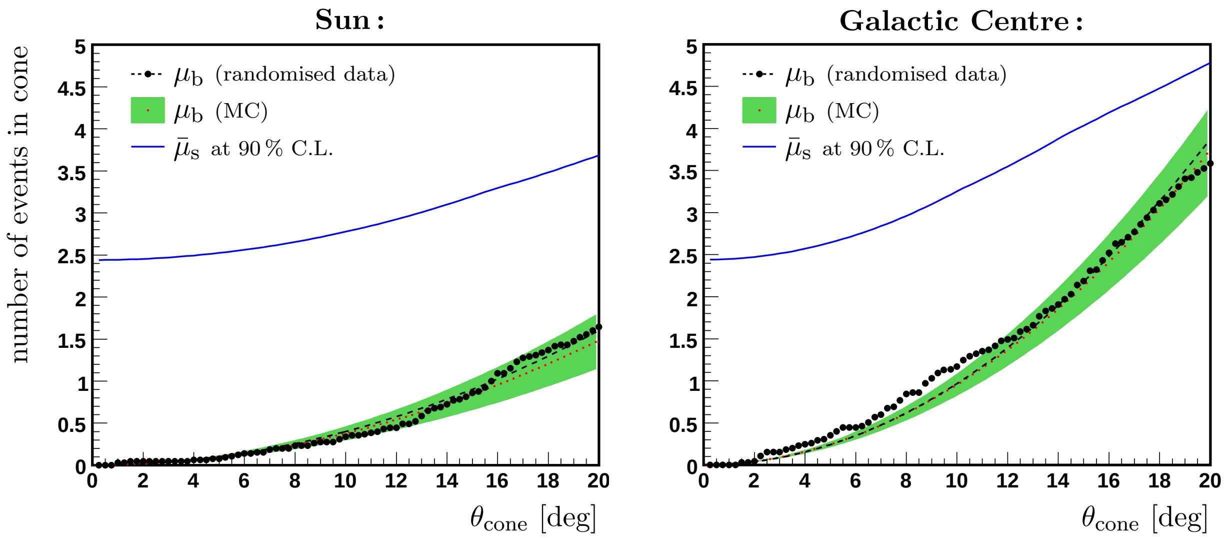

Figure 7.19: The number of expected background events in a cone around the Sun and the Galactic Centre μ_b, from randomised data and simulation, as a function of the half-aperture of the cone θ_{cone}. The expected background from simulation is normalised to the number of selected neutrino candidates in data and shown in green. The expected background from randomised data is indicated by black markers and fitted with a second order polynomial, as shown by the dashed lines. The fitted $\mu_b(\theta_{cone})$ is used to derive the signal sensitivity $\bar{\mu}_s(\theta_{cone})$ at 90 % C.L., as shown by the blue lines.

rived from the atmospheric neutrino simulation. For small cone angles, the latter can be approximated by weighting the zenith-azimuth distribution of the selected atmospheric neutrino candidates $N(\theta, \phi)$ with the directional probability density function for neutrinos from the object $p_{\hat{r}}(\theta, \phi)$, integrating over all angles θ and ϕ and multiplying the outcome with the ratio of the solid angle of the cone and the zenith-azimuth bin size considered in $N(\theta, \phi)$:

$$\mu_b(\text{MC}) \approx \sum_{\theta_i,\,\phi_i}^{\text{all bins}} N(\theta_i, \phi_i)\; p_{\hat{r}}(\theta_i, \phi_i)\; \frac{2\pi\,(1 - \cos(\theta_{cone}))}{\Delta\theta_i\,\Delta\phi_i} \tag{7.27}$$

The expected background in a cone around the Sun and the Galactic Centre derived from the randomised data set and from the atmospheric neutrino simulation is shown as a function of the half-aperture of the cone θ_{cone} in figure 7.19. The expected background from simulation is normalised to the number of selected neutrino candidates in data, and shown in green. The expected background from the randomised data set is indicated by black markers. The latter is fitted with a second order polynomial, since the background in the cone is proportional to the solid angle of the cone. Hence, for small cone size, $\mu_b \propto \theta^2_{cone}$. The fitted $\mu_b(\theta_{cone})$ are indicated by dashed lines in figure 7.19. As can be seen, the expected background in a cone around the Sun and the Galactic Centre

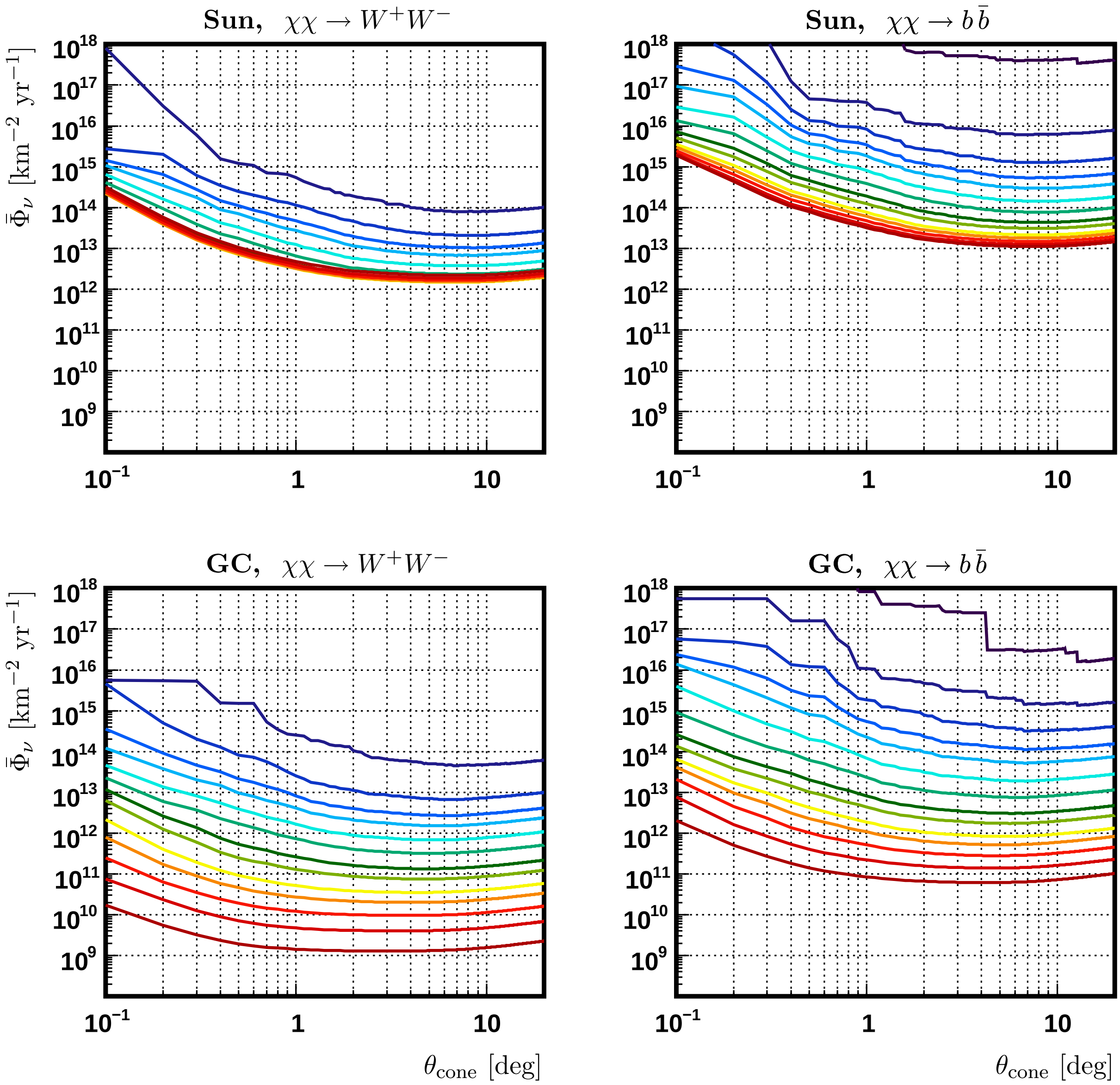

Figure 7.20:

The neutrino flux sensitivity $\bar{\Phi}_\nu(m_\chi, \theta_{\text{cone}})$ at 90 % C.L. for $\chi\chi \to W^+W^-$ and $\chi\chi \to b\,\bar{b}$ annihilation in the Sun and the Galactic Centre, as a function of the half-aperture of the cone θ_{cone}, for various values of the WIMP mass m_χ.

derived from the randomised data set agrees with the atmospheric neutrino simulation. The fitted $\mu_\mathrm{b}(\theta_\mathrm{cone})$ is used in equation (7.20) to derive the signal sensitivity $\bar{\mu}_\mathrm{s}(\theta_\mathrm{cone})$ at 90 % C.L.. The results are indicated by blue lines in figure 7.19.

Optimum cone size

After deriving the neutrino effective area including cone selection efficiency for the Sun and the Galactic Centre, $A_{\mathrm{eff},\nu}(m_\chi, \theta_\mathrm{cone})$, and the signal sensitivity of a cone around these objects, $\bar{\mu}_\mathrm{s}(\theta_\mathrm{cone})$, the neutrino flux sensitivity, $\bar{\Phi}_\nu(m_\chi, \theta_\mathrm{cone})$, can be calculated from equation (7.25). The neutrino flux sensitivity at 90 % C.L. for $\chi\chi \rightarrow W^+W^-$ and $\chi\chi \rightarrow b\,\bar{b}$ annihilation in the Sun and the Galactic Centre is shown as a function of the half-aperture of the cone θ_cone in figure 7.20, for various values of the WIMP mass m_χ. As can be seen, the neutrino flux sensitivity increases for smaller cone sizes. This is due to the loss of signal in small cones. For larger cone sizes, the neutrino flux sensitivity increases as well due to the increase of the background accepted by the cone.

The optimum cone size θ_cone for a particular annihilation channel in an astrophysical object and a particular WIMP mass m_χ, is the size of the cone which minimises the corresponding neutrino flux sensitivity. The optimum cone size $\hat{\theta}_\mathrm{cone}$ for $\chi\chi \rightarrow W^+W^-$ and $\chi\chi \rightarrow b\,\bar{b}$ annihilation in the Sun and the Galactic Centre is shown as a function of the WIMP mass m_χ in figure 7.21. As can be seen, the optimum cone size is slightly smaller for the $\chi\chi \rightarrow W^+W^-$ process, and larger for lower values of m_χ in general. This is due to the neutrino energy spectrum of the $\chi\chi \rightarrow W^+W^-$ process which is harder than for $\chi\chi \rightarrow b\,\bar{b}$, and the decrease of the average scattering angle between the neutrino and the induced muon for higher energy.

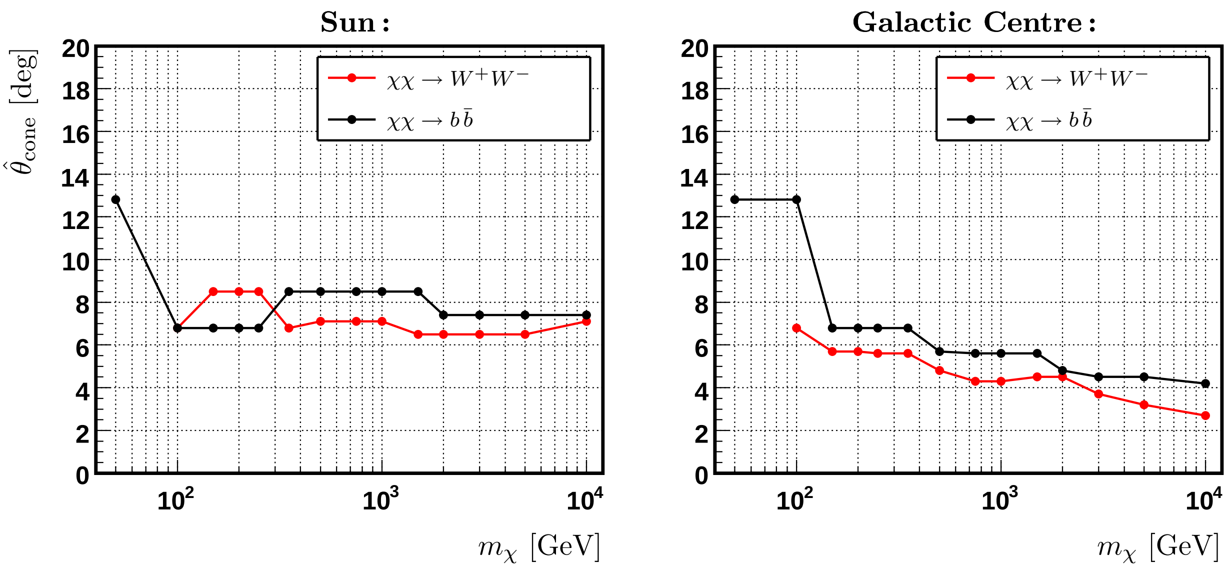

Figure 7.21: The optimum cone size $\hat{\theta}_\mathrm{cone}$ which minimises the neutrino flux sensitivity $\bar{\Phi}_\nu(m_\chi, \theta_\mathrm{cone})$ at 90 % C.L. for $\chi\chi \rightarrow W^+W^-$ and $\chi\chi \rightarrow b\,\bar{b}$ annihilation in the Sun and the Galactic Centre, for various values of the WIMP mass m_χ.

7.8 Exclusion limits

The optimum cone size $\hat{\theta}_{\rm cone}(m_\chi)$ shown in figure 7.21 is used to calculate the upper limit on the integrated neutrino flux $\Phi_\nu(m_\chi)$ and the corresponding upper limit on the integrated muon flux $\Phi_\mu(m_\chi)$, for $\chi\chi \to W^+W^-$ and $\chi\chi \to b\,\bar{b}$ annihilation in the Sun and the Galactic Centre. The results are compared to results from other experiments and the theoretical predictions from mSUGRA presented in chapter 4.

7.8.1 Upper limit on the number of signal events

The upper limit on the integrated neutrino flux, $\hat{\Phi}_\nu(m_\chi, \hat{\theta}_{\rm cone})$, for $\chi\chi \to W^+W^-$ and $\chi\chi \to b\,\bar{b}$ annihilation in the Sun and the Galactic Centre, can be calculated from equation (7.24), if the upper limit on the number of signal events in the optimal cone, $\hat{\mu}_{\rm s}(\hat{\theta}_{\rm cone})$, is known. The upper limit on the number of signal events in a cone around the Sun and the Galactic Centre is shown at 90 % C.L. as a function of the half-aperture of the cone $\theta_{\rm cone}$ in figure 7.22, along with the corresponding signal sensitivity $\bar{\mu}_{\rm s}(\theta_{\rm cone})$. The number of detected events $n_{\rm det}(\theta_{\rm cone})$ and the number of expected background events $\mu_{\rm b}(\theta_{\rm cone})$ in the cone are also shown. As can be seen, the upper limit on the number of signal events is slightly lower than the signal sensitivity for (almost) all optimum cones around the Sun. In contrast, the upper limit on the number of signal events is about a factor of 2 higher than the signal sensitivity for all optimum cones around the Galactic Centre. These differences are due to random fluctuations of the background in the data sample with respect to the expected background $\mu_{\rm b}$.

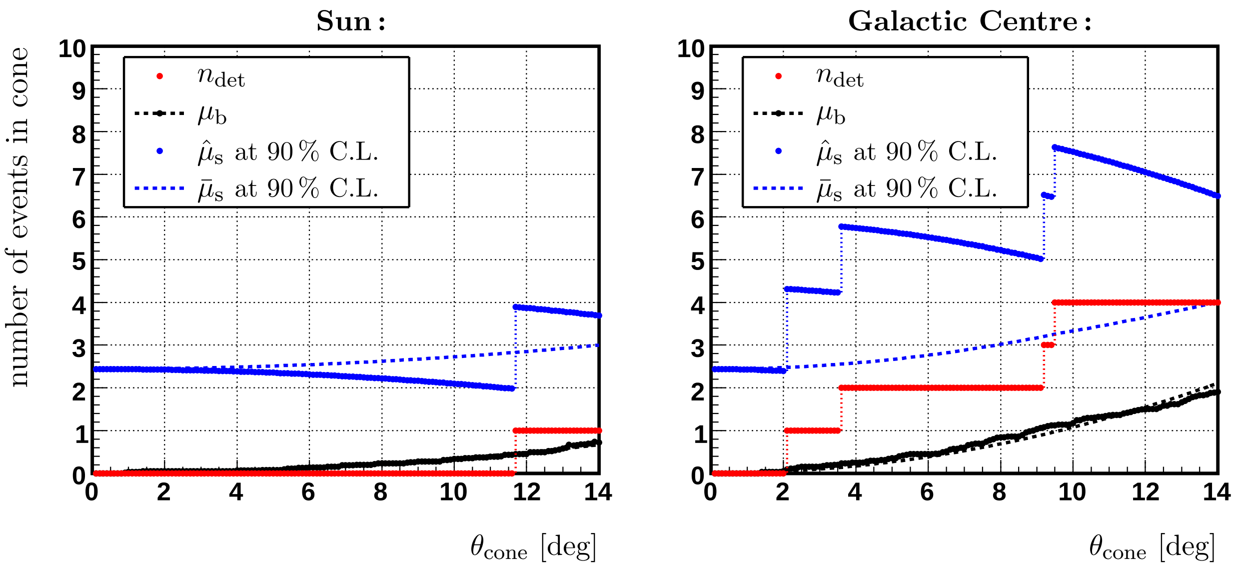

Figure 7.22: The upper limit on the number of signal events, $\hat{\mu}_{\rm s}(n_{\rm det}, \mu_{\rm b})$ at 90 % C.L., and the corresponding signal sensitivity $\bar{\mu}_{\rm s}(\mu_{\rm b})$ in a cone around the Sun and the Galactic Centre, as a function of the half-aperture of the cone $\theta_{\rm cone}$. The number of detected events $n_{\rm det}$ and the number of expected background events $\mu_{\rm b}$ in the cone are also shown.

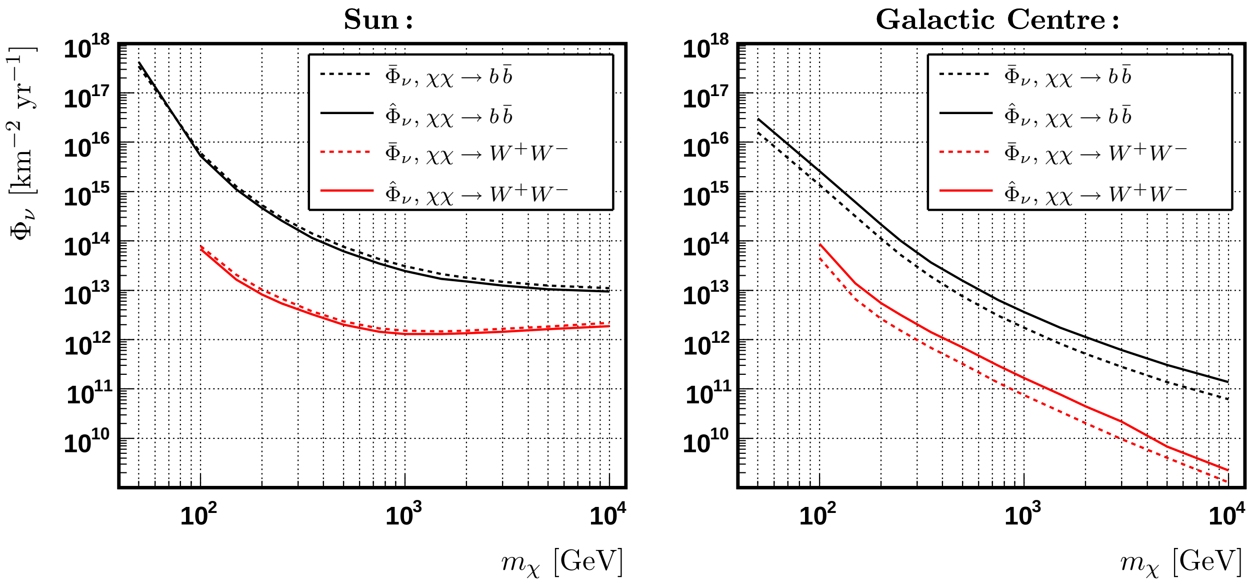

Figure 7.23: The upper limit on the integrated neutrino flux, $\hat{\Phi}_\nu(m_\chi)$ at 90 % C.L., and the corresponding neutrino flux sensitivity $\bar{\Phi}_\nu(m_\chi)$, for $\chi\chi \to W^+W^-$ and $\chi\chi \to b\,\bar{b}$ annihilation in the Sun and the Galactic Centre, as a function of the WIMP mass m_χ.

7.8.2 Upper limit on the integrated neutrino flux

The upper limit on the integrated neutrino flux $\hat{\Phi}_\nu(m_\chi, \hat{\theta}_{\text{cone}})$ at 90 % C.L., and the corresponding neutrino flux sensitivity $\bar{\Phi}_\nu(m_\chi, \hat{\theta}_{\text{cone}})$, for $\chi\chi \to W^+W^-$ and $\chi\chi \to b\,\bar{b}$ annihilation in the Sun and the Galactic Centre, are calculated from equations (7.24) and (7.25) by using the neutrino effective area $\bar{A}_{\text{eff},\nu}(m_\chi, \hat{\theta}_{\text{cone}})$ shown in figure 7.17, and the upper limit on the number of signal events $\hat{\mu}_{\text{s}}(\hat{\theta}_{\text{cone}})$ and the signal sensitivity $\bar{\mu}_{\text{s}}(\hat{\theta}_{\text{cone}})$ shown in figure 7.22.

The results are shown as a function of the WIMP mass m_χ in figure 7.23. As can be seen, the neutrino flux limit and sensitivity are lower for $\chi\chi \to W^+W^-$, since the neutrino effective area of this annihilation channel is higher than for $\chi\chi \to b\,\bar{b}$. The neutrino flux limit and sensitivity are lower for the Galactic Centre, especially for larger WIMP masses. This is due to the suppression of the neutrino energy spectra for the Sun, caused by energy loss and absorption of neutrinos in the Sun. The neutrino flux limit is lower than the neutrino flux sensitivity for the Sun, and vice versa for the Galactic Centre. This is expected from the difference between the upper limit on the number of signal events and the signal sensitivity in the cone for the data-taking period considered in this analysis.

7.8.3 The muon effective area

In neutrino experiments, it is customary to publish results on the observed muon flux instead of the neutrino flux. Hence, for comparison with other experiments, the neutrino flux limits have to be converted into limits on the induced muon flux. This can be done by considering the relationship between a muon flux at a detector Φ_μ due to a neutrino flux at the surface of the Earth Φ_ν. By using the quantities defined in equation (7.1), these fluxes are related by [105]

$$\begin{aligned}
\frac{d\Phi_\mu(E_\nu,\hat{r})}{dE_\nu} &= \frac{d\Phi_\nu(E_\nu,\hat{r})}{dE_\nu}\, P_{\rm Earth}(E_\nu,\hat{r})\, \rho\, N_A \int_0^{E_\nu} \frac{d\sigma_{\rm CC}(E_\nu,E_\mu)}{dE_\mu}\, R_\mu(E_\mu)\, dE_\mu \\
&= \frac{d\Phi_\nu(E_\nu,\hat{r})}{dE_\nu}\, P_{\rm Earth}(E_\nu,\hat{r})\, \rho\, N_A\, \sigma_{\rm CC}(E_\nu)\, R_{\rm eff}(E_\nu) \\
&= \frac{d\Phi_\nu(E_\nu,\hat{r})}{dE_\nu}\, \frac{A_{{\rm eff},\nu}(E_\nu,\hat{r})}{V_{\rm eff}(E_\nu,\hat{r})}\, R_{\rm eff}(E_\nu) \\
&= \frac{d\Phi_\nu(E_\nu,\hat{r})}{dE_\nu}\, \frac{A_{{\rm eff},\nu}(E_\nu,\hat{r})}{A_{{\rm eff},\mu}(E_\nu,\hat{r})} \qquad (7.28)
\end{aligned}$$

where $R_\mu(E_\mu)$ is the propagation distance of a muon with energy E_μ, the effective muon range $R_{\rm eff}(E_\nu)$ is the average propagation distance of a muon produced by a neutrino with energy E_ν, and the *muon effective area* $A_{{\rm eff},\mu}(E_\nu,\hat{r})$ is the area with which a muon flux must be multiplied to determine the detection rate :

$$A_{{\rm eff},\mu}(E_\nu,\hat{r}) \;\equiv\; \frac{V_{\rm eff}(E_\nu,\hat{r})}{R_{\rm eff}(E_\nu)} \qquad (7.29)$$

The muon effective area $A_{{\rm eff},\mu}$ of the ANTARES detector for the data-taking conditions and all data-selection criteria considered in this analysis is derived from the

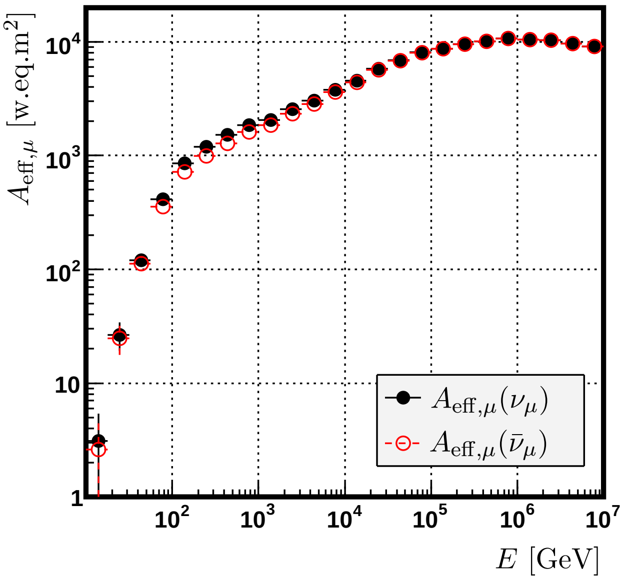

Figure 7.24:

The muon effective area $A_{{\rm eff},\mu}$ of the ANTARES detector for the data-taking conditions and all data-selection criteria considered in this analysis, averaged over all directions, as a function of the neutrino energy E.

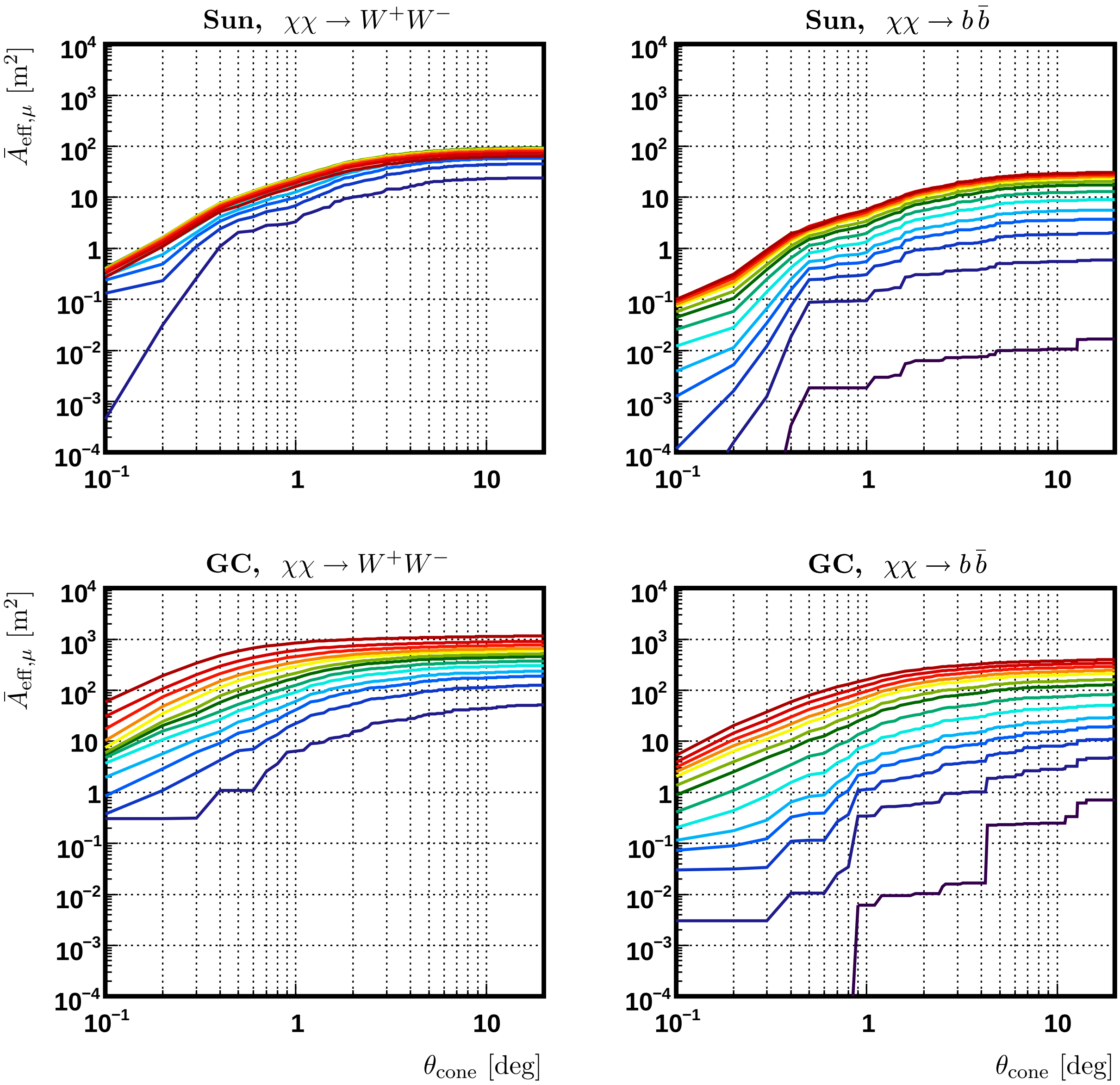

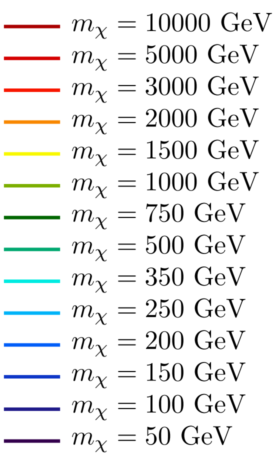

Figure 7.25:

The muon effective area $\bar{A}_{\mathrm{eff},\mu}(m_\chi, \theta_{\mathrm{cone}})$ for $\chi\chi \to W^+W^-$ and $\chi\chi \to b\,\bar{b}$ annihilation in the Sun and the Galactic Centre, as a function of the half-aperture of the cone θ_{cone} for various values of the WIMP mass m_χ.

simulated neutrino samples. The weighted average with respect to the effective live-times of each of the two distinct `highThreshold` data-taking periods is shown as a function of the neutrino energy in figure 7.24, averaged over all neutrino directions. As can be seen, the anti-muon effective area is slightly smaller for $E_\nu \lesssim 10^5$ GeV. This is caused by differences in the interaction of neutrinos and anti-neutrinos with nucleons.

The muon effective area including cone selection efficiency, $\bar{A}_{\mathrm{eff},\mu}(m_\chi, \theta_{\mathrm{cone}})$, for muons induced by neutrinos from $\chi\chi \to X$ annihilation in an astrophysical object is defined similarly to the corresponding neutrino effective area in equations (7.15), (7.23) and (7.26). The muon effective area including cone selection efficiency for muons induced by neutrinos from $\chi\chi \to W^+W^-$ and the $\chi\chi \to b\,\bar{b}$ annihilation in the Sun and the Galactic Centre is shown as a function of the half-aperture of the cone θ_{cone} in figure 7.25, for various values of the WIMP mass m_χ.

7.8.4 Upper limit on the integrated muon flux

Following the derivation of equation (7.11), the relationship between a muon flux at the detector, $\Phi_\mu^{\circledS}$, caused by a neutrino flux at the surface of the Earth from WIMP annihilation in an astrophysical object, $\Phi_\nu^{\circledS}$, and the muon detection rate, $R_{\mathrm{det}}^{\circledS}$, can be written as

$$\begin{aligned} R_{\mathrm{det}}^{\circledS}(m_\chi, \hat{r}) &= \int_0^{m_\chi} \frac{d\Phi_\nu^{\circledS}(m_\chi, E_\nu, \hat{r})}{dE_\nu}\, A_{\mathrm{eff},\nu}(E_\nu, \hat{r})\, dE_\nu \\ &= \int_0^{m_\chi} \frac{d\Phi_\mu^{\circledS}(m_\chi, E_\nu, \hat{r})}{dE_\nu}\, A_{\mathrm{eff},\mu}(E_\nu, \hat{r})\, dE_\nu \end{aligned} \tag{7.30}$$

The upper limit on the integrated muon flux, $\hat{\Phi}_\mu(m_\chi, \hat{\theta}_{\mathrm{cone}})$, and the muon flux sensitivity, $\bar{\Phi}_\mu(m_\chi, \hat{\theta}_{\mathrm{cone}})$, for $\chi\chi \to X$ annihilation in an astrophysical object are defined similarly to the neutrino upper limit and sensitivity in equations (7.24) and (7.25):

$$\hat{\Phi}_\mu(m_\chi, \hat{\theta}_{\mathrm{cone}}) \equiv \frac{\hat{\mu}_{\mathrm{s}}(\hat{\theta}_{\mathrm{cone}})}{\bar{A}_{\mathrm{eff},\mu}(m_\chi, \hat{\theta}_{\mathrm{cone}})\; t_{\mathrm{det}}} \tag{7.31}$$

$$\bar{\Phi}_\mu(m_\chi, \hat{\theta}_{\mathrm{cone}}) \equiv \frac{\bar{\mu}_{\mathrm{s}}(\hat{\theta}_{\mathrm{cone}})}{\bar{A}_{\mathrm{eff},\mu}(m_\chi, \hat{\theta}_{\mathrm{cone}})\; t_{\mathrm{det}}} \tag{7.32}$$

The muon flux limit and sensitivity at 90 % C.L. for $\chi\chi \to W^+W^-$ and the $\chi\chi \to b\,\bar{b}$ annihilation in the Sun and the Galactic Centre are shown as a function of the WIMP mass m_χ in figure 7.26. As can be seen, the muon flux limit and sensitivity are not as dependent on the WIMP mass as the neutrino flux limit and sensitivity shown in figure 7.23. This is due to the definition of the muon flux in equation (7.28), which includes the neutrino-nucleon interaction cross section and the effective muon range.

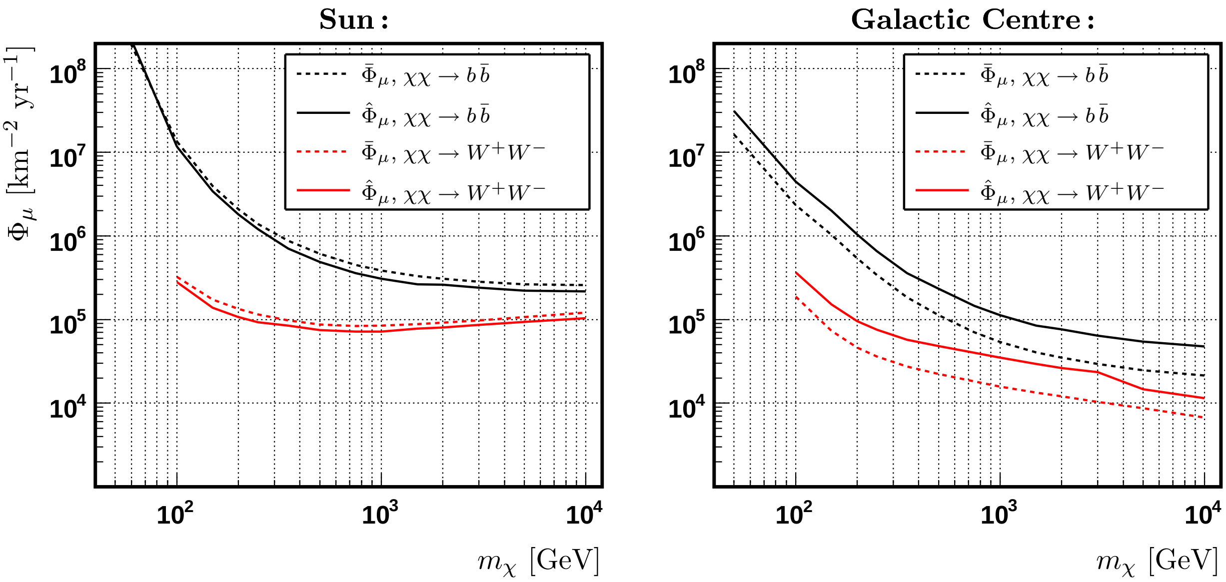

Figure 7.26: The upper limit on the integrated muon flux, $\hat{\Phi}_\mu(m_\chi)$ at 90 % C.L., and the corresponding muon flux sensitivity $\bar{\Phi}_\mu(m_\chi)$, for $\chi\chi \to W^+W^-$ and $\chi\chi \to b\,\bar{b}$ annihilation in the Sun and the Galactic Centre, as a function of the WIMP mass m_χ.

7.8.5 Upper limit on the spin-dependent WIMP-proton cross section

As mentioned in section 4.3.1, the neutrino-induced muon flux in a neutrino detector from WIMP annihilation in an astrophysical object can be related to the WIMP annihilation rate in that object. There is a direct correlation between the annihilation rate and the SI/SD WIMP-nucleon cross section, assuming the capture and annihilation rates of WIMPs in the object are in equilibrium and the capture process is dominated by the SI or SD cross section only. For the SD neutralino-proton cross section and neutralino annihilation in the Sun in mSUGRA, these assumptions are justified as shown in figures 4.9 and 4.13. The conversion factor $\kappa_{\chi p}^{\mathrm{SD}}$ between the integrated muon flux Φ_μ^{Sun} from WIMP annihilation in the Sun and the spin-dependent WIMP-proton cross section $\sigma_{\chi p}^{\mathrm{SD}}$ [67]

$$\kappa_{\chi p}^{\mathrm{SD}} \equiv \frac{\sigma_{\chi p}^{\mathrm{SD}}}{\Phi_\mu^{\mathrm{Sun}}} \tag{7.33}$$

is shown as a function of the WIMP mass m_χ in the left panel of figure 7.27, assuming the annihilation process is dominated by $\chi\chi \to W^+W^-$ and $\chi\chi \to b\,\bar{b}$.

The upper limits and sensitivities at 90 % C.L. on the SD WIMP-proton cross section, derived by applying equation (7.33) to the muon flux limits and sensitivities from the Sun shown in figure 7.26, are shown as a function of the WIMP mass m_χ in the right panel of figure 7.27.

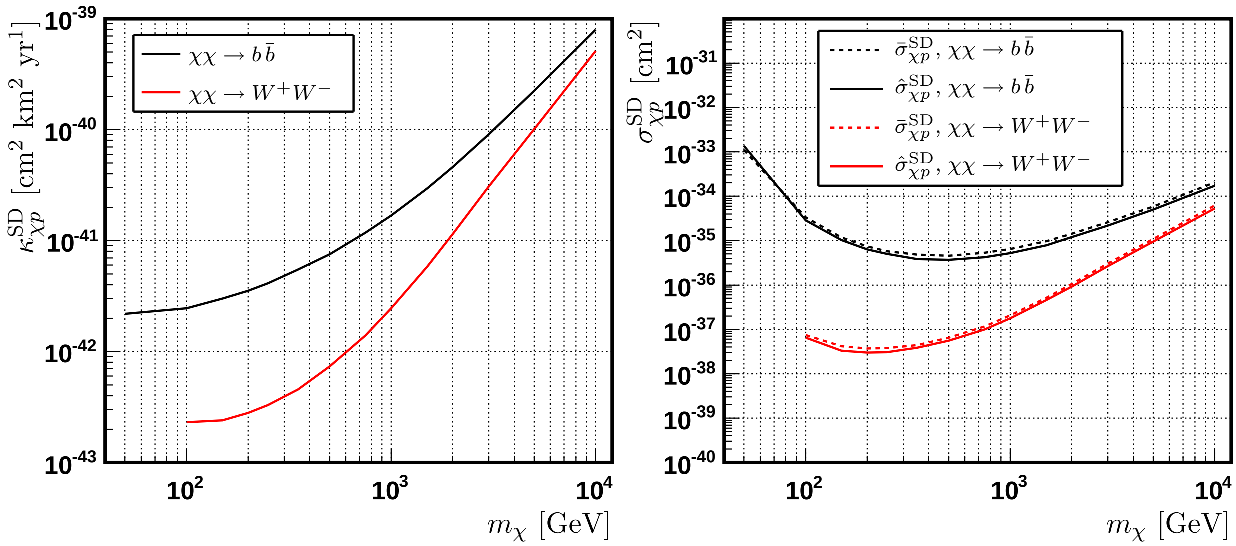

Figure 7.27: The conversion factor $\kappa_{\chi p}^{\rm SD}$ for $\chi\chi \to W^+W^-$ and $\chi\chi \to b\,\bar{b}$ annihilation in the Sun [67] and the upper limits at 90 % C.L. on the SD WIMP-proton cross section, as a function of the WIMP mass m_χ.

7.9 Conclusion

In this chapter, data from the ANTARES neutrino telescope is analysed to search for an excess of neutrinos from WIMP annihilation in the Sun and the Galactic Centre, as an indication for the presence of dark matter. After defining the data-selection criteria to suppress the atmospheric muon flux, the detection efficiency is calculated and a cone search in the direction of the Sun and the Galactic Centre during data-taking is performed. The search results do not show a significant excess of detected neutrino candidates for either case. The number of detected neutrino candidates is compatible with the expected atmospheric neutrino flux. The upper limit on the number of neutrinos from WIMP annihilation in the Sun and the Galactic Centre during data-taking is calculated. The outcome is combined with the detection efficiency to calculate the upper limit on the neutrino and muon flux from WIMP annihilation in the Sun and the Galactic Centre during data-taking. Finally, the muon flux limit from the Sun is converted into a limit on the spin-dependent WIMP-proton cross section.

A comparison between the analysis results of this chapter and results from other experiments, as well as the theoretical predictions from mSUGRA presented in chapter 4, is given in the next chapter.

Chapter 8

Summary and conclusions

The nature of dark matter is widely considered as one of the major unsolved mysteries in modern physics. Experimental observations on cosmological length scales indicate that dark matter comprises about 23 % of the total energy density of the present observational Universe in the standard cosmological model. In contrast, less than 5 % of the total energy density consists of ordinary baryonic matter such as stars and interstellar material, while the remainder is attributed to dark energy. Various independent observations at smaller length scales support the suggestion that 80 % of all matter in the Universe is non-luminous. The suggestion that dark matter has to be non-baryonic is in agreement with predictions from primordial nucleosynthesis and results from gravitational microlensing experiments. However, direct evidence of the existence of dark matter and a concrete understanding of its nature have so far remained elusive.

Candidates for dark matter include new kinds of elementary particles produced in the early Universe which do not participate in the electromagnetic or strong interactions. The observed structures in the Universe indicate that these particles had to be non-relativistic at the time of decoupling from the thermal plasma. The most favoured class of cold dark matter candidates are the so-called weakly interacting massive particles (WIMPs). Various well-motivated extensions of the Standard Model contain elementary particles that possess WIMP characteristics. Basic thermodynamical arguments imply that the present value of the dark matter energy density can be explained by any theory which contains a WIMP which has an interaction probability and mass similar to the gauge bosons of the weak interaction.

This is the case for many supersymmetric models. Supersymmetry is regarded as a natural extension of the Standard Model. It offers several solutions to some known problems and short-comings of the Standard Model by introducing a new symmetry involving transformations between bosons and fermions. Supersymmetry predicts the existence of a so-called superpartner for every Standard Model particle. Since none of these superpartners have been detected yet, supersymmetry must be broken at the electro-weak scale. To reduce the number of free parameters in the theory due to supersymmetry breaking, supersymmetry is typically combined with the idea of grand unification, which is motivated by the apparent unification of elementary forces at the so-called grand unification scale. In so-called minimal supergravity (mSUGRA), only four additional parameters and a sign are introduced. In most of mSUGRA parameter space, the lightest superpartner is the lightest of the four neutralinos, which are combinations of the superpartners of the electro-weak gauge and higgs bosons. The neutralino is a favourite amongst WIMP candidates.

The hypothesis that dark matter consists of WIMPs can be experimentally verified by using direct and indirect detection methods. Direct detection experiments are designed to detect the effects of interactions between WIMPs and nuclei inside a detector. Results are generally presented as a bound on the spin-(in)dependent (SI/SD) WIMP-proton elastic scattering cross section. The indirect detection principle is based on the detection of particles that are produced by self-annihilation of WIMPs, such as anti-matter particles, gamma-rays and neutrinos. A potentially interesting WIMP annihilation source is the Galactic Centre (GC), where the dark matter density is expected to peak sharply. For neutrinos specifically, massive astrophysical objects in the vicinity of Earth such as the Sun and the Earth itself constitute additional promising WIMP annihilation sources. The dark matter density is expected to be significantly enhanced at the centre of these objects, due to the capture of WIMPs caused by the combined effect of elastic scattering of WIMPs with nuclei in the object and gravity. Since neutrinos only interact weakly with other particles, they are able to escape from regions with high matter density and their direction points straight back at the centre of the source. Direct and indirect detection experiments are ongoing but have not yet found conclusive evidence for the existence of WIMPs.

WIMP annihilation at the centre of the Sun and the Earth has been simulated using the `WimpSim` simulation package, assuming the standard oscillation scenario. The ν_μ and $\bar{\nu}_\mu$ energy spectra at the surface of the Earth have been derived for various WIMP annihilation channels and WIMP masses. Regarding these spectra some generic remarks can be made. Generally, annihilation into vector-bosons results in harder spectra than annihilation into fermions. For the Sun, the $\bar{\nu}_\mu$ energy spectrum is always slightly harder than the ν_μ energy spectrum corresponding to the same channel and mass, since the ν_μ-nucleon cross section is slightly larger than the $\bar{\nu}_\mu$-nucleon cross section. For the Earth, the $\bar{\nu}_\mu$ and ν_μ energy spectra corresponding to the same channel and mass are always equal, indicating that neutrino interactions with matter during its propagation from the centre of the Earth to the detector are not significant for the neutrino energies considered here. Hence energy spectra for the Earth are always harder than for the Sun. Since the energy spectra for the Earth have not been influenced by neutrino propagation through matter, they should resemble the neutrino energy spectra from WIMP annihilation at the GC assuming the latter occur in vacuum. Simulation results show that neutrino emission from WIMP annihilation at the centre of the Sun can be considered point-like. In contrast, the angular distribution of neutrinos from WIMP annihilation at the centre of the Earth follows a Gaussian distribution with a standard deviation of several degrees.

The mSUGRA model has been used to evaluate the expected neutrino flux from neutralino annihilation at the centre of the Sun, the Earth and the GC. All results have been obtained with the `DarkSUSY` package for supersymmetric dark matter calculations. The calculations indicate that in most of mSUGRA parameter space, the neutralino is bino-like. The only exception is the so-called Hyperbolic Branch or Focus Point (HB/FP) region, where the neutralino is predominantly higgsino-like. The higgsino component enables neutralino annihilation into weak vector bosons, which significantly enhances the annihilation cross section. This suppresses the present neutralino energy density since the latter is inversely proportional to the total annihilation cross section. As a result, the present neutralino energy density in the HB/FP region is of the same order as the experimentally preferred value. The higgsino component of the neutralino in the HB/FP region of mSUGRA parameter space also significantly enhances the neutralino-nucleon elastic scattering cross section, which is dominated by the spin-dependent part. Regarding neutralino capture and annihilation in the Sun and the Earth, calculations indicate that the capture and annihilation processes are in equilibrium for the Sun, but only in the HB/FP region of mSUGRA parameter space. This is not the case for the Earth, which is simply not massive enough. The total muon-neutrino flux and the total induced muon flux at the surface of the Earth from neutralino annihilation in the Sun, the Earth and the GC have been calculated. As expected, the fluxes are significantly enhanced in the HB/FP region of mSUGRA parameter space. For the Earth and the GC, the total induced muon flux is smaller than one muon per km^2 per year for all cosmologically interesting mSUGRA models considered here, which is more than three orders below the current experimental limits. For the Sun however, the total induced muon flux in the same mSUGRA models can reach several thousand muons per km^2 per year. Hence, regarding the detection of neutrinos from WIMP annihilation, the Sun constitutes the most interesting candidate of the three sources considered here.

The ANTARES collaboration is currently operating the largest neutrino detector in the Northern Hemisphere. The detector is located at a depth of about 2.5 km in the Mediterranean Sea offshore from Toulon, France. The detector is based on the water-Cherenkov neutrino telescope concept. If a high-energy muon-neutrino interacts in the vicinity of the detector and produces a muon with a velocity that exceeds the speed of light in water, the muon will emit coherent radiation at a characteristic angle due to the Cherenkov effect. This radiation can be detected by an array of photo-multiplier tubes (PMTs) to reconstruct the direction and energy of the incident neutrino. Neutrino telescopes are most sensitive to muon-neutrinos due to the relatively long lifetime and mass of the muon. The ANTARES detector consists of 12 vertical detector lines in an octagonal layout. Each detector line comprises 25 storeys and each storey contains a triplet of 10-inch PMTs. The average distance between detector lines is 70 m, and vertically between adjacent storeys 14.5 m, resulting in an instrumented detector volume of about 0.02 km^3. The detector has been completed in May 2008. Prior to its completion, ANTARES has been taking data in intermediate configurations for more than two years.

The data acquisition system of ANTARES is based on the all-data-to-shore concept, in which all digitised PMT signals are sent to the onshore control station. Since most of the detected hits are due to random optical background, the data has to be filtered onshore to alleviate the data storage demand. Several trigger algortihms that search for muon signatures in the online data stream can run in parallel. The standard trigger algorithm searches for clusters of hits of a certain minimum size which are causally connected to each other within a certain time window. The source tracking trigger has been developed for any continuous neutrino source with a known direction. The directional information can be used to constrain the causality window, and thereby reduce the cluster condition. Additional cluster selection steps based on a linear track fit and the distribution of hits with respect to the track are implemented to suppress random clusters. The source tracking trigger is currently used during data-taking to monitor the GC. A detailed comparison study between the source tracking trigger and the standard trigger indicates that the trigger efficiency of the source tracking trigger is more than a factor of 10 higher in the low energy regime relevant to dark matter searches. A Monte Carlo study suggests that the observed periodical structure in the source tracking trigger rate is caused by the atmospheric muon flux and random optical background due to alignment of neighbouring detector lines with the direction of the source. This is conformed in data obtained with the GC trigger.

ANTARES data taken during the operation of the first 5 detector lines, from the end of January until the beginning of December 2007, has been used to search for neutrino signals from WIMP annihilation in the Sun and the GC. The effective livetime of this period corresponds to 132.4 days, of which the Sun (GC) was under the horizon for 66.1 (110.2) days. In the offline processing, the following steps are taken. First, data selection criteria are applied to ensure the detector was working nominally. Only data taken with the standard trigger are considered. The data sample is calibrated with the appropriate and most accurate calibration parameters available. The calibrated data are processed with the so-called AartStrategy reconstruction algorithm, which comprises four consecutive track fitting and hit selection procedures. Finally, track selection criteria are applied to reject the atmospheric muon background and to ensure an unambiguous determination of the azimuthal angle.

A detailed Monte Carlo study indicates that the number of selected tracks in the selected data sample can be reasonably well described by the atmospheric neutrino flux. The impurity caused by atmospheric muons is of the order of 1 %. The simulated atmospheric neutrino samples are used to derive the performance of the detector in terms of detection efficiency and pointing accuracy, taking into account the data-taking conditions and all data and track selection criteria used in this analysis. The angular resolution for neutrino energies less than 1 TeV, as expected for neutrinos from WIMP annihilation, is of the order of one degree. The effective area is calculated as function of the neutrino energy and direction. It is convoluted with the directional probability density function of the Sun and the GC during data-taking, as well as with the energy spectra for muon neutrinos for a typical hard ($\chi\chi \rightarrow W^+W^-$) and soft ($\chi\chi \rightarrow b\,\bar{b}$) WIMP annihilation channel and various WIMP masses, to derive the effective area as a function of the WIMP mass.

The agreement between the number of selected tracks in the data and the simulated atmospheric neutrino samples suggests that a distinct signal from WIMP annihilation has not been found in the data considered here. Hence, the aim of the analysis is to derive an upper limit on the muon-neutrino flux from WIMP annihilation in the Sun and the GC. Energy reconstruction is not used since the majority of the selected atmospheric neutrinos are of the same order as the typical WIMP mass. The calculation of the limit is based on the number of selected tracks in a cone around the Sun and the GC in data and in background. The expected number of background events from Monte Carlo simulations is in good agreement with the estimation obtained by randomising the direction and arrival time of the observed events. The upper limit on the number of tracks due to neutrinos from WIMP annihilation in the cone is calculated at 90 % C.L. assuming Poisson statistics and using the Feldman-Cousins approach. Similarly, the average upper limit in the absence of signal or signal sensitivity at 90 % C.L. is calculated. These are combined with the effective livetime and the effective area to calculate the upper limit on the total neutrino flux and the integrated neutrino flux sensitivity from pure WIMP annihilation into W^+W^- bosons and into $b\bar{b}$ quarks in the Sun and the GC, as a function of the WIMP mass and cone size. The size of the search cone is optimised by minimising the integrated neutrino flux sensitivity as a function of cone size. The optimum cone size is 8 degrees or smaller, depending on the WIMP mass. After calculating the muon effective area, the neutrino flux limits are transformed into muon flux limits. The flux limits for the GC are better than for the Sun, as expected from the harder energy spectra and the zenith angle distribution of the GC.

The total muon flux from WIMP annihilation in the Sun, $\Phi_{\mu^+ + \mu^-}$, is shown as a function of the WIMP mass m_χ in figure 8.1. The muon fluxes in mSUGRA, integrated above 1 GeV and in a cone with a half-aperture of 3° in the direction of the Sun, are indicated by colored dots. Only mSUGRA models in which $\Omega_\chi < 1$ are shown, divided into three categories according to their compatibility with the experimentally preferred value of the present dark matter energy density (dark blue models lie within $2\,\sigma$ of the preferred value). The upper limits at 90 % C.L. derived in this thesis are labeled as 'Antares-5'. Also shown are upper limits at 90 % C.L. from other experiments.

The total muon flux from WIMP annihilation in an astrophysical object can be related to the WIMP annihilation rate in that object. There is a direct correlation between the WIMP annihilation rate and the SI/SD WIMP-nucleon cross section, assuming the capture and annihilation rates of WIMPs in the object are in equilibrium and the capture process is dominated by the SI or SD cross section only. For the SD neutralino-proton cross section and neutralino annihilation in the Sun in mSUGRA, these assumptions are justified. The spin-dependent WIMP-proton cross section, $\sigma^{\mathrm{SD}}_{\chi p}$, is shown as a function of the WIMP mass m_χ in figure 8.2. The cross sections in mSUGRA are indicated by colored dots, only mSUGRA models in which $\Omega_\chi < 1$ are shown. The upper limits at 90 % C.L. derived in this thesis are labeled as 'Antares-5'. Also shown are the upper limits at 90 % C.L. from other experiments.

As can be seen from figures 8.1 and 8.2, the ANTARES limits derived in this thesis are not yet competitive with other experiments. However, taking into account the limited effective livetime of the data set (132 days in which the Sun was under the horizon for 66 days) and the partial completion of the detector (5 out of 12 detector lines), these limits should improve significantly in the coming years. Additionally, several improvements in the analysis can be made. The analysis in this thesis is based on a 'cut-and-count' method, in which events are selected if they satisfy reconstruction and directional requirements. Although the directional cut was optimised, the fit quality cut was simply chosen to reject essentially all misreconstructed atmospheric

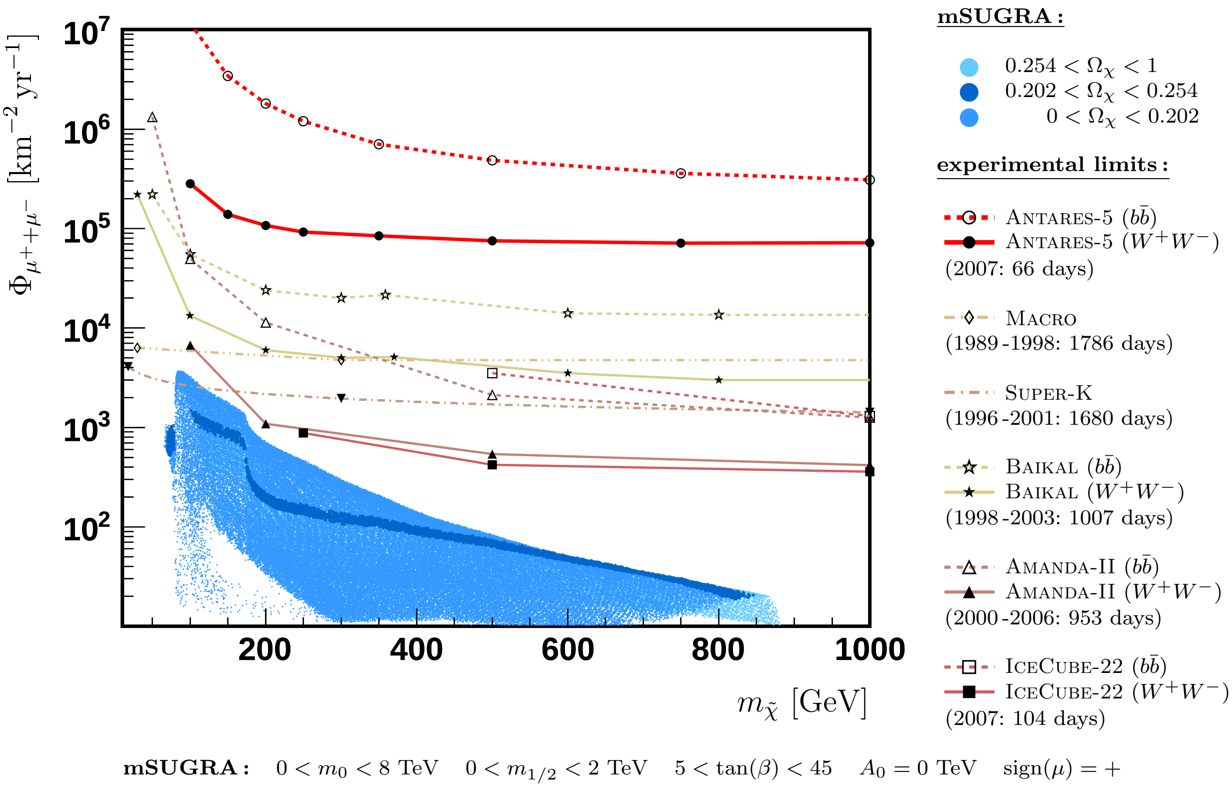

Figure 8.1: The total muon flux from WIMP annihilation in the Sun, $\Phi_{\mu^+ + \mu^-}$, as a function of the WIMP mass m_χ. The muon fluxes in mSUGRA, integrated above 1 GeV and in a cone with a half-aperture of 3° in the direction of the Sun, are indicated by colored dots. Only mSUGRA models in which $\Omega_\chi < 1$ are shown, divided into three categories according their compatibility with $\Omega_{\mathrm{DM}} = 0.228 \pm 0.013$ (dark blue models lie within $2\,\sigma$ of the preferred value). The upper limits at 90 % C.L. derived in this thesis are labeled as 'ANTARES-5'. Also shown are upper limits at 90 % C.L. from MACRO [57], Super-Kamiokande [58], Baikal [59], AMANDA [61] and IceCube [62].

muons. Instead, more sophisticated search techniques involving a hypothesis test based on a likelihood-ratio are typically more powerful. For instance, a likelihood involving probability density functions regarding the direction of the reconstructed track for signal and background. While background probability density functions can typically be derived using randomised data, signal probability density functions would have to be derived from Monte Carlo simulations. This allows for a less stringent fit quality cut by introducing some additional model-dependency. Furthermore, several improvements in data processing can be made. The trigger efficiency in the low energy regime, relevant to dark matter searches, increases by more than a factor of 10 by using the source tracking trigger instead of the standard trigger. Similarly, the reconstruction algorithm used in this thesis has been designed for high-energy neutrinos. A reconstruction algorithm with less stringent hit selection criteria should improve the efficiency in the

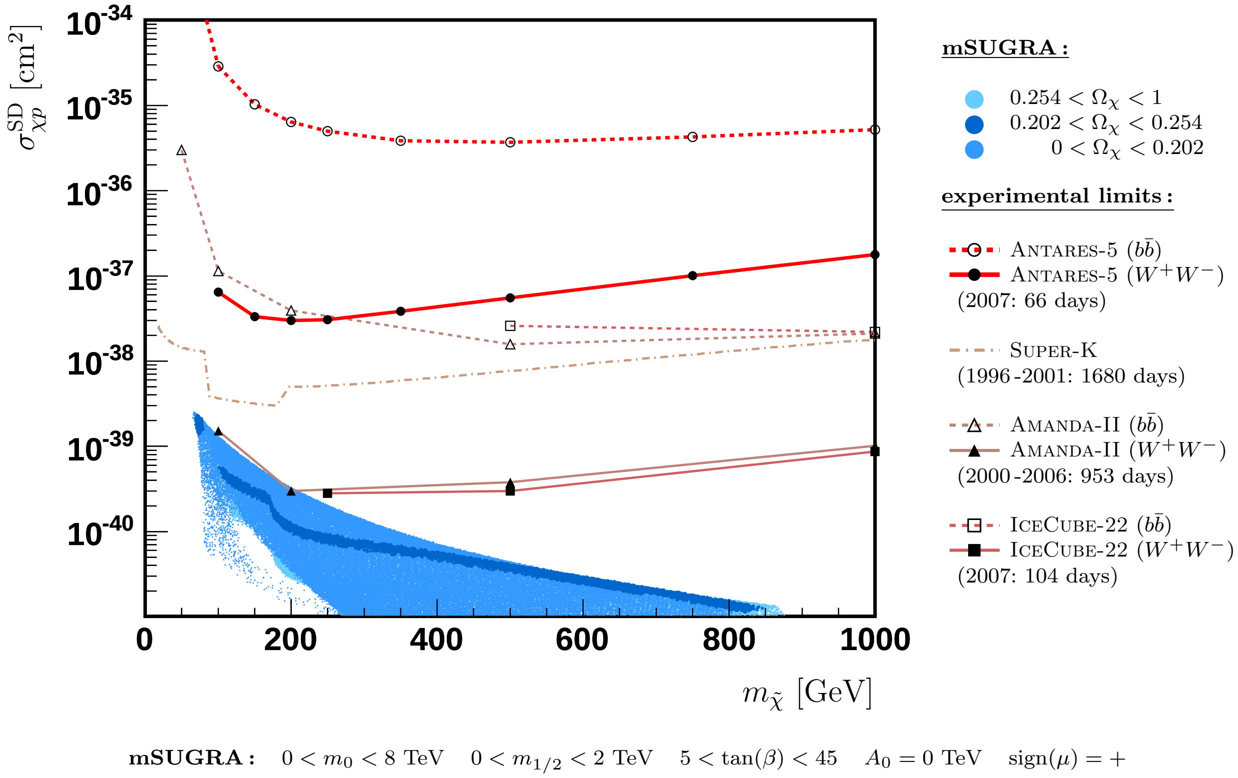

Figure 8.2: The spin-dependent WIMP-proton cross section, $\sigma^{\mathrm{SD}}_{\chi p}$, as a function of the WIMP mass m_χ. The cross sections in mSUGRA are indicated by colored dots. Only mSUGRA models in which $\Omega_\chi < 1$ are shown, divided into three categories according their compatibility with $\Omega_{\mathrm{DM}} = 0.228 \pm 0.013$ (dark blue models lie within $2\,\sigma$ of the preferred value). The upper limits at 90 % C.L. derived in this thesis are labeled as 'ANTARES-5'. Also shown are the upper limits at 90 % C.L. from Super-Kamiokande [58], AMANDA [61] and IceCube [62].

low-energy regime.

Indirect detection experiments using neutrinos are expected to start to constrain parts of the HB/FP region of mSUGRA parameter space in the coming years. Detection experiments that are sensitive to the spin-independent neutralino-nucleon cross section are expected to do the same. Neutralinos could also be produced in high-energy collisions at the currently operating Large Hadron Collider (LHC) at CERN, Switzerland. A study of the prospects for supersymmetry discovery in mSUGRA at the LHC shows that, assuming an integrated luminosity of 1 fm^{-1} and a centre of mass energy of 7 TeV (as expected at the end of 2011), the ATLAS and CMS experiments at the LHC will be able to cover the HB/FP region of mSUGRA parameter space up to $m_0 \simeq 2.3$ TeV and $m_{1/2} \simeq 450$ GeV [121]. For 100 fm^{-1} and a centre of mass energy of 14 TeV, the coverage of the HB/FP region of mSUGRA parameter space would extend up to $m_0 \simeq 5$ TeV and $m_{1/2} \simeq 700$ GeV [121].

Appendix A

Random optical background

The random optical background is simulated according to the actual PMT counting rates as measured during data taking. In this way, also the effects of broken PMTs and ARS chips, the quantum efficiency and gain of active PMTs, and the deadtime due to (the read out of) active ARS chips are taken into account. In the assessment of the trigger algorithms in Chapter 6, data runs 28712, 29105, 35428 and 37218 were used to simulate the random optical background. The background conditions during a run can be summarised by the following quantities :

- The baseline rate of a data run corresponds to the average PMT counting rate of all PMTs that were active during the data run.
- The burst fraction of a data run corresponds to the fraction of time for which the PMT counting rates were more than 20 % higher than the baseline rate.
- The active PMT fraction of a data run is the average ratio of active PMTs over total number of PMTs in the detector during the data run.

The values of these quantities corresponding to data runs 28712, 29105, 35428 and 37218 can be found in table A.1. The average PMT counting rates are shown in figure A.1, figure A.2, figure A.3 and figure A.4, respectively. The layout used in these figures reflects the detector configuration during data taking.

Data run	**28712**	**29105**	**35428**	**37218**
date	11/07/2007	16/08/2007	15/09/2008	18/11/2008
detector configuration	Line 1-5	Line 1-5	Line 1-12	Line 1-12
baseline rate	63.1 kHz	84.1 kHz	84.9 kHz	63.2 kHz
burst fraction	7 %	40 %	44 %	17 %
active PMT fraction	90.3 %	83.3 %	84.9 %	80.5 %

Table A.1: Data runs used to simulate the random optical background.

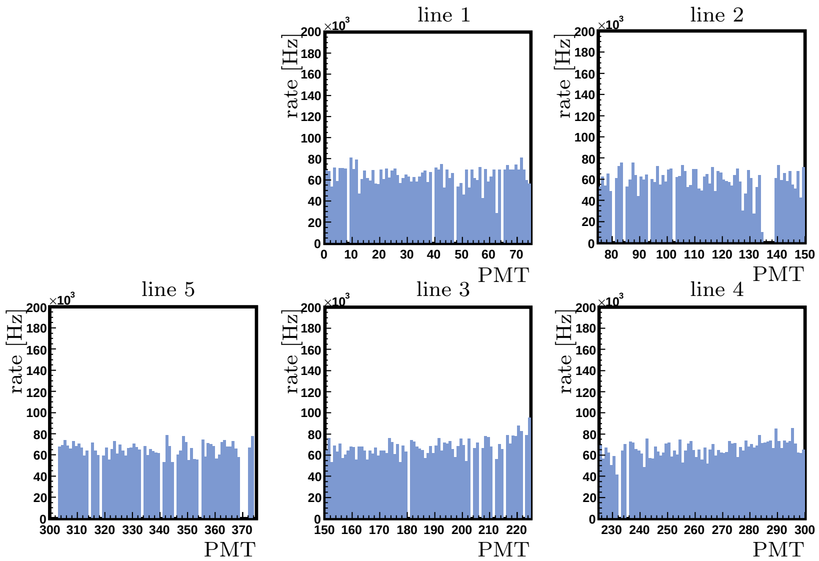

Figure A.1: The average PMT counting rates during data run 28712 (11/07/2007). The active PMT fraction is 90.3 %, the baseline rate is 63.1 kHz, the burst fraction is 7 %.

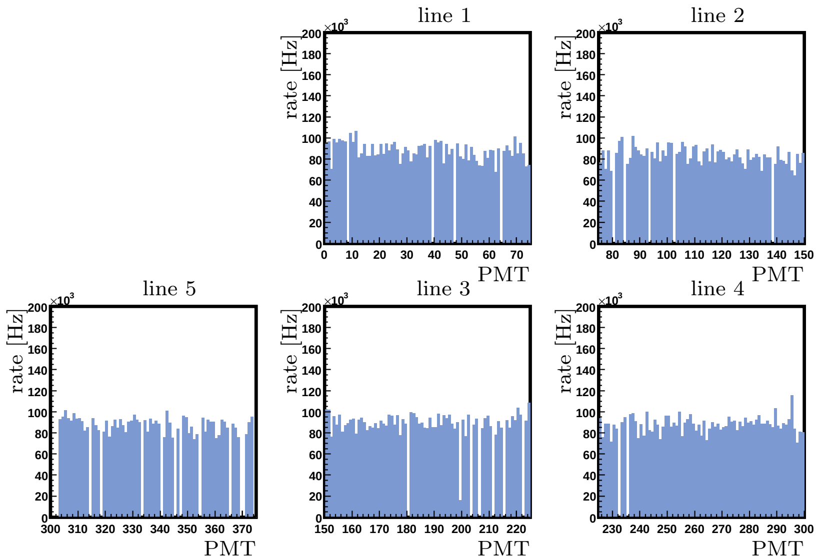

Figure A.2: The average PMT counting rates during data run 29105 (16/08/2007). The active PMT fraction is 83.3 %, the baseline rate is 84.1 kHz, the burst fraction is 40 %.

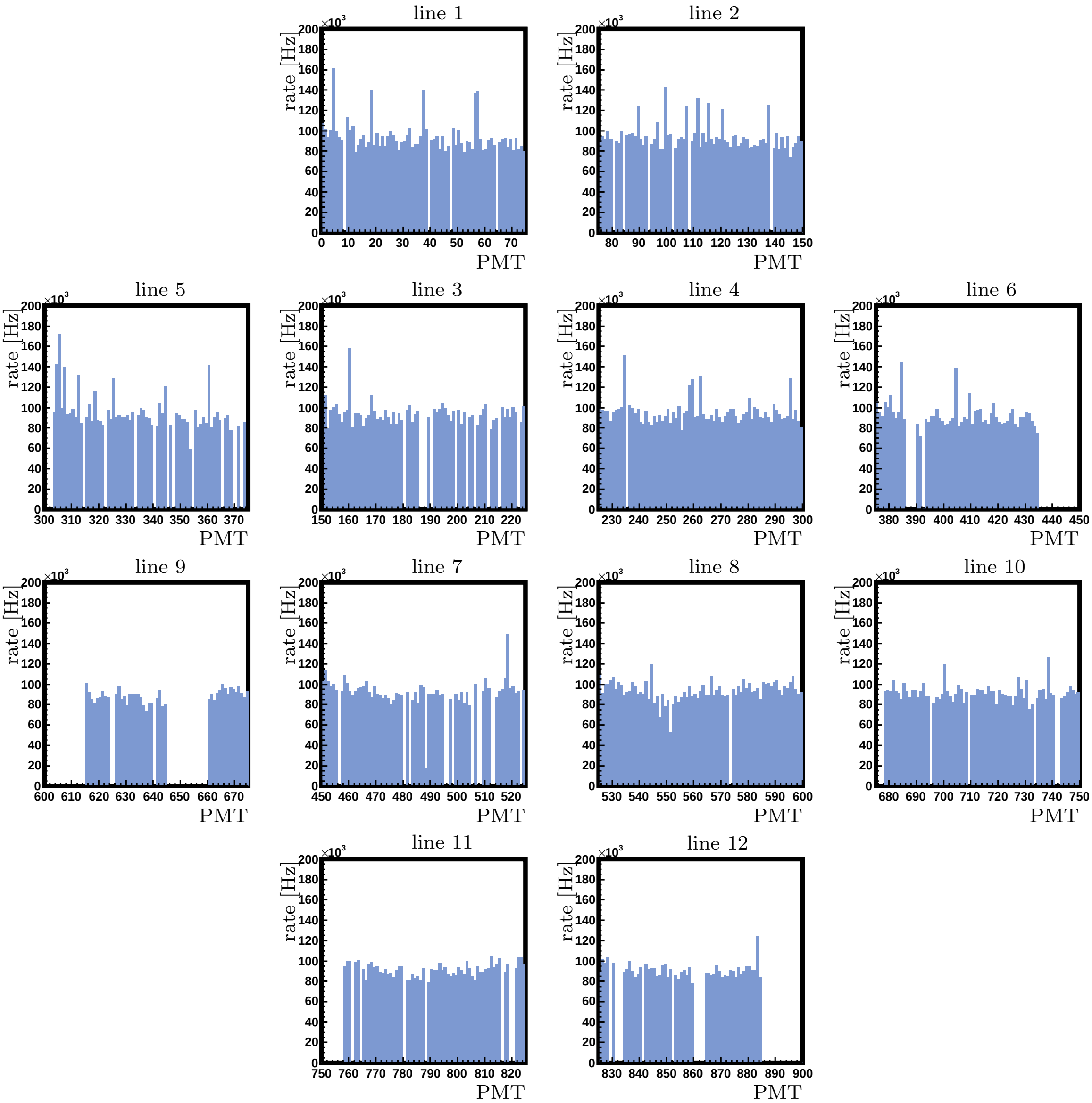

Figure A.3: The average PMT counting rates during data run 35428 (15/09/2008). The active PMT fraction is 84.9 %, the baseline rate is 84.9 kHz, the burst fraction is 44 %.

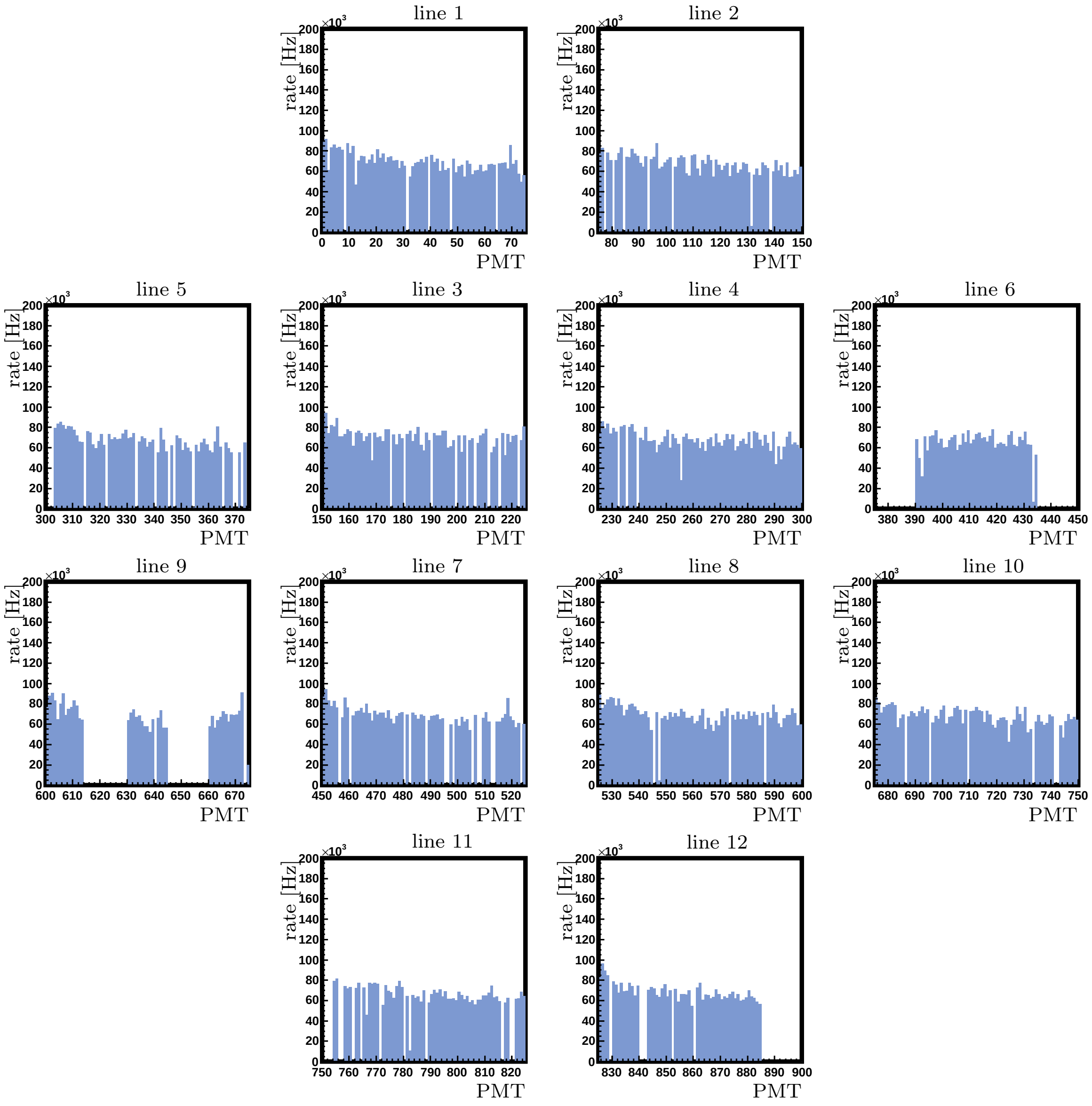

Figure A.4: The average PMT counting rates during data run 37218 (18/11/2008). The active PMT fraction is 80.5 %, the baseline rate is 63.2 kHz, the burst fraction is 17 %.

Appendix B

Positional astronomy

In this thesis, the correlation between potential neutrino sources and reconstructed tracks in ANTARES is calculated with the `SLALIB` positional astronomy library [122].

Coordinate systems and transformations

The positions of celestial objects in the Universe are generally defined in the equatorial coordinate system, as shown in figure B.1. As can be seen from this figure, the equatorial coordinate system is based on the projection of celestial objects on to a sphere in which the Earth sits at the centre, the so-called celestial sphere. The equatorial system is fixed to this sphere, while the Earth rotates in the centre. As in any spherical system, a position on the celestial sphere can be described by a longitudinal and a latitudinal angle. In the equatorial system, this is done with respect to the projection of the Earth's poles and the equator on the celestial sphere. The origin of longitude and latitude lies at the vernal equinox, the crossing point of the celestial equator and the Ecliptic (i.e. the apparent annual path of the Sun on the celestial sphere due to the Earth's rotation around the Sun) when the Sun moves to the North. The longitudinal and latitudinal angles are referred to as right ascension, α, and declination, δ, respectively. Right ascension is sometimes measured in units of time, where 24 hr $\sim 360°$. Since the Earth's rotation is influenced by the effects of precession and nutation, the positions of celestial objects in the equatorial system are not completely time independent. Hence, the position of a celestial object is always stated with respect to the epoch of observation. The change in equatorial coordinates between two different epochs is obtained using the `sla_preces` routine. The positions of all stars with an apparent magnitude $m < 6$ in the Julian epoch 2000 are shown in figure B.1. Also shown are the Galactic Centre and the plane of the Milky Way. The equatorial coordinates of the objects in the solar system such as the Sun are obtained using the `sla_rdplan` routine. Other celestial coordinate systems such as the ecliptic, galactic or super-galactic coordinate systems are similarly defined, but use a different plane of reference.

Reconstructed tracks in ANTARES are defined in the local horizontal coordinate system, as shown in figure B.2. This system is fixed to the location of ANTARES on the Earth. The cartesian coordinates x, y and z point to the East, the North and directly upwards, respectively. In the local system, a direction is defined in terms of

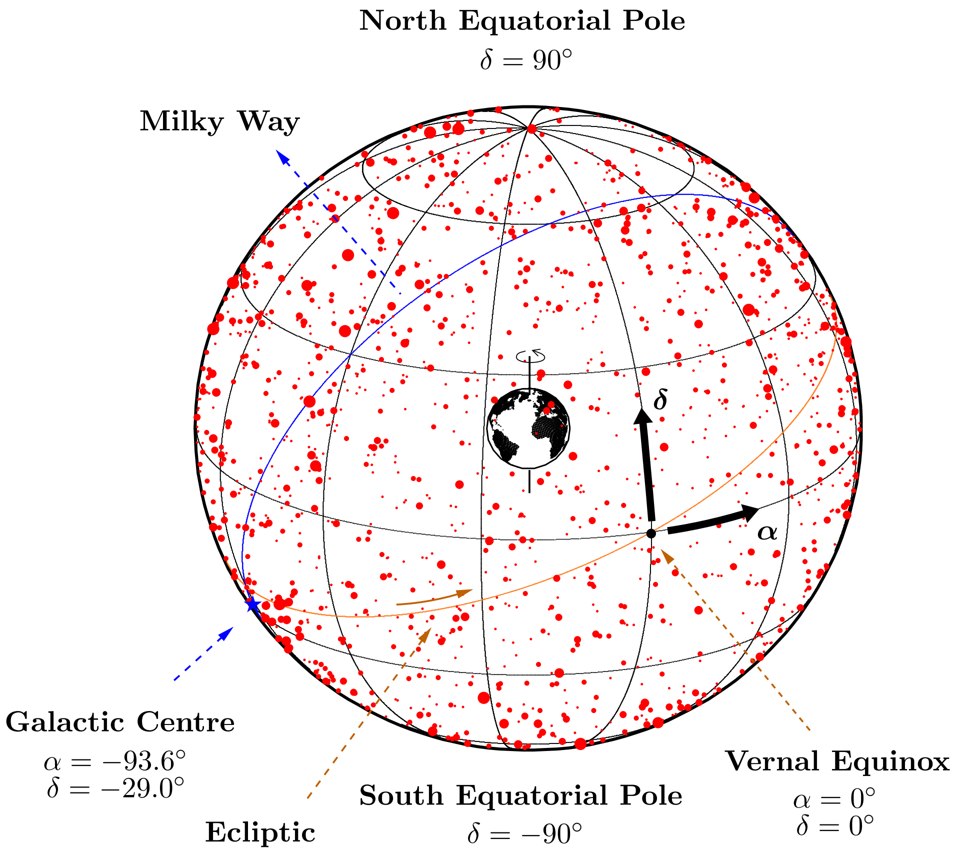

Figure B.1: The equatorial coordinate system. The celestial sphere includes all stars with an apparent magnitude $m < 6$, the Ecliptic, the Milky Way and the Galactic Centre (J2000).

two angles: The zenith angle θ, defined as the angle with respect to the positive z-axis (i.e. $0 \leq \theta \leq 180°$), and the azimuthal angle ϕ, defined as the counter-clockwise angle in the horizontal plane with respect to the positive x-axis (i.e. $0 \leq \theta \leq 360°$). Except for celestial objects in the direction of the celestial poles, the direction of any celestial object in the local system is a periodical function of time due to the rotation of the Earth. For objects outside the solar system, the time period is equal to one sidereal day, i.e. the amount of time it takes for the Earth to rotate once around its axis with respect to the stars [1].

Given the coordinates of a celestial neutrino source in the equatorial system, the direction of the source in the local horizontal system at ANTARES can be calculated by considering the rotation of the Earth and the position of Antares on the Earth. The transformation procedure is explained in figure B.2, which shows the direction

[1] In one year, the Earth makes about 365.25 rotations with respect to the Sun, but one extra rotation with respect to the stars. Hence, sidereal time units are about 365.25/366.25 times shorter than normal (solar) time units, e.g. there are 86164 seconds in one sidereal day.

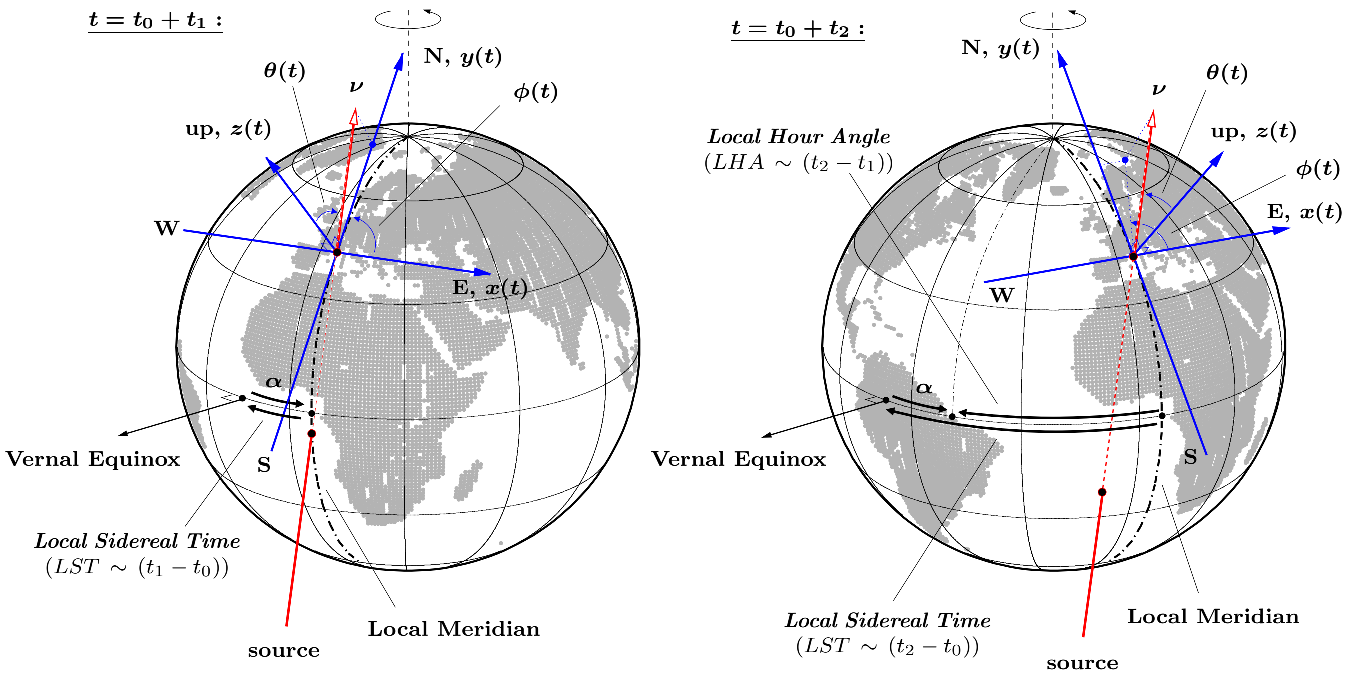

Figure B.2: The local horizontal coordinate system at ANTARES. The direction of a celestial neutrino source is shown at two different instances of time: In the left figure at $t = t_0 + t_1$, the source is directly above the local meridian at ANTARES. The right figure shows the situation at a later time $t = t_0 + t_2$.

of a celestial neutrino source at two different instances of time. In the left figure, at $t = t_0 + t_1$, the source is directly above the local meridian at ANTARES when the zenith angle of the source is minimal, i.e. the source is at upper culmination at ANTARES. The right figure shows the situation some time later at $t = t_0 + t_2$. Two quantities are needed for the transformation. The local sidereal time of an observer is defined as the amount of sidereal time that has passed since the vernal equinox was at upper culmination at the observer. The local sidereal time at ANTARES, LST_{ANT}, is related to the local sidereal time at the Greenwich meridian, LST_{GR}, through

$$LST_{\mathrm{ANT}} \;=\; LST_{\mathrm{GR}} \;+\; \phi_{\mathrm{ANT}} \;+\; EQX \tag{B.1}$$

where $\phi_{\mathrm{ANT}} = 6°10'$ is the longitude of ANTARES. The term EQX represents the so-called equation of the equinoxes, and takes into account the effects of precession and nutation on the position of the Vernal Equinox. Given the date and time, LST_{GR} and EQX are obtained from the `sla_gmst` and `sla_eqeqx` routines, respectively. The local hour angle (LHA) is defined as the difference between the local sidereal time of the observer and the right ascension of the source

$$LHA \;\equiv\; LST \;-\; \alpha \tag{B.2}$$

The LST and the LHA are angles that range between 0 and 24 sidereal hours, or equivalently $[0°, 360°]$. Their positive direction is clockwise (i.e. opposite to right ascension), so they increase with time as the Earth rotates counter-clockwise. The local hour angle and the declination can be transformed into local horizontal coordinates θ and ϕ via

$$
\begin{aligned}
\cos(\theta) &= \sin(\delta)\sin(\lambda_{\mathrm{ANT}}) + \cos(\delta)\cos(\lambda_{\mathrm{ANT}})\cos(LHA) \\
\sin(\phi') &= \frac{\sin(\delta) - \cos(\theta)\sin(\lambda_{\mathrm{ANT}})}{\sin(\theta)\cos(\lambda_{\mathrm{ANT}})} \Rightarrow \begin{cases} \phi = \phi' & \text{if } \sin(LHA) < 0 \\ \phi = \pi - \phi' & \text{if } \sin(LHA) > 0 \end{cases}
\end{aligned} \tag{B.3}
$$

where $\lambda_{\mathrm{ANT}} = 42°48'$ is the latitude of ANTARES. A plot of some examples of the time-dependent paths of various sources with different declinations in the ANTARES horizontal coordinate system is shown in figure 6.4. Oppositely, given the zenith and azimuthal angles of a reconstructed track in ANTARES and the time of its detection, the corresponding equatorial coordinates can be calculated with equation (B.2) and

$$
\begin{aligned}
\sin(\delta) &= \cos(\theta)\sin(\lambda_{\mathrm{ANT}}) + \sin(\theta)\cos(\lambda_{\mathrm{ANT}})\sin(\phi) \\
\cos(LHA') &= \frac{\cos(\theta) - \sin(\delta)\sin(\lambda_{\mathrm{ANT}})}{\cos(\delta)\cos(\lambda_{\mathrm{ANT}})} \Rightarrow \begin{cases} LHA = LHA' & \text{if } \cos(\phi) < 0 \\ LHA = 2\pi - LHA' & \text{if } \cos(\phi) > 0 \end{cases}
\end{aligned} \tag{B.4}
$$

The transformation from the equatorial to the horizontal system [2] and vice versa is done with the `sla_e2h` and `sla_h2e` routines, respectively.

The visibility of the ANTARES detector for an upgoing neutrino source is defined as the fraction of time the source is below the local horizon at ANTARES. The visibility can be calculated from equation (B.4) and equation (B.3), and is shown as a function of the declination of the source in figure B.3.

The Hammer-Aitoff projection

The Hammer-Aitoff projection is an equal-area projection method to map points on a sphere on to a plane. It is a particularly popular projection method amongst astronomers. The longitude ϕ and latitude λ on a sphere can be transformed to the x_{HA} and y_{HA} coordinates of the projection through

$$
x_{\mathrm{HA}} \equiv \frac{2\sqrt{2}\cos(\phi)\sin(\frac{\lambda}{2})}{\sqrt{1-\cos(\phi)\cos(\frac{\lambda}{2})}} \quad \text{and} \quad y_{\mathrm{HA}} \equiv \frac{\sqrt{2}\sin(\phi)}{\sqrt{1-\cos(\phi)\cos(\frac{\lambda}{2})}} \tag{B.5}
$$

[2] The definition of the horizontal coordinate system in the `SLALIB` library differs from the definition used in ANTARES and described in this appendix. In the `SLALIB` library, the cartesian coordinates x, y and z point to the North, the West and directly upwards, respectively. Hence, the azimuthal angle ϕ runs clockwise starting from the North.

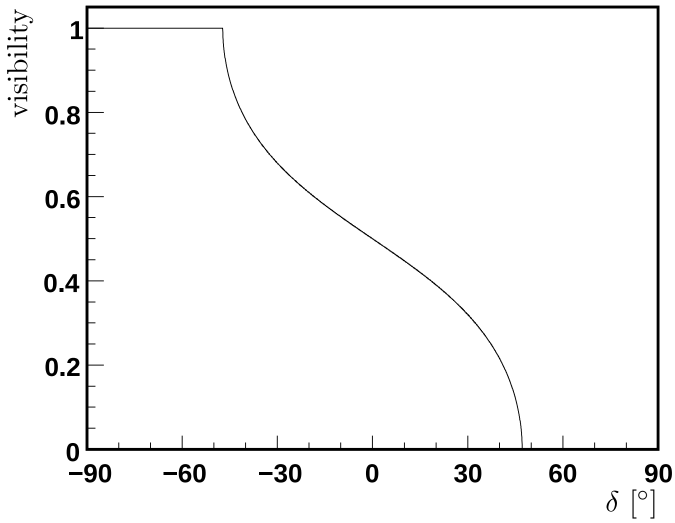

Figure B.3: The visibility of ANTARES for upgoing neutrino sources as a function of the declination of the source.

The Hammer-Aitoff projection is illustrated in figure B.4, which shows the projection of the celestial sphere in equatorial coordinates. Note that the positive direction of the x_{HA} coordinate is towards the left, as is customary in astronomy maps. The color scale indicates the ANTARES visibility, i.e. neutrino sources in the black and the white area are always above and below the local ANTARES horizon, respectively. Also shown are the positions of various potential galactic and extra-galactic neutrino sources such as supernova remnants (SNRs), active galactic nuclei (AGN), binary systems (BINs), pulsar wind nebulae (PWNe) and unidentified gamma-ray objects (UnIDs). Figure B.5 shows the projection of the celestial sphere in galactic coordinates. The origin of the galactic longitude l and latitude b lies in the direction of the Galactic Centre, while the equator corresponds to the Galactic Plane. The conversion between equatorial and galactic coordinates is done with the `sla_eqgal` and `sla_galeq` routines.

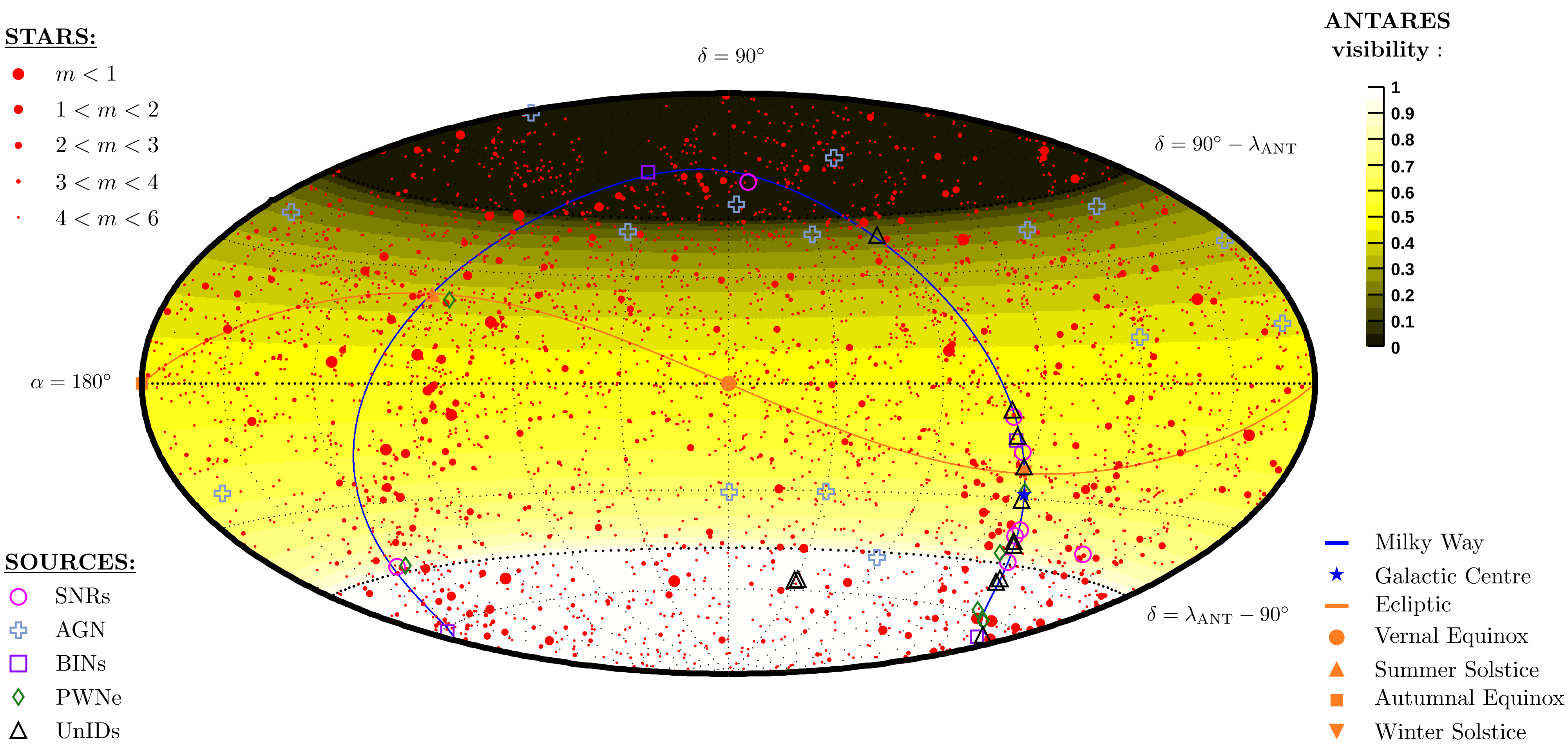

Figure B.4: The Hammer-Aitoff projection of the celestial sphere in equatorial coordinates.

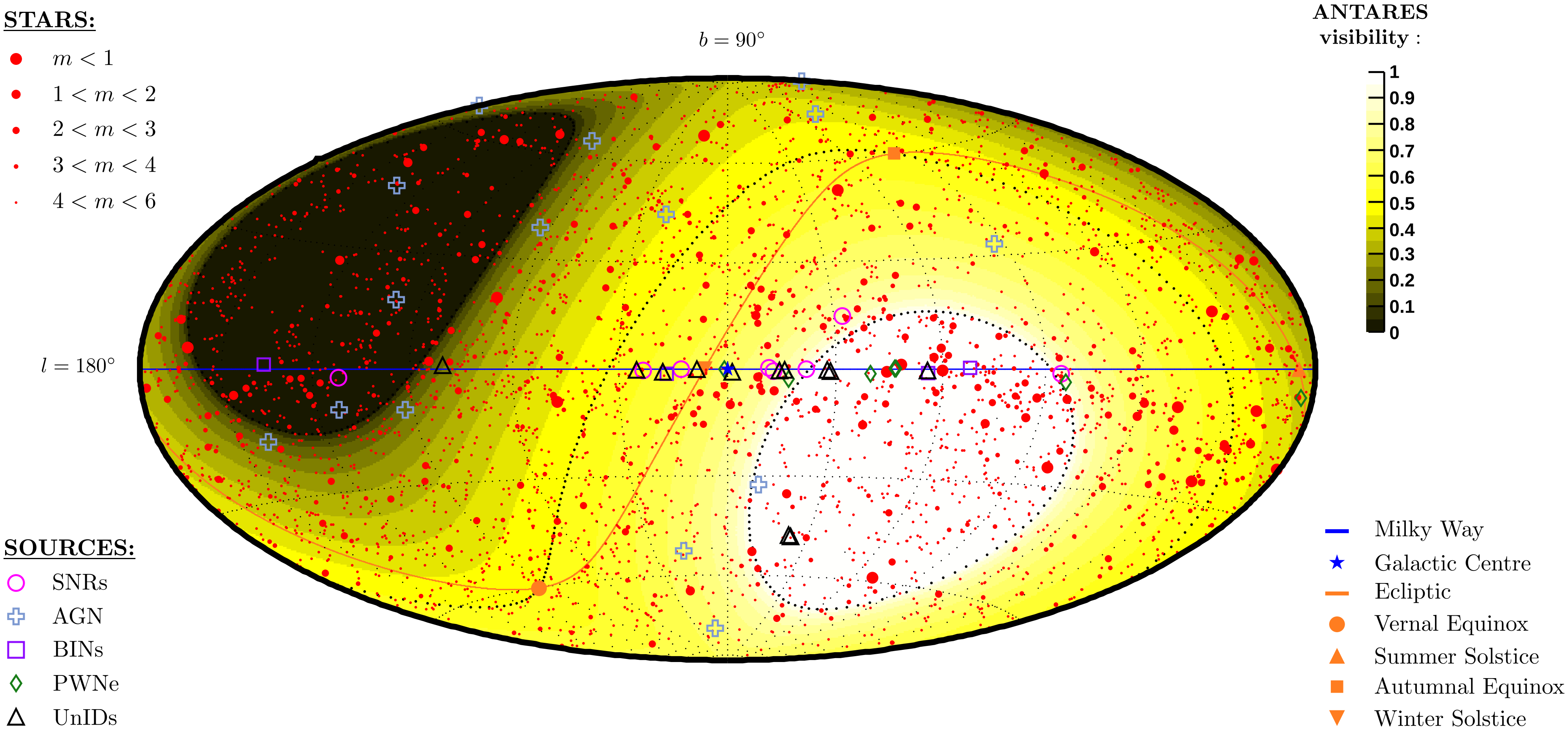

Figure B.5: The Hammer-Aitoff projection of the celestial sphere in galactic coordinates.

References

[1] M. Milgrom, *A modification of the Newtonian dynamics as a possible alternative to the hidden mass hypothesis*, The Astrophysical Journal 270, 365 (1983).

[2] G. Bertone et al., *Particle dark matter: evidence, candidates and constraints*, Physics Reports 405, 279 (2005).

[3] H. W. Babock, *The rotation of the Andromeda nebula*, Lick Observatory Bulletin 498, 41 (1939).

[4] V. C. Rubin et al., *Rotational properties of 21 Sc galaxies with a large range of luminosities and radii, from NGC 4605 (R = 4kpc) to UGC 2885 (R= 122kpc)*, The Astrophysical Journal 238, 471 (1980).

[5] T. S. van Albada et al., *Distribution of dark matter in the spiral galaxy NGC 3198*, The Astrophysical Journal 295, 305 (1985).

[6] A. Dekel et al., *Lost and found dark matter in elliptical galaxies*, Nature 437, 707 (2005).

[7] F. Zwicky, *Die Rotverschiebung von extragalaktischen Nebeln*, Helvetica Physica Acta 6, 110 (1933).

[8] A. D. Lewis et al., *Chandra observations of Abell 2029: the dark matter profile down to below 0.01 R_{VIR} in an unusually relaxed cluster*, The Astrophysical Journal 586, 135 (2003).

[9] G. Squires et al., *The dark matter, gas and galaxy distributions in Abell 2218: a weak gravitational lensing and X-ray analysis*, The Astrophysical Journal 461, 572 (1996).

[10] G. Hinshaw et al. (The WMAP Collaboration), *Five-year Wilkonson Microwave Anisotropy Probe. Observations: data processing, skymaps, and basic results*, The Astrophysical Journal Supplement 180, 225 (2009).

[11] L. Bergström, A. Goobar, *Cosmology and Particle Astrophysics*, Praxis Publishing Ltd (1999).

[12] S. Burles et al., *Big Bang Nucleosynthesis Predictions for Precision Cosmology*, The Astrophysical Journal Letters 552, 1 (2001).

[13] P. Tisserand et al. (EROS Collaboration), *Limits on the Macho content of the Galactic halo from the EROS-2 survey of the Magellanic Clouds*, Astronomy & Astrophysics 469, 387 (2007).

[14] K. Nakamura et al. (Particle Data Group), *Review of particle physics*, Journal of Physics G 37, 075021 (2010).

[15] V. Springel et al., *Simulations of the formation, evolution and clustering of galaxies and quasars*, Nature 435, 629 (2005).

[16] L. D. Duffy, K. van Bibber, *Axions as dark matter particles*, New Journal of Physics 11, 105008 (2009).

[17] E. W. Kolb, R. Slansky, *Dimensional reduction in the early universe: Where have the massive particles gone?* Physics Letters 135, 378 (1984);
G. Servant, T. M. P. Tait, *Is the lightest Kaluza-Klein particle a viable dark matter candidate?*, Nuclear Physics B 650, 391 (2003).

[18] H. Cheng, I. Low, *TeV symmetry and the little hierarchy problem*, Journal of High Energy Physics 09, 051 (2003).

[19] E. W. Kolb, M. S. Turner, *The Early Universe*, Addison-Wesley Publishing Company (1990).

[20] J. Binney, S. Tremaine, *Galactic Dynamics*, Princeton University Press (1987).

[21] F. J. Kerr, D. Lynden-Bell, *Review of galactic constants*, Royal Astronomical Society, Monthly Notices 221, 1023 (1986)

[22] G. Jungman et al., *Supersymmetric dark matter*, Physics Reports 267, 195 (1996).

[23] J. F. Navarro et al., *The structure of cold dark matter halos*, The Astrophysical Journal 463, 563 (1996).

[24] D. N. Spergel, *Motion of the Earth and the detection of weakly interacting massive particles*, Physical Review D 37, 1353 (1988).

[25] D. R. Tovey et al., *A new model-independent method for extracting spin-dependent cross section limits from dark matter searches*, Physics Letters B 488, 17 (2000).

[26] R. Bernabei et al. (DAMA/LIBRA Collaboration), *First results from DAMA/LIBRA and the combined results with DAMA/NaI*, The European Physical Journal C 56, 333 (2008).

[27] C. E. Aalseth et al. (CoGeNT Collaboration), *Results from a search for light-mass dark matter with a P-type point contact Germanium detector*, http://arxiv.org/abs/1002.4703.

[28] Z. Ahmed et al. (CDMS Collaboration), *Search for weakly interacting massive particles with the first five-tower data from the Cryogenic Dark Matter Search at the Soudan Underground Laboratory*, Physical Review Letters 102, 011301 (2009).

[29] E. Aprile et al. (XENON Collaboration), *First dark matter results from the XENON100 experiment*, Physical Review Letters 105, 131302 (2010).

[30] H. S. Lee et al. (KIMS Collaboration), *Limits on Interactions between weakly interacting massive particles and nucleons obtained with CsI(Tl) crystal detectors*, Physical Review Letters 99, 091301 (2007).

[31] S. Archambault et al. (PICASSO Collaboration), *Dark matter spin-dependent limits for WIMP interactions on ^{19}F by PICASSO*, Physics Letters B 682, 185 (2009).

[32] O. Adriani et al. (PAMELA Collaboration), *New measurement of the anti-proton-to-proton flux ratio up to 100 GeV in the cosmic radiation*, Physical Review Letters 102, 051101 (2009).

[33] O. Adriani et al. (PAMELA Collaboration), *An anomalous positron abundance in cosmic rays with energies 1.5-100 GeV*, Nature 458, 607 (2009).

[34] Q. H. Cao et al., *Dark matter: The leptonic connection*, Physics Letters B 673, 152 (2009).

[35] D. Hooper et al., *Pulsars as the sources of high energy cosmic ray positrons*, Journal of Cosmology and Astroparticle Physics 01, 025 (2009).

[36] A. Pullen et al., *Search with EGRET for a gamma ray line from the Galactic Center*, Physical Review D 76, 063006 (2007); ERRATUM: Physical Review D 83, 029904 (2011).

[37] F. Aharonian et al. (HESS Collaboration), *HESS Observations of the Galactic Center region and their possible dark matter interpretation*, Physical Review Letters 97, 221102 (2006).

[38] W. de Boer et al., *EGRET excess of diffuse galactic gamma rays as tracer of dark matter*, Astronomy & Astrophysics 444, 51 (2005).

[39] M. Ackermann (on behalf of the Fermi LAT Collaboration), *Observations of the extragalactic diffuse gamma-ray emission with the Fermi Large Area Telescope*, The 5$^{\text{th}}$ TeV Particle Astrophysics Conference (2009).

[40] J. D. Lykken, *Introduction to supersymmetry*, http://arxiv.org/abs/hep-th/9612114.

[41] U. Amaldi et al., *Comparison of grand unified theories with electroweak and strong coupling constants measured at LEP*, Physics Letters B 260, 447 (1991).

[42] S. Coleman, J. Mandula, *All possible symmetries of the S-Matrix*, Physical Review 159, 1251 (1967).

[43] R. Haag et al., *All possible generators of supersymmetries of the S-Matrix*, Nuclear Physics B 88, 257 (1975).

[44] S. P. Martin, *A supersymmetry primer*, http://arxiv.org/abs/hep-ph/9709356.

[45] M. Blennow et al., *Neutrinos from WIMP annihilations obtained using a full three-flavor Monte Carlo approach*, Journal of Cosmology and Astroparticle Physics 01, 021 (2008).

[46] P. Gondolo et al., *DarkSUSY manual and long description of routines*, http://www.physto.se/ edsjo/darksusy/docs/Manual.pdf.

[47] C. Amsler et al. (Particle Data Group), *Review of particle properties*, Physics Letters B 667, 1 (2008).

[48] M. Maltoni et al., *Status of global fits to neutrino oscillations*, New Journal of Physics 6, 122 (2004).

[49] L. Wolfenstein, *Neutrino oscillations in matter*, Physical Review D 17, 2369 (1978).
S. P. Mikheyev, A. Y. Smirnov, *Resonance Amplification of Oscillations in Matter and Spectroscopy of Solar Neutrinos*, Soviet Journal of Nuclear Physics 42,913 (1985).

[50] J. Edsjö, *Calculation of neutrino cross sections and the nusigma neutrino-nucleon scattering Monte Carlo*, http://copsosx03.physto.se/wimpsim/code/nucross3.pdf.

[51] J. N. Bahcall et al., *Solar Models: current epoch and time dependences, neutrinos, and helioseismological properties*, The Astrophysical Journal 555, 990 (2001);
N. Grevesse, A. J. Sauval, *Standard solar composition*, Space Science Reviews 85, 161 (1998).

[52] W. F. McDonough, *Treatise on Geochemistry, Volume 2*, Elsevier-Pergamon (2003).

[53] T. Sjöstrand et al., *PYTHIA 6.4 physics and manual*, Journal of High Energy Physics 05, 026 (2006).

[54] A. Gould, *Resonant enhancements in weakly interacting massive particle capture by the earth*, The Astrophysical Journal 321, 571 (1987).

[55] P. Ullio et al., *Cosmological dark matter annihilations into gamma-rays - a closer look*, Physical Review D 66, 123502 (2002).

[56] M. M. Boliev et al. (Baksan Collaboration), *Search for supersymmetric dark matter with Baksan Underground Telescope*, Nuclear Physics B - Proceedings Supplements 48, 83 (1996).

[57] M. Ambrosio et al. (MACRO Collaboration), *Limits on dark matter WIMPs using upward-going muons in the MACRO detector*, Physical Review D 60, 082002 (1999).

[58] S. Desai et al. (Super-Kamiokande Collaboration), *Search for dark matter WIMPs using upward-going muons in Super-Kamiokande*, Physical Review D 70, 083523 (2004).

[59] A. Avrorin et al. (on behalf of the Baikal Collaboration), *Search for neutrinos from dark matter annihilation in the Sun with the Baikal neutrino experiment*, Proceedings of the 31st International Cosmic Ray Conference (2009).

[60] A. Achterberg et al. (AMANDA Collaboration), *Limits on the muon flux from neutralino annihilations at the center of the Earth with AMANDA*, Astroparticle Physics 26, 129 (2006).

[61] J. Braun, D. Hubert (on behalf of the IceCube Collaboration), *Searches for WIMP dark matter from the Sun with AMANDA*, Proceedings of the 31st International Cosmic Ray Conference (2009).

[62] R. Abbasi et al. (IceCube Collaboration), *Limits on a muon flux from neutralino annihilations in the Sun with the IceCube 22-string detector*, Physical Review Letters 102, 201302 (2009).

[63] P. Gondolo et al., *DarkSUSY: computing supersymmetric dark matter properties numerically*, Journal of Cosmology and Astroparticle Physics 07, 008 (2004).

[64] H. Baer et al., *ISAJET 7.69: A Monte Carlo event generator for pp, $\bar{p}p$, and e^+e^- interactions*, http://arxiv.org/abs/hep-ph/0312045, http://www.nhn.ou.edu/~isajet/.

[65] K. Hagiwara et al. (Particle Data Group), *Review of particle properties*, Physical Review D 66, 010001 (2002).

[66] M. Drees, M. M. Nojiri, *Neutralino relic density in minimal N=1 supergravity*, Physical Review D 47, 376 (1993).

[67] G. Wikström, J. Edsjö, *Limits on the WIMP-nucleon scattering cross section from neutrino telescopes*, Journal of Cosmology and Astroparticle Physics 04, 009 (2009).

[68] The ANTARES Collaboration, *A deep sea telescope for high energy neutrinos*, http://arxiv.org/abs/astro-ph/9907432.

[69] D. J. L. Bailey, *Computation of maximum and effective muon ranges*, ANTARES internal note, `ANTARES-SOFT-2002-003`.

[70] P. Lipari, T. Stanev, *Propagation of multi-TeV muons*, Physical Review D 44, 3543 (1991).

[71] D. J. L. Bailey, *The effect of group velocity and dispersion on photon arrival times in the ANTARES detector*, ANTARES internal note, `ANTARES-PHYS-2001-005`.

[72] J. A. Aguilar et al. (ANTARES Collaboration), *Transmission of light in deep sea water at the site of the ANTARES neutrino telescope*, Astroparticle Physics 23, 131 (2005).

[73] C. Spiering, *Neutrino astrophysics in the cold: AMANDA, Baikal and IceCube*, Physica Scripta T 121, 112 (2005).

[74] M. A. Markov, *On high energy neutrino physics*, Proceedings of the 10^{th} International Conference on High Energy Physics (1960).

[75] A. J. Heijboer, *Track reconstruction and point source searches with ANTARES*, Ph.D. thesis, University of Amsterdam (2004).

[76] The Deep Underwater Muon and Neutrino Detection (DUMAND) Project, http://www.phys.hawaii.edu/~dumand/.

[77] The Baikal Neutrino Telescope, http://baikalweb.jinr.ru/.

[78] The Antarctic Muon And Neutrino Detector Array (AMANDA) Project, http://amanda.uci.edu/.

[79] The IceCube Neutrino Observatory, http://icecube.wisc.edu/.

[80] Astronomy with a Neutrino Telescope and Abyss environmental RESearch (ANTARES), http://antares.in2p3.fr/.

[81] The Neutrino Mediterranean Observatory (NEMO), http://nemoweb.lns.infn.it/.

[82] Neutrino Extended Submarine Telescope with Oceanographic Research (NESTOR), http://www.nestor.noa.gr/.

[83] P. Bagley et al. (KM3NeT Consortium), *KM3NeT: Technical design report for a deep-sea research infrastructure in the Mediterranean Sea incorporating a very large volume neutrino telescope*, http://www.km3net.org/KM3NeT-TDR.pdf.

[84] P. Amram et al. (ANTARES Collaboration), *The ANTARES optical module*, Nuclear Instruments and Methods in Physics Research A 484, 369 (2002);
J. A. Aguilar et al. (ANTARES Collaboration), *Study of large hemispherical photomultiplier tubes for the ANTARES neutrino telescope*, Nuclear Instruments and Methods in Physics Research A 555, 132 (2005).

[85] J. A. Aguilar et al. (ANTARES Collaboration), *The data acquisition system for the ANTARES neutrino telescope*, Nuclear Instruments and Methods in Physics Research A 570, 107 (2007);
B. A. P. van Rens, *Detection of magnetic monopoles below the Cherenkov limit*, Ph.D. thesis, University of Amsterdam (2006).

[86] J. A. Aguilar et al. (ANTARES Collaboration), *Performance of the front-end electronics of the ANTARES Neutrino Telescope*, Nuclear Instruments and Methods in Physics Research A 622, 59 (2010).

[87] R. Brun, F. Rademakers, *ROOT: an object oriented data analysis framework*, Nuclear Instruments and Methods in Physics Research A 389, 8186 (1997).

[88] M. Ageron et al. (ANTARES Collaboration), *The ANTARES optical beacon system*, Nuclear Instruments and Methods in Physics Research A 578, 498 (2007);
J. A. Aguilar et al. (ANTARES Collaboration), *Time Calibration of the ANTARES neutrino Telescope*, Astroparticle Physics 34, 539 (2011).

[89] A. M. Brown (on behalf of the ANTARES Collaboration), *Positioning system of the ANTARES neutrino telescope*, Proceedings of the 31st International Cosmic Ray Conference (2009).

[90] U. Fritsch (on behalf of the ANTARES Collaboration), *The ANTARES neutrino telescope*, Poster at the 12th Vienna Conference on Instrumentation (2010).

[91] J. Brunner, *Upgrade of K40 simulation*, ANTARES internal note, `ANTARES-PHYS-2006-005`.

[92] J. A. Aguilar et al. (ANTARES Collaboration), *Measurement of the atmospheric muon flux with a 4 GeV threshold in the ANTARES neutrino telescope*, Astroparticle Physics 33, 86 (2010); ERRATUM: Astroparticle Physics 34, 185 (2010).

[93] J. A. Aguilar et al. (ANTARES Collaboration), *Acoustic and optical variations during rapid downward motion episodes in the deep North Western Mediterranean*, Submitted to Deep Sea Research Part I (2011).

[94] M. de Jong, *The ANTARES trigger software*, ANTARES internal note, `ANTARES-SOFT-2005-005`.

[95] M. de Jong, *The ANTARES trigger parameters*, ANTARES internal note, `ANTARES-SOFT-2008-010`.

[96] M. C. Bouwhuis, *Detection of neutrinos from gamma-ray bursts*, Ph.D. thesis, University of Amsterdam (2005).

[97] M. de Jong, *Partial linearisation of the track fit problem*, ANTARES internal note, `ANTARES-PHYS-2007-001`.

[98] M. de Jong, *The convex hull of a point set*, ANTARES internal note, `ANTARES-PHYS-2007-008`.

[99] G. Carminati et al., *Atmospheric MUons from PArametric formulas: a fast GEnerator for neutrino telescopes (MUPAGE)*, Computer Physics Communications 179, 915 (2008);
M. Bazzotti et al., *An update of the generator of atmospheric muons from parametric formulas (MUPAGE)*, Computer Physics Communications 181, 835 (2010).

[100] D. J. L. Bailey, *Genhen v5r1 : software documentation*, ANTARES internal note, `ANTARES-SOFT-2002-004`.

[101] D. J. L. Bailey, *KM3 v2r1: User Guide*, ANTARES internal note, `ANTARES-SOFT-2002-006`.

[102] J. Brunner, ANTARES detector simulation based on GEANT 3.21, `http://antares.in2p3.fr/internal/software/geasim.html`.

[103] M. de Jong, *The TriggerEfficiency program*, ANTARES internal note, `ANTARES-SOFT-2009-001`.

[104] J. A. Aguilar et al. (ANTARES Collaboration), *Zenith distribution and flux of atmospheric muons measured with the 5-line ANTARES detector*, Astroparticle Physics 34, 179 (2010).

[105] D. J. L. Bailey, *Monte Carlo tools and analysis methods for understanding the ANTARES experiment and predicting its sensitivity to Dark Matter*, Ph.D. thesis, University of Oxford (2002).

[106] R. Bruijn, *The ANTARES neutrino telescope: performance studies and analysis of first data*, Ph.D. thesis, University of Amsterdam (2008).

[107] J. Brunner, *Analysis of 2007 and 2008 data with BBfit*, ANTARES internal note, ANTARES-PHYS-2009-006.

[108] V. Agrawal et al., *Atmospheric neutrino flux above 1 GeV*, Physical Review D 53, 1314 (1996);
G. D. Barr et al., *Three-dimensional calculation of atmospheric neutrinos*, Physical Review D 70, 023006 (2004).

[109] D. Heck et al., *CORSIKA: a Monte Carlo code to simulate extensive air showers*, Forschungszentrum Karlsruhe Report FZKA-6019 (1998).

[110] N. N. Kalmykov, S. S. Ostapchenko, *The nucleus-nucleus interaction, nuclear fragmentation, and fluctuations of extensive air showers*, Physics of Atomic Nuclei 56, 346 (1993).

[111] P. Antonioli et al., *A three-dimensional code for muon propagation through the rock: MUSIC*, Astroparticle Physics 7, 357 (1997).

[112] S. I. Nikolsky et al., *The composition of cosmic rays at energies of* 10^{15} *eV and higher*, Soviet Physics JETP 60, 10 (1984);
E. V. Bugaev et al., *Prompt leptons in cosmic rays*, Nuovo Cimento 12, 41 (1988).

[113] M. Anghinolfi et al., *New measurement of the angular acceptance of the Antares Optical Module*, ANTARES internal note, ANTARES-OPMO-2008-001.

[114] C. Reed, *Physics and Real (CalReal) release v2r0*, ANTARES internal note, ANTARES-SOFT-2008-006.

[115] C. Reed, *Calibration procedures for signal processing*, ANTARES internal note, ANTARES-CALI-2010-001.

[116] J. Hoessl et al., *ANTARES alignment (the linefit part)*, ANTARES internal note, ANTARES-CALI-2009-001.

[117] N. Cottini, *Real and Physics release v1r7*, ANTARES internal note, ANTARES-SOFT-2008-001.

[118] Numerical Algortihms Group, *NAG library manual*, http://www.nag.co.uk/.

[119] G. J. Feldman, R. D. Cousins, *Unified approach to the classical statistical analysis of small signals*, Physical Review D 57, 3873 (1998).

[120] G. C. Hill, K. Rawlins, *Unbiased cut selection for optimal upper limits in neutrino detectors: the model rejection potential technique*, Astroparticle Physics 19, 393 (2003).

[121] H. Baer et al., *Indirect, direct and collider detection of neutralino dark matter in the minimal supergravity model*, Journal of Cosmology and Astroparticle Physics 08, 005 (2004);
H. Baer et al., *Capability of LHC to discover supersymmetry with* $\sqrt{s}$ *=7 TeV and 1* fb^{-1} http://lanl.arxiv.org/abs/1004.3594.

[122] P. T. Wallace, *SLALIB - Positional astronomy library 2.5-3, programmer's manual*, http://star-www.rl.ac.uk/star/docs/sun67.htx/sun67.html.

Samenvatting

Donkere materie wordt alom beschouwd als een van de grootste onopgeloste mysteries in de hedendaagse natuurkunde. Experimentele waarnemingen op kosmologische lengteschalen tonen aan dat in het standaard kosmologische model bijna een kwart van de totale energie-dichtheid van het huidige observationele heelal bestaat uit donkere materie. Minder dan 5 % van de totale energie-dichtheid bestaat uit gewone baryonische materie zoals sterren en planeten, terwijl de rest wordt toegeschreven aan donkere energie. Diverse onafhankelijke waarnemingen op kleinere lengteschalen bevestigen dat ongeveer 80 % van alle materie in het heelal geen electromagnetische signatuur heeft. De suggestie dat donkere materie niet bestaat uit baryonen is in overeenstemming met voorspellingen van primordiale nucleosynthese en resultaten van gravitationele microlensing experimenten. Echter, direct bewijs voor het bestaan van donkere materie en een concreet begrip van de achterliggende natuur van donkere materie zijn tot dusver nog niet gevonden.

Kandidaten voor donkere materie zijn nieuwe types elementaire deeltjes, die zijn geproduceerd in het vroege heelal en die niet deelnemen aan de elektromagnetische- of sterke interacties. De waargenomen structuren in het heelal suggereren dat deze deeltjes niet langer relativistisch waren op het tijdstip van ontkoppeling van de rest van het heelal. De meest geliefde groep van deze koude donkere materie kandidaten zijn de zogenaamde zwakke interactieve massieve deeltjes (WIMPS). Diverse goed gemotiveerde uitbreidingen van het Standaard Model bevatten nieuwe elementaire deeltjes die WIMP eigenschappen bezitten. Basale thermodynamische argumenten impliceren dat de huidige waarde van de energie-dichtheid van de donkere materie kan worden verklaard door een theorie die een WIMP bevat welke een vergelijkbare interactie waarschijnlijkheid en massa heeft als de ijkbosonen van de zwakke interactie.

Dit is het geval voor vele supersymmetrische modellen. Supersymmetrie wordt alom beschouwd als een natuurlijke uitbreiding van het Standaard Model. Het biedt verschillende oplossingen voor enkele bekende problemen en tekortkomingen van het Standaard Model door de invoering van een nieuwe symmetrie die is gebaseerd op transformaties tussen bosonen en fermionen. Supersymmetrie voorspelt het bestaan van een zogenaamde superpartner voor elk deeltjes type in het Standaard Model. Aangezien geen van deze superpartners tot nog toe is ontdekt moet supersymmetrie een gebroken symmetrie zijn op de elektro-zwakke schaal. Om het aantal vrije parameters in de theorie te verminderen, wordt supersymmetrie meestal gecombineerd met het idee van 'Grand Unification', dat wordt gemotiveerd door de schijnbare vereniging van de elementaire krachten op de 'Grand Unification' schaal. In de zogenaamde minimale supergravitatie (mSUGRA) variant worden slechts vier aanvullende parameters en een teken ingevoerd. In het grootste gedeelte van de mSUGRA parameter ruimte is de lichtste superpartner de lichtste van de vier neutralinos, combinaties van de superpartners van de neutrale elektro-zwakke ijkbosonen en de neutrale Higgs-bosonen. Het neutralino is een favoriet onder alle voorgestelde WIMP kandidaten.

De hypothese dat donkere materie bestaat uit WIMPS kan experimenteel worden geverifieërd met behulp van directe en indirecte detectie methoden. Directe detectie experimenten zijn ontworpen om de effecten van interacties tussen WIMPs een atoomkernen in de detector te kunnen meten. Resultaten worden over het algemeen uitgedrukt als een limiet op de spin-(on)afhankelijke (SI/SD) WIMP-proton elastische verstrooings werkzame doorsnede. Het indirecte detectie principe is gebaseerd op de detectie van deeltjes die worden geproduceerd door de zelf-annihilatie van WIMPs, zoals anti-materie deeltjes, gamma-straling en neutrino's. Een potentieel interessante bron van WIMP zelf-annihilaties is het Galactische Centrum (GC), waar de dichtheid van donkere materie naar verwachting erg hoog is. Hetzelfde geldt voor de centra van massieve astrofysische objecten, als gevolg van de accumulatie van WIMPS die wordt veroorzaakt door enerzijds elastische verstrooiing van WIMPS met de atoomkernen in het object en anderzijds de zwaartekracht van het object. Dit maakt objecten dicht bij de Aarde zoals de Zon en de Aarde zelf interessant voor neutrino experimenten, aangezien neutrino's slechts zwak interageren met andere deeltjes waardoor ze in staat zijn om te ontsnappen uit regios met een hoge materie dichtheid en hun richting lijnrecht terug wijst naar de bron. Tot nu toe hebben diverse directe en indirecte detectie experimenten echter nog geen overtuigend bewijs voor het bestaan van WIMPs gevonden.

WIMP annihilatie in het centrum van de Zon en de Aarde is gesimuleerd met behulp van het `WimpSim` simulatie pakket, uitgaande van het standaard neutrino oscillatie scenario. De ν_μ en $\bar{\nu}_\mu$ energie spectra aan het oppervlak van de Aarde zijn uitgerekend voor verschillende WIMP massa's en annihilatie kanalen. Hieruit kunnen een aantal algemene conclusies worden getrokken. In het algemeen resulteert de annihilatie van vector-bosonen in hardere spectra dan de annihilatie van fermionen. Voor de Zon zijn de $\bar{\nu}_\mu$ energie-spectra altijd iets harder dan de ν_μ energie spectra, aangezien de ν_μ-nucleon werkzame doorsnede iets groter is dan de $\bar{\nu}_\mu$-nucleon werkzame doorsnede. Voor de Aarde zijn de $\bar{\nu}_\mu$ en ν_μ energie spectra altijd gelijk, wat aangeeft dat in dit energie regime de neutrino interacties met materie tijdens de propagatie van het centrum van de Aarde tot de detector geen significante invloed hebben. Vandaar ook dat de energie spectra voor de Aarde altijd harder zijn dan voor de Zon. De spectra voor de Aarde zouden gelijk moeten zijn aan die van het GC als wordt verondersteld dat de annihilaties in het GC plaats vinden in vacuum. Simulatie resultaten tonen aan dat neutrino emissie van WIMP annihilatie in het centrum van de Zon als puntvormig kan worden beschouwd. In tegenstelling, de hoekverdeling van neutrino's van WIMP annihilatie in het centrum van de Aarde volgt een Gaussische verdeling met een standaard deviatie van enkele graden.

Het mSUGRA model is gebruikt om de neutrino flux van neutralino annihilatie in het centrum van de Zon, de Aarde en het GC te berekenen. Alle resultaten zijn verkregen met behulp van het `DarkSUSY` pakket voor supersymmetrische donkere materie berekeningen. De berekeningen geven aan dat in het grootste gedeelte van de mSUGRA parameter ruimte, de bino-component van het neutralino dominant is. De enige uitzondering is de zogenaamde Hyperbolische Branch of Focus Point (HB/FP) regio, waar het neutralino tevens een significante higgsino-component heeft. De higgsino component maakt neutralino annihilatie in zwakke vector bosonen mogelijk, wat de werkzame doorsnede voor zelf-annihilatie aanzienlijk vergroot. Dit onderdrukt de huidige neutralino energie-dichtheid omdat deze omgekeerd evenredig is met de totale annihilatie werkzame doorsnede. Als gevolg daarvan is de huidige neutralino energie-dichtheid in de HP/FP regio van dezelfde orde als de experimenteel gemeten waarde. De higgsino component van het neutralino in de HP/FP regio vergroot tevens de neutralino-nucleon elastische verstrooiings werkzame doorsnede, die wordt gedomineerd door de spin-afhankelijke component. Uit simulaties blijkt dat de neutralino accumulatie en annihilatie processen in de Zon tegenwoordig in evenwicht verkeren, maar alleen in de HB/FP regio van de mSUGRA parameter ruimte. Dit is niet het geval voor de Aarde, omdat deze simpelweg niet genoeg massa bevat. De totale muon-neutrino flux en de totale geïnduceerde muon flux aan het oppervlak van de Aarde door neutralino annihilatie in de Zon, de Aarde en het GC zijn berekend. Zoals verwacht zijn de fluxen het hoogst in de HB/FP regio van de mSUGRA parameter ruimte. In het geval van de Aarde en het GC is de totale geïnduceerde muon flux minder dan een muon per km^2 per jaar, voor alle kosmologisch interessante mSUGRA modellen die hier zijn beschouwd. Dit is meer dan drie orders lager dan de huidige experimentele limieten. In dezelfde mSUGRA modellen kan de totale geïnduceerde muon flux van de Zon echter enkele duizenden muonen per km^2 per jaar bereiken. Dit maakt de Zon tot de meest interessante van de drie neutralino annihilatie bronnen die hier zijn beschouwd.

De ANTARES Collaboratie bestuurt momenteel de grootste neutrino detector op het noordelijk halfrond. De detector is gelegen op een diepte van ongeveer 2.5 km in de Middellandse Zee voor de kust van Toulon, in Frankrijk. De detector is gebaseerd op het water-Cherenkov neutrinotelescoop concept. Als een hoge-energetisch muon-neutrino interageert in de buurt van de detector kan het een muon produceren met een snelheid die de snelheid van het licht in het water overschrijdt. In dat geval zal het muon coherente straling uitzenden met een karakteristieke hoek als gevolg van het Cherenkov effect. Deze straling kan worden gedetecteerd door een matrix van foto-multiplicatie buizen (PMTs), waarmee uiteindelijk de richting en energie van het inkomende neutrino kan worden gereconstrueerd. Neutrino telescopen zijn het meest gevoelig voor muon-neutrino's vanwege de relatief lange levensduur en hoge massa van het muon. De ANTARES detector bestaat uit 12 verticale detector lijnen in een octagonale lay-out. Elke detector lijn bestaat uit 25 verdiepingen en elke verdieping bevat een triplet van 10-inch PMTs. De gemiddelde afstand tussen de detector lijnen is 70 m, en verticaal tussen aangrenzende verdiepingen 14.5 m, wat resulteert in een geïnstrumenteerd detector volume van ongeveer 0.02 km^3. De detector is voltooid in mei 2008. De metingen met ANTARES zijn echter al meer dan twee jaar daarvoor begonnen, in verschillende tussenliggende configuraties.

Het data acquisitie systeem van ANTARES is gebaseerd op het zogenaamde alle-data-aan-wal concept, waarbij alle gedetecteerde en gedigitaliseerde PMT-signalen (hits) worden doorgestuurd naar het kust station. Aangezien het merendeel van alle hits het gevolg is van de willekeurige optische achtergrond, worden de data-stroom aan wal gefilterd om de data-opslag te verlichten. Verschillende onafhankelijke filter algoritmes kunnen tegelijkertijd zoeken naar muon signaturen in de online data-stroom. Het standaard filter algoritme zoekt naar clusters van hits van een bepaalde minimale omvang die causaal met elkaar verbonden zijn binnen een bepaald tijdsvenster. Het bronvolg filter algoritme is ontwikkeld voor potentiële continue neutrino bronnen waarvan de positie op de hemelbol bekend is. De directionele informatie wordt gebruikt om het causaliteitsvenster te beperken. Daardoor is het mogelijk om de minimum cluster grootte te verminderen. Om willekeurige clusters te onderdrukken worden extra cluster selectie stappen op basis van een lineaire spoor fit en de verdeling van de hits met betrekking tot het spoor toegevoegd. Het bron-volg filter algoritme wordt momenteel gebruikt om het GC te volgen. Een gedetailleerde vergelijking tussen het bron-volg en standaard filter algoritmes geeft aan dat de filter-efficiëntie van het bron-volg filter algoritme meer dan een factor 10 hoger is voor lage energieën, wat interessant is voor de zoektocht naar donkere materie. Monte Carlo simulaties tonen aan dat de waargenomen periodieke structuur in de output van het bron-volg filter algoritme wordt veroorzaakt door de atmosferische muon flux en door de willekeurige optische achtergrond als gevolg van het samenvallen van naburige detector lijnen met de richting van de bron. Dit wordt bevestigd in de data verkregen met de GC filter.

Data die zijn verkregen met de eerste 5 detector lijnen van de ANTARES detector, van eind januari tot begin december 2007, zijn gebruikt om te zoeken naar neutrino's van WIMP annihilatie in de Zon en het GC. De effectieve levensduur van deze periode komt overeen met 132.4 dagen, waarvan de Zon (GC) onder de horizon was voor 66.1 (110.2) dagen. In de offline data verwerking zijn de volgende stappen genomen. In de eerste plaats zijn data selectie criteria toegepast om ervoor te zorgen de detector nominaal werkzaam was. Alleen gegevens die met het standaard filter algoritme zijn gevonden zijn geanalyseerd. De data zijn gekalibreerd met de meest nauwkeurige overeenkomstige kalibratie parameters die beschikbaar zijn. De gekalibreerde data zijn verwerkt door het zogeheten AartStrategy reconstructie algoritme, waarin vier opeenvolgende spoor recontructie en hit selectie procedures worden toegepast. Tenslotte zijn spoor reconstructie criteria toegepast op de atmosferische muon achtergrond te onderdrukken en een eenduidige bepaling van de azimutale hoek te waarborgen.

Een gedetailleerde Monte Carlo studie geeft aan dat het aantal geselecteerde sporen in de geselecteerde data redelijk goed kan worden beschreven door de atmosferische neutrino flux. De onzuiverheid veroorzaakt door atmosferische muonen is van de orde van 1 %. Atmosferische neutrino simulaties zijn gebruikt om de detector prestatie in termen van detectie efficientie en nauwkeurigheid af te leiden. Hierin is rekening gehouden met de willekeurige optische achtergrond tijdens de meetperiode en alle data en spoor reconstructie criteria die zijn gebruikt in de data analyse. De hoek resolutie van de detector voor neutrino energieën kleiner dan 1 TeV, zoals verwacht voor neutrino's van WIMP annihilatie, is van de orde van één graad. Het effectieve oppervlak van de detector is berekend als functie van de neutrino energie en richting. Deze is vervolgens geconvolueerd me de directionele waarschijnlijkheid-dichtheidsfunctie van de Zon en het GC tijdens de meetperiode, evenals met de energie spectra voor muon-neutrino's voor een typisch hard ($\chi\chi \to W^+W^-$) en zacht ($\chi\chi \to b\,\bar{b}$) WIMP annihilatie kanaal voor diverse WIMP massa's, om het effective oppervlak voor zachte/harde annihilatie in de Zon/GC te bepalen als functie van de WIMP massa.

De overeenkomst tussen het aantal geselecteerde sporen in de data en in de atmosferische neutrino simulaties blijkt dat er geen duidelijke signaal van WIMP annihilatie is gevonden in de geanalyseerde data. Het uiteindelijke doel van de analyse is daarom een berekening van de bovengrens van de muon-neutrino flux van WIMP annihilatie in de Zon en het GC. Energie-reconstructie is niet gebruikt aangezien de verwachte energieën van de geselecteerde atmosferische neutrino's van dezelfde orde als de typische WIMP massa. De berekening van de bovengrens is gebaseerd op het aantal geselecteerde sporen in een kegel rondom de Zon en het GC in de data en in de verwachte achtergrond. Het verwachte aantal achtergrond gebeurtenissen in de Monte Carlo simulatie is in goede overeenstemming met de schatting die wordt verkregen door het willekeurig verwisselen van de gereconstrueerde richting en aankomsttijd van alle waargenomen gebeurtenissen. De bovengrens op het aantal neutrino's van WIMP annihilatie in een kegel is berekend op 90 % CL door middel van de Feldman-Cousins methode uitgaande van Poisson statistiek. Tevens is de gemiddelde bovengrens in het geval dat er geen signaal is, ook wel signaal gevoeligheid genoemd, berekend op 90 % CL. De bovengrens op het aantal neutrinos is gecombineerd met de effectieve levensduur en het effectieve oppervlak om de bovengrens van de geïntegreerde neutrino flux van WIMP annihilatie naar W^+W^- bosonen en $b\bar{b}$ quarks in de Zon en het GC te berekenen als functie van de WIMP massa en kegel grootte. De kegel grootte is vervolgens geoptimaliseerd door de minimalisatie van de geïntegreerde neutrino flux gevoeligheid als functie van de kegel grootte. De optimale kegel grootte is 8 graden of kleiner, afhankelijk van de WIMP massa. Na de berekening van het effectieve muon oppervlak zijn de neutrino flux limieten omgezet in muon flux limieten. De flux limieten voor het GC zijn beter dan voor de Zon, zoals verwacht uit de hardere energie-spectra en de zenith hoek verdeling van het GC.

De totale muon flux van WIMP annihilatie in de Zon, $\Phi_{\mu^+ + \mu^-}$, is weergegeven als een functie van de WIMP massa m_χ in figuur 8.1. De verwachte muon flux in mSUGRA, geïntegreerd vanaf 1 GeV in een kegel met een halve openings hoek van 3° in de richting van de Zon, is aangegeven met gekleurde stippen. Alleen mSUGRA modellen waarin $\Omega_\chi < 1$ zijn weergegeven, onderverdeeld in drie categorieën afhankelijk van hun overeenkomst met de experimenteel gemeten waarde van de huidige donkere materie energie dichtheid (donkerblauw modellen liggen binnen $2\,\sigma$ van de gewenste waarde). De bovengrenzen op 90 % CL die zijn berekend in dit proefschrift zijn aangeduid met 'ANTARES-5'. Bovengrenzen op 90 % CL van andere experimenten zijn eveneens weergegeven.

De totale muon flux van WIMP annihilatie in een astrofysisch object kan worden gerelateerd aan de WIMP annihilatie snelheid in dat object. Er is een directe correlatie tussen de annihilatie snelheid en de SI(SD) WIMP-nucleon werkzame doorsnede, als wordt verondersteld dat de WIMP accumulatie en annihilatie processen in het object in evenwicht zijn en het accumulatie proces wordt gedomineerd door de SI (SD) WIMP-nucleon werkzame doorsnede. Deze veronderstellingen zijn gerechtvaardigd in mSUGRA in het geval van de SD neutralino-proton werkzame doorsnede en neutralino annihilatie in de Zon. De spin-afhankelijke WIMP-proton werkzame doorsnede, $\sigma_{\chi p}^{\mathrm{SD}}$, is weergegeven als een functie van de WIMP massa m_χ in figuur 8.2. De werkzame doorsnedes in mSUGRA voor modellen waarin $\Omega_\chi < 1$ zijn aangegeven met gekleurde stippen. De bovengrenzen op 90 % CL die zijn berekend in dit proefschrift zijn aangeduid met 'ANTARES-5'. Bovengrenzen op 90 % CL van andere experimenten zijn eveneens weergegeven.

Figuren 8.1 en 8.2 geven aan dat de ANTARES limieten berekend in dit proefschrift nog niet competitief zijn met andere experimenten. Echter, rekening houdend met de beperkte effectieve levensduur van de data set (ongeveer 132 dagen waarvan 66 onder de horizon in het geval van de Zon) en de gedeeltelijke voltooiing van de detector (5 van de 12 detector lijnen) in deze analyse, kunnen deze limieten in de komende jaren aanzienlijk worden verbeterd. Daarnaast kunnen verscheidene verbeteringen in de analyse worden aangebracht. De analyse in dit proefschrift is gebaseerd op een "knip-en-tel" methode, waarin de gebeurtenissen worden geselecteerd indien zij aan reconstructie en directionele eisen voldoen. Hoewel de directionele snede is geoptimaliseerd, is de reconstructie-kwaliteitssnede simpelweg zo gekozen om het merendeel van de (mis)gereconstrueerde atmosferische muonen te verwerpen. Meer geavanceerde zoek methodes waarin gebruik wordt gemaakt van een hypothese test op basis van een waarschijnlijkheid-ratio zijn over het algemeen efficienter. Bijvoorbeeld een waarschijnlijkheidsfunctie die is opgebouwd uit waarschijnlijkheid-dichtheidsfuncties met betrekking tot de richting van een gereconstrueerde spoor voor signaal en voor achtergrond. De waarschijnlijkheid-dichtheidsfunctie voor achtergrond kan worden afgeleid met behulp van willekeurig verwisselde data, terwijl de waarschijnlijkheid-dichtheidsfunctie voor signaal moet worden afgeleid met behulp van Monte Carlo simulaties. Hierdoor kan de reconstructie-kwaliteitssnede worden versoepeld ten koste van extra model-afhankelijkheid. Tevens kunnen een aantal verbeteringen in de data selectie worden gemaakt. De filter-efficiëntie in het lage energie regime, wat van belang is in de zoektocht naar donkere materie, is meer dan een factor 10 hoger als het bron-volg filter algoritme in plaats van het standaard filter algoritme wordt gebruikt. Hetzelfde geldt voor het reconstructie algoritme. Het algoritme dat is gebruikt in dit proefschrift is ontworpen voor de reconstructie van hoog-energetische neutrino's. Een reconstructie algoritme waarin minder strenge hit selectie criteria worden toegepast zal een efficiëntie verbetering geven in het lage energie regime.

Indirecte detectie experimenten met behulp van neutrino's zullen naar verwachting de komende jaren beginnen met de beperking van de mSUGRA parameter ruimte, voornamelijk in de HB/FP regio. Directe detectie experimenten die gevoelig zijn voor de spin-onafhankelijke neutralino-nucleon werkzame doorsnede zullen naar verwachting hetzelfde zullen doen, eveneens voornamelijk in de HB/FP regio. Neutralinos zouden echter ook kunnen worden geproduceerd in hoog-energetische botsingen in een deeltjes versneller zoals de momenteel actieve Large Hadron Collider (LHC) op CERN, in Zwitserland. Studies van de vooruitzichten voor de ontdekking van supersymmetrie in het mSUGRA scenario bij de LHC tonen aan dat, uitgaande van een geïntegreerde luminositeit van 1 fm^{-1} en een zwaartepunts-energie van 7 TeV (zoals verwacht aan het eind van 2011), de ATLAS en CMS experimenten bij de LHC in staat zullen zijn om de mSUGRA parameter ruimte te beperken tot $m_0 \simeq 2.3$ TeV en $m_{1/2} \simeq 450$ GeV [121]. Voor 100 fm^{-1} en een zwaartepunts-energie van 14 TeV, wordt verwacht dat de dekking van de mSUGRA parameter ruimte zich zal uitstrekken tot $m_0 \simeq 5$ TeV en $m_{1/2} \simeq$ 700 GeV [121].

Acknowledgements

Finally, the acknowledgements, an essential part of any PhD thesis. Because nobody writes a PhD thesis alone. I would like to thank everyone that has contributed to my thesis, in particular the following people.

First of all, I would like to thank the three wise men that guided me through my PhD, and I will do so in 'chronological' order. I want to thank Gerard van der Steenhoven and Maarten de Jong, for taking me on as a PhD student in the Nikhef ANTARES group. With his intricate knowledge of all aspects of the ANTARES project, I was fortunate enough to have Maarten as my supervisor. Maarten, I don't have to explain to you that without your help and your endless list of ideas, this would have been a very different thesis. I want to thank Gerard as group leader and neutralino working group coordinator for creating the pleasant working environment that I enjoyed during the first years of my PhD. Gerard, it was a dark day for Nikhef when you decided to leave and take on the position of Dean of the Faculty of Science and Technology at my old university. Since I had a contract with the University of Amsterdam, Paul Kooijman became my new promotor. Paul, I want to thank you for taking me under your wing in the final part of my PhD. Without your help, suggestions and encouragement, I would still be analysing data. I could not have asked for a better way to finish my PhD.

It was a pleasure for me to work in the multi-cultural melting pot that is the ANTARES group at Nikhef. I want to thank Jelle Hogenbirk for an excellent introduction to the Côte d'Azur during the Line Zero operation. I want to thank Els de Wolf, Jelena Petrovic, Mieke Bouwhuis and Patrick Decowski for their advice and encouragement. I am indebted to thank Ronald Bruijn and Salvatore Mangano for many useful discussions and their help. I am grateful to computer programming masterminds Andrea Sottoriva, Aart Heijboer and Corey Reed for sharing their tips and tricks. I want to thank Claudine Colnard and Eleonora Presani for the memorable halloween and sinterklaas parties. I want to thank Claudio Bogazzi for teaching me the tipo da spiaggia lifestyle. I want to thank Ching-Cheng Hsu, Dimitris Palioselitis, Nikos Tsirintanis and Tri Astraatmadja for good food, drinks and more. And last but not least, thanks to Guus Wijnker for making H350 such a cool place to work.

I enjoyed working with many people in the ANTARES Collaboration and I am thankful to everybody that contributed to ANTARES for making it possible for me to do my PhD in such a remarkable project. In particular, I want to thank Holger Motz for sharing the load in the neutralino working group. It was a pleasure for me to work with Niccolò Cottini on the reconstruction. I am grateful to Jürgen Brunner for his help whenever I experienced problems at the IN2P3 computing centre in Lyon. I want to thank Pascal Coyle for his help during my first shifts. I would like to thank the INFN Bologna group for their hospitality during my visit, and Annarita Margiotta for answering all my questions regarding the Monte Carlo productions.

I very much appreciated the social environment at Nikhef, including the countless happy hours, christmas dinners, herring-parties, et cetera. I would like to thank the Personnel Association and Johan Dokter for the seemingly unlimited supply of drinks and bitterballen. A week at Nikhef is not complete without the friday afternoon borrel. I would like to thank all organisers, including Fabian Jansen, Javraamarcopo, Martijn Gosselink and Party Centrum Heijboer for their generosity and hospitality. A silent coffee break or a quiet night at home was never an option thanks to many people, including Alex Koutsman, Alexander Doxiades, Aras Papadelis, Chiara Farinelli, Daan van Eijk, Eduard Simioni, Edwin Bos, Ermes Braidot, Eva Schenk, Francesco Zappon, Gabriel Ybeles-Smit, Giampiero Fanizzi, Gideon Koekoek, Giulia Vannoni, Hegoi Garitaonandia, Hella Snoek, Jeroen Dreschler, Joana Montenegro, John Ottersbach, Lisa Hartgring, Maaike Limper, Marcello Barisonzi, Marten Bosma, Menelaos Tsiakiris, Mikolaj Krzewicki, Pieter van den Berg, Serena Oggero, Surya Bonam and Zdenko van Kesteren.

Nothing beats a long day of segmentation faults and other computer trouble like running after a spherical object with a group of grown men for an hour or two. It was a pleasure for me to play in the traditional Cern-versus-the-Rest matches and UvA Roeters Eiland tournaments, the SHELL Indoor League with the AMolf-nikhEF (AMEF) team and the Science Park in- and outdoor games. I had the honour to play alongside football legends such as Alex Ter Beek, Claudio Bogazzi, Dimitri John, Ed van Willigen, Egge van der Poel, Eric Laenen, Fred Bulten, Ido Mussche, Ivo van Vulpen, Jochem Snuverink, Manuel Kayl, Martijn Overbeek, Michele Maio, Muzaffer Pancar, Niels Tuning, Patrick Motylinksi, Paul de Jong, Paul Kooijman, Reinier de Adelhart Toorop, Sascha Caron, Salvatore Mangano, Thomas Bernard, Tristan Dupree, Victor Guevara and Yves Fomekong Nanfack.

There were also valuable lessons to be learned in less injury-prone games. Make sure you have a proper warm-up before you pick up a ping-pong bat against the likes of Andrea Sottoriva, Bob Dirks, Bram van Rens, Claudio Bogazzi, Manouk Rijpstra, Marco Bazzotti or Salvatore Mangano. In a pool hall, do not get hustled by the innocent faces of Antonello Sbrizzi, Antonio Pellegrino, ATLAS-II, Golden Ballz, Jacopo Nardulli, Jan Visser, Niels Tuning or Tristan Dupree. How about a friendly game of tablesoccer against Martijn Gosselink and Salvatore Mangano, or a round of Mario Kart against Aart Heijboer or Jan Amoraal? Forget about it.

Starting up in the morning was always a pleasure thanks to Abdul Mejdoubi and Trees van Dongen. Lunch at Nikhef was fun thanks to Rob Korver and Khalid El Mouzaine at the Nikhef cafeteria. I am grateful to Hayo Timmerman for opening the gate whenever I forgot to register my key again. I want to thank Nico Rem for helping me out whenever my car was giving me hassle, and thanks to Frank Linde for not towing it away. I want to thank Caroline Magrath and her family for their support at the start of my PhD. I want to thank Bob Dirks, Bram van Rens and the rest of de JMW19 for the good times at the old coffee factory. I am indebted to Ed van Willigen for hooking me up at the CMacG when I needed it. I want to thank AJW, Aukie Baas, de Dope Show, Ome Hein and Don Vedat for klaverjas, snowfun and other nonsense.

I am honoured to have Fabian Jansen and Sipho van der Putten as my paranymphs. With these bright young men of science by my side, the scientific content of my thesis defense ceremony is already guaranteed. Thanks guys, for sharing this moment with me in style.

I am grateful to my family for their unwavering care and unconditional support, and for listening to all my nerd talk during family get-togethers. Thanks to all of you I will never forget what *really* are the important things in life.

Finally, I want to thank Giada Carminati, for all her help and support, and for being brava and stepping into the future with me. Amore, fra tutte le cose conquistate durante il mio dottorato, tu sei di gran lunga il tesoro più grande.